Exciton Diffusion in Perovskite Nanocrystal Assemblies

Michael Franz Lichtenegger

München, 2023

Exziton Diffusion in Perowskit Nanokristall Ensembles

Dissertation

zur Erlangung des Doktorgrades der Naturwissenschaften (Dr. rer. nat.)

an der Fakultät für Physik

der Ludwig-Maximilians-Universität München

vorgelegt von

Michael Franz Lichtenegger

aus Regensburg

München, 16.08.2023

Erstgutachter:	Prof. Dr. Alexander Urban
Zweitgutachter:	Prof. Dr. Thomas Weitz
Tag der mündlichen Prüfung:	25.09.2023

dedicated to my family
Stefanie, Monika and Franz-Xaver

Publications and conferences

Scientific Publications of Results Presented in This Work
*** denotes equal contribution**

- M. F. Lichtenegger, J. Drewniok, A. Bornschlegl, C. Lampe, A. Singldinger, N. A. Henke, A. S. Urban
  Electron–Hole Binding Governs Carrier Transport in Halide Perovskite Nanocrystal Thin Films
  ACS Nano 16(4): 6317-6324 (2022)

- Andreas J. Bornschlegl*, Michael F. Lichtenegger*, Leo Luber, Carola Lampe, Maryna I. Bodnarchuk, Maksym V. Kovalenko, Alexander S. Urban
  Dark-Bright Exciton Splitting Dominates Low-Temperature Diffusion in Halide Perovskite Nanocrystal Assemblies
  under review (2023)

Additional Publications

- Sirri B. Kalkan, Emad Najafidehaghani, Ziyang Gan, Jan Drewniok, Michael F. Lichtenegger, Uwe Hübner, Alexander S. Urban, Antony George, Andrey Turchanin, Bert Nickel
  High-Performance Monolayer MoS_2 Field-Effect Transistors on Cyclic Olefin Copolymer-Passivated SiO_2 Gate Dielectric
  Adv. Opt. Mater. 11(2): 2201653 (2023)

Contributions to Conferences and Workshops

- *8th SolTech Conference* (Poster)
  Nürnberg, Germany, September 2019

- *TUM-IAS Focus Workshop* (Poster)
  Munich, Germany, October 2019

- *11th International Conference on Quantum Dots* (Poster)
  Munich, Germany, December 2020

- *NANOHYBRID - Hamburg Conference on Complex Nanostructures* (Talk)
  Hamburg, Germany, October 2022

- *MRS Fall Meeting* (Talk)
  Boston, USA, December 2022

Zusammenfassung

Perowskit-Nanokristalle (PNKs) haben im letzten Jahrzehnt ihr herausragendes optoelektronisches Verhalten unter Beweis gestellt. Für Anwendungen ist ihr Transportverhalten in Ensembles von entscheidender Bedeutung, wobei es weiterer Forschung zu verschiedenen Parametern bedarf, die die Exzitonendiffusion beeinflussen. Zu den intrinsischen Parametern gehören PNK-Größe, -Form und -Fallendichte, wohingegen extrinsische Parameter die Systemtemperatur, die Anregungsleistung und PNK-Filmeigenschaften wie die Filmordnung und die Dichte der Hohlräume sind.
Hier berichten wir über die Exzitonendiffusion in $CsPbBr_3$ PNK-Filmen und Übergitterstrukturen (ÜG) im Temperaturbereich von 10 – 350 K. Die Abhängigkeit der Exzitonendiffusion von der PNK-Größe wird experimentell beobachtet und durch Monte-Carlo-Simulationen unterstützt. Hierfür werden Perowskit-Nanoplättchen (PNPs) unterschiedlicher Dicke, d.h. 3 oder 5 Monolagen (MLs), mit würfelförmigen PNKs verglichen. Bei größeren PNKs ist der Exzitonentransport stärker ausgeprägt, was auf die geringere Anzahl an Förster-Resonanzenergietransfer (FRET) Schritten zurückzuführen ist, die für gleiche Exzitonenstrecken erforderlich sind, und auf weniger Fallenzustände, die die Diffusion in größeren PNKs behindern. Während die Exzitonendiffusion in den größten PNKs am größten ist, ist sie in PNP-Filmen immer noch überraschend groß. Der Grund für die hohe Exzitonendiffusion in PNP-Filmen liegt an ihrer anisotropen Form, da sie sich entlang ihrer größeren Facette ausrichten, was zu PNP-Stapel führt. In diesen Stapeln können Exzitonen über mehrere PNPs delokalisiert werden, was die Exzitonendiffusion verbessert. Hohlräume in PNK-Filmen und endliche PNP-Stapellängen begrenzen die Diffusion, was zu einem subdiffusiven Exzitonentransport führt. Die Exzitonendiffusion hängt stärker von den intrinsischen PNK-Eigenschaften als von der Filmordnung ab, was durch den Vergleich der Exzitonendiffusion in ÜG und in ungeordneten PNK-Filmen deutlich wird, bei denen die PNK-Würfelgröße die Ordnung übertrifft. Neben den intrinsischen PNK-Eigenschaften, dem Filmtyp und der Qualität ist die Exzitonendiffusion auch von extrinsischen Parametern wie der Systemtemperatur abhängig. Die Diffusion nimmt zu, wenn die Temperatur von 9 K auf 100 K erhöht wird, und nimmt dann bei weiterer Temperaturerhöhung ab. Der Ursprung dieses Verhaltens ist komplex und umfasst mehrere konkurrierende Mechanismen. Der Niedertemperaturbereich wird durch die hell-dunkel-Exzitonenaufspaltung für 3 ML PNPs und ÜG, bestehend aus 5 nm- und 8 nm-PNKs, bestimmt. Exzitonen, die den energetisch tiefen liegenden dunklen Zustand besetzen, weisen eine unterdrückte FRET-Rate auf, wohingegen Exzitonen in hellen Zuständen sehr mobil sind. So führen helle Exzitonen zu frühen Zeiten zu einer schnellen Diffusion. Aufgrund der kurzen Lebensdauer der hellen Zustände, bleiben nach einiger Zeit nur noch dunkle Exzitonen übrig und bestimmen die Diffusionsdynamik. Die hell-dunkel-Aufspaltung ist für 14 nm PNK Würfel zu gering, daher beeinflusst es den Exzitonentransport kaum. Bei Temperaturen über 100 K reicht die thermische Energie aus, um von den dunklen in die hellen Zustände zu gelangen, und thermisch aktivierte tiefe Exzitonenfallen dominieren den Diffusionsprozess. Eingefangene Exzitonen haben eine verringerte Rekombinationsrate und können ihre Energie nicht auf benachbarte PNKs übertragen. Die unterschiedlichen Strahlungszerfallsraten führen schließlich dazu, dass nach Vielfachen der Exzitonenlebensdauer, mehr eingefangene als mobile Exzitonen vorliegen. Da gefangene Exzitonen die Photolumineszenzemission dominieren, schrumpft das Photolumineszenzemissionprofil mit der Zeit. Die Auswirkungen der Fallenzustände auf die Exzitonendiffusion wird mit einer zusätzlichen Anregungsquelle in Form einer LED untersucht. Die LED bewirkt eine Saturierung der Fallenzustände und eine Erhöhung der Diffusion.

Abstract

Perovskite nanocrystals (PNCs) have proven their outstanding optoelectronic behavior over the past decade. In favor of applications where excited states must be induced or extracted from PNCs, their transport behavior in ensembles is crucial. However, there needs to be more research on extrinsic and intrinsic parameters which modify exciton diffusion. Intrinsic parameters include PNC size, shape, and trap density whereas crucial the extrinsic parameters are the system temperature, excitation power, and PNC film properties like the film order and the density of voids. Characterizing exciton diffusion concerning all these parameters enables deeper physical understanding and can pave the way for future applications.

Herein we report on exciton diffusion in $CsPbBr_3$ PNC films and superlattice (SL) structures in the temperature range of 10 - 350 K. A clear dependence of exciton diffusion on PNC size can be observed in experiments. This is further supported by Monte Carlo simulations. The experimental results compare perovskite nanoplatelets (PNPLs) of different thicknesses, i.e., 3 or 5 monolayers (MLs), with cube-shaped PNCs. For larger PNCs, exciton transport is generally more pronounced, which is caused by the lower amount of Förster resonance energy transfer (FRET) steps necessary for equal exciton travel distances and by less trap states impeding diffusion in larger PNCs. While exciton diffusion is most efficient in the largest PNCs, it is still surprisingly large in PNPL films. The reason for the high exciton diffusion in PNPL films originates from their anisotropic shape, which, as PNPLs, favorably form stacks along their larger facets upon drying on substrates. In these stacks, excitons can be delocalized over several PNPLs, and a better dipole alignment is ensured compared to isotropic PNC cubes, enhancing exciton diffusion. Voids in PNC films and finite PNPL stack lengths limit diffusion, resulting in subdiffusive exciton transport, which is investigated in sparse PNC films where the void size is variable. Exciton diffusion is more dependent on the intrinsic PNC properties than the film order, manifested by comparing exciton diffusion in SLs and in unordered PNC films where PNC cube size outperforms order. Besides intrinsic PNC characteristics, film type, and quality, exciton diffusivity is also susceptible to extrinsic parameters like the system temperature. The diffusivity increases as the temperature is raised from 9 K to 100 K and then decreases for further increases of the temperatures. The origin of this seemingly strange behavior is complex, with several competing mechanisms. The low-temperature regime is governed by the bright-dark exciton splitting for 3 ML PNPLs and SLs consisting of 5 nm and 8 nm PNCs. Excitons occupying the energetically lower-lying dark state have a suppressed FRET rate, whereas excitons in bright states are highly mobile. Thus, at early times, bright excitons lead to a rapid diffusion. However, due to their short radiative lifetimes, soon nearly only dark excitons remain and determine the photoluminescence (PL) profile widths and the diffusion dynamics. The bright-dark splitting is too small for weakly confined PNCs, e.g., 14 nm PNC cubes; therefore, it hardly affects the exciton transport behavior. At temperatures above 100 K, the thermal energy is sufficient to breach the bright-dark splitting energy, and thermally activated deep radiative traps dominate the diffusion process. Trapped excitons have a reduced recombination rate and cannot transfer their energy to adjacent PNCs. The different radiative decay rates eventually result in more trapped than mobile excitons after a period corresponding to several times the PL lifetime. Thus, with trapped excitons dominating the PL emission, the PL profile contracts with time. The hypothesis about trap state-dominated diffusion is supported by applying an additional excitation source in the form of an LED leading to trap filling, which translates into an established normal exciton diffusion if a sufficient number of trap states are occupied.

Table of Contents

1

Introduction

Perovskite nanocrystals (PNCs) have emerged as a promising class of materials for various optoelectronic applications.[1] These nanoscale crystals, typically composed of hybrid organic-inorganic or fully inorganic halide perovskite compounds, exhibit remarkable optical properties such as high photoluminescence quantum yields (PLQY), tunable bandgaps, and high absorption cross sections.[2–5] Those properties make this novel semiconductor class the new protégé for promising future applications and academic research.[6–10] One of the key factors regarding device implementation is exciton diffusion in an ensemble of those nanomaterials. When the nanocrystal (NC) absorbs a photon, it generates an exciton, the dominant excited state in this material. The generated exciton can subsequently migrate through the NC ensemble via energy transfer processes.[11,12] These successive processes lead to the propagation of excitons over long distances compared to the NC dimensions.[13–16] Understanding the mechanisms and dynamics of exciton diffusion in PNCs is crucial for optimizing their performance in various applications, including photovoltaics, light-emitting diodes, and photodetectors. By manipulating exciton diffusion, it is possible to enhance the overall device efficiency and functionality. Furthermore, it is essential to understand the specific exciton features contributing to the transfer, whether an optical bright or dark exciton is present, accompanied by an immense or low oscillator strength.

Consequently, exciton diffusion is influenced by intrinsic factors, including defects, NC size, and exciton-phonon interactions. The presence of defects, such as vacancies or impurities, can introduce localized energy states stopping the migration of excitons, thus impacting the overall exciton diffusion performance of a PNC film. The film formation also influences diffusion, e.g., voids hamper diffusion, whereas perfect PNC arrangements enhance exciton transport. Furthermore, extrinsic parameters like temperature and excitation power also significantly influence exciton diffusion.[15] Higher temperatures lead to increased thermal energy, resulting in enhanced exciton hopping between neighboring NCs due to the supply of excess energy bridging energy discrepancies of adjacent PNCs. Conversely, excitons may become localized at low temperatures, leading to decreased diffusion lengths. Thus, the interplay between excitons and lattice dynamics affects the kinetics of exciton diffusion. Understanding this

interaction provides insights into the complex temperature-dependent exciton diffusion behavior of PNCs.

In recent years, significant progress has been made in characterizing and manipulating exciton diffusion in NC films. Advanced spectroscopic techniques, such as time-resolved photoluminescence (PL) and transient absorption spectroscopy, enable the direct observation and measurement of exciton dynamics with sub-nanosecond temporal and high spatial resolutions.[13,16] These experimental approaches, combined with theoretical modeling and simulations, provide valuable insights into the underlying mechanisms and kinetics of exciton diffusion. Furthermore, developing novel strategies for enhancing exciton diffusion has gained attention. Surface engineering techniques, such as ligand passivation or interface engineering, can modify the surface properties of PNCs, suppressing surface traps and enhancing the interparticle coupling, thereby facilitating efficient exciton migration.[17] Additionally, integrating PNCs into various device architectures, such as thin films, enhances the exciton diffusion lengths. The above-given considerations of exciton diffusion show that exciton diffusion in PNCs is a complex phenomenon where different parameters must be handled with care to unravel the underlying physical processes, which is the major task of this thesis.

The thesis begins with a comprehensive theoretical background and state of the art characteristics of $CsPbBr_3$ NCs the material under consideration throughout the work (Chapter 2). In particular, the interaction of PNCs with light and transport mechanisms within ensembles of several PNCs are discussed. Chapter 3 introduces the PNC synthesis, the confocal low temperature time-resolved microscope and the applied simulations used for investigating exciton diffusion in PNC systems. The results are listed in Chapter 4 in which initially the intrinsic PNC properties affecting exciton diffusion are investigated. The PNC assembly order and PNC film thickness are then studied closely. The second part of the results chapter summarizes the findings of the influence of extrinsic parameters on exciton diffusion performance like system temperature and excitation power. The concluding chapter Chapter 5 summarizes all findings and gives a short outlook.

2

Fundamentals

Within this chapter, all fundamental physical concepts will be presented, which are needed for following the discussions in this thesis. All investigations were conducted with PNC films. Thus, this semiconductor material is discussed with a particular interest in its nanocrystalline form. The distinctions to other typical NCs, e.g., CdSe, vastly investigated over the past decades, have worked out why perovskite semiconductors are of special interest nowadays due to their exceptional optoelectronic properties. Upon elaborating on the fundamental properties of this material class, the impact of defect induced trap states on the optical properties of the material will be discussed. Especially in nanocrystalline form these trap states can cause non-radiative excited state sinks or long radiative decays, extending the life time of these decay channels up to three orders of magnitude. The following section discusses light-matter interactions. Since light is used as the excitation source, the chapter is devoted to its interactions with dispersive media, regarding transmission and reflection with a special focus on absorption as re-emission of light or non-radiative energy transfer to adjacent NCs can occur. Finally, a microscopic random walk model to connect the energy transfer process to a macroscopic diffusion description is introduced, considering different inter-NC transfer rates and exciton sink terms. Those transfer rates are sensitive to NC order, NC shape (i.e., exciton dipole direction), and excitonic fine level ordering, which is indirectly mimicked by temperature dependence.

2.1 Semiconductor

This section will give a general overview of semiconductors, their formation, and different semiconductor kinds. Particular interest is paid to halide perovskites, being the material investigated in this thesis. Their fundamental bulk properties are discussed such as the bandgap and which atomic levels contribute to the conduction band minimum and valence band maximum. After the discussion of perfect semiconductors, which are not disturbed by anything, a section follows which considers imperfections, which are always present in crystal structures to some extent. The influence of the crystal lattice on the excited states in the system is discussed then. This can be managed by introducing phonons, lattice vibrations that interact with excited electrons or holes. The chapter ends with describing excitons in bulk semiconductor materials. Those excitons result from the attractive Coulomb potential of an electron and hole.

2.1.1 Bulk Semiconductor

Semiconductors are vastly used in applications, and avoiding them in modern life is virtually impossible. Their use as basic elements for applications like electronic switches, sensors, amplifiers, light sources, and even solar energy converting tools is convincing enough to necessitate an understanding of their fundamental characteristics to improve their performance. Semiconductors can be divided into two classes, depending on their constitution, namely organic and inorganic. Inorganic semiconductors consist of regular lattice structures where translation symmetry is present. The whole crystal is established by unit cells, which normally consist of a few atoms. The latter can be seen as a consortium of larger molecules/independent building blocks of the semiconductor, where charge transfer is impossible between those blocks. Since the semiconductors under consideration consist of inorganic materials, only the inorganic semiconductors are discussed in detail.
To describe those semiconductors crystals, a real space lattice, known as direct lattice, can be introduced and established by three linear independent primitive lattice vectors $\vec{a}_1$, $\vec{a}_2$ and $\vec{a}_3$ (note that those basis lattice vectors have not to be an orthogonal system), resulting in the lattice vector:

$$\vec{R} = n_1\vec{a}_1 + n_2\vec{a}_2 + n_3\vec{a}_3 \tag{2.1}$$

where $n_1, n_2, n_3 \in \mathbb{Z}$. Thus, with $\vec{R}$ every lattice site can be reached. The atoms, which are the smallest building blocks forming the semiconductor, are located at those lattice sites or a small set of atoms called basis. Different crystal bonding types can be established depending on the atoms, i.e., covalent bonds, van der Waal bonds, or ionic bonding. A unit cell covers the whole space by only translating with the lattice vector, where each atom within the unit cell has an invariant position. Exploiting this translation invariance, the physical system, namely its describing Hamiltonian, can be transformed from real space representation to reciprocal space, utilizing reciprocal lattice vectors. Note that the translation invariance is only strictly valid for an infinite large crystal and may get insufficiently fulfilled concerning crystals with a small expansion, i.e., for NCs. Bloch introduced a description for eigenstates of those periodic systems with a plane wave part, reflecting the periodicity of the lattice and a function that represents the periodicity of the atomic structure of the crystal, i.e., the atoms resting at lattice sites within the unit cell. Two approaches (tight binding or free electron gas in weak ionic background lattice) lead to similar energy band structures. Both approaches start from somewhat

different assumptions: electrons are tightly bound to their host atoms, whereas an inter-atomic transfer can happen to only adjacent atoms. The other approach assumes highly delocalized electrons over the lattice and can be described as Bloch states, i.e., harmonic waves and an envelope function reflects the ionic background potential. Those bands give the energy to a state having specific quantum numbers, one integer for the band n and the other is the reciprocal lattice wavevector $\vec{k}$, consisting of direction and length. Therefore, the energy band structure of a crystal can be represented along lattice wavevector directions in reciprocal space where the bands describe the corresponding energies of the states.

If the amount of quasi-free electrons in the system fill one band completely and the next higher energetic lying band is empty one speaks of a semiconductor or insulator. The total filled band is termed valence band and the empty band is the conduction band. The distinction between insulator and semiconductor depends on the energy separating those two special bands. The smallest energetic difference between conduction and valence band is termed bandgap. If a semiconductor is present and the bandgap appears at the same lattice wavevector position, one speaks of a direct semiconductor. If not, the semiconductor is termed indirect. This distinction in semiconductors or insulators can also be made by evaluating the chemical potential. The chemical potential is the energy needed to insert a particle in a system into the next free state. The particles in the context of semiconductors are electrons (or holes), i.e., fermions, which are not allowed to occupy a quantum state where already a fermion with the same quantum numbers sits, i.e., Pauli exclusive principle. Thus, free states around the chemical potential serve as potential occupational states. The chemical potential and the Fermi level are similar for very low temperatures, and for zero K, they are equivalent. The distinction is only of minor interest since the deviation of both quantities is also for elevated temperatures only in the percentage range.[18]

The band structure of semiconductors is of immense interest since it enables one to describe the semiconductor at a quantitative level by predicting, for example, optical characteristics like absorption and PL spectra and electronic properties like charge carrier densities if the temperature is known. There are some approaches to calculating the band structure of semiconductors, e.g., density functional theory or measurement methods like angle-resolved photoemission spectroscopy. The effective mass model can lead to intriguing physical understanding depending on the bandgap position in the Brillouin zone, i.e., the energetic distance between the conduction band minimum and valence band maximum. It is applicable if the bands can be described as parabolic and the semiconductor is direct, which we will utilize below.

The next section investigates bulk perovskite properties, since all presented semiconductors within this thesis have a perovskite crystal structure.

2.1.2 Perovskite Semiconductors

This thesis deals with semiconductors with perovskite crystal structure ABX_3, thus, this section is devoted to presenting details about this special semiconductor class. The binding in these crystals is normally ionic, and all perovskites investigated within this thesis contain a monovalent A-cation, a divalent B-cation, and three monovalent X-anions. The left panel in Fig. 2.1 depicts the perovskite crystal structure in the cubic phase. The corner-sharing octahedra highlighted in light green are formed by the X-anions shown in solid green. In each octahedral center is a B-cation located, and the A-cation sits in the body center of the cube formed by the B-cations. The right panel emphasizes the

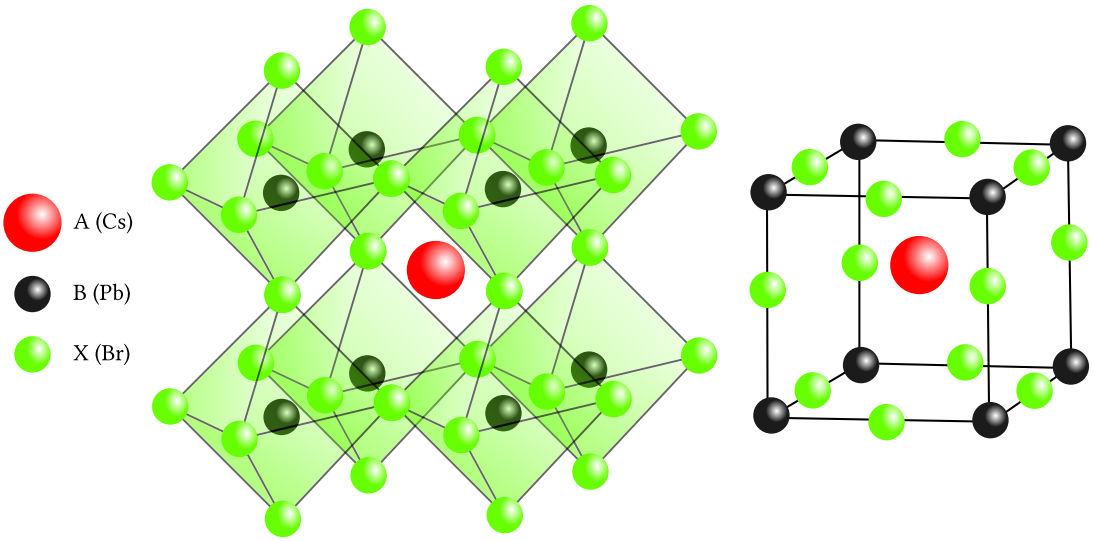

Figure 2.1: The left panel depicts the perovskite crystal structure. The corner-sharing octahedra shown in light green are spanned by X-anions depicted as solid green spheres. A black B-cation is located in the center of each octahedron. Every center of eight octahedra contains a solid red A-cation.

actual perovskite unit cell in the cubic phase. It is easy to expand the crystal structure to its tetragonal and orthorhombic phase by tilting the octahedra along the orthogonal crystal axis so that different lattice constants along the orthogonal crystal axis are established.

The ABX_3 structure is quite general, and several different compositions of cations and anions form the perovskite structure. The A-cation can be occupied by organic molecules like formamidinium and methylammonium or by cesium.[19,20] The B-cation is often lead since those perovskite semiconductors turned out to be most efficient concerning their optoelectronic performance.[21] However, there is high interest in changing the B-cation to a lead-free perovskite synthesis with a less poisonous constituent.[22] There are some attempts with germanium.[23] The X-anion can be varied, which changes the color of the perovskite semiconductor from blue to green to red for chlorine to bromine to iodine, respectively.[24] We will deal only with $CsPbBr_3$ and discuss this particular choice in more detail. The crystal structure of bulk $CsPbBr_3$ is orthorhombic, tetragonal, or cubic from low to high temperatures, where the two phase transitions happen at $T_1 = 88\ ^\circ C$ and at $T_2 = 130\ ^\circ C$.[25] Thus, one would expect an orthorhombic crystal structure for bulk like $CsPbX_3$ at room temperature.[26] Fig. 2.2 a) depicts the energetic band structure of bulk $CsPbBr_3$ calculated with density functional theory without considering spin-orbit interactions. Each inset of the panels shows the crystal structure considered. The left panel in a) shows the energy diagram for $CsPbBr_3$ in the cubic phase where the bandgap appears at the R point. The valence band maximum is not degenerated, whereas the conduction band minimum is three-fold degenerated. By lifting the crystal symmetry from cubic to the tetragonal phase, the conduction band degeneracy in the band structure disappears, and the bandgap appears at the Γ-point in the Brillouin zone, which is visible in the middle panel. The six lowest lying conduction bands and the two highest valence bands at the Γ-point are marked with $|CBM1-6\rangle$ and $|VBM1-2\rangle$, respectively. The six conduction band states correspond to hybridizations of the 6p-orbitals stemming from lead and belong to the irreducible representations of the D2h point group (factor group for the Pnma space group at Γ point). The two valence bands consist of hybridizations of the 6s-orbitals corresponding to lead and 5p-orbitals of bromide and are associated with nonpolar irreducible representations of the point group.[28] The right panel shows the energy band diagram for bulk $CsPbBr_3$ in the orthorhombic phase, qualitatively similar to the tetragonal phase. All considered phases lead to band diagrams

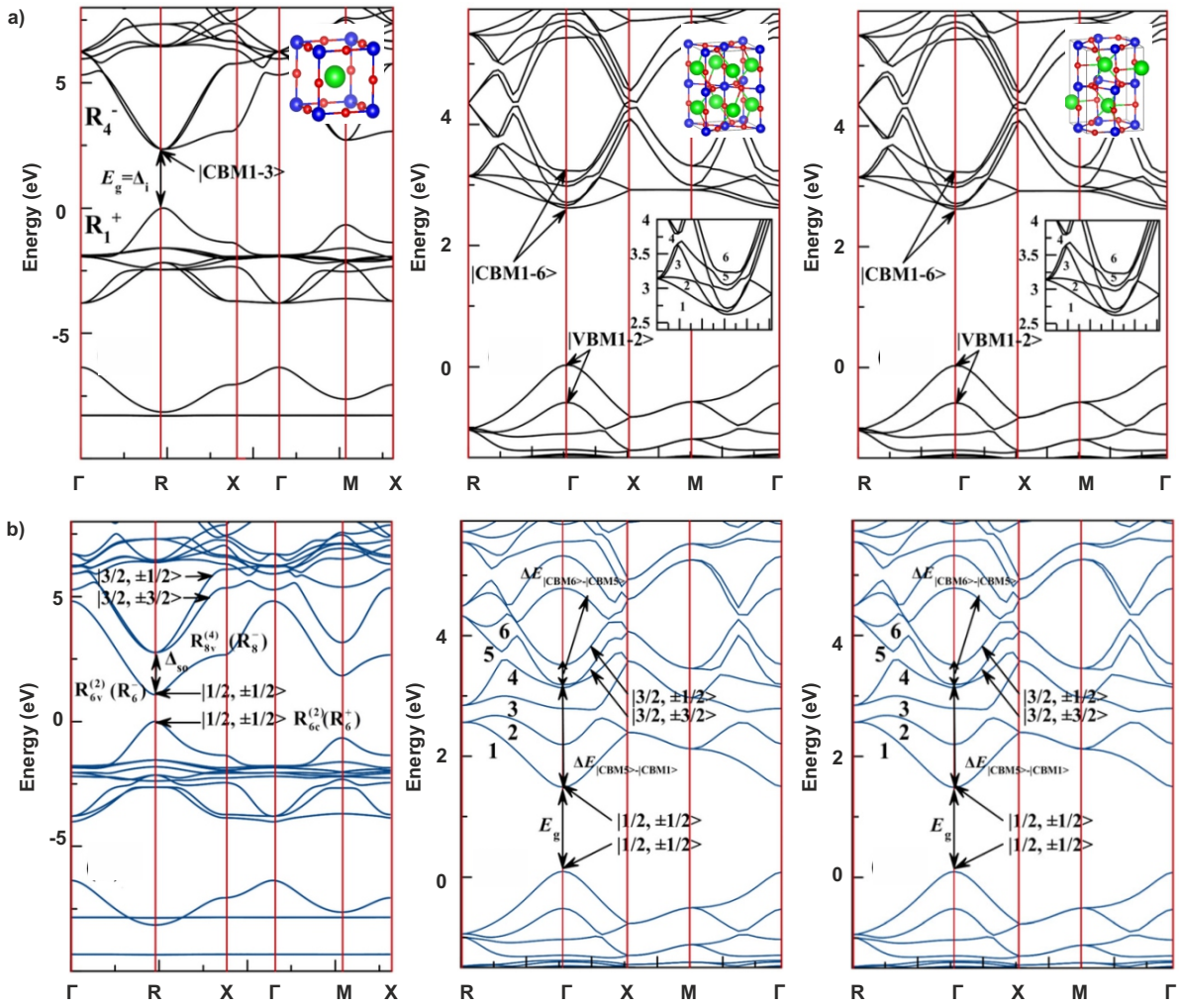

Figure 2.2: The figure presents the energy band structure of $CsPbBr_3$ in cubic (left), tetragonal (middle), and orthorhombic (right) phase where a) shows the density functional theory results without and b) with spin-orbit coupling. The insets in a) depict the considered crystal structures. The two insets in the middle and right panel show the magnified band structure close to the conduction band minimum for the respective band diagram. The figure is adapted from[27].

where bulk $CsPbBr_3$ is a direct semiconductor.[27]

Fig. 2.2 b) presents the energy band diagrams of bulk $CsPbBr_3$ where spin-orbit interactions are considered in the density functional theory calculations. To consider spin-orbit interactions is reasonable since lead has a large atomic number. The different panels show the bands for the cubic (left), the tetragonal (middle), and the orthorhombic (right) phase where the band gaps appear at the same positions in the Brillouin zone as for the systems where no spin-orbit interactions were taken into account. The main difference between including spin-orbit interactions and omitting them lies in the splitting and total distance between the lowest lying conduction bands. The spin-orbit interaction lifts the heavy electron and light electron band farther apart from the conduction band minimum, which is then described only by the spin-orbit split off band $|1/2, \pm 1/2\rangle$. The triply degenerate conduction band $|CBM1-3\rangle$ states shown in the left panel of Fig. 2.2 a) are associated to the vectorial representation of the simple group commonly described by the $|X\rangle$, $|Y\rangle$, $|Z\rangle$ kets. In the corresponding double group, including spinors, it is split by spin-orbit interaction into twofold degenerate states and fourfold degenerate states, which is depicted in the left panel of Fig. 2.2 b). This situation is usually encountered in the valence band of cubic conventional semiconductors. Thus, orbital momentum and

spin are not conserved quantities on their own, one introduces a new quantum number $J = L + S$, which is a good quantum number with projections $m_j = \pm 1/2$ for the case of $J = 1/2$. Thus, optical transitions are dictated by the two conduction bands $|1/2, 1/2\rangle = 1/\sqrt{3}(|X + iY, \uparrow\rangle + |Z, \downarrow\rangle)$ and $|1/2, -1/2\rangle = 1/\sqrt{3}(|X - iY, \downarrow\rangle + |Z, \uparrow\rangle)$, and two s-like valence bands which are only represented by their spin $|\Updownarrow\rangle$.[28]
The interplay between those four bands, which eventually result in excitonic states, will be discussed at the end of this chapter for bulk perovskite and when PNCs are discussed. Since the electron-hole interaction gets enhanced for the quantum-confined perovskite system, excitons get the dominant excited state in NCs especially at low temperatures.

2.1.3 Imperfections and Traps in Bulk $CsPbBr_3$ Perovskite

Generally, traps are always present in crystals which lead to unwanted or wanted effects, e.g., non-radiative decay channels which lower the PLQY or generation of color centers that serve as single photon sources. Until now, perfect crystal structures were assumed. However, this is a simplified picture since traps or lattice imperfections can be formed under non-perfect synthesis conditions, e.g., poor mixture conditions or different temperature regions. Fortunately, lead halide perovskite $CsPbBr_3$ has a high defect tolerance.[29] Nevertheless, we want to state the main point defects that can appear in bulk $CsPbBr_3$ perovskite.
Several restrictions to the chemical potentials must be fulfilled for a stable $CsPbBr_3$ phase. By respect-

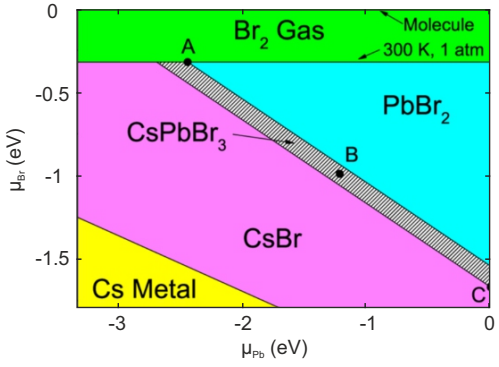

Figure 2.3: The figure shows stability regions of different compounds against bromide and lead chemical potentials. The shaded region indicates the available equilibrium chemical potential region for $CsPbBr_3$. The three named points in the figure, i.e., A, B, and C, mark the chosen chemical potentials for the defect formation energy calculations. The results are given in Tab. 2.1. The figure is adapted from[29].

ing all of these requirements, the available equilibrium chemical potential region for $CsPbBr_3$ is shown in Fig. 2.3 as the dashed narrow area. The horizontal axis represents the lead chemical potential μ_{Pb}, and the vertical one states the chemical potential of bromine μ_{Br}. For instance, the corridor where μ_{Br} is below zero, and larger than -0.35 eV represents the conditions where bromine is in its gas phase. To calculate the point defect formation energies, one has to choose constant chemical potentials. This calculation was done by Kang et al., and their results are presented in Tab. 2.1. They choose three different equilibrium points, namely A, B, and C. Those points represent other growth conditions, e.g., Br-rich (A) or Br-poor (C) synthesis environments. All possible point defects were considered, namely, vacancies (V_{Cs}, V_{Pb}, V_{Br}), interstitials (Cs_i, Pb_i, Br_i), and antisites (Cs_{Br}, Pb_{Br}, Br_{Cs}, Cs_{Pb}, Br_{Pb}, Pb_{Cs}). Depending on the growth conditions, there are only some point defects with formation

energy below 1 eV. The absolute amount of defects is inversely proportional to their corresponding formation energy. By calculating the band diagram energy position of all of those 12 point defect

-	Cs_{Br}	Cs_i	Pb_i	Pb_{Br}	Pb_{Cs}	V_{Br}	Br_{Cs}	Br_{Pb}	Cs_{Pb}	Br_i	V_{Cs}	V_{Pb}
A	6.22	3.55	4.66	6.28	2.44	2.67	0.8	1.4	0.81	0.7	0.2	0.49
B	4.77	2.77	3.44	4.38	1.99	2.00	2.25	3.30	1.26	1.37	0.98	1.71
C	3.27	1.95	2.22	2.48	1.59	1.32	3.75	5.20	4.66	2.05	1.80	2.93

Table 2.1: The table gives the calculated formation energies in eV for neutral point defects. The calculated values were stated by Kang et al.[29].

types, it turns out that only three of them are deep traps. In contrast, the rest are shallow traps which can be seen in Fig. 2.4 a). Deep traps refers to those defect states which are located far apart from either the conduction band or valence band within the band gap, whereas shallow traps are located in the vicinity of those band gap maxima. The marked blue levels are donor-like defects, and the red levels correspond to acceptor-like defects. The interstitials of a lead atom and the two antisites Pb_{Br} and Br_{Pb} can be considered as deep traps. However, all those have point defect formation energies above 1 eV for all three chosen synthesis conditions, i.e., their formation rarely happens. On the other hand, all other traps, especially those with low formation energy, are shallow traps where detrapping is easy.

Fig. 2.4 b) shows the contributing orbitals of the atoms which form the conduction and valence band. The valence band maximum originates from the s-p antibonding interaction between lead and bromine

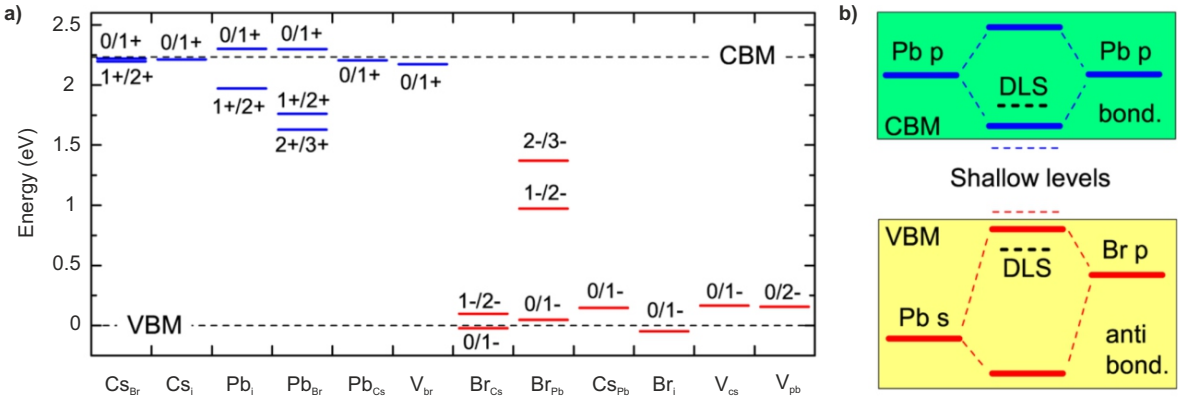

Figure 2.4: a) depicts the conduction band minimum (CBM) and valence band maximum (VBM) and the energetic positions of all 12 point defects. b) shows the anti-bonding and bonding states which form the CB and VB in comparison to the atomic energy levels of its constitutionals. The figure is adapted from[29].

depicted in the lower panel highlighted in yellow. The defect localized state (DLS) lies below the valence band, i.e., a shallow defect. The conduction band originates from the hybridization of empty lead p-orbitals depicted in the upper panel in green, where the bonding state lays energetically below the single lead atom p-orbital. The DLSs established by acceptor-like defects are bromine dangling bonds, which are close to the energy of the atomic bromine p-orbital. For donor-like defects, DLSs are either lead dangling bonds, which have a similar energy to the atomic lead p-orbital, or dangling cesium bonds, which are even higher than lead p-orbitals. Hence, all of these DLSs created by the defects lie either below the valence band maximum or above the conduction band minimum leading to shallow traps.[29]

As we will see below, free charge carrier or excitonic traps influence the diffusion characteristics. There is a primary distinction between shallow and deep traps. Besides the disturbed perfect crystal

lattice considered here, the following section considers the influence of the lattice in a crystal that was, to this end, considered entirely at rest.

2.1.4 Phonons in Bulk Perovskite Semiconductors

Until now, the ionic lattice background was assumed to be in total rest, thus, charge carriers, i.e., electron and hole excited states, feel only a static Coulomb potential of the atoms which do not move in a crystal. However, for temperatures higher than zero K, the atoms that form the crystal lattice can oscillate around their equilibrium position. This deviation from total rest has to be fulfilled so that the uncertainty principle is not violated, and the thermal energy has to be stored in the crystal in some way that the energy conversation is valid. Note, the charge carriers also carry heat. However, their contribution to the thermal heat capacity becomes only relevant at low temperatures. Those lattice vibrations can be described by quasiparticles representing them, i.e., phonons. Phonons can interact with other excited states in the crystal, like conduction band electrons or valence band holes. A phonon can be annihilated or created, where the prior event will give the phonons energy to the interaction partner, whereas the latter process consumes energy from the interaction medium, making it a temperature dependent process. With the temperature and the phonon energy, one can estimate the number of phonons in a system by the Bose-Einstein distribution:

$$f_{BE}(T) = \frac{1}{\exp(\frac{E_p}{k_B T}) - 1} \tag{2.2}$$

$k_B T$ is the thermal energy and E_p is the phonon energy, which is in principle dependent on the k-space as one can see in Fig. 2.5, which depicts the phonon dispersion relation for bulk $CsPbBr_3$. Besides the phonon energy distribution, the phonon density of states is the second crucial part dictating large or small interaction phonon behavior. The phonon density of states is proportional to the inverse first derivative of the phonon energy dispersion relation $1/\frac{\partial E(k)}{\partial k}$. Thus, for a flat phonon energy band, the density of states peaks.

Phonons can be divided into two major classes, corresponding to the contributing atomic vibrations. For atomic oscillations within the unit cell of a crystal, the phonons are termed optical since those mainly interact with visible light. The distorted atom positions within a unit cell can be seen as an electromagnetic dipole driven by an electromagnetic wave and are, therefore, optically active. The second phonon type are acoustic phonons which correspond to an oscillation of entire unit cells relative to each other. Those oscillations do not drive a dipole, are locally and globally electrically neutral, and can be seen as sound waves.[30]

As depicted in the phonon dispersion relation for bulk $CsPbBr_3$ in Fig. 2.5, the optical and acoustic modes mentioned above can be distinguished by their respective energetic bands. Optical phonons have a flat energy dispersion, whereas acoustic phonons are proportional to the quasi momentum k around the Γ point. The shown energy band diagram depicts a multitude of bands since the perovskite unit cell consists of five atoms. This results in three acoustic phonons and 12 optical phonon branches. Phonons are bosons with no spin $s = 0$. However, they carry momentum, making them crucial for transitions in crystals to maintain momentum conservation, for example in optical excitation and radiative decay processes in indirect band gap semiconductors.[30] As we will see below, they are important to make dipole-forbidden transitions possible. In semiconductors, transitions between bands are optically forbidden (dark states) due to crystal symmetry exclusion, which can be interpreted

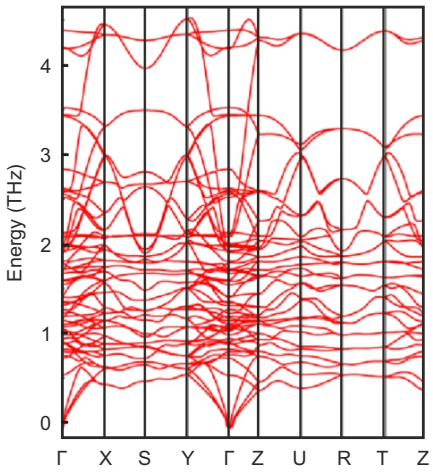

Figure 2.5: The figure shows the phonon dispersion relation of $CsPbBr_3$ in the orthorhombic phase in the reciprocal space along high symmetry directions. Many phonon branches cover a large span of energies (0 - 4 THz). The figure is adapted from[29].

as momentum and spin conservation restrictions. This strict exclusion can be lifted by including phonon interactions, allowing the transition from dark to bright. The dipole-allowed states are termed bright states, i.e., they have a high dipole oscillator strength, and their energy level can deviate from the dark state. This bright-dark state energy splitting, which will be introduced in Sec. 2.2.2 in more detail, can be bridged by phonon energies.
To this stage, the excited states within a semiconductor were treated individually, and their possible interaction with each other was omitted. However, since both excited states can be seen as oppositely charged quasi-particles, they feel a Coulomb potential from each other. This interaction will modify their energy dispersion and wavefunctions, which will be discussed in the following section.

2.1.5 Excitons in Bulk Direct Semiconductors

Until now, the properties of excited states in a semiconductor, i.e., electrons and holes, were described by their band structure within the one-electron approximation as depicted in Fig. 2.6 a). Here, the valence and conduction band can be approximated by parabolas in the reciprocal vicinity of the direct band gap. A photoexcitation process is shown, i.e., an electron is lifted from the valence band to the conduction band by an absorbed photon whose energy is larger than the bandgap $E_{ph} > E_g$. The electron-electron interaction of the excited states, i.e., the excited electron in the conduction band and the excited hole in the valence band was not considered so far. In terms of the two particle's interaction, only the Coulomb interaction will be considered. Correlation and exchange interaction contributions will be omitted in this case, as they become more relevant for quantum confined systems, which will be discussed in detail in Sec. 2.2.2.
The electric field lines from a hole to an electron within a bulk semiconductor are depicted in Fig. 2.6 b) in the upper left corner, illustrating the effect of two charged particles, whose electric fields are interacting with each other. Since the interaction term is attractive, bound states establish a binding energy called excitons. Such an exciton is schematically shown in the lower left corner, where both charged particles form an exciton. There are two limits of excitons, tightly bound Frenkel excitons, which exist in a unit cell of a semiconductor due to a comparably high Coulomb attraction

like in an ionic crystal.[31] Whereas weakly bound Wannier-Mott excitons predominantly appear in semiconductors since valence electrons which do not contribute to the free electron states highly screen the Coulomb interaction.[32] Wannier-Mott excitons can spread out over a large distance of several unit cells within the semiconductor.[30] We will focus on Wannier-Mott excitons since those are

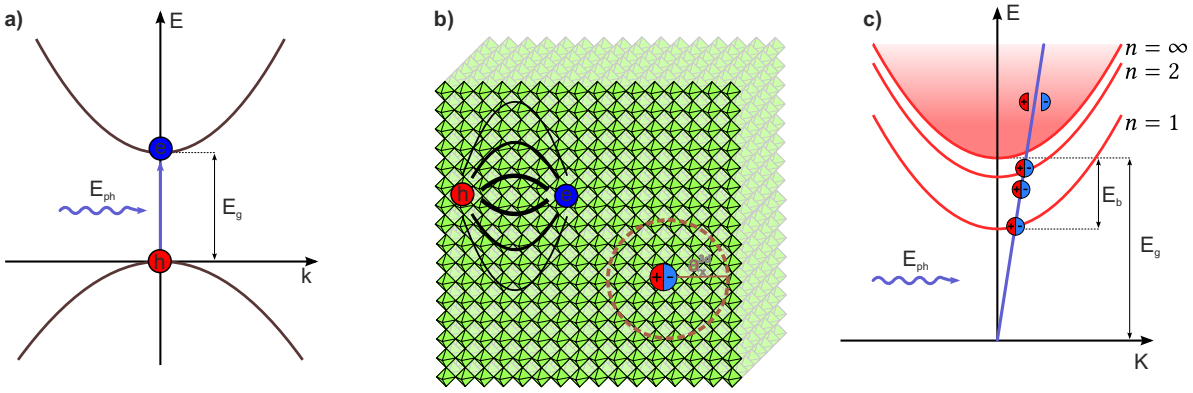

Figure 2.6: a) depicts the photon absorption process at the band edge vicinity of a direct semiconductor. The bands can be approximated via a parabola. The excited state is a missing electron in the valence band, i.e., a hole, and an electron in the conduction band. b) shows a schematic representation of an unpaired electron and a hole in the left upper corner. The lines illustrate the Coulomb attraction. A bound exciton is depicted in the right lower corner, with a Bohr exciton radius of a_x^{3d}. c) Energy dispersion ratio of excitons depicted in the two particle picture.

the predominately appearing excitons in perovskite semiconductors. By applying the effective mass theory for both electron and hole, the properties of Wannier-Mott excitons can be investigated. The effective mass difference of electrons and holes in a semiconductor are not as large as the difference in masses between an electron and a proton, but rather resemble an electron-positron pair. If the Coulomb attraction is now considered, the translation invariance for the electron and hole is lost. However, one can decompose both spatial coordinates into a center of mass and relative motion. This restores the translation symmetry in the crystal for the center of mass coordinates, i.e., the exciton center of mass behaves like a free particle with mass $M = m_e + m_h$, since the Coulomb attraction is only dependent on the relative coordinates of hole and electron. The Coulomb interaction can be treated like it is done for the hydrogen atom, there are bound and continuum states, where the bound states have two quantum numbers, i.e., the principal quantum number n and the angular momentum l. The continuum states are ionized excitons, i.e., free electrons and holes. However, their wavefunctions are still modified by the considered Coulomb interaction. For the exciton eigenenergies, one finds:

$$E_n = E_G + \frac{\hbar^2 K^2}{2M} - \frac{\mu e^4}{2\hbar^2 (4\pi\epsilon_0\epsilon_r)^2}\frac{1}{n^2} = E_G + \frac{\hbar^2 K^2}{2M} - \frac{E_b^{3d}}{n^2} \tag{2.3}$$

Which depends on the principle quantum number n like the Coulomb interaction term in the hydrogen model with a reduced mass $\mu^{-1} = m_e^{-1} + m_h^{-1}$ represented by the last of the three terms. The first term corresponds to the fundamental energy gap of the semiconductor, and the middle term describes the dispersion relation of a free-moving particle, i.e., the exciton, with the center of mass $M = m_e + m_h$ and exciton wavevector $K = k_e + k_h$.

The energy dispersion relation of excitons in the two-particle picture is shown in Fig. 2.6 c). Here, also a photon absorption process is shown. However, one state represents the linear combination of arbitrary electron and hole states with the conserved good quantum number K, i.e., the center of mass wavevector. Due to momentum conservation, excited states can be only established along

intersections of the photon dispersion relation, i.e., the straight blue line and the dispersion relation of the excitons (red lines). The exciton binding energy in a three-dimensional unconfined semiconductor can be seen as modified Rydberg energy, where the reduced mass and the dielectric screening ϵ_r change the binding energy:

$$E_b^{3d} = \frac{\mu e^4}{2\hbar^2(4\pi\epsilon_0\epsilon_r)^2} = \frac{\hbar^2\pi^2}{2\mu(a_x^{3d})^2} \tag{2.4}$$

Here, μ is the the reduced mass for the electron-hole two-particle system, ϵ_r as the relative permittivity constant, which is material dependent, and the ordinary natural constants $\hbar$,e, and ϵ_0 are used. In the last term of Eqn. 2.4 the exciton Bohr radius a_x^{3d} is introduced, giving a measure of the exciton extension in the bulk semiconductor via:

$$a_x^{3d} = \frac{4\pi\epsilon_0\epsilon_r\hbar^2}{\mu e^2} \tag{2.5}$$

Since the particular interest of this thesis lies in the investigation of all inorganic halide perovskites, we list here the exciton Bohr radii and exciton binding energies for $CsPbX_3$ perovskites with bromine, iodine, and chlorine as halides:

	$CsPbCl_3$	$CsPbBr_3$	$CsPbI_3$
Bohr exciton radius (nm)	2.5	3.5	6
exciton binding energy (meV)	75	40	20

Table 2.2: The Bohr exciton radius and exciton binding energies for all inorganic bulk perovskite semiconductors are listed for three halides: Chloride, bromide, and iodide.[33]

According to the exciton Bohr radii stated in Tab. 2.2 the excitons are spread over several perovskite unit cells within the bulk semiconductor, i.e., 4 - 10 from chlorine to iodine, for instance.
So far, we discussed bulk semiconductors with a special interest in all-inorganic perovskite. The following sections consider the same material, however, the lateral crystal dimensions are assumed to be relatively small. These small crystals are termed NCs, and they have some interesting changed optoelectronic properties compared to their bulk versions, which follow directly from quantum confinement.

2.2 Perovskite Nanocrystals

All semiconductors discussed hereafter are PNCs, which implies that the translation symmetry is broken since the constituting semiconductor lattice structure is disturbed and limited by ligands. Those serve as stabilizers for the PNC shape and are necessary for the synthesis and formation.[17,34] They can be seen as barriers, separating single NCs, and preventing inter-PNC charge transfer, which will become important during this thesis when transport phenomena are discussed.
This section will discuss some specialties that change for a nanoscale semiconductor compared to its bulk version. In particular, quantum confinement effects have to be considered since for small enough PNCs, the exciton extension is comparable to the PNC size. Their small size also leads to enhanced exciton binding. Consequences of this size confinement are for example, that both constitutionals of the exciton are forced to be closer together, and secondly, that the Coulomb interaction screening is smaller, if the Coulomb field is confined within the ligand shell of the PNC.

As we discussed phonons in bulk materials above, we will also spend some effort describing phonon exciton interaction in PNCs since phonons will always be present and have some other features than their bulk counterparts. Trap states in PNCs are mainly located at the PNC surface, which will also be considered in more detail here. Finally, the fraction of free charge carriers to its bound state version is investigated since only excitons can transfer their energy. The dominant excitation species is crucial concerning exciton transport performance. In its simplest form, this fraction is governed by the Saha equation, which is temperature, exciton binding energy, and intensity-dependent, as we will see below.

2.2.1 Confinement Effects in Semiconductors

The PNCs investigated during the thesis are either of cubic shape or of platelet shape and consist of $CsPbBr_3$. The PNC cubes can carry in size with an edge length of 14 nm, 8 nm to 5 nm. The smaller 5 nm cubes can display minor anisotropy regarding their lateral dimensions.[35–37] The perovskite nanoplatelets (PNPLs) have lateral dimensions of 20 x 20 nm and a thickness which is variable from 2 - 6 Monolayers (MLs), i.e., from 1.18 - 3.54 nm.[17]

The quantum confinement effect is shown in Fig. 2.7 for the weak, intermediate, and strong confine-

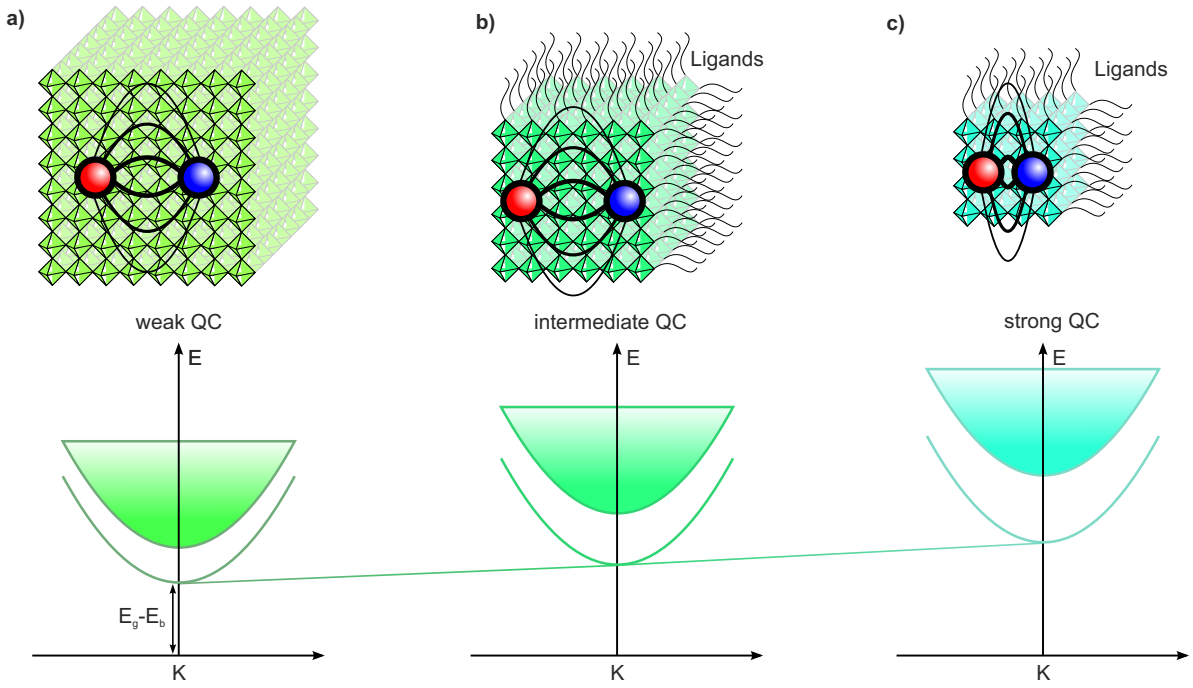

Figure 2.7: The Figure shows PNC cubes of $CsPbBr_3$ of a) 14 nm (weak confinement regime), b) 8 nm (intermediate confinement regime), and c) 5 nm (strong confinement regime) lateral expansion in the upper panels. In each PNC cube, an exciton is schematically depicted via a bound electron (blue sphere) and hole (red sphere) pair. The lower panels show the exciton dispersion relation around the bandgap in the two particle picture where quantum confinement and excitonic effects lead to an overall increase of $E_g - E_b$ for decreasing PNC size.

ment regime, from a)-c), respectively. There are PNC cubes of different sizes depicted, starting from the 14 nm PNC cubes in Fig. 2.7 a). The schematically illustrated exciton is the bound state of the hole (red sphere) and electron (blue sphere) where the connecting lines correspond to the electrical field lines. The lower panel depicts the exciton dispersion relation in the two particle picture around the bandgap following Eqn. 2.3, i.e., at the Γ point for the non cubic phase. For the 14 nm cubes, the exciton is in the weak confinement regime since the exciton Bohr radius of $CsPbBr_3$ is smaller compared to

the PNC dimensions, which becomes clear by comparing Tab. 2.2.
Fig. 2.7 b) depicts the intermediate confinement regime, for PNC cubes with 8 nm edge length, where the exciton Bohr radius is of the same size of the PNC cube dimension. For this PNC cube, the surrounding ligands are also depicted, which serve as stabilizers and are crucial within the synthesis. The depicted band structure for this quantum mechanical system in the lower panel reflects the quantum confinement effect, namely, the continuum onset shifts to higher energy compared to the dispersion relation for larger PNCs. However, the exciton binding energy increases as well lowering the bound exciton levels to the continuum band onset. The total energy change of the lowest lying exciton level to the ground state by decreasing the crystal size is a blue shift, i.e., $E_g - E_b$ increases, since the confinement effect is larger than the enhanced Coulomb interaction term for decreasing system size.[38]
Fig. 2.7 c) presents the strong quantum confinement regime. The upper panel depicts the exciton in such a system where the electron and hole are even closer together, i.e., feel a stronger attractive Coulomb force, reflected by an enlarged exciton binding energy E_b. However, the overall band structure is shifted to higher energies like for the system in the intermediate regime, i.e., the trends proceeds, $E_g - E_b$ gets larger, resulting in a more pronounced PL blue shift.
As it is visible in the depicted schematic of a PNC cube in the strong confinement regime, the electric field lines are partly located outside the PNC cube, which means that the dielectric screening of the Coulomb force of electron and hole is lowered, which can be expressed by[39]:

$$V_{Coul}(r_e, r_h) = -\frac{e^2}{\epsilon^{in}|r_e - r_h|} - V_{im}(r_e, r_h) \tag{2.6}$$

The first term on the right side corresponds to the Coulomb interaction of the electron and hole pair within the PNC with dielectric constant ϵ^{in} and inter charge carrier distance $|r_e - r_h|$. $V_{im}(r_e, r_h)$ corresponds to the interaction of the hole (electron) with the electron (hole) induced surface polarization charge. It can be written here as a quasi-interaction term, depending on both charge carrier positions and the dielectric medium surrounding the PNC ϵ^{out}. The exact expression of $V_{im}(r_e, r_h)$ depends on the PNC geometry. This effect is part of the so-called dielectric confinement and enhances the electron-hole Coulomb interaction for confined PNCs. For semiconductor/semiconductor heterostructure, this dielectric confinement effect is small since both dielectric constants (ϵ^{in} and ϵ^{out}) are close to each other.[39] However, for PNCs where the semiconductor with dielectric constant ϵ^{in} is embedded in an insulator matrix or ligand shell with ϵ^{out}, the dielectric constants can deviate by one order of magnitude, enhancing this effect.
Additionally to the above-mentioned dielectric confinement influence of the electron-hole interaction term, there is a self-energy potential term $V_{self}(r_{e(h)})$ caused by the image charge outside the PNC resulting from the charged particle itself. For semiconductor NCs, it is generally repulsive since $\epsilon^{in}/\epsilon^{out} > 1$. The confinement potential for the electron, resulting from lateral confinement and its image charge, can be written as:

$$V_{conf}(r_e) = V_{pot}(r_e) + V_{self}(r_e) \tag{2.7}$$

The excited hole state in the NC has similar confinement potential dependencies as the electron. The first potential in Eqn. 2.7 respects the spatial quantum confinement mentioned above. A simple model would be the infinite potential well. Within the PNC, the potential is zero and infinite outside. The

energy spectrum is given by:

$$E_n^{\infty well} = \frac{n^2 \pi^2 \hbar^2}{2\, m\, L^2} \tag{2.8}$$

m is the confined particle mass (electron or hole effective mass), L is the size of the quantum well along the confined direction, and n is the band index.[40]
The quantum confinement affects optoelectronic properties, which will be discussed in Sec. 2.3.1 where fundamental processes of light-matter interaction are investigated. We have seen in this section that excitons are altered in PNCs compared to their bulk counterparts, like their binding energies. Hence, it is worthwhile to discuss the exciton wavefunctions for the first excited states and possible interaction terms that influence the exciton energy level ordering, which we will consider in the following section.

2.2.2 Excitons in PNCs

Excitons were already discussed in Sec. 2.1.5 for bulk semiconductors. As the main focus of this thesis is on semiconductors in nanocrystalline form, special interest lies in excitons existing in these quantum-confined systems. Therefore, this section will focus on the spatial confinement effects in isotropic and anisotropic PNCs on the exciton fine structure and the consequences for the optical properties of the system.
By taking only the size decrease in one dimension into account and omitting confinement effects, the analytical expression for the two-dimensional exciton binding energy is four times higher than for the three-dimension version of the material:[41]

$$E_b^{2d} = 4E_b^{3d} \tag{2.9}$$

The exciton binding energy in a three-dimensional system is given by Eqn. 2.4. The result in Eqn. 2.9 is only valid for a perfect two-dimensional structure. However, suppose one starts to consider the increasing exciton binding energy trend for shrinking the system size in one or more dimensions. In that case, it exerts to be a considered influence on the expression in Eqn. 2.9. The influence becomes even more pronounced in low temperature regimes, where $k_B T$ is smaller than E_b, which is why consideration of the contributing hole and electron wavefunctions for the formation of an exciton need to be examined in detail.
As we have seen above, the effective mass theory is applicable (parabolic band description) near exciton dispersion minima.[42] The top valence band hybridization of lead-6s and bromide-4p leads to a maximum overall s-symmetry valence band, resulting in $J_h = 1/2$, causing a twofold degenerated valence band with $m_J = \pm 1/2$.[28] The conduction band consists of a lead-6p orbital, leading to three possible orthogonal spatial components for the Bloch states: X, Y, and Z. Due to strong spin-orbit coupling, these states are mixed with spin and the spin-orbit coupled system, described by the good quantum number J_e, resulting in a two-fold degenerated $J_e = 1/2$ state for the electron at the bottom of the conduction band as introduced in Sec. 2.1.2. Thus the resulting electronic states, which form the conduction band minimum are:

$$\begin{aligned} |\Uparrow\rangle_e &= -\frac{1}{\sqrt{3}}[(|X\rangle + i\,|Y\rangle)\,|\downarrow\rangle + |Z\rangle\,|\uparrow\rangle], \\ |\Downarrow\rangle_e &= \frac{1}{\sqrt{3}}[-(|X\rangle - i\,|Y\rangle)\,|\uparrow\rangle + |Z\rangle\,|\downarrow\rangle] \end{aligned} \tag{2.10}$$

Fig. 2.8 a) shows schematically an exciton in a PNC cube, where the hole and the electron are depicted

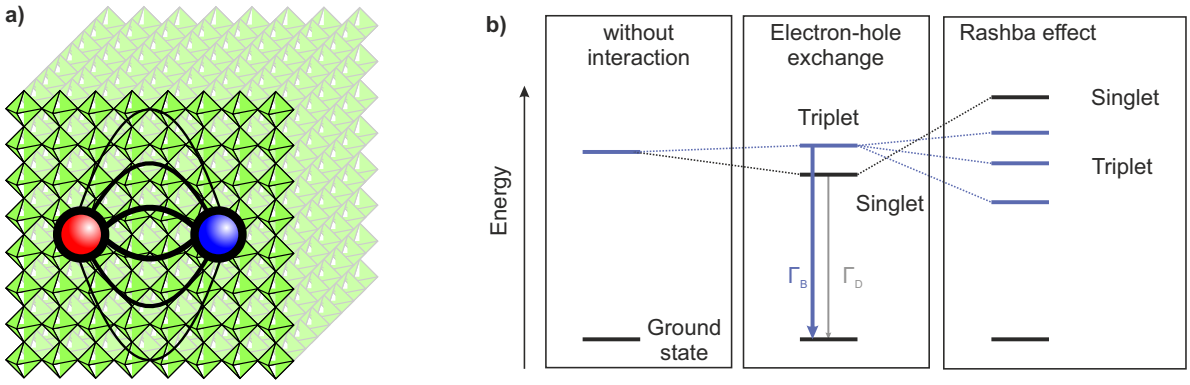

Figure 2.8: a) depicts an exciton state in a PNC cube schematically. b) shows the excitonic energy states of a PNC cube by including different electron-hole interaction terms. The left energy diagram depicts the degenerated levels where no electron-hole interaction is considered. Thus, the levels are purely given by the bulk electron and hole wavefunction, which are not bound. Turning on the electron-hole exchange interaction leads to the middle energy diagram, and additionally, considering the Rashba effect results in the right diagram. The dark exciton state is black, and the bright exciton state is blue, with corresponding radioactive decay rates of Γ_D and Γ_B, respectively. The degeneracy is (partly) lifted there, and depending on the considered interaction, the bright-dark exciton level ordering is inverted. The figure is adapted from[42].

as a red and blue sphere, respectively. Fig. 2.8 b) illustrates the energy diagram for the first excited states by including different interaction terms for the isotropic PNC in the two-particle representation. The left energy level diagram shows the bulk energy band diagram of the ground state (black) and the degenerated first excited states (blue) where no many-body interactions are considered. Thus, the first excited states are product states of the valence band hole and conduction band electron Bloch states, which are energetically degenerate at this stage.

By considering the electron-hole exchange interaction, the degeneracy is lifted to some extent as shown in the energy diagram in the middle. There is a dipole-allowed degenerated triplet state ($J = 1$) and a dipole-forbidden singlet state ($J = 0$), where the total exciton momentum $J = J_e + J_h$ serves as a new quantum number. The excitonic singlet state is given by:

$$|\Phi_{0,0}\rangle = \frac{1}{\sqrt{2}}[|\Downarrow\rangle_e|\uparrow\rangle_h - |\Downarrow\rangle_e|\downarrow\rangle_h] \tag{2.11}$$

and the three degenerated triplet states are:

$$\begin{aligned} |\Phi_{1,-1}\rangle &= |\Downarrow\rangle_e|\downarrow\rangle_h \\ |\Phi_{1,0}\rangle &= \frac{1}{\sqrt{2}}[|\Downarrow\rangle_e|\uparrow\rangle_h + |\Downarrow\rangle_e|\downarrow\rangle_h] \\ |\Phi_{1,1}\rangle &= |\Uparrow\rangle_e|\uparrow\rangle_h \end{aligned} \tag{2.12}$$

The triplet states are referred to hereafter as bright exciton states and the singlet as dark exciton state due to their optoelectronic characteristics.[43] If only electron-hole interaction is considered, the bright state is energetically higher than the singlet state. The energetic distance between the dark and bright exciton states is PNC size dependent. This bright-dark splitting energy increases for decreasing PNC size, which is crucial for interpreting the low temperature diffusion behavior in systems for different PNC sizes in Sec. 4.3.1.1. Besides the absolute splitting energy, the energetic level order of the dark and bright states is important for understanding the decay behavior and exciton diffusion performance in those systems.

The right energy diagram in Fig. 2.8 b) was first suggested by Becker et al. which regards a Rashba term as an additional interaction term. For such a system, the energetic level ordering is inverted, causing the bright states to be energetically lower than the dark state, and resolving the bright triplet degeneracy completely. They used this theory to explain the relatively fast decay in $CsPbBr_3$ at low temperatures.[42]

Rossi et al. investigated the excitonic bright-dark level ordering in $CsPbBr_3$ PNCs of different shapes and forms (cubes, rods, and PNPLs). They stated that the lowest exciton level is found for systems with an optical dark state. In particular, they claimed a low-lying dark excitonic state in PNC cubes for lateral sizes below 9 nm.[44] Rossi et al. also speculate about a possible energetic level inversion of the bright-dark excitons for sufficient large PNC cubes (larger than 9 nm), which would be consistent with the results of Becker et al., where they observed low lying bright triplet states in 14 nm PNC cubes.[45] Besides those investigations in $CsPbBr_3$-based PNCs, Tamarat et al. investigated $FaPbBr_3$ PNCs which always have a dark exciton ground state.[46] This controversial discussion about the bright-dark level ordering in inorganic PNCs has ended with the observations made by low temperature magneto-optical experiments, which show that the lowest lying state in PNCs is a dark singlet state, as observed for all other NC systems to date.[47] Therefore, the theory where only electron-hole exchange lifts the degeneracy of the four excitonic states is incorporated during this thesis, where the bright states are energetically above the dark state.

PNPL films and the exciton diffusion within those ensembles will also be discussed. Therefore, the following summarizes the features of their bright-dark level ordering and their splitting energies. The splitting energies are even more prominent in PNPLs than in PNC cubes, which becomes crucial for decay dynamics and exciton diffusion at low temperatures.[48,49] Fig. 2.9 a) shows a schematic depiction of a PNPL, containing bright exciton in its upper half and a dark exciton in its lower half. The dipole moments of the bright exciton have a p-symmetry, and, therefore, they can be either in-plane as p_{xy} (yellow) or perpendicular to the PNPL large facet denoted by p_z (red). The dipole moment corresponding to p_z lays mainly outside the PNPL. This penetration of the surrounding space depends on the PNPL thickness. In the lower half of the PNPL is a dark exciton depicted in gray, it has overall s-symmetry, and its lateral extension is smaller than the bright exciton states. For a PNPL which has the same size in the x and y directions, the in-plane exciton states degenerate, whereas the exciton with dipole moment aligned perpendicular to the larger PNPL facet has a different energy compared to the other two bright excitons. To investigate the energetic exciton levels for PNPLs, Gramlich et al. used the same approach as Becker et al., i.e., including electron-hole exchange interactions in their calculations, however, without considering the Rashba effect. The electron-hole exchange interaction can be split into short- and long-term interactions. The short-range interaction can be written as an effective spin operator, and the long-range interaction can be represented as the Coulomb interaction of charge densities at distinct exciton locations (any exciton states is accompanied by a transition dipole density P(R), which is induced by a charge density).[42,49]

In Fig. 2.9 b) the bright-dark splitting energies are depicted depending on the PNPL thickness. The energy differences are plotted here from the dark exciton energy baseline. Thus, all energies given here refer to the dark exciton energy. The crosses originate from TRPL measurements for six different PNPL thicknesses from 2 - 6 MLs. The red and yellow curves correspond to theoretical calculations applying the Kp-method and are the bright-dark exciton splitting energy for the out-of-plane and in-plane excitons, respectively. Interestingly, a bright exciton level inversion is predicted here for PNPLs with only 2 MLs or lower. This refers to the penetration argument stated above, for such thin

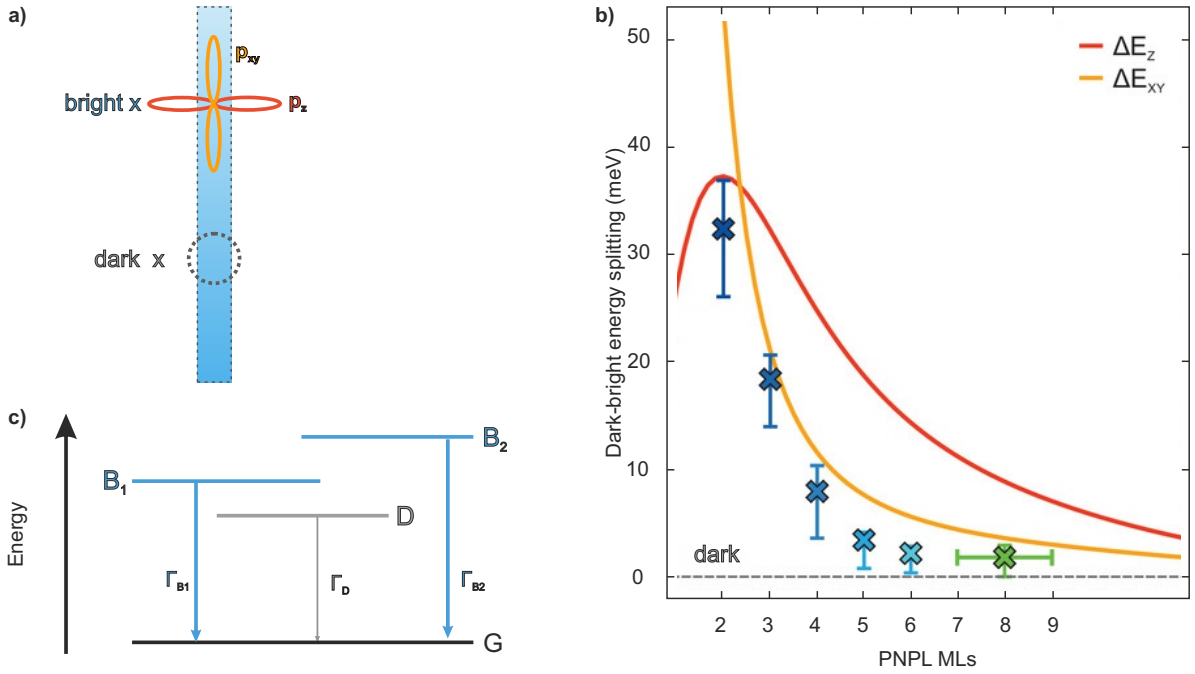

Figure 2.9: a) shows a PNPL from the side (light blue). A bright exciton sits in the upper half of the PNPL, where its different p symmetric dipole moments are depicted. There are two in-plane bright excitons p_{xy} (yellow) and on out-of-plane p_z concerning the PNPL larger facet. A dark s symmetric exciton (gray) is depicted within the lower half of the PNPL. b) depicts the experimentally gained bright dark splitting energies for different sized PNPLs via the colored data crosses. The yellow and red curves are the theoretically calculated bright-dark splitting energies for the p_{xy} and p_z exciton, respectively. c) illustrates the excitonic band diagram highlighting the lifted degeneracy. The lowest exciton is the dark one, followed by the first bright (B_1) and energetic higher located bright exciton (B_2). The radiative decay channels are denoted with Γ, whereas the nonradiative intra exciton transitions are omitted. Figure is adapted from[49].

PNCs, the dipole moment also lays outside the PNPL for the in-plane excitons. However, for all other PNPL thicknesses, the p_z exciton is always energetically higher and therefore less favorable to occupy the p_{xy} excitons. The experimentally gained splitting energies always consider the energetically lower lying bright state since the upper level is depopulated via a decay channel to the lower bright state.[49] For our interest, the splitting energy of 3 ML PNPLs is important since those are the only PNPL samples that were examined at low temperatures.

Fig. 2.9 c) shows the energy band diagram for a PNPL of a not further specified thickness. Thus, one is not able to induce the bright exciton levels (B_1 and B_2) with the out-of-plane or perpendicular dipole orientation due to the thickness dependent bright state inversion. The dark exciton state (gray) always lies below the bright exciton levels (blue). The internal exciton transitions are omitted for clarity. The radiative decay channels to the ground state are depicted as arrows. The dark decay rate is approximately 100 times smaller than the bright decay rate.

Besides excitons as dominant excited states in PNCs, phonons are also present. Phonons were introduced above for bulk perovskite structures, however, since translation symmetry is broken in NCs, the next section is devoted to working on the special features of phonons in PNCs.

2.2.3 Phonons in NCs

The dominant phonon charge carrier interaction in ionic NCs is the Fröhlich interaction. The long-wavelength longitudinal optical phonon can induce an electric field that interacts with the system's free charge carriers. The interaction of free charge carriers with phonons is well described by only

considering the longitudinal optical phonons.[50,51] The effects on optoelectronic properties like PL spectral broadening will be discussed in Sec. 2.3.1.
Since PNCs have a sizable surface-to-volume ratio, the following section briefly overviews surface trap states not discussed for bulk semiconductors so far.

2.2.4 Surface Traps in PNCs

As pointed out in Sec. 2.1.3 where general point defects in bulk perovskite $CsPbBr_3$ are discussed, there are additional exciton or free charge carrier traps in PNCs where the surface-to-volume ratio is large.[3] Since we are mainly interested in transport phenomena in ensembles consisting of PNCs, this section is devoted to discussing possible trap states which modify exciton diffusion.
Possible trap sites correspond to bromide and lead vacancies in PNPLs or generally within PNCs.[17] Bohn et al. introduced a synthesis approach that repairs those surface vacancies. The resulting PL

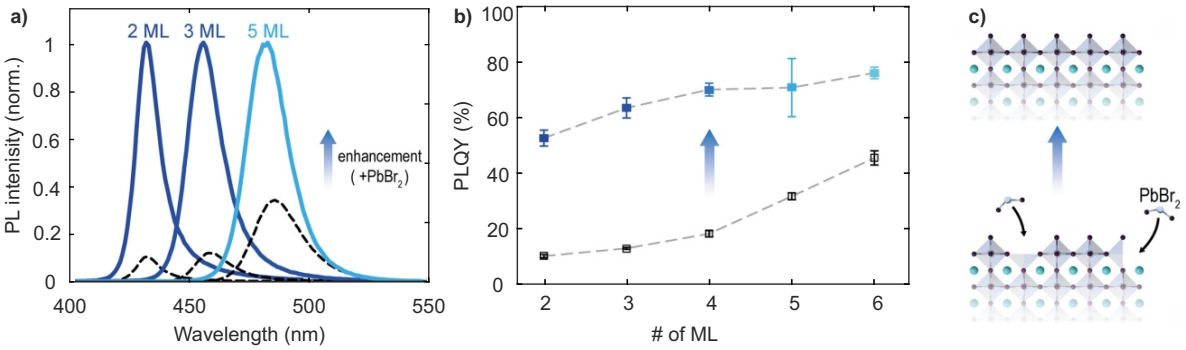

Figure 2.10: a) shows the PL spectra for 2 ML, 3 ML, and 5 ML PNPL samples before (dashed black lines) and after (dark blue to light blue curves) post-synthetic enhancement of the PNPL solution. b) illustrates the effect on the PLQY of PNPLs after addition of $PbBr_2$-containing enhancement solution after the synthesis to samples of 2-6 ML thickness. c) depicts the repair mechanism of adding $PbBr_2$ after synthesizing $CsPbBr_3$ PNPLs of different size. The lower panel shows vacancies at the PNC surface, and the upper panel depicts the repaired $CsPbBr_3$ PNPLs surface. The figure is adapted from[17].

spectra of samples before and after post-synthetic treatment are depicted in Fig. 2.10 a) for 2 ML, 3 ML, and 5 ML PNPL samples. The PL spectra recorded before the treatment are plotted as dashed lines for the 2 ML, 3 ML, and 5 ML PNPL samples. The PL spectra corresponding to the treated PNPLs are plotted from dark to light blue from thin to thick PNPL, respectively. The PL spectra were normalized to the maximum PL value for each PNPL thickness. This enables a qualitative evaluation of the post-synthetic treatment with additional $PbBr_2$ solution through its PL enhancement effects. As shown from those PL spectra, the PL is enhanced for all PNPL samples, which were treated with the enhancement solution. A quantitative assessment of the PLQY improvement of PNPLs upon post-synthetic enhancement depending on their thickness is depicted in Fig. 2.10 b). Here, the enhancement is largest for the thinner PNPLs and gets lower for 5 and 6 ML PNPLs. This smaller effect of PLQY enhancement in thicker PNPLs can result from a lower surface-to-volume ratio in the thicker PNPLs. The surface-to-volume ratio is largest for the smallest thickness, thus, the repair mechanism is highest for the 2 ML PNPL sample compared to thicker ones that are indeed observable.
A schematic mechanism of the enhancement solution treatment is depicted in Fig. 2.10 c) where the pre (lower panel) and post (upper panel) synthetic crystal structure of the PNC is visible. The addition of $PbBr_2$ repairs surface vacancies leading to a reduced surface trap density, resulting in an enhanced PLQY. The ligand shell is omitted in this schematic. Additionally to the repair effect,

the ligand-passivation of PNPLs of different thicknesses results in an initial large PLQY with a near mono-exponential PL decay behavior, which points to a defect tolerant system.[52,53] In addition to the surface traps, the bulk neutral point defects also contribute to the total trap density, which renders PNCs less emissive than its bulk counterpart. However, perovskite bulk material is often disturbed by grain boundaries in its macroscopic structure, which also serve as non-radiative seeds within those structures.[54] Since the exciton binding energy in non-quantum confined perovskite structures is lower than in its PNC counterpart, there are more free charge carriers in the systems, which can be trapped more easily. Thus, in favor of PLQY, there is a trade off between the trap state density that is actually present in the underlying semiconductor and the number of free charge carriers as excited states.
According to the energetic trap depth and the recombination process which follows after trapping, one can characterize traps in deep or shallow traps, as pointed out above, as well as radiative and non-radiative states. In this thesis, it will be shown that depending on temperature, there are different regions where shallow or deep traps are dominant. Radiative deep trap states seem to be the dominant trap species for temperatures in the range of 140 - 280 K which will be discussed in depth in Sec. 4.3.2. Excited state trapping is often more likely for charged particles than neutral excitons. Thus, the actual possibility of an excited state to be in the bound exciton phase compared to the free charge carrier phase within a PNC matters. Besides the higher likelihood for charge carrier trapping compared to exciton trapping, another crucial fact concerning transfer processes in PNC systems is that only excitons can transfer their energy to adjacent PNCs. This means it is worthwhile to investigate the exciton to free charge carrier distribution within PNCs in more detail, which depends on the exciton binding energy, temperature, and laser excitation power which generates the excitons.

2.2.5 Free Charge Carriers to Excitons Ratio Governed by the Saha-Equation

As we have seen above, excitons are the dominant excited states in PNCs. However, we disregarded the excitation power of the laser during an optical measurement, which translates into exciton generation per cube per pulse, and the system temperature. If the system temperature gets close to the exciton binding energy, the assumption to have only excitons in the system is not valid anymore. Furthermore, this holds also true at lower temperatures since one can always assume the underlying excitation energy spectra as a two-level system consisting of bound states (excitons) and ionized excitons (free charge carriers). To describe the system at temperatures where neither only excitons nor free carriers are dominant, one can utilize the Saha–Langmuir equation in organic perovskites and all inorganic PNCs.[15,55,56]
Saha first introduced this description by explaining the observation of ionization of calcium, strontium, and barium, which becomes increasingly visible in their spectral lines as one approaches the upper layers of the solar atmosphere.[57] The interpretation was then used in solid-state physics to explain the observation of exciton to free charge carrier ratio in quantum wells.[58] In this context, the excitons can be seen as the unionized particles, where the free charge carriers are the ionized particles. The ionization energy is the exciton binding energy E_b. By assuming charge neutrality $n_e = n_h$ which is a valid assumption upon optical excitation, one can calculate the number of excitons n_x to all excited

states $N = n_x + n$:

$$\frac{n_x}{N} = 1 - \frac{A'T^{3/2}\exp(-E_b/k_BT)}{2N}\left(\sqrt{1+4\frac{N}{A'T^{3/2}\exp(E_b/k_BT)}} - 1\right)$$
$$A' = \frac{\nu_x}{\nu_h\nu_e} = \left(\frac{2\pi\mu_X k_B}{h^2}\right)^{3/2} \tag{2.13}$$

ν_i is the quasiparticle's thermal volume, μ_X is the reduced exciton mass. Only one excited species should be present in a NC, free charge carriers or the bound version. Thus, in the low excitation regime where bi-excitons and Auger recombinations are negligible, the exciton to all excited states ratio in a NC is independent of absorption cross-section and excitation power. This sharply contrasts investigations in systems where more excitations can be located in the same crystal,[56] where the fraction is also sensitive to excitation power.

2.3 Light-Matter Interactions

In the previous sections, bulk and noncrystalline semiconductors were discussed with a particular interest in perovskites or PNCs, which are the material of interest in this thesis. This section deals with the interaction of electromagnetic waves with matter. In particular, we are interested in the dominant excitation and emission processes of light interaction with PNCs. A portion is devoted to temperature-dependent optoelectronic properties like thermal-induced PL broadening or an increasing Stokes shift for increasing temperature. After discussing the individual properties of PNCs, the remaining part of this section is devoted to briefly introducing the dominant exciton transfer process between adjacent PNCs.

2.3.1 PL Decay Dynamics and Spectrum in PNCs

As discussed in the previous sections, a semiconductor can be excited, which results in excited states. There are several mechanisms that excite those states, e.g., thermal, chemical, electronic, and optical processes.[30] In this thesis, our focus is solely on the direct optical excitation of states. As such, we will concentrate exclusively on this particular mechanism.
Photons can be absorbed from semiconductors. Several processes can occur depending on the photon energy and the number of photons: Multiphoton absorption allows an excitation by photons with lower energy than the fundamental band gap energy of the absorbing semiconductor. For this process, more than one photon has to be absorbed at the same time so that energy conservation is fulfilled.[59] Photons that have energy larger or equal to the fundamental bandgap can generate an excited state in a semiconductor by themselves. If the excitation source is tuned to the PL absorption peak of the semiconductor material, the semiconductor is excited resonantly. If the excitation source consists of photons with an energy larger than the fundamental bandgap, i.e., energy exceeding the first absorption lines, one speaks of non-resonant excitation. The difference in energy between the photon energy and the fundamental bandgap is conserved by phonon generation. We will exclusively deal with non-resonant excitation since, during this thesis, the optical excitation source was set to energy values above the fundamental band gap of the considered PNC.
The quantum mechanical transition rate for exciting an electronic state from an initial state i to an

final state f is given by Fermi's golden rule:

$$W_{if} = \frac{2\pi}{\hbar}|M|^2 g(\hbar\omega) \tag{2.14}$$

$g(\hbar\omega)$ is the electronic density of states depending on the frequency (energy) and the matrix element M is the sum of all possible transitions from the initial to the final state. Thus, a high transition rate can only be established if there are both many possible transitions between the two states and a large density of states right at the transition energy.[41]

Different features can be observed in the absorption spectra depending on the material and the confinement. There is an absorption onset at the fundamental bandgap. Following quantum confinement, the bandgap and absorption onset is shifted, and if an exciton forms, there is a pronounced peak at lower energies than the fundamental bandgap. The excitonic absorption peak is higher for more confined systems, yielding a larger oscillator strength.[60] For perovskite semiconductors, the absorption band edge (and the PL maximum) shift to lower energies for lower temperatures in contrast to other semiconductors.[61] This is also true for PNCs, except for very thin PNPLs, as we will see below. This is a direct consequence of the conduction and valence band formation since those are inverted to ordinary semiconductors. The thermal expansion of the PNC leads to a PL blue shift.[62]

The absorption cross-section measures how strong matter interacts with light, i.e., how much light a specific material area absorbs. Thus, it has dimension of squared length. It is needed to calculate the average energy which is absorbed. The excitation source used during this work is a pulsed laser, which is characterized by three major properties: Pulse duration, laser power, and repetition rate. The size of the laser beam diameter results from the lens system which is utilized. The average absorbed energy per pulse is then given by:

$$E_{abs} = \frac{P_L}{f_{rep}\, A_L}\sigma_{abs} \tag{2.15}$$

Here, P_L is the laser power, f_{rep} is the laser pulse repetition rate, A_L is the laser beam cross-section, and σ_{abs} is the absorption cross-section. The absorbed energy per pulse is averaged since the laser pulse has a specific temporal length.

Concerning exciton diffusion, it is relevant how, on average, excitons get generated in a film of PNCs. To calculate the probability of generating one exciton in one PNC per pulse, one needs the averaged absorbed energy given by Eqn. 2.15, the excitation photon energy E_{ph}, and the total amount of PNCs within the excitation area $n_{cubes} = A_L/A_{cube}$ which is the ratio of the laser beam cross-section and the PNC cube cross-section A_{cube}:

$$n_X = \frac{E_{abs}}{E_{ph}\, n_{cubes}} \tag{2.16}$$

This quantity should be small to exclude nonlinear decay channels, which will be introduced below. Besides omitting additional excitonic decay channels, it is crucial for exciton diffusion to only generate a small number of excitons within the PNC film. For instance, if on average every PNC cube is occupied by an exciton, this would result in a deviation of free exciton diffusion. An exciton transfer from one PNC to an already occupied one is suppressed since this would cost additional energy due to the repulsive forces of the constitutionals of both excitons.

After exciton formation, i.e., free charge carrier generation, hot electron cooling, and exciton binding, the excitons can undergo several decay channels. Fig. 2.11 a) depicts a spontaneous emission of a photon with energy E_{ph} which results from an exciton recombination. In this scenario, the exciton occupies the first exciton level, and due to quasi momentum conservation of the total exciton quasi

momentum K, the exciton has to have the quasi-momentum which corresponds to the interception between the light energy dispersion line and the exciton dispersion curve given by Eqn. 2.3. This

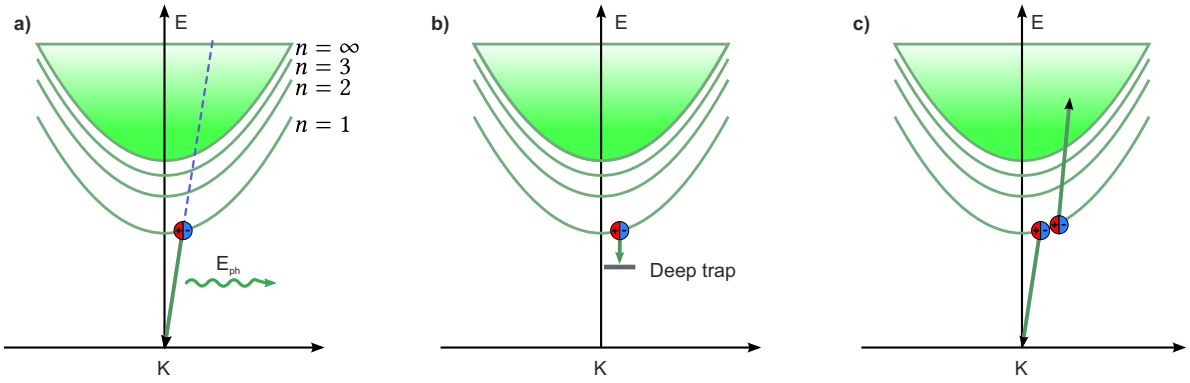

Figure 2.11: a) presents a radiative exciton recombination process. The photon is depicted as a squiggly arrow and the exciton as a red-blue sphere, located at the intersection of the light dispersion relation and the first excitonic level. b) depicts the trapping event of an exciton in a deep trap. c) illustrates an exciton-exciton annihilation process, where one exciton recombines nonradiatively, and the other exciton absorbs the excess energy and severed into in its constitutionals.

recombination process is proportional to the exciton density $n(t)$. Excitons can also be trapped, which is depicted in Fig. 2.11 b) where an exciton is trapped in a deep trap. Deep means in this context that detrapping is not possible since the trap energy level sits too deep in the band gap. The trapped exciton can decay non-radiatively or radiatively. In the case of a trapped exciton which decay radiatively, the emitted photon has a lower energy as the first exciton state. The exciton trapping process is also linearly proportional to the excitonic density. A higher-order process in the exciton density is shown in Fig. 2.11 c) which is a nonradiative recombination. Two excitons interact with each other, and one of them recombines without emitting a photon. The non-recombining exciton is excited to a higher energetic state since it absorbs the excess energy from its recombining partner. The electron-hole bonding is severed since the excited state is located in the continuum in the two-particle picture, where relaxation to the band edge and the lowest exciton level happens by phonon emissions afterward.[63] This process is proportional to $n^2(t)$ since it needs two excitons and is called exciton-exciton annihilation. Decay channels that are proportional to higher powers in the exciton density, are neglected, since the excitation power is kept low. Thus, those contributions are low. The temporal evolution of the exciton density illustrated by Fig. 2.11 can be combined in the rate equation:

$$\frac{dn(t)}{dt} = -k_r\, n(t) - k_{nr}\, n(t) - k_{EEA}\, n(t)^2 \tag{2.17}$$

The rates, k_r, k_{nr}, and k_{EEA} are the radiative, nonradiative, and exciton-exciton annihilation rates, respectively. Note that depending on the recombination process of the trapped exciton, it can be either radiative or nonradiative. Thus, this contribution is governed by the first or the second term in Eqn. 2.17.

The radiatively decaying excited states described by Eqn. 2.17 can be found according to their photo energy as PL emissions spectrum. Since the laser-induced excitation is low, we will only focus on spontaneous emission. Stimulated emission needs higher excitation power. The PL spectrum is one basic characteristic of a light-emitting material. It can be described by its full width at half maximum (FWHM), peak position, and asymmetry if there is only one peak. PNC has a narrow PL spectrum even at room temperature, and depending on the constitutionals considered, the peak position is shifted from

red to blue (iodine, chlorine). We will deal with $CsPbBr_3$, which emits green to blue depending on the

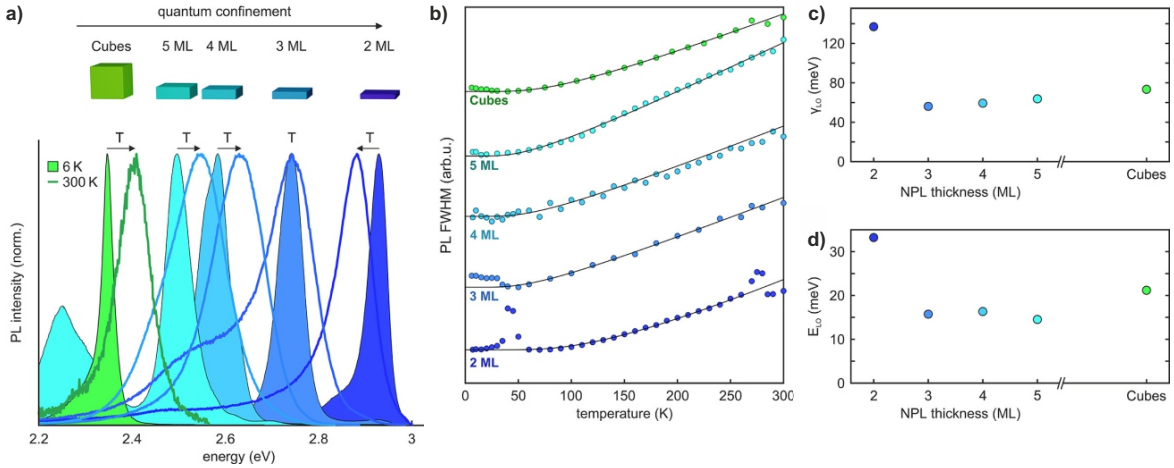

Figure 2.12: a) shows the PL spectra for 14 nm PNC cubes and 5 - 2 ML PNPLs from green to dark blue. The PL spectra with the marked area below the curve were measured at 6 K, whereas the other PL spectra were recorded at room temperature. b) depicts the temperature-dependent FWHM of PL spectra for the measured PNCs from a). The black curves correspond to a fit to Eqn. 2.18. c)+d) illustrates the temperature-dependent fit parameter gained from b), which are the Fröhlich coupling constant γ_{LO} and the longitudinal optical phonon energy E_{LO}. The figure is adapted from[51].

PNC size as it is illustrated in Fig. 2.12 a) for 14 nm PNC cubes down to 2 ML PNPLs (green to dark blue). The PL spectra for 6 K (solid area below the curves) and for room temperature are depicted. For thicker PNCs, the PL spectrum peak shifts with increasing temperature to higher energies which is shown by the arrows pointing from the low temperature PL spectrum to the room temperature PL spectrum. For the 3 ML PNPL sample, there is no absolute peak position shift in temperature. For the 2 ML PNPL sample, the PL spectrum peak position shift is opposite to the thicker PNCs resulting in a total change to lower energies. The PL linewidth broadening can be disentangled into a inhomogeneous part due to nonidentical PNCs and a homogeneous part due to exciton–phonon coupling.[64,65] Fig. 2.12 b) depicts for the investigated PNCs the PL FWHM evolution for increasing temperature. The PL FWHM decreases with decreasing temperature due to the reduction of homogeneous broadening. The data points are offset for clarity. To quantify the contribution of homogeneous broadening to the total PL FWHM Γ, one evaluates the temperature dependent PL FWHM with:

$$\Gamma(T) = \Gamma_0 + \Gamma_{LO}(T) = \Gamma_0 + \frac{\gamma_{LO}}{\exp(\frac{E_{LO}}{k_B T}) - 1} \tag{2.18}$$

Here, Γ_0 is the PL FWHM resulting from the inhomogeneous broadening of single PNCs of different size, and the second term yielding $\Gamma_{LO}(T)$ takes the exciton phonon interaction into account. Eqn. 2.18 states that the temperature induced broadening results from the Fröhlich interaction quantified by the Fröhlich coupling constant γ_{LO} of excitons with longitudinal optical phonons of energy E_{LO}.[51] The curves in[64,65] Fig. 2.12 b) correspond to the fit function Eqn. 2.18. One easily gets both fit parameters that characterize the temperature-induced PL spectral broadening from those fits. γ_{LO} is shown in Fig. 2.12 c) for four PNPL thicknesses and for PNC cubes (green). The 2 ML PNPLs have a large 2.5-fold coupling constant compared to the other PNCs, which have comparable Fröhlich coupling. The coupling constant measures how large the interaction between excitons and phonons in the PNC is, thus, for larger coupling, one would assume a greater impact of phonon-induced effects in the smallest PNPLs. Another major quantity that describes the interaction is depicted in Fig. 2.12 d) for

the five evaluated PNC systems. The longitudinal optical phonon energy is like the coupling γ_{LO} size and shape independent for the larger PNCs, with an exception for the smallest PNPLs. For the 2 ML PNPLs, the phonon energy is twice as large as for the other PNCs. In the results section, we will mainly deal with 3 ML PNPLs and 14 nm PNC cubes, which have a phonon energy of 16 meV and 21 meV, respectively.[51] The energy of the dominant phonons for the 3 ML PNCs are similar to the above introduced bright-dark splitting (see Fig. 2.9 d)). This becomes important when low temperature measurements will be conducted within those PNPLs. Of course, other phonons can also occur, however, for ionic bound NC and PNCs, the longitudinal optical phonon branch is the dominant one, and by considering it, the temperature-induced FWHM broadening can be reproduced quite well. After discussing fundamental optoelectronic processes in PNCs, the following section will deal with the discrepancy of absorption and PL spectra. Namely, the different energetic onsets of both which is termed Stokes shift.

2.3.2 Stokes Shift in PNCs

As it will be introduced in Sec. 2.3.3, a spectral overlap between donor PL and acceptor absorption is favorable for a large Förster resonant energy transfer (FRET) rate between the donor-acceptor pair. Hence, a good overlap is beneficial for transport in ensembles of those pairs. Since exciton diffusion is discussed hereafter only within PNC ensembles consisting of the same PNCs, the above-stated overlap is governed by the Stokes shift. The Stokes shift is the difference between the same semiconductor material's absorption onset and PL emission maximum. The absorption is energetically higher than the PL spectrum for a normal Stokes shift. The anti-Stokes shift describes the reverse situation, i.e., the absorption maximum is energetically lower than the PL spectrum maximum position. However, anti-Stokes needs an additional energy supply to lift the PL spectrum above the absorption, which will not be the case for the following discussion. Thus, we will only discuss the normal Stokes shift in semiconductors.

For $CsPbBr_3$ PNC cubes, a size-dependent Stokes shift was reported by Brennan et al.[66]: They measured for the first time an increasing Stokes shift for decreasing PNC cube size. They explained the behavior with a confined hole state which is dark in absorption, i.e., a low absorption cross-section, but bright in emission. The confined hole state lays above the valence band edge, and thus radiative recombination from a conduction band electron to the confined hole state is favorable. The energetic difference between the confined hole level and valence band maximum governs the appearing Stokes shift, which is size dependent.[67] Later, the same group discovered similar qualitative trends for other PNC cubic systems, i.e., with iodine or chlorine as halides. There, they out rule polaron formation to be responsible for the size-dependent Stokes shift. They state that the excitonic fine-level structure shall be taken into account.[68] In 2021, Shcherbakov-Wu et al. investigated temperature-dependent Stokes shift in $CsPbBr_3$ PNC cubes of different sizes.[69] There is a decreasing trend of the Stokes shift for decreasing temperature, like for the bulk. However, the Stokes shift for bulk goes to zero for low temperature (35 K), whereas, for PNCs, it does not decrease with the same speed. It seems that the Stokes shift does also not drop to zero like for bulk. They stated that the confined hole state model, introduced above, could not explain the temperature Stokes shift trend. It seems more likely to be of phonon nature.

The overlap of acceptor absorption and donor emission spectra is dictated by the Stokes shift for

energy transfers in systems consisting of the same material. In the next section other crucial properties of the PNC film and the individual PNCs for optimizing the transfer are discussed.

2.3.3 Förster Resonance Energy Transfer

A possible gateway for transporting carriers between NCs is a non-radiative energy transfer process. Since an isolating ligand shell surrounds the here-discussed PNC, charge carrier transfer is strongly suppressed. The process where free charge carriers can actively tunnel between NCs is termed Dexter. Instead, non-radiative processes transporting the excited states via energy transfer are happening. Here, FRET is the predominant process which is regarded as the predominant type of energy transfer in colloidal NC ensembles.[13] After recombination, the generated carriers within one PNC transfer their energy to a neighboring PNC. This energy transfer is accompanied by a new excited state in the adjacent PNC, i.e., a new electron-hole pair is generated without any physical carrier transport.[70,71] FRET was theoretically addressed by T. Förster and described by considering two point-like fluorophores.[72,73] A fluorophore is a fluorescent chemical compound emitting light after optical excitation. If now two fluorophores are located close enough (dependent on the FRET radius), an excited state in one of them, the donor, can be transferred non-radiatively to the other fluorophore, the acceptor. This process is

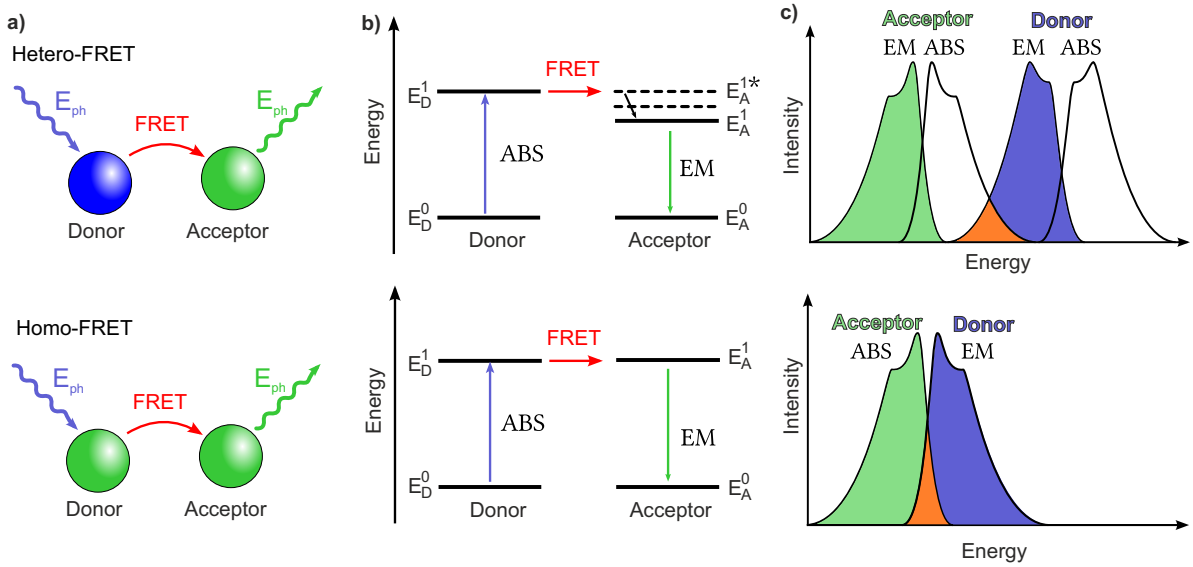

Figure 2.13: a) schematically shows a hetero-FRET process where the fluorophores are of different materials (upper panel). The lower panel depicts the homo-FRET process of a donor-acceptor pair of the same material. The donor is optically excited by a photon (blue arrow), and a non-radiative FRET process transfers the energy to the acceptor (red arrow), where the transferred excited state radiatively recombines (green arrow). b) illustrates the processes described in a) by utilizing the energy band diagrams of the donor (left) and acceptor (right) for hetero-FRET (top panel) and homo-FRET (bottom panel). c) illustrates the emission spectra (EM) and absorption spectra (ABS) of the donor and acceptor in the upper panel for Hetero-FRET. The lower panel only shows the donor EM and acceptor ABS. The crucial part for maximizing FRET is the overlap of donor EM and acceptor ABS depicted in both panels as the orange area.

schematically depicted in the upper panel of Fig. 2.13 a), where the donor is excited optically (blue photon arrow). The donor and acceptor NCs interact via dipole-dipole interaction, which can be described as a virtual photon exchange illustrated by the red arrow in the schematics.[70,74,75] After the transfer, the excited state in the acceptor can recombine to the ground state by emitting a photon illustrated with the green arrow. The original explanation of FRET considers two different fluorophores, where the donor excited states E_D^1 are generally above the acceptor excited states E_A^1. This situation

is illustrated in Fig. 2.13 b) upper panel for a resonant energy transfer from E_D^1 to $E_A^{1\star}$ which is the vibronically excited energy level of the acceptor. By emitting phonons, the vibronic energy from the $E_A^{1\star}$ level dissipates and the exciton occupies the E_A^1 state. A back transfer is unlikely in those heterogeneous structures due to the missing resonant state in the donor NC. Thus the only gateway is radiative or non-radiative decay to the acceptor ground state E_A^0.
However, for the here considered PNC ensembles, the donor and acceptor are from the same kind which is depicted in the lower panel of Fig. 2.13 a). Thus, their energy levels are, in principle, the same. Therefore, there is a direct resonant energy transition possible between E_D^1 and E_A^1 without the detour over a vibrational mode of the acceptor excited state, which is depicted in Fig. 2.13 b) lower panel. For both considered cases, i.e., hetero-FRET and homo-FRET, an overlap between the donor emission and acceptor absorption spectra is crucial for maximizing the energy transfer via FRET. This spectral overlap is shown for both cases in Fig. 2.13 c) highlighted by the orange area. Of course, so that homo-FRET is possible, some preconditions have to be fulfilled, which get clear by considering the FRET rate between point-like fluorophores, which is given by:

$$R_{FRET} = \frac{9c^4\kappa^2}{8\pi n^4 \tau_D} \frac{1}{r^6} \int_0^\infty \frac{f_D(\omega)\sigma_A(\omega)}{\omega^4} d\omega \tag{2.19}$$

This formula yields the FRET rate for an interacting donor-acceptor pair, where c is the vacuum speed of light, n is the refractive index of the host medium, and τ_D is the donor exited state radiative lifetime. κ quantifies the respective dipole orientation of donor and acceptor dipoles. If the dipole moments of the excited state are perpendicularly oriented, κ is zero, and it is one if they are parallel. For isotropic orientation implying s-like excitons $\kappa^2 = 2/3$ which is often utilized. Thus, it is crucial how the excited excitonic states are oriented if one considers p-like excitons (the dipole allowed transitions in PNC). The integral considers the spectral overlap between the donor emission and acceptor absorption spectrum, where $f_D(\omega)$ is the integral-normalized PL spectrum of the donor and $\sigma_A(\omega)$ the absorption cross-section of the acceptor. As mentioned above, the overlap must be as large as possible so that FRET processes get relevant. For homo-FRET, that means a small Stokes shift of the individual PNC and a homogeneous energy landscape of adjacent PNCs, which is both fulfilled in PNCs.[1,14]
The most important FRET-rate dependence, however, is the distance between the acceptor and donor NC. For a one-dimensional system, the distance dependence is $r_{FRET}^{1d} \propto 1/r^6$. It becomes less important

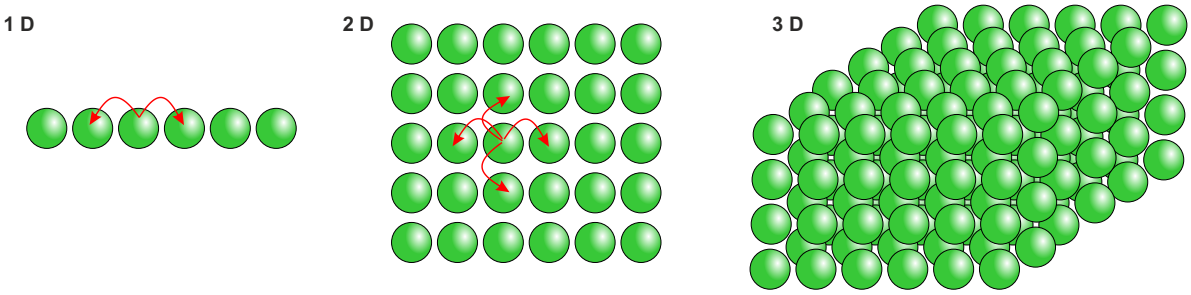

Figure 2.14: The figure shows different NC ensembles: A one dimensional chain (left panel), a two dimensional film (middle), and a three dimensional NC structure (right panel). The green spheres correspond to the donor and acceptor NCs for homo-FRET. Those ensembles have different distance dependencies of the FRET rate, given in the main text.

for higher dimensions where due to integration considerations, the power dependence goes down to $r_{FRET}^{2d} \propto 1/r^4$ for a two-dimensional and $r_{FRET}^{3d} \propto 1/r^3$ for a three-dimensional system, respectively.[71] Those NC systems are illustrated in Fig. 2.14. For a one-dimensional chain shown in the left panel,

there are only two nearest neighbors for the donor NC. There are more FRET transfer partners for a higher dimensional system, as can be seen from the middle and left panels, where the two-dimensional and three-dimensional cases are shown. Therefore, the distance dependence where a FRET transfer occurs goes down with distance. However, the distance dependency of a single donor-acceptor FRET is the same.
After discussing the microscopic transfer mechanism which leads to exciton transport in PNC films, we will try to describe the macroscopic transport by a diffusion description in the following section.

2.4 Diffusion

After discussing the fundamental individual properties of semiconductors, this section describes exciton transport processes within PNC structures. In principle, other excited states can experience spatial displacement like free charge carriers in ordinary bulk semiconductors. However, the section's particular interest lies in excitons since those are the dominant excited states in PNCs, as described in previous sections. Furthermore, free charge carriers can be ruled out as responsible for transport in PNCs as the dominant transfer mechanism FRET is impossible for a single electron or hole. Since excitons are macroscopically neutral, an applied voltage would not lead to any drift. Thus, the macroscopic exciton transport is governed by a diffusion process, i.e., it is exciton density gradient driven. The following sections introduce general diffusion and diffusion models for PNC or NC structures. Finally, a connection to a more appropriate microscopic understanding of a single exciton which performs a series of random walks as opposed to the macroscopic density gradient driven exciton diffusion model will be introduced.

2.4.1 Macroscopic Diffusion Model

This section introduces a continuous diffusion model, which describes the local carrier density evolution on a macroscopic level. The general diffusion equation in one dimension with only one particle species $n(x,t)$ is governed by:[13,76]

$$\frac{\partial n(x,t)}{\partial t} = D(t)\frac{\partial^2 n(x,t)}{\partial x^2} - k(t)n(x,t) + g(x,t) \tag{2.20}$$

Here, the general time dependent diffusion coefficient $D(t)$ dictates the speed of the diffusion process, and the sink term is governed by the total exciton decay rate $k(t)$. All nonradiative and radiative decay recombination channels which are proportional to the density $n(x,t)$ are included. A source term is represented by $g(x,t)$, which is, in principle, time and space dependent. However, it is often reduced to be time independent and entirely governed by the initial condition of the particle density $n(x,0) = g(x)$. Higher terms in the particle density are omitted here, which can be justified if only low excitation powers are used where exciton-exciton interactions are unlikely.[13,14]
For a time independent diffusivity and a decay rate with an instantaneous source term $n(\tilde{x},t)$, the solution of the one dimensional diffusion equation is:

$$n(x,t) = \exp(-kt) \cdot [n(\tilde{x},0) * G(x,t)] \tag{2.21}$$

Where $G(x,t) = \frac{1}{\sqrt{4\pi Dt}} \exp\left(-\frac{x^2}{4Dt}\right)$ is a Gaussian function with variance $\sigma^2(t) = 2\,Dt$, which is convoluted with the initial time independent exciton distribution. The exponential term considers the finite exciton lifetime $\tau = 1/k$. It is responsible for the non-conservation of the particle density, unlike other diffusive systems of macroscopic sizes where no particle decay or particle generation happens.
The measurable PL intensity profile, I(x,t), has an initial time independent broadening due to the point spread function (PSF) for the emitted photons $f_{PSF}(x)$, and the PSF resulting from the collecting fiber $f_f(x)$. The PSFs generally broaden the PL intensity profile according to the following equation:

$$I(x,t) = n(x,t) * f_{PSF}(x) * f_f(x) \tag{2.22}$$

The temporal evolution of the actual measurable PL profile is then only governed by the exciton density evolution, which allows a direct connection between those quantities. The PSFs only broaden the exciton density profile spatially. If one assumes now the PSF are Gaussian functions, Eqn. 2.22 are convolutions of only Gaussian profiles, i.e., the result is also a Gaussian function with a variance which is the sum of all individual variances:

$$\sigma_{PL}^2(t) = \sigma_X^2(t) + \sigma_{PSF}^2 + \sigma_f^2 := \sigma_X^2(t) + \sigma_0^2 \tag{2.23}$$

σ_{PL}^2 is the variance of the recorded PL and σ_X^2 is the variance resulting from exciton diffusion. This can be rewritten in terms of the mean squared displacement (MSD), which only accounts for the temporal evolution of the variances irrespective of the initial profile broadening σ_0^2:

$$MSD(t) = \sigma^2(t) - \sigma_0^2 = 2Dt \tag{2.24}$$

If the MSD evolves as predicted by Eqn. 2.24 one speaks of normal diffusion, which is time independent since the diffusivity is a constant. The profile expansion is linear in time irrespective at which specific time it happens.
The particle diffusivity is generally time dependent if one departure from systems which conduct linear diffusion processes like in systems where the FRET transfer rate is time and space independent. It is connected to the temporal evolution of MSD through the following relationship:

$$D(t) = \frac{1}{2}\frac{dMSD(t)}{dt} \tag{2.25}$$

In favor of getting a scalar value that characterizes the transport abilities within a film consisting of PNCs, one can average the time dependent diffusivity. This averaged diffusivity can then be used to compare diffusion processes within different materials more conveniently. It is given by:

$$\bar{D} = \frac{1}{2}\int_{t_i}^{t_f} dt \frac{dMSD(t)}{dt} \tag{2.26}$$

Here, the diffusivity is averaged from an initial time t_i to a final time t_f. For a system where the transferring particles undergo a normal diffusion process, the time integral of the averaged diffusivity collapses to a constant. However, when the diffusion process is more complex than normal diffusion, the averaged diffusivity is generally sensitive to the integration range.
One has to treat Eqn. 2.26 with caution since it only averages over the excitons at specific time steps and does not take into account the actual amount of excitons which are present at this time. In other

words, it weights excitons that diffuse initially to the same amount as the surviving excitons at a later time. However, there can be an immense discrepancy between the exciton numbers at those times. Below we will introduce a method that respects the exciton decay when the average diffusivity is calculated.

For an estimation of how long excitons can transfer within a PNC system, the diffusion length can be calculated via the following:

$$L_D = \sqrt{\tau \bar{D}} \tag{2.27}$$

τ is the exciton PL lifetime introduced in Eqn. 2.17, and $\bar{D}$ is the averaged diffusivity. The exciton diffusion length states the average distance an exciton travels through a medium. This quantity is crucial for designing active layers in devices, where it is important how long excited states have to travel.

For systems where the MSD is not linearly proportional to time, the averaged diffusivity is not the best measure to characterize the full transport process. For instance, this will be the case for a subdiffusive exciton behavior, which will be the topic of the following section.

2.4.1.1 Subdiffusion

For PNC systems where the individual PNC energetic levels are broadened,[13,77] the PNC film deviates from a perfect film,[14] or the resting times for excitons at PNCs are non-uniform,[78] the MSD behavior differs from a purely linear time dependence. The broadening of the exciton distribution is often better characterized by a subdiffusive model description, implying a MSD temporal evolution like:

$$MSD(t) = 2At^{\alpha} \tag{2.28}$$

Where the exponent $0 < \alpha < 1$ characterizes the degree of subdiffusion. For exponents closer to zero, the diffusion process is increasingly disturbed. Akselrod et al.[77] connected energetic downhill exciton hopping to the subdiffusion process, i.e., the broadening of the PL profile decreases at later times. They argued that the lower lying excitons do not have as many reachable acceptor FRET partners after active downhill transfers, which means a reduced exciton diffusion over time. These subdiffusion MSD trends

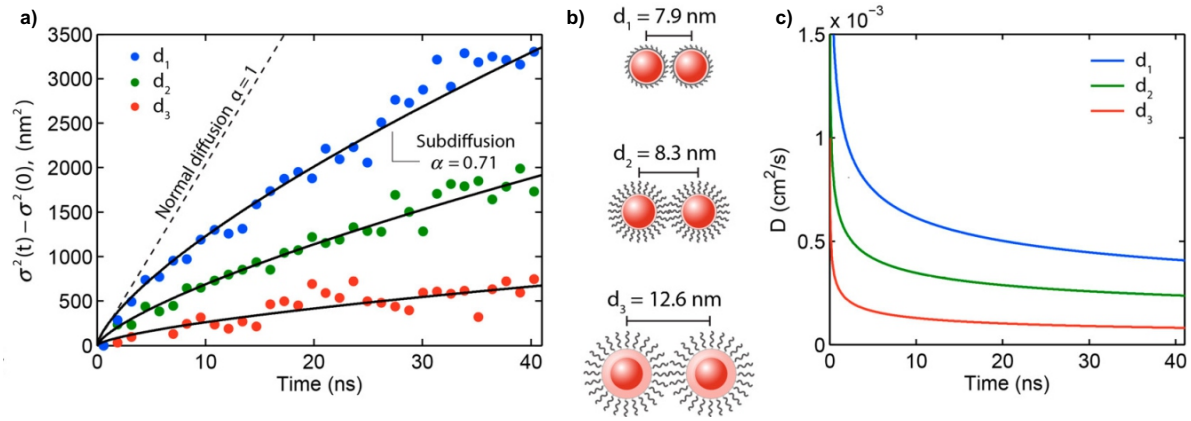

Figure 2.15: a) depicts the temporal MSD evolution for different QD systems of varying distance between NCs. b) shows schematically three different CdSe/ZnCdS core/shell QD pairs which represent the NCs used in a). The top and middle panel show core/shell systems with different ligand lengths, and the middle and low panels show QDs with different shell thicknesses. c) The time dependent diffusivity for the QD systems from a). The figure is adapted from[13].

are depicted in Fig. 2.15 a) for three different CdSe/ZnCdS core/shell quantum dot (QD) assemblies. The crucial difference of those QD assemblies concerning exciton diffusion is the center-to-center distance for two individual QD, which are depicted in Fig. 2.15 b). The assemblies described by d_1 and d_2 differ by the surrounding ligand shell thickness, whereas the assemblies described by d_2 and d_3 deviate from each other by different ZnCdS shell thicknesses. The MSD curves follow a subdiffusive trend where the absolute MSD values depend on the center-to-center distance, i.e., the MSD values increase with decreasing distance. The subdiffusion nature appears due to the heterogeneous energy landscape. The available exciton energy levels are randomly occupied upon excitation. Thus, for the first few PNC FRET transfers, adjacent PNCs have lower and higher lying energy levels compared to the starting exciton energy level. However, after some FRET transfers, the exciton occupies successively lower lying energy levels, and therefore, the surrounding PNCs' energy levels are not as reachable for an additional FRET transfer as for the first FRET transfers. Thus, the diffusivity goes down with time, which is one characteristic feature of subdiffusive behavior. Since the NCs can have different lateral sizes due to the synthesis procedure, the energy landscape of the PNC system under consideration can be heterogeneous. The discrepancy of energy mismatch of adjacent PNC is material and size dependent, e.g., CdSe NCs are more size dependent than PNCs.[13,14] In Sec. 4.2.1 we describe another origin for subdiffusive exciton behavior which is closely connected to the underlying PNC film type. Fig. 2.15 c) shows the time dependent diffusivities for the described QD systems. By following Eqn. 2.26 one gets the averaged diffusivity in case of subdiffusion with:

$$\bar{D}_{sub} = \frac{1}{2} 2A\alpha \int_{t_i}^{t_f} dt\, t^{\alpha-1} = A\frac{t_f^{\alpha} - t_i^{\alpha}}{t_f - t_i} = A\, t_f^{\alpha-1} \tag{2.29}$$

Here, the initial time is set to zero. For a strictly subdiffusive MSD trend, the averaged diffusivity depends on the integration times, which leads to some disadvantages. For instance, if one averages long enough $\bar{D}_{sub}$ approaches zero even though the initial exciton transfer can be quite fast.
Sec. 2.4.1.3 is devoted to resolving this issue by considering the actual amount of excitons. Below, we show that a subdiffusion MSD trend can also result from a void structure, i.e., a PNC film with missing PNCs. The subdiffusion model resulting in a MSD trend described by Eqn. 2.28 is only phenomenological, i.e., it does not have its origin in a microscopic model. Nevertheless, it gives access to the macroscopic parameters like time dependent diffusivity and exciton diffusion length, which are crucial for optimizing a device architecture.
An exciton diffusion model description taking a microscopic transfer into account will be the topic of the next section. There, exciton trapping will be considered, also resulting in subdiffusive exciton behavior.

2.4.1.2 Trapped Exciton Diffusion Model

The previous sections investigate exciton diffusion within a free system or in a heterogeneous energy landscape, resulting in either normal or subdiffusive exciton transport, respectively. Extending those descriptions by introducing exciton traps, i.e., spatially distributed sites within the PNC film where excitons become localized, one also ends up at diffusivities generally lower than for free systems. The first groups which included traps in their considerations concerning exciton transport are Seitz et al.[76] who investigated exciton transport in two dimensional metal-halide perovskites, e.g., $(PEA)_2PbI_4$ and Folie et al.[79] in inorganic perovskite nanowires, e.g., bundles of $CsPbBr_3$. The model considers

two kinds of excitons, i.e., mobile excitons, which can diffuse freely, and trapped excitons which are not able to move. Free excitons can be trapped, whereas the reverse process is not considered, i.e., there is no possible transition from a trapped to a free exciton. Those two descriptions vary in the treatment of the traps, i.e., Seitz et al. did not assume radiative recombinations from trapped excitons. In contrast, Folie et al. set both radiative decay channels for free and trapped exciton states to the same value. Both independently developed derivations led to the same PL broadening described by:

$$MSD = 2\,D_0\,\tau_d\,(1 - e^{-t/\tau_d}) \tag{2.30}$$

D_0 is the diffusivity describing the free exciton diffusion, and τ_d is the average trapping time. Once an exciton is trapped, it can not become a free exciton again, at least for the considered time scale. The temporal limits of Eqn. 2.30 are a linear time dependency for short times, already seen for normal diffusion, and constant MSD at long times, meaning no broadening of the PL spot anymore, i.e., diffusion eventually stops.
Folie et al. stated that this deep trap model can adequately replicate their observed MSD. However,

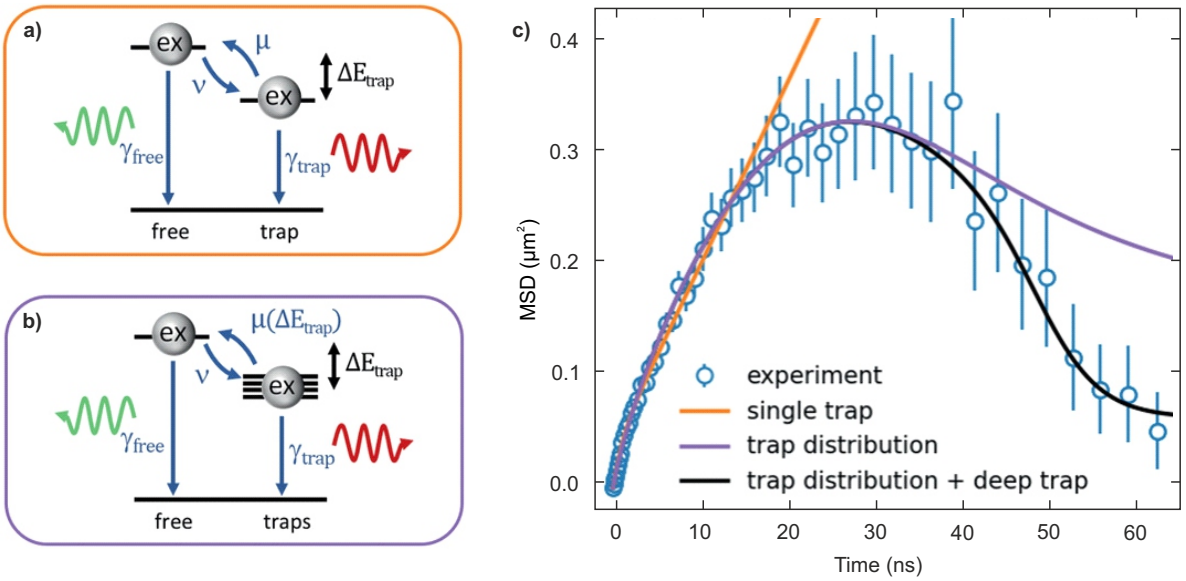

Figure 2.16: a) shows an energy diagram of a NC with a shallow trap and the excitonic level. Detrapping and trapping of excitons are allowed, and both levels have only radiative recombination channels. b) depicts the energy diagram where the trap state energy is distributed over several meVs. c) Temporal MSD evolution over 60 ns, where MSD expansion and contraction are visible. The orange, purple, and black lines correspond to fits resulting from the energetic models presented in a), b), and a combination of both models with including deep traps. The figure is adapted from[80].

several assumptions must be checked before applying their developed deep trap model. There also may be other excited states which have to be considered, namely non-bound excitons, i.e., free electrons and holes, which are not allowed to transfer via FRET in a PNC system. For their system, i.e., microscopic large single crystals, free charge carrier diffusion may contribute to the total diffusivity. The exciton decay channel is not only of mono-exponential nature, i.e., the dynamics are more complicated than assumed. More radiative or nonradiative channels can lead to a non-mono-exponential temporal exciton population decay, resulting in a more complex time dependence of the decay rate. Finally, the traps may not be distributed uniformly in space, and the trapping can also be time-dependent. Nonetheless, the deep exciton trap model can be used as a starting point for describing more complex systems where, e.g., the radiative decay dynamics are more complicated or detrapping is allowed, i.e.,

a shallow trap model.
The energy diagram of a possible shallow trap model is depicted in Fig. 2.16 a). Detrapping is allowed with a rate μ and trapping with a rate ν. Both states are radiative, i.e., the exciton and trap state levels emit photons with rates γ_{free} and γ_{trap}, respectively. This model leads to temporal MSD evolution described by:[80]

$$\sigma^2(t) - \sigma_0^2 = 2\,(D_0 - D_T)\,\tau_d\,(1 - e^{-t/\tau_d}) + 2D_T t \tag{2.31}$$

The additional parameter D_T describes the longterm diffusivity, since at elaborate times, the MSD behaves like a normal diffusion curve with D_T as its diffusion parameter. However, this model captures only the MSD evolution at early times, i.e., 0 - 15 ns, visible in the orange line of Fig. 2.16 c). Additional extensions of the model are a broadening of the trap state energy level presented in Fig. 2.16 b) which results in a slight MSD contraction within the proposed temporal evolution (purple MSD trend in Fig. 2.16 c)).
The best fitting curve results from a numeric fit (black line) of a combination of the models presented in Fig. 2.16 a)+b) and additionally deep traps are allowed. Seitz et al. were able to reproduce the MSD extension and compression observed within 60 ns adequately. We will introduce an amended model in Sec. 4.3.2, where the radiative decay channels of the mobile excitons and the trapped excitons deviate by two orders of magnitude. As we will see below, this influences the MSD behavior at later times and can result in a full MSD contraction.
The following section introduces a more elaborate method to calculate an averaged diffusivity which takes the exciton decay into account.

2.4.1.3 Numeric Averaged Diffusivity

The models mentioned above have some limitations. Either they do not allow a microscopic interpretation directly which is the case for the subdiffusion model, or the MSD trends can not be modeled by the applied models adequately. However, the macroscopic diffusivity can be helpful concerning applications as a figure of merit. Therefore, estimating it for all MSD curves is favorable, irrespective of the exact physical origin. We average the measured MSD slopes and weigh them with the exciton PL decay which yields an averaged diffusivity:

$$D_a = \frac{1}{2}\frac{1}{t_{bin}\sum_{i=0}^{N} w(t_i)}\sum_{i=0}^{N}(MSD(t_{i+1}) - MSD(t_i))w(t_i) \tag{2.32}$$

This calculation takes into account that exciton diffusion happens mainly in the first nanoseconds. Due to the exponential exciton decay, there are more excitons in the PNC system for early times compared to later times. Therefore, the contribution of those short-lived excitons to the MSD increase and thus, to the averaged diffusivity, is larger than that of a few later excitons. This is reflected by the introduced weights, $w(t_i) = I_{PL,norm}$, which take the exciton decay into account. The temporal information of the absolute amount of excitons gets lost by normalization of every spatial Voigt profile to its maximum, i.e., normalizing Eqn. 2.21 and Eqn. 2.22. For the special case of normal diffusion, i.e., time independent diffusivity, the MSD curve slope is time independent, i.e., $MSD(t_{i+1}) - MSD(t_i) = \Delta MSD$ and Eqn. 2.32 yields $D_a = \frac{1}{2}\frac{\Delta MSD}{t_{bin}} = \frac{1}{2}\frac{MSD_\tau}{\tau}$ which is time independent. τ is how long the diffusion process persists.
Until now, we have described the exciton diffusion with density functions, where the diffusion process tries to equalize the spatial exciton distribution over time. The following section will introduce the

exciton transport via a random walk process which also results in the same macroscopic observations as we have seen before.

2.4.2 Exciton Diffusion Description via a Random Walk Model

As we will see below, the measurement principle applied to investigate exciton diffusion behavior in PNC structures is not best described by the physical description presented in Sec. 2.4.1. Namely, the exciton density has to stay low so that only a few PNCs are excited and host excitons. If this is not fulfilled, the exciton transport can not be assumed free. For example, donor and acceptor PNC is already occupied with an exciton, and therefore a FRET transition between those PNCs are suppressed. Furthermore, suppose more excitons occupy the very same PNC. In that case, other recombination channels have to be considered in Eqn. 2.20, which will change the PL spatial profile, i.e., it will deviate from Eqn. 2.22. This behavior was observed by Kulig et al. in WS_2 monolayers where they extended the general one-dimensional diffusion equation Eqn. 2.20 by a nonlinear Auger recombination term.[81] The exciton diffusion process described in Sec. 2.4.1 relies on many simultaneously excited excitons to apply the macroscopic interpretation of a density gradient and it can thus not be used to describe free exciton diffusion as explained by the previous examples. Therefore, this current section is devoted to resolving this at-first-glance controversy by connecting the diffusion process to a random walk description, which suits the experimental circumstances more.
Starting from a particle whose movement trajectory can be described by Brownian motion, Einstein developed the one-dimensional diffusion differential equation.[82] This implies that each single particle movement is independent of other particle movements. The movement of one particle for different time intervals has to be considered as a mutually independent processes if the time interval is not too small. Suppose n particles change their particle position Δ in a short time interval τ. Δ can vary for each individual particle and for each Δ a certain probability $\phi(\Delta)$ holds. This results in a change of the particle density dn, which can be expressed via $dn = n\phi(\Delta)d\Delta$. Expanding the particle density in time yields:

$$n(x, t+\tau) = n(x,t) + \tau\frac{\partial n(x,t)}{\partial t} + \mathcal{O}(\tau^2) \tag{2.33}$$

And expanding the particle density in space up to the fourth order in Δ results in:

$$\begin{aligned} n(x, t+\tau) &= \int n(x+\Delta, t)\phi(\Delta)d\Delta \\ &= n(x,t)\int \phi(\Delta)d\Delta + \frac{\partial n}{\partial x}\int \Delta\phi(\Delta)d\Delta + \frac{\partial^2 n}{\partial x^2}\int \frac{\Delta^2}{2}\phi(\Delta)d\Delta + \mathcal{O}(\Delta^4) \\ &= n(x,t) + \frac{\partial^2 n}{\partial x^2}\int \frac{\Delta^2}{2}\phi(\Delta)d\Delta + \mathcal{O}(\Delta^4) \end{aligned} \tag{2.34}$$

Here, $\int \phi(\Delta)\, d\Delta = 1$ is used and due to symmetry arguments all odd spatial expansions in Δ like $\int \Delta\, \phi(\Delta)\, d\Delta$ are zero.
By comparing both Taylor expansions one gets the diffusion equation in one dimension:

$$\begin{aligned} \tau\frac{\partial n(x,t)}{\partial t} &= \frac{\partial^2 n}{\partial x^2}\int \frac{\Delta^2}{2}\phi(\Delta)d\Delta \\ \frac{\partial n(x,t)}{\partial t} &= \frac{\partial^2 n}{\partial x^2}\int \frac{\Delta^2}{2\tau}\phi(\Delta)d\Delta := D\frac{\partial^2 n(x,t)}{\partial x^2} \end{aligned} \tag{2.35}$$

Where the diffusion parameter $D = \int \frac{\Delta^2}{2\tau}\phi(\Delta)d\Delta$ is introduced. Here, particle conservation is given, i.e., no sink or generating terms are included since Einstein was interested in the description of moving particles suspended in a fluid, where all particles survive. In this work, we consider quasi-particles with a few nanoseconds PL lifetimes, whereas the time between two consecutive excitation pulses is up to 500 ns. Therefore, we must consider sink and generation terms within the diffusion rate equation.

Fig. 2.17 a) depicts an unbiased random walk in one dimension, i.e., the step length for every time step has the same length. By progressing time, each random walker takes an individual way as it is shown

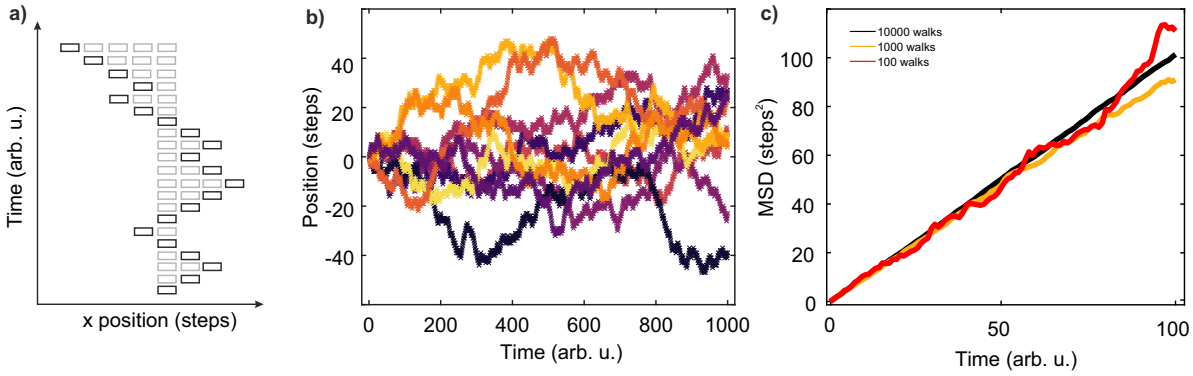

Figure 2.17: a) shows a one-dimensional random walk model. b) depicts ten simulated random walks for 1,000 time steps. c) gives the MSD of one-dimensional random walks for the first 100 time steps for 100, 1,000, and 10,000 random walks (red, yellow, and black lines, respectively).

in Fig. 2.17 b) for ten different walks. There, 1000 time steps are observed, and the individual random walks get farther apart from the start position or even go back randomly. The mean of individual walks and the sum of all walks is the start position, since no bias is considered. However, the standard deviation and thus the MSD is not zero for an unbiased random walk in one (or more) dimensions as it is depicted in Fig. 2.17 c) for the MSD. There, three simulations of random walks are shown with different amounts of conducted random walks. Starting from performing 100 (red curve), 1,000 (yellow curve), and 10,000 walks (black curve) and calculating the MSD for each time step. Considering fewer walks results in larger deviations from a linear behavior as can be observed by comparing the red and black line. The signal-to-noise ratio goes up for an increasing number of experiments which later will be the number of laser pulses exciting excitons in the sample which perform the random walks. For a free (unbiased) random walk, the MSD has a linear dependence on time, as is the case here. The slope reflects the ability of the particles to diffuse in the media and is connected to the diffusivity as shown before via Eqn. 2.25.

This random walk description is closest to the basic measurement principle, which will be introduced and explained in the next chapter.

3
Methods

This chapter introduces the synthesis procedures for all $CsPbBr_3$ PNC shapes and sizes used throughout this thesis. The film preparation method and superlattice (SL) formation will be also discussed. The second part introduces the optical microscopy setup. The measurement setup utilized for measuring exciton diffusion in thin films of PNC is described. The experimental data gained by conducting exciton diffusion experiments are accompanied by Monte Carlo simulations which serve as contributing parts to explain our findings based on a microscopic random walk model. The realization of the simulation concludes this section.

3.1 Synthesis and Sample Preparation

The exciton diffusion was investigated in PNC films or higher-ordered ML ensembles. Hereafter, the PNC synthesis for different PNC shapes and sizes is introduced for PNC cubes of different sizes and PNPLs of different thicknesses. Since exciton transport can only occur in close-packed, ordered arrangements of PNCs, attention is paid to the actual film preparation. The sample preparation affects the ensemble order, thickness, and void structure, which are crucial properties concerning exciton transport. For the smaller PNC cubes, SLs can be established, which have the highest PNC ensemble order within the scope of this thesis.

3.1.1 Synthesis of 14 nm $CsPbBr_3$ PNC Cubes by Tip-Sonication

The synthesis of colloidal PNC cubes with a $CsPbBr_3$ and 14 nm size follows the procedure first introduced by Tong et al..[35] The synthesis routine produces colloidal NCs of uniform size in a one-step process by applying ultrasonication to a mixture of precursor salts and organic capping ligands in a high boiling solvent. This is all done in one pot under ambient atmospheric conditions. Firstly, the organic capping ligands oleic acid (0.5 mL, Sigma Aldrich, technical grade 90 %) and oleylamine (0.5 mL, Sigma Aldrich, technichal grade 90 %) are mixed in the non-polar solvent 1-octadecene (10 mL,

Merck, technical grade 90 %). Next, the precursor salts cesium carbonate (Cs_2CO_3) (0.1 mmol, 32.58 mg, Sigma Aldrich, 99.9 %) and lead(II) bromide ($PbBr_2$) (0.3 mmol, 110.1 mg, Sigma Aldrich, 98 %) are added to the solution. Then the reaction mixture is immediately subjected to tip sonication at 30 W for 10 minutes. Sonication induces the formation of a soluble cesium-oleate complex, which reacts with $PbBr_2$ in the presence of organic capping ligands. During this step, the colorless reaction mixture gradually changes its color, due to the formation and growth of PNCs, the growth process is controlled by the organic capping ligands which can bind to the PNC surface and also provide colloidal stability to the PNCs. After sonication, the PNC dispersion is purified by centrifugation at 9000 rpm for 10 minutes to separate the PNCs from the unreacted precursor salts. After the first centrifugation step, the yellow NC precipitate is redispersed in n-hexane (5 mL, VWR chemicals, 97 %) and centrifuged one more time at 2000 rpm for 10 minutes to remove unwanted perovskite bulk material. The supernatant of the second centrifugation step contains the colloidal $CsPbBr_3$ PNCs with a side length of 14 nm and is used for further characterization. Those PNC cubes are the largest PNC cubes considered within the scope of this thesis.

3.1.2 Synthesis of 8 nm $CsPbBr_3$ PNC Cubes by Hot-Injection

Smaller PNC cubes of 8 nm side length were synthesized as previously described in[36,83]. The $PbBr_2$ stock solution (0.04 M) is prepared by dissolving $PbBr_2$ (1 mmol, 0.367 g, Sigma Aldrich, 99.999 %) and trioctylphosphineoxide (TOPO) (5 mmol, 2.15 g, Strem Chemicals, 90 %) in octane (5 mL) at 100 °C, followed by dilution with hexane (20 mL). The cesium diisooctylphosphinate (Cs-DOPA) solution (0.02 M) is prepared by mixing Cs_2CO_3 (0.3 mmol,100 mg, Sigma Aldrich) with diisooctylphosphinic acid (1 mL, Sigma Aldrich) and octane (2 mL) at 100 °C, followed by dilution with hexane (27 mL). The synthesis is conducted in a 25 mL one-neck round bottom flask in which, at first, 0.7 mL $PbBr_2$ stock solution is combined with 6 mL hexane. Under vigorous stirring, 0.35 mL of Cs-DOPA stock solution is swiftly injected. After 4 minutes, 75 µL of didodecyldimethylamonium bromide (DDAB) in toluene (0.65 mmol, 300 mg of DDAB from Alfa Aesar are solubilized in 3 mL anhydrous toluene) is added, and then the reaction is stopped after 2 minutes. To purify the resulting PNC cubes, the volume of the reaction mixture is decreased to 1 mL by evaporation on the rotary evaporator at room temperature. A threefold excess of antisolvent (ethyl acetate and acetone mixture, v/v 2:1) is added, and PNCs are isolated by centrifugation at 12,100 g for 2 minutes and redispersed in 1 mL anhydrous toluene.
After synthesis, the purification and size-selection of 8 nm large $CsPbBr_3$ NCs is crucial with respect to superlattice formation. A critical factor for self-assembly of cubic-shaped $CsPbBr_3$ PNCs is to start with colloidal PNC sample with a high level of monodispersity. The crude solution was centrifuged at 12,100 rpm for 5 minutes, the supernatant was discarded, and the precipitate was redispersed in 300 µL hexane. The hexane solution was centrifuged again, and the precipitate was discarded. The supernatant was diluted twice and used for further purification. Subsequently, two methods of purification of the NCs were applied: (1) 50 µL hexane, 0.6 µL oleic acid, and 0.6 µL oleylamine were added to 50 µL NCs in hexane. The colloid was destabilized by adding 50 µL acetone, centrifuged again and the NC precipitate was redispersed in 300 µL toluene. This solution was used further to prepare the three-dimensional SLs. (2) 50 µL hexane and 100 µL toluene were added to 50 µL NCs in hexane. The colloid was destabilized by adding 50 µL acetonitrile, centrifuged again and the NC precipitate was redispersed in 300 µL toluene. This solution was used further for the preparation of the three-dimensional SLs.

3.1.3 Synthesis of 5 nm $CsPbBr_3$ PNC Cubes by Hot-Injection

The smallest quasi-cubic PNCs of 5 nm side length were synthesized by adapting a synthesis procedure introduced in[83]. Cs_2CO_3 (0.77 mmol, 250 mg, Sigma Aldrich), and oleic acid (0.8 mL), and octadecene (8.8 mL) are mixed in a 25 mL flask. The mixture is degassed three times and then heated to 100 - 120 ℃ under N_2 until it becomes clear. Cesium oleate in octadecene is stored in the glove box. For the synthesis, $PbBr_2$ (0.2 mmol,75 mg, Sigma Aldrich, 99.999 %), $ZnBr_2$ (0.8 mmol, 180 mg, Alfa Aesar), and distilled mesitylene (5 mL, Acros) are mixed in a 25 mL flask under N_2, stirring at 1,400 rpm. The mixture is heated to 120 ℃, and distilled oleylamine (2 mL) and dried oleic acid (2 mL) are injected. The mixture is heated to 145 ℃, and cesium oleate (0.4 mL) is injected from a 0.5 mL glass syringe. The reaction is quenched after 15 s with an ice bath.
In favor of SL formation, size selection and purification are carried out like for the 8 nm PNC cubes. The crude solution is centrifuged for 3 minutes at 20, 130 g, and the precipitate is discarded. 27 mL ethyl acetate is added to the supernatant, followed by centrifugation for 5 minutes at 20,130 g, the supernatant is discarded, and the precipitate is dispersed in 1 mL anhydrous toluene. For the post-synthesis treatment, 1 mL of NCs in toluene are mixed with 100 µL DDAB solution in toluene (0.01 M) and stirred for 1 hour. The DDAB solution in toluene is prepared by dissolving DDAB (0.02 mmol, 9.2 mg, Alfa Aesar) in anhydrous toluene (2 mL).

3.1.4 Synthesis of $CsPbBr_3$ PNPLs of Different Thicknesses

For the PNPL synthesis, the following chemicals were purchased from Sigma-Aldrich: Cs_2CO_3 (cesium carbonate, 99 %), $PbBr_2$ (lead(I) bromide, ≥98 %), oleic acid (technical grade 90 %), oleylamine (technical grade 70 %), acetone (technical grade ≥ 99.9 %), toluene (technical grade ≥ 99.9 %) and hexane (technical grade ≥ 97 %, GC). All chemicals were used as received.
The $PbBr_2$ and Cs-oleate precursor solutions and a solution for enhancing the PL were prepared as reported previously.[17] The synthesis of the PNPLs, carried out under an ambient atmosphere at room temperature, was modified slightly. A vial was charged with a $PbBr_2$ precursor solution, and a Cs-oleate precursor solution was added under stirring at 1,200 rpm. The corresponding volumes for different thicknesses are listed in Tab. 3.1.
After 10 seconds, acetone was added, and the reaction mixture was stirred for 1 minutes. The mixture

	$PbBr_2$ (mL)	Cs-oleate (mL)	Aceton (mL)
3 ML	1.5	0.15	2.0
5 ML	0.897	0.249	1.850

Table 3.1: Precursor and acetone amount for the synthesis of PNPLs with different ML thickness.

was centrifuged at 4000 rpm for 3 minutes, and the precipitate was redispersed in a solution of hexane (1.8 mL) and PL enhancement solution (200 µL). The PL enhancement solution consists of $PbBr_2$ and is added to colloidal PNPLs to repair lead and bromide vacancies on the PNPL surface.
After describing the PNC synthesis of different shapes and sizes, the following sections describe the film preparation method and the SL formation procedure.

3.1.5 SLs and Film Preparation

The 5 nm and 8 nm large PNC cubes form individual SLs, i.e., PNC cube arrangements of thousands of highly ordered cubes. The SL formation is carried out in a similar manner for the two different PNC sizes. $CsPbBr_3$ PNC SLs were prepared on 5 mm x 5 mm silicon substrates. Before the self-assembly process, the silicon substrate was dipped into a 4 % solution of hydrofluoric acid in water for one minute, followed by washing with deionized water. The cleaned substrate was placed in a teflon well, and

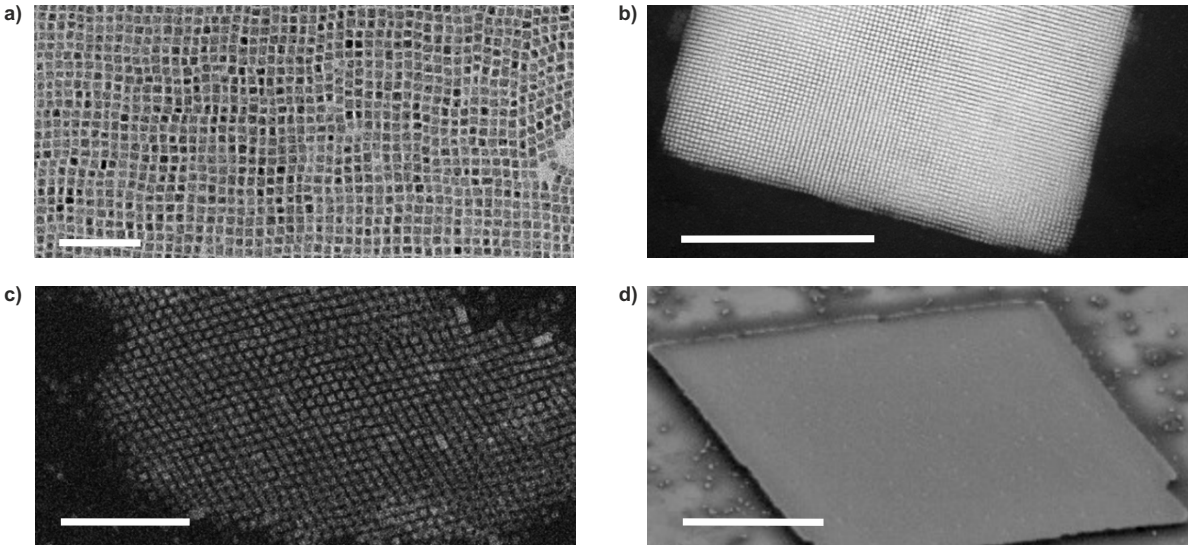

Figure 3.1: a) shows a SEM image of dropcasted film of 8 nm PNC cubes. The scale bar is 100 nm. b) depicts a HAADF–STEM image of a SL of the PNC cubes shown in a). The scale bar is 500 nm. c) presents a SEM image of a dropcasted film of 5nm PNC cubes. The scale bar is 100 nm. A SL of 5 nm PNC cubes is visible in d) where the scale bar is 10 µm. Figures are adapted from[36,37].

10 µL of purified PNCs in toluene were dropcasted onto the substrate for the 8 nm PNC SLs[36] and 7 µL of 5 nm PNC cubes with a concentration of 1 - 1.2 mg/mL[37]. Fig. 3.1 a,c) show scanning electron microscope (SEM) images of the dropcasted 8 nm and 5 nm large PNC cubes, respectively. The well was covered with a glass slide, and the toluene was then allowed to evaporate slowly. three-dimensional SL of $CsPbBr_3$ PNCs were formed upon complete evaporation of the toluene after roughly 3 days. Typical lateral dimensions of individual SLs ranged from 1 µm to 10 µm, wherein some of them are arranged into clusters of several SLs and others remain spatially well-isolated so that PL measurements can be performed on an individual SL. Furthermore, the formation of PNC SLs can serve to further narrow the size distribution and shape uniformity within the ensemble (with smaller or larger PNCs being repelled from the PNC SL domain), especially in the case of simple cubic packing of cubes, which is particularly intolerant of size and shape variations. By comparing panel Fig. 3.1 a) and Fig. 3.1 c) it becomes clear that the film formation for the 8 nm PNCs is of simple cubic nature, whereas for the 5 nm PNC cubes it deviates from such a simple cubic arrangement. The 5 nm PNCs have an orthorhombic crystal structure. The resulting SLs consisting of the two PNC cube sizes are depicted in Fig. 3.1 b,d). Panel b) depicts a high-angle annular dark-field scanning transmission electron microscopy (HAADF–STEM) image of a single SL of 8 nm cubic PNCs. Panel d) shows a rhombic SL consisting of 5 nm PNC cubes. The SL sizes range from a few µm up to 10 µm.

To produce a 14 nm PNC cube film on a SiO_2 substrate, the pure PNC cube dispersion obtained from the synthesis is typically diluted 1:10 in hexane. 40 µL of these dispersed PNC cubes then dropcasted on a SiO_2 substrate. The 14 nm PNC cube film forms upon evaporation of the hexane solvent and

consists of one to several layers of cubic PNCs. In some places, the perfect 14 nm PNC cube film is also disturbed by larger void structures. The PNC film thickness and the appearing voids within the film will be discussed in more detail in the results sections.
All PNPL films used during this thesis are processed similarly to the 14 nm PNC cube film. However, there is no further dilution step before the 40 µL dropcast, this is done with the as-synthesized PNPL dispersion right after synthesis.

3.2 Low Temperature Time-Resolved Confocal Microscope

The employed measurement setup allows spatially resolved time correlated single photon counting (TCSPC) measurements at temperatures between 9 K to 300 K. For this, a vacuum objective is placed inside a cryostate. The setup is shown in Fig. 3.2 where the excitation path is depicted in blue, illustrating the laser beam for the excitation. The excitation laser enters the cryostate which cools the sample to temperatures between 9 K and 300 K. The signal or PL emissions path is shown in green which leaves the cryostate and is traced to a fiber collecting the signal for TCSPC measurements and a PL spectrometer. Mirrors and lenses which are not described further are optical standard parts which were purchased from ThorLabs for visible light applications.
The pulsed laser beam is generated by a variable white light source (NKT Photonics, SuperK Fianium FIU-15) from which a narrow spectral band (10 nm) at a center wavelength between 400 nm and 840 nm can be applied. The center wavelength tuneability is ensured by means of a tunable filter (NKT Photonics, SuperK VARIA). The laser pulse duration is below 200 ps, whereas the laser repetition rate is tuneable from 0.3 MHz up to 72 MHz. The laser beam is guided into the setup with an optical fiber (NKT Photonics, FD7) and coupled out through a fiber collimator (NKT Photonics). Two mirrors are used to align the beam to the center of the optical elements of the excitation path. A motorized continuous neutral density filter wheel (ThorLabs, NDM4) is used to attenuate the signal by reflecting a tunable fraction of the beam from 0 to 4.0 optical density. Together with a power diode (ThorLabs, S120C), this allows for precise control over the power density of the excitation laser. The laser beam is expanded with two lenses spaced by the sum of their focal lengths 30 mm + 200 mm magnify the beam by a factor of $\frac{200\text{ mm}}{30\text{ mm}} = 6.67$. This is performed to allow for a small spot diameter d on the sample, as $d \propto D^{-1}$, where D is the diameter of the collimated laser beam. A byproduct of the beam expansion is a smaller divergence angle of the laser beam resulting in a longer collimated beam. At the end of the signal path, the laser beam is reflected in the direction of the focusing optics inside the cryostate with the help of a suitable dichroic (DC) beam splitter (either Semrock, HC 495 or Chroma, T 450 LPXR depending on the utilized center excitation laser wavelength). This optical component reflects light below its characteristic wavelength (laser beam) and transmits light above this wavelength (PL signal), thus separating excitation and emission light.
The insides of the closed-cycle helium cooled cryostate (attocube, attoDRY800) consist of a vacuum objective (Zeiss, EC Epiplan-Neofluar 100x/0.9 NA DIC Vac M27) with a working distance of 1.0 mm and a sample holder on a 3-axis piezo-controlled translation stage (attocube). The objective focuses the laser beam to a diffraction-limited Gaussian shaped beam profile on the sample. A thermal bridge between the cryostate cold plate and the sample holder enables cooling of the sample to 9 K. An inserted heater is able to heat the sample up to 300 K, even though the cryostate is still cooling. The generated PL is collected and collimated by the vacuum objective and exits the cryostate in the

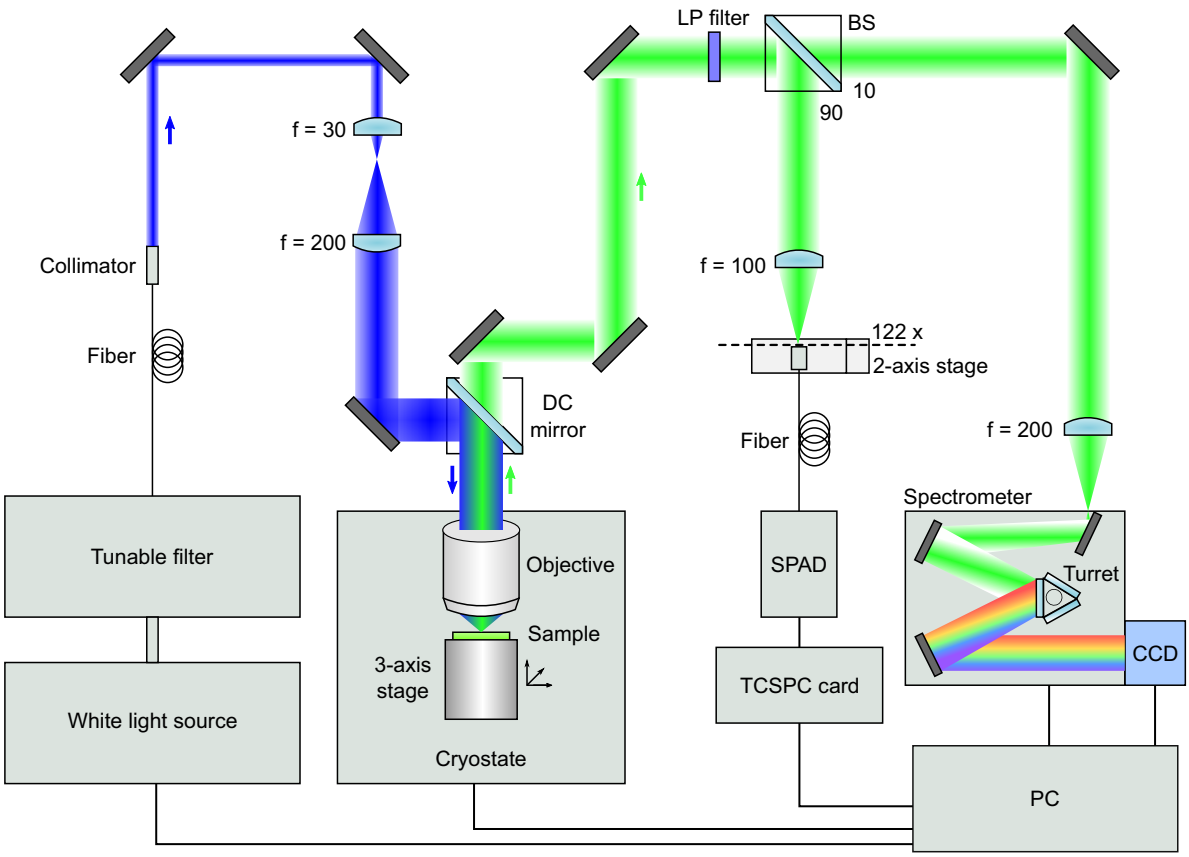

Figure 3.2: The micro PL setup is depicted here. Starting from a pulsed white light laser source, the beam path is guided through optical elements (lenses and mirrors) and finally enters in a cryostate and is focused on the sample which is positioned there. The PL of the sample is separated from the excitation laser via a DC beam splitter and is further guided through a spectrometer/charge-coupled device camera or to a fiber mounted in the focal plane of the PL emission.

direction of the DC mirror.

The DC mirror allows for transmission of the PL signal, thus separating it from the excitation signal (laser beam). An additional suitable long pass filter (either Semrock, 496/LP-25 or Semrock, AT465LP) is included to ensure that no laser light is left in the signal path by reflecting all light below its characteristic wavelength. Two mirrors are used to align the PL signal to the center of the optical elements of the signal path. A beam splitter (BS) (ThorLabs, BSN10R) guides 10 % of the PL signal to the spectrometer and 90 % to the TCSPC system. Along the spectrometer and PL image path a lens with a focal length of $f = 200$ mm focuses the PL signal into the slit of the spectrometer (Teledyne Princeton Instruments, HRS-500-MS). Inside the spectrometer, the PL is reflected from different optical parts on a rotating turret and detected by a charge-coupled device camera (Teledyne Princeton Instruments, PIXIS 400BR eXcelon) which has a single pixel size of 20 x 20 µm. By setting the turret to either a mirror or a grating, PL images or PL spectra can be recorded, respectively. Within the other signal path, a lens with focal length of $f = 200$ mm focuses the PL light onto a plane, where it is magnified by a factor of 122 compared to the initial sample plane. The magnification factor was determined with a gold scale. The gold scale is depicted in Fig. 3.3 a). The distance between the alternating gold stripes is 14 µm. Within the image, 5 gold stripes and the separation of them is measured, yielding a distance of 70.70 µm. Fig. 3.3 b) depicts the gold strips within the PL microscope used for the diffusion measurements, the gold strip distance is equal to 86 pixels of the camera. By comparing the PL image recorded via the confocal microscope and the SEM image of the gold stripes, the magnification can be

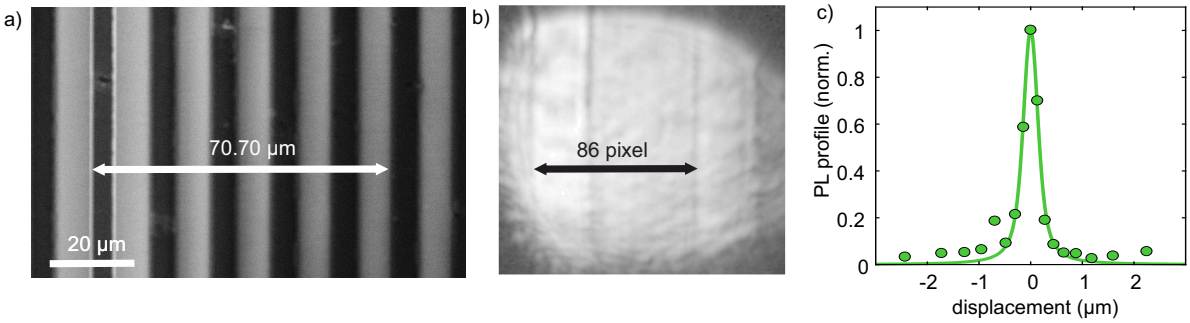

Figure 3.3: Gold scale a) SEM image and b) a PL microscope image. c) Cross-section of a single 14 nm PNC cube PL measured with our confocal low temperature microscope setup. The FWHM of the systems' PSF is γ=270 nm.

calculated via $M = \frac{86\times20\mu m}{70.7\mu m/5} \approx 122$, yielding the above stated magnification.
Fig. 3.3 c) depicts the PSF of the microscope. A single 14 nm PNC cube was screened by means of the confocal microscope. This means that the fiber in the focal plane in the emission path records single PL decay traces gathered from the PNC cube for different positions within the focal plane. Due to the small size of the cube it can be assumed as a point source. Thus, the lateral PL profile expansion is than the point spread function of the microscope. The lateral PL FWHM of the single quantum dot depicted yields 270 nm which is the lower bound of the lateral resolution of the microscope.
A motorized neutral density filter wheel (ThorLabs, NDM4) can be used to attenuate the PL signal, e.g., to guarantee single-photon statistics in TCSPC measurements. The PL signal is collected by a glass fiber with a diameter of 10 µm (ThorLabs, M64L01) connected to a fiber-coupled SPAD (MPD, PDM series). Both laser and SPAD are connected to a TCSPC card (PicoQuant, TimeHarp 260) in the PC to allow for TCSPC measurements. The glass fiber is mounted on a piezo-controlled 2-axis translation stage (Physik Instrumente, Q-521), which enables capturing local PL decays at different positions of the magnified PL signal. This setup is used to measure exciton diffusion in this work which is explained in the following section.

3.3 Data Processing from the Time-Resolved Confocal Microscope

To analyze and study exciton diffusion, we fitted Voigt profiles to each spatial PL intensity distribution for every time bin using an adapted Matlab code from Ruzi.[84] The recorded data sets are intensity matrices with one spatial and one temporal coordinate $n(x,t)$. The spatial coordinate depends on the lateral screening process with the mounted fiber in the focal plane. For instance, a typical fiber displacement step in the focal plane of 10 µm translates to a step size of 82 nm on the sample. A Voigt profile, being the convolution of a Gaussian and a Lorentzian function, can be expressed as an exciton density according to: $n(x,t) = e^{-t/\tau}[L(x,0) * G(x,t)] = e^{-t/\tau}V[\mu, A, \sigma, \lambda](x,t)$. Here, τ is the monomolecular recombination time, and A is the profile amplitude. For the first time bin, both broadening parameters of the Lorentzian λ and the Gaussian part σ serve as free fit parameters for the Voigt profile. For all subsequent time bins, only the parameters of the Gaussian part act as free fit parameters, namely, μ, A and σ. The Lorentzian parameters retain their initial values since the Lorentzian profile best describes the initial exciton distribution. Thus, it does not evolve over time. This implies that the time-dependent Gaussian line shape is the only parameter characterizing the PL broadening and therefore the exciton diffusion. In favor to get rid of the parameter A, $n(x,t)$

is normalized for every time bin, thus A can be set to unity as initial parameter. The Voigt profile maximum position μ can be set to zero for a proper chosen coordinate system, i.e., when the lateral maximum position is set to zero. The Voigt profile fits yield the time dependent Gaussian profile broadness parameter σ which is connected to the MSD via $MSD(t) = \sigma^2(t) - \sigma_0^2$.
Based on the temporal evolution of the MSD, the exciton diffusion process within investigated samples can be discussed further by evaluating to specific models discussed in previous sections (see for example Sec. 2.4.1). However, this method of extracting MSD values fails if the exciton density is too large that other decay channels which do not show a linear power dependency have to be considered. This can result in time dependent PL profiles which deviate from a normal Voigt profile. Thus, one has to ensure that the excitation power is low enough to exclude those deviations to apply this method correctly.

3.4 Exciton Diffusion Simulation

In order to obtain a more fundamental understanding of exciton diffusion in PNC ensembles Monte Carlo simulations were used to simulate the exciton random walks. The Monte Carlo simulations were conducted in python by filling a regular grid of PNCs sites (150 x 150) with excitons which initially follow a Gaussian distribution, thus mimicking the exciton population right after laser excitation. To prevent the injection of too many excitons into the system or even more than one exciton at the very same lattice site, the total amount of injected excitons is fixed to a threshold value. The excitation laser spot size is adjusted to experimental conditions, i.e., the laser spot size at the PNC sample is 170 nm large.
After filling the lattice with a Gaussian distribution of excitons they are allowed to transfer to adjacent PNC sites, either to the nearest neighbor with a distance of r_{FRET}^{NN} (black arrow) or to the next nearest neighbor within a distance of r_{FRET}^{NNN} (grey arrow). Alternatively, excitons can undergo radiative recombination (wiggled arrow). Those processes are depicted in the left schematic of Fig. 3.4 a). Both FRET transfer rates follow the FRET p_{FRET}/r^6 law (p_{FRET} is the probability of a single FRET transition), yielding a nearest neighbor FRET rate in lattice units: $r_{FRET}^{NN} = p_{FRET}/1^6$ and a next nearest neighbor FRET rate of $r_{FRET}^{NNN} = p_{FRET}/(\sqrt{2})^6 = p_{FRET}/8$ which gives a total FRET rate of $r_{FRET}^{tot} = 4.5 p_{FRET}$ for a two-dimensional lattice, i.e., depending on the FRET probability between a single acceptor donor FRET pair, the total FRET rate is 4.5-fold that value. A second exciton is depicted which undergoes a radiative decay. In a realistic representation of PNC films, the film is intercepted with voids, i.e., missing PNC lattice sites within the lattice, where no FRET transfer is possible due to the missing host PNC which is illustrated with the crossed black arrow in the schematics. Voids exist as single missing PNCs or as shown here as multiple missing PNC sites. For instance, the void shown in the schematic of Fig. 3.4 a) is comprised of nine missing PNCs. In this thesis different void sizes as well as different PNC/void coverage are simulated which is relevant and will be discussed in Sec. 4.2.1. For each single simulated random walk, 200 - 300 time steps are conducted, after this time almost all excitons have recombined for a suitable radiative recombination rate. For example, the simulation radiative decay rate is $\gamma_{rad} = 0.03$, yielding a exciton density behavior according to $n(t) = 0.97^t = e^{tln(0.97)} = e^{-ln(1/0.97)t}$. At each time step, a random number is generated which decides what transfer or recombination channel happens. The right panel of Fig. 3.4 a) shows the energy diagrams of two adjacent PNCs. The radiative decay processes are depicted with wiggled arrows and the FRET transition between two PNCs is represented

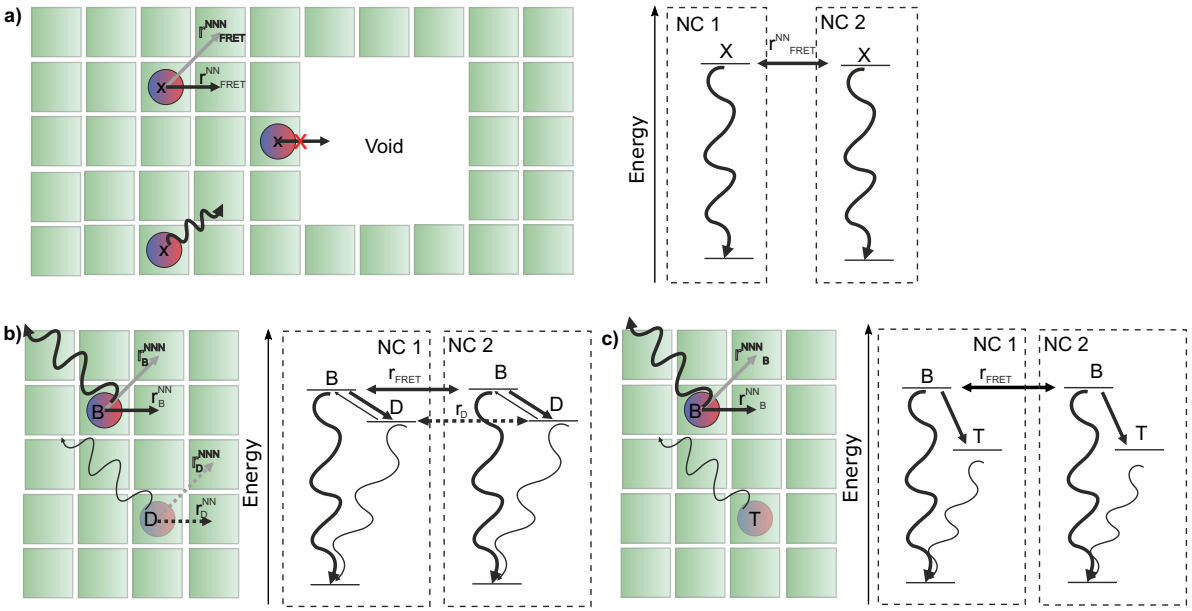

Figure 3.4: a) Schematics of a PNC lattice structure with the relevant FRET transfers of excitons are depicted on the left and the radiative decay channel of an exciton is shown on the right. The lack of PNCs in the center of the film is hereafter termed void, i.e., missing PNCs in an otherwise perfect lattice arrangement. The right panel depicts two adjacent PNCs and their energy levels as well as their different transfer/decay channels for FRET transfer between the excitonic states and radiative decay to the ground state. b) shows all considered decay and FRET transfer channels in the dark (D) bright (B) exciton model with lattice schematics on the left panel and the energy diagrams of two adjacent PNCs on the right panel. c) shows the schematic of the exciton trap model and two adjacent PNC energy levels with all considered FRET transfer and decay channels.

by a double arrow between the exciton levels.

A more elaborate microscopic exciton diffusion model can be seen in Fig. 3.4 b). It considers two exciton populations, which are termed bright (B) and dark (D) excitons as introduced in Sec. 2.2.2. Those exciton species have notably different transport and radiative recombination rates. The dark exciton states have a hundredfold lower decay rate than the bright exciton state and the dark exciton FRET transfer rate is also far lower than the bright exciton FRET transfer rate.[42,49] The dark state is situated energetically below the bright state as described in Sec. 2.2.2 and can repopulate the bright state depending on the temperature and bright-dark exciton splitting energy of the system. This process is illustrated in the energy diagram by the black thin arrow going from the dark to the bright state. The reverse process is assumed to be temperature independent and is depicted by the black arrow from the bright exciton level to the dark exciton level. The FRET rates of the dark to dark transition can be set to zero in PNC cubes. However, in the left PNC lattice those transitions are indicated by the dashed gray arrows to adjacent PNCs and they can become relevant, if the PNC size is smaller than the exciton Bohr radius, which is the case of PNPLs.

A radiative deep trap state PNC system is depicted in Fig. 3.4 c). In general, traps hinder exciton transport, and those deep traps affect the temporal evolution of the MSD. Excitons within those traps can not be thermally activated since those are assumed to be too deep, so there is no transition channel between the deep trap and bright exciton state. The trap state density can be temperature dependent, thus, the rate from the bright exciton level to the trap state can be assumed to be temperature dependent. Excitons which are trapped are not allowed to transfer to adjacent PNCs, they stack in the trap and finally recombine radiatively (or nonradiatively). In principle, the transfer of trapped excitons would be possible, however, traps are randomly located and depending on the trap density not every PNC

cube hosts a possible trap. Therefore, neglecting trap to trap transitions is a valid assumption even though it would be an energetically allowed process.
Furthermore, one can also consider nonradiative shallow trap states. However, those only reduce the absolute diffusivity and do not change the MSD trends qualitatively, hence, those are omitted within all simulations used hereafter. The parameters used for the Monte Carlo simulations of the bright-dark

model	γ_B	γ_D	γ_T	γ_{BD}	γ_{DB}	γ_{XT}	γ_{FRET}	γ_{HOP}	γ_0
bright-dark	3 %	0.03 %	-	3 %	0-2.5 %	-	9-15 %	40.5-67.5 %	43.5-24 %
trap exciton	3 %	-	0.03 %	-	-	0-2.5 %	15 %	67.5 %	29.5-27 %

Table 3.2: The table presents the implemented parameters for the Monte Carlo simulations for the bright-dark exciton diffusion model and for the trap exciton diffusion model. The Monte Carlo simulation for the bright-dark exciton diffusion model results in the MSD trends presented in Fig. 4.13 and the MSD trends shown in Fig. 4.23 are established for the Monte Carlo simulation obeying the trap exciton model.

exciton model and for the trap exciton model are summarized in Tab. 3.2. The corresponding MSD trends resulting from the chosen model parameters are depicted in in Fig. 4.13 for the bright-dark exciton model and for the radiative deep trap model in Fig. 4.23. The radiative decay rate of the bright exciton γ_B is set to the same value for both models. The radiative decay rates of the dark exciton γ_D and of the trapped exciton γ_T have the same decay probability which is set hundredfold below the radiative recombination of the bright states. For simulating the temperature increase for low temperatures, the nonradiative rate of populating the bright state from the dark state γ_{DB} is increased from zero (0 K) up to 0.025 (80 K). The downward rate from bright to dark γ_{BD} is set to be a constant and therefore temperature independent and larger than the maximal γ_{DB} rate. For the trap exciton model, the exciton trapping rate γ_{XT} is increased from zero up to 0.025 for increasing temperature. The FRET rate γ_{FRET} is varied for the low temperature exciton diffusion model from 0.09-015, considering the increasing diffusivity within this temperature region. γ_{FRET} is fixed for the high temperature regime at $\gamma_{FRET} = 0.15$. The overall hopping probability is the sum of all nearest and next nearest neighbor FRET rates $\gamma_{HOP} = 4 \times \gamma_{FRET} + 4/8 \times \gamma_{FRET}$. The last rate γ_0 represents the possibility that the exciton does not undergo any transfer processes but remains in the occupied PNC site within this time step. It is therefore given by $\gamma_0 = 1 - \sum_{i=all} \gamma_i$.

4

Results

All gathered results and findings about exciton diffusion in PNC systems are presented here. Initially, the focus lies on intrinsic characteristics, i.e., individual PNCs' shape and size differences and their impact on exciton diffusion in nanocrystal films. The effect of traps on the (exciton) transport is investigated.
A discussion on how the order of any PNC films affects the exciton diffusion follows. For instance, film imperfections like voids diminish the exciton diffusion performance. Additionally, highly ordered PNC systems are also under closer investigation, so-called super lattices, with nearly no voids.
The concluding part discusses extrinsic parameters that affect exciton transport in PNC ensembles. The main concern is about temperature, which influences fundamental optoelectronic properties of semiconductors like PL and absorbance spectra broadening at increased temperatures, changing the fundamental bandgap, establishing traps and serving as energy sources for lifting trapped excitons or excitons which occupy optical dark states to bright energy levels with a large oscillator strength. Those changes in optoelectronic properties undoubtedly influence the macroscopic exciton transport behavior in PNC films.
Finally, a short discussion about other measurement parameters, such as excitation power, which surprisingly also has an influence on exciton transport, will follow.

4.1 Intrinsic PNC Properties Impact Exciton Diffusion

In this section, the influence of PNC intrinsic properties on inter-PNC diffusivity is under closer investigation. Their differences in shape and size crucially affect their excited states, i.e., the energetic ordering and lifting of energetic degeneracy of the ground exciton states.[44–46] The alignment of the dipole moments of the excitons in the point dipole approximation is highly sensitive to shape anisotropy, which in reverse can be either beneficial or disadvantageous for inter-exciton transport. Furthermore, the exact size of individual PNCs has to be considered to estimate the free charge carrier to exciton ratio inside a single PNC. Since only excitons can transfer their energy to neighboring PNCs, this tremendously impacts inter-PNC diffusion coefficients.[15] For anisotropically shaped systems like PNPLs, whose thickness can be controlled with monolayer precision, the size of the exciton binding energy, which is highly sensitive to the confinement length, also varies considerably. Increasing the thickness also yields increased center-to-center PNC distances, which can be non-beneficial for the overall diffusivity performance. The presented experimental results within this section are considered only under room temperature and ambient conditions.

4.1.1 Different PNC Cube Sizes

The PNC size and its effect on exciton diffusion within films of those PNCs are investigated at this stage. Three cases exist, i.e., weakly, intermediately, and strongly confinement systems, discussed hereafter. For large PNCs where the exciton Bohr radius is far smaller than the PNC dimensions $r_B \ll a$, one must consider both intra-PNC exciton diffusion within a single PNC and inter-PNC exciton diffusion.

On average, the exciton is excited in the PNC center with a decreasing probability of coming closer to the surrounding ligand shell, i.e., getting farther apart from the NC center. As the energy transfer rate is highly distance-dependent, the closer the exciton resides to the PNC edge the higher the transfer rate will be. According to the film dimension, the distance dependence is $1/r^3$, $1/r^4$ or $1/r^6$ for three-dimension, two-dimension or one-dimension, respectively.[70] For PNCs with lateral sizes considerably larger than their exciton Bohr radius, the diffusion within the PNC has to be considered. This internal PNC exciton mobility follows the exciton transport behavior in single crystals, i.e., in Ruddelson-Popper perovskite single crystals[76,80] or in other monolayer semiconductors.[81,85–87] The transport process is not FRET-mediated since no insulating ligand shell has to be overcome.

If the exciton gets closer to the PNC periphery, the exciton consequently gets closer to the ligand shell. There, the exciton is more likely to become trapped, since surface traps are the dominant trap type in PNCs as discussed in Sec. 2.2.4. The total exciton diffusivity D_{tot} amounts to $\frac{1}{D_{tot}} = \frac{1}{D_{intra}} + \frac{1}{D_{inter}}$ since it should be dominated by the weaker diffusivity where D_{intra} is the diffusivity inside a single PNC and D_{inter} is the diffusivity between adjacent PNCs. In most semiconductor materials, the bulk or intra-PNC diffusivity is more than one order larger than the inter-PNC diffusivity.[88] Hence, the intra-PNC exciton diffusion is often not considered and $D_{tot} = D_{inter}$. If the finite intra-diffusivity is considered but unknown, the inter-diffusion can be seen as a lower bound of the total exciton diffusion. As the time-resolved PL diffusion measurement cannot resolve these two diffusivities, only the total diffusivity can be extracted from the measurements. Other methods are needed to distinguish between intra- and inter-exciton transport. For example, terahertz spectroscopy can tackle the problem of measuring intra-transport behavior, however, only for free charge carriers, not neutral excitons.[89]

PNCs of comparable size to the exciton Bohr radius reside in an intermediate regime. For those systems, the intra-PNC diffusivity does not affect the overall diffusion performance, hence, it can be omitted. The excitons can be treated as point dipoles located at the center of the PNC where they are excited. Therefore, the above mentioned decay and transfer channels are possible: radiative and non-radiative PL decay and FRET transfer to adjacent PNCs as introduced in Sec. 2.3.3. Thus, the total or macroscopic exciton diffusivity is entirely governed by the inter-PNC transport $D_{tot} = D_{inter}$. For all PNC cube films investigated here, the exciton Bohr radius is comparable to the cube size so the intermediate regime is applicable.
For very small PNC's with side lengths comparable to the exciton Bohr radius, the exciton wavefunction is mainly located at the PNC center. However, the exciton wavefunction can leak into the ligand shell, and an exciton can be delocalized over more than one PNC, as shown by Zhang et al. for quantum dot solids fulfilling these conditions. Therein, excitons could be delocalized over ten NCs.[16] This limit is not reached for the PNC cubes discussed here. However, it will be reconsidered when at least one PNC dimension is strongly reduced, as for the highly anisotropic PNPLs as well as for microsheets and nanorods or nanowires.[44] The degree of overlap depends on the dielectric surrounding of the exciton, namely the type and length of insulating molecules comprising the ligand shell. By changing the used ligands, the PNCs shell can strongly modify the exciton diffusion.[13]

4.1.1.1 Monte Carlo Simulations

To investigate the effect of PNC size on exciton diffusion behavior, a Monte Carlo simulation is used, which is introduced in Sec. 3.4 in more detail. Initially, we will assume the PNCs form a perfect lattice without voids. These will be introduced later when we consider the actual PNC film formation in Sec. 4.2.1. Only the nearest and next nearest neighbor's FRET transitions are taken into account. All direct transitions via FRET to PNCs farther away are neglected. For estimating the error which appears by this consideration, all distant FRET transition rates can be summed up to get an approximation for all non-regarded transitions. This truncation can be done by approximating the sum to an integral that has an analytic solution. Note that this is an approximation and holds only true if the integral distance is larger than the lattice spacing. The lattice is assumed to consist of PNC cubes positioned on a two-dimensional quadratic grid. The lattice can be approximated by a circle:

$$r_{FRET,trunc} = \sum_{\{allPNCs\}} \frac{p_{FRET}}{n^6} = 2\pi p_{FRET} \int_2^\infty dn' n' \frac{1}{n'^6} = 2\pi p_{FRET} \left. \frac{-1}{4n'^4} \right|_{n'=2} = \frac{\pi \ p_{FRET}}{8} \tag{4.1}$$

Here, n is the integer distance in units of the PNC cube size. For the Monte Carlo simulation, the FRET probability to reach a nearest neighbor is set to $p_{FRET} = 0.15$ as introduced in Sec. 3.4. Thus, Equ. 4.1 sums up to a probability of all (infinite) FRET transitions, which is smaller than $r_{FRET,trunc} < 0.06$. Therefore, if more FRET transitions are allowed, the diffusivity of the macroscopic exciton transport will increase. Thus, the exciton diffusivities gathered by the simulation can be understood as a lower bound to the actual values. However, the simulations are carried out without units, and, absolute values are not of further interest. Only general trends, scaling behavior, and comparison to experimental results lead to a better understanding of the macroscopic exciton diffusion processes. We conclude that the associated error is acceptable in favor of reduced simulation costs by only considering nearest neighbor and next nearest neighbor FRET transitions.

In Fig. 4.1 a), two simple cubic lattices of PNCs are depicted. The upper panel illustrates a PNC film

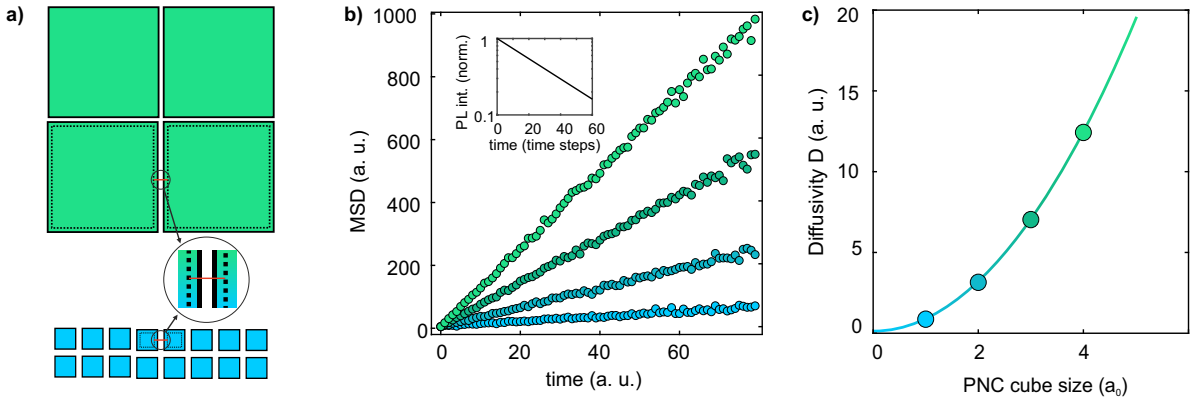

Figure 4.1: a) presents sketches of two simulated PNC systems, the upper lattice consists of PNCs with a fourfold size of the smallest PNC size (4 a_0), and the lower film consists of the smallest PNCs, i.e., with lateral dimension of a_0. Ligand lengths are equal for both systems. b) depicts the MSD time evolution for four different PNC sizes, from the smallest PNC size (blue) to the fourfold PNC size (green). The inset shows the mono-exponential PL decay of the simulated PL intensity with a lifetime of 25 time steps, similar for all four simulations. c) illustrates the diffusivity dependence on PNC cube size follows a power law. Points are the extracted diffusivity for the four simulated PNC sizes in b) according to normal diffusion, and the curve is a parabolic fit to these.

consisting of the largest simulated PNCs (green PNC cubes with a side length of 4 a_0, where a_0 is the smallest simulated PNC size). The lower panel shows the smallest PNCs simulated system (blue PNC cubes). The spacing of both systems is governed by the surrounding ligand shell and is expected to be the same for all simulated PNC sizes, as illustrated by the zoom-in of the area between two PNCs. The ligand length does not only change the PNC cubes' center-to-center distance it also affects the FRET rate due to the different dielectric composition of the FRET center-to-center transition path, which can be included into the simulation by changing p_{FRET} if the ligand length (or type, composition) is altered. The ligands surrounding the PNCs used in the experiment are the same for all investigated PNCs samples. Hence, one can neglect the effects of different ligands in the simulation. As we will see below, the actual size of the PNC cubes is in the intermediate or weakly confined regime (5 and 8 nm to 14 nm), as discussed in the previous section. We further assume by considering the simulation results that the FRET hop probability is the same for all considered PNC cube sizes. Comparing the largest with the smallest PNC systems, an exciton must undergo four FRET transfers in one direction in a film comprising the smallest PNCs, to traverse the same distance as in a film comprising the largest PNCs. The resulting temporal MSD evolution of the Monte Carlo simulation is plotted in Fig. 4.1 b) for four different PNC cube sizes (cube sizes: a_0, 2 a_0, 3 a_0 and 4 a_0). A clear linear increase of the MSDs in time is visible for all sizes, and the slopes increase with increasing PNC cube size. This linearity in MSD is characteristic of an unbiased random walk, where the MSD is proportional to the number of steps (or equivalent to time) as presented in Sec. 2.4.1. This linear increase will, in principle, never stop, however, for the system simulated here (and generally if one considers excitons), the total amount of excited states is not a conserved quantity. Since the exciton is unstable, i.e., it decays to the ground state within a finite time. This is shown in the inset where the temporal evolution of the PL intensity, which is proportional to the number of excitons present in the system, is shown in a semi-logarithmic plot. For this perfect system, a pure mono-exponential PL decay is visible with a PL lifetime of 25-time steps. Thus, at long enough times, no excitons remain within the lattice and the transport description becomes obsolete. The direct consequence is that the signal-to-noise ratio in the experimental data or the error in the simulation rises for increasing time. This can be seen in Fig. 4.1 b) at elaborated times.

There, the MSD values deviate from a linear trend. How long exciton diffusion occurs is determined by the exciton PL lifetime or the exciton decay rate. This is important in determining when the evaluation should be truncated. For our experiments, we have decided to evaluate exciton diffusion up to a time corresponding to five times the exciton PL lifetime.
The slope of the temporal MSD evolution is connected with the time-independent diffusivity as already discussed in Sec. 2.4.1. In Fig. 4.1 c) the diffusivities for the different sized PNC systems simulated in Fig. 4.1 b) are shown. The fitted diffusivities nicely show a parabolic dependence on PNC cube size. To investigate the diffusivity functional dependence on PNC cube size, one can scale the PNC size $r \rightarrow r' = sr$ in the defining equation for calculating the linear diffusivity Eqn. 2.26:

$$D'(s) = \frac{1}{2}\frac{d < r'^2 >}{dt} = s^2 \frac{1}{2}\frac{d < r^2 >}{dt} = s^2 D_0 \tag{4.2}$$

Here, s is the scaling parameter, and D_0 is the diffusivity for a film consisting of unscaled PNC cubes. This functionality of diffusion parameter and PNC cube size is fitted to the simulated diffusivities in Fig. 4.1 c) and is depicted as a line representing the parabolic trend.
A large diffusivity is generally crucial for applications where the excited states must be transferred fast or overcome large distances. The speed of exciton transport is governed by the diffusivity alone, whereas the average exciton travel distance (diffusion length) is dictated by the interplay of exciton PL lifetime and diffusivity. However, tuning the PNC cube size to larger and larger sizes results in a breakdown of the above-made assumptions. For instance, excitons will only be present in quantum confined systems. Thus, for unconfined systems, one has to consider standard charge transfer in a semiconductor that is not a FRET process, and the conducted random walk simulations are not useful. Also, the assumption of omitting intra-exciton diffusivity in all four different-sized PNCs has to be reconsidered if the PNC size is considerably larger than the exciton Bohr radius.
The next subsections summarize the experimentally gained exciton transport abilities of PNC films consisting of different PNC sizes and compare the results with the Monte Carlo simulation outcome obtained so far. Furthermore, there is a discrepancy in results extracted from the simulations compared to the experiment, which will be discussed in the next section.

4.1.1.2 Experimental Results

Utilizing the gained knowledge of PNC size-dependent exciton diffusion in PNC films by the Monte Carlo simulations, we want to connect those insights to the real world. Thus, this section is devoted to experimentally investigating the exciton diffusion dependence on PNC cube size in PNC cube films. All measurements are conducted under ambient conditions and at room temperature. Three different PNC cube sizes are used, i.e., 5 nm, 8 nm, and 14 nm lateral dimensions. Electron microscopy images of these films are shown in Fig. 4.2 a) with the PNC size increasing from left to right. From those TEM images, it is visible that the PNC films deviate from the perfect lattice arrangement discussed in the previous section. In particular, there are imperfections like missing PNC within the film, which are termed voids. The impact of voids will be addressed in a later section. The lattices can also be distorted, i.e., deviate from the perfect simple cubic structure as can be seen in the middle panel of Fig. 4.2 a). PNC cube size deviations, which are always present to some extent, are the cause for the deviation from a perfect lattice. If there are different-sized PNC cubes present, the film has such distortions since the PNC cubes form a closed-packed film to minimize its surface and the PNC ligands favorable

attache to other PNC ligands.
A broad spectrum of PNC sizes also leads to small voids, as well as farther distances between adjacent PNC ligand shells. Those deviations of a perfect lattice structure influence the FRET transfer distances, accompanied by a broadening of FRET transfer rates. The simulations above assume a sharp FRET rate corresponding to the smallest distance between two PNCs. Thus, we expect a worse exciton diffusion performance in a real PNC cube film.
The above discussed PNC size deviations have a direct impact on the optical characteristics of the PNCs. Thus, it is worthwhile to take a closer look at the room temperature PL spectra for the investigated

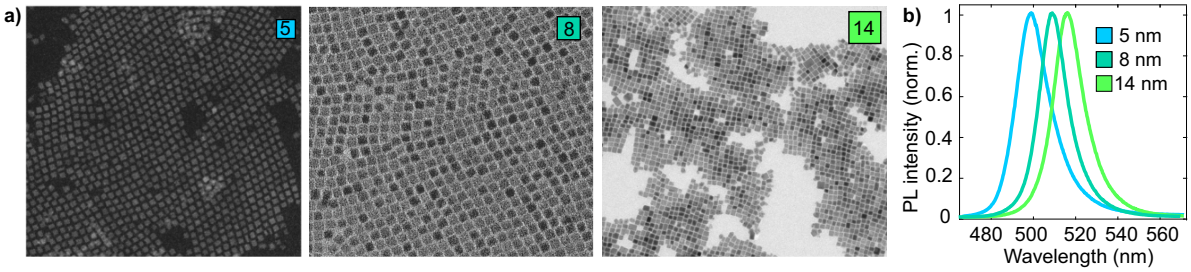

Figure 4.2: a) shows SEM and TEM images of dropcasted 5 nm (left), 8 nm (middle), and 14 nm (right) PNC films. The scale bars correspond to 100 nm. The side lengths of the 5 nm PNCs are not completely isotropic and correspond to $a = 4.7 \pm 0.1$ nm, $b = 5.6 \pm 0.2$ nm, and $c = 5.8 \pm 0.2$ nm. The side length of the 8 nm PNCs is 8.0 ± 0.5 nm. b) depicts the room temperature PL spectra of films consisting of different-sized PNCs according to sizes introduced in a).

PNC cube samples which are depicted in Fig. 4.2 b). The PL spectra show a blue shift for decreasing PNC cube size, which can be explained by increasing exciton confinement, as introduced in Sec. 2.2.1. The most important properties extracted from the spectra are presented in Tab. 4.1. The PL spectral broadening, i.e., the FWHM, is comparable for all PNCs and does not follow an obvious trend. (Smaller PNCs have broader PL spectra which is visible in Fig. 4.2 b) or by comparing them in Tab. 4.1). Considering that quantum confinement is stronger in smaller PNCs, a comparable size deviation should lead to larger spectral broadening than in larger PNCs. The observed spectral broadening in the three samples is thus due to size deviation and varying quantum confinement. This explains the large FWHM value of the 5 nm PNCs which only exhibit size deviations around 0.2 nm as well as the small FWHM of the 14 nm PNCs which have by far the highest sized dispersion.

PNC cube size	5 nm	8 nm	14 nm
FWHM (nm)	18.5	15.6	17.2
FWHM (meV)	92.6	74.5	80.4
Peak position (nm)	497.7	509.3	514.9
Peak position (eV)	2.491	2.434	2.408

Table 4.1: PL spectral information for the three different sized PNC cubes. The PL spectrum FWHMs and the maximum positions in wavelength and eV are stated corresponding to the PL spectra depicted in Fig. 4.2 b).

In Fig. 4.3 a) the experimentally determined time-dependent MSD values of the three samples 14 nm (green), 8 nm (dark blue) and 5 nm (bright blue) are presented. An apparent deviation from the expected linear behavior of free exciton diffusion is detected for all curves at later times. However, a linear MSD increase is visible within the first few nanoseconds. The absolute amount of MSD values are always higher for films consisting of larger PNC cubes, which is consistent with the results gained

by simulations discussed in the previous section. The lines correspond to fits using the subdiffusion model introduced in Sec. 2.4.1.1. This model allows the evaluation of MSD behavior that departs from the strict linear regime. The inset shows the exponents β of the subdiffusion fits dependent on the PNC cube size. The 5 nm PNC cube film has an exponent quite close to one, i.e., it displays nearly perfectly a linear exciton diffusion behavior. Both other exponents are still high but not as close to linear diffusion as the smallest PNC cube film. This deviation is surprising since the smallest PNCs have a broad PL spectrum as a result of the broader energy landscape than that of the other PNC samples. This higher energetic disorder is often used in literature to explain subdiffusive behavior, contrasting the above-presented data.[13,14] To resolve this contradiction, the PNC assembly has to be taken into account, namely, the influence of voids, which will be discussed in Sec. 4.2.1.

In Fig. 4.3 b) the MSD values of the 8 nm PNC cube sample (dark blue dots) are scaled with a scaling factor of $s = \frac{14}{8} \approx 2$ (dark blue rings) taking into account the PNC size deviation. The scaled 8 nm

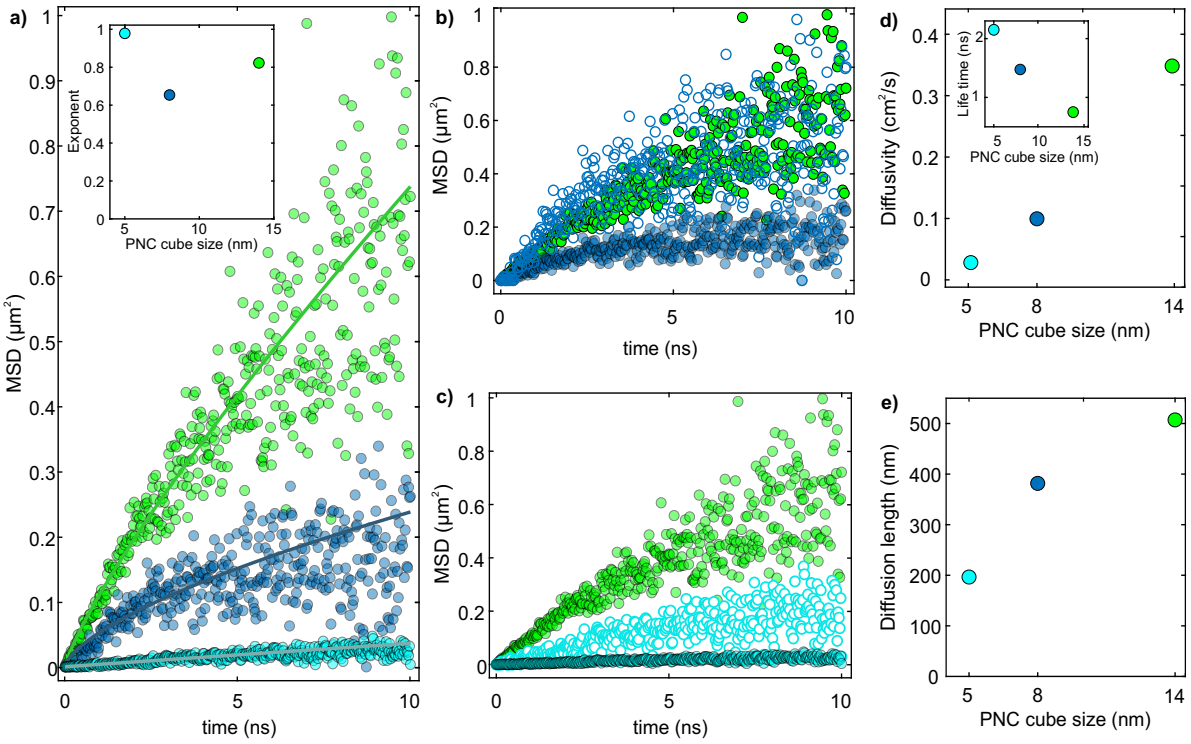

Figure 4.3: a) shows the MSD time evolution measured for 5 nm PNC film (bright blue dots), 8 nm PNC film (dark blue dots), and 14 nm PNC film (green dots) for 10 ns. The lines correspond to subdiffusion fits, yielding an exponent shown in the inset for the three PNC cube sizes. b) depicts the same MSD data points as in a) for the 14 nm and 8 nm PNC films. The MSD values for the 8 nm PNCs are scaled according to the scaling law introduced in the main text. c) illustrates the same scaling as in b) for the 5 nm PNC film. d) shows the diffusivities for the three different-sized PNC systems according to the subdiffusion model. The inset shows the corresponding exciton PL lifetimes. e) depicts the diffusion lengths for the three systems depend on the PNC cube size.

PNC cube MSD values fit quantitatively quite well to the 14 nm MSD curve (green data points), which is expected by revisiting the insights of the previous simulation section, i.e., the MSD values scale with s^2 (Eqn. 4.2). Performing the same evaluation as done for the 8 nm PNC cube sample, one ends up with Fig. 4.3 c), where the MSD values for the 5 nm PNC sample are scaled with a scaling factor of $s = \frac{14}{5} \approx 3$. Those scaled MSD values are depicted as bright blue rings while the data points qualitatively follow the 14 nm PNC sample curve, i.e., a similar linear and non-linear temporal regime are detectable, quantitatively the two curves are very different. The absolute MSD values of the scaled MSD curve are still far below those of the larger PNC sample. This strongly disagrees with the behavior expected

by the simulations.
As expected, the exciton diffusion performance is even worse for smaller PNC sizes. To quantify this, Fig. 4.3 d) compares the diffusivities in films comprising the three different PNC samples. The diffusivity dependence on the PNC cube size deviates from the parabolic scaling law, discovered in the previous sections and captured by Eqn. 4.2. The inset shows the exciton PL lifetimes for different cube sizes. The downward trend with increasing size can hint that the smaller PNCs have higher PLQY, because a faster PL decay could result from a higher probability of non-radiative decays, which is directly visible in the total PL decay curve. However, one would expect a higher trap density for smaller samples since the surface-to-volume ratio is larger for smaller NCs, and traps are more likely at the surface.
Since exciton PL lifetime and diffusivity exhibited inverse dependence on PNC size, the exciton diffusion length does not rise as fast as the exciton diffusivity with increasing PNC size, which is depicted in Fig. 4.3 e). From the simulations, one would expect a linear dependence on diffusion length in PNC cube size (for constant exciton PL lifetimes) since $L_D = \sqrt{D'\tau} = s\sqrt{D_0\tau}$, however, the measured diffusion lengths show no such trend.
The above presented data mismatch to the simulations shows that the model used for simulations is an oversimplification and does not predict all exciton diffusion features in PNC cube films at room temperature. Therefore, additional effects must be incorporated into the model to understand the exciton diffusion behavior to a more appropriate level. Furthermore, the subdiffusion model allows only a macroscopic interpretation and does not offer further insight into intrinsic PNC film characteristics. Additionally, one can apply a microscopic diffusion model, e.g., the exciton deep trap model, to obtain knowledge on the exciton trap density, which is present in the PNC film. This is the focus of the next subsection.

4.1.1.3 Energetic Traps

The MSD curves presented in the previous section show a subdiffusive trend. This behavior is often explained by the prevalence of energetic traps in the PNCs.[13] We will therefore include these in the model.
Applying the deep trap exciton diffusion model introduced in Sec. 2.4.1.2 the MSD curves already presented in the previous section can be better described by applying Eqn. 2.30 as fit function. The results are presented in Fig. 4.4 a). The MSD behavior fits quite well also for later times. The model captures the observed flattening and asymptotic nature of the temporal MSD evolution for later times. This can be seen clearly in the MSD curves of the 8 nm PNC cube film represented by the dark blue data points. In particular, the measured data seems to reach a plateau for later times, which cannot be captured by the subdiffusion model discussed in the previous section since the subdiffusion function diverges. The comparison of the subdiffusion fit (dashed green line) to the deep trap fit (solid green line) of the 14 nm PNC cube film data is even more intriguing. Here, in the early times, both curves are very similar; however, for later times, the diffusion model deviates from the experimental data while the deep trap model matches the data more accurately. Note also that the observed time range is now extended to 15 ns, whereas previous MSD trends were only depicted up to 10 ns (compare Fig. 4.3).
Besides capturing the plateau in the MSD curves, the model can also capture linear exciton diffusion behavior, which can be interpreted as slow exciton trapping, i.e., large τ_d as introduced in Sec. 2.4.1.2. This trapping time is largest for the 5 nm sample. In this sample, the MSD curve follows a linear trend,

sign of slow exciton trapping in the system. In the previous section, a close to one exponent within the subdiffusion model was attributed to the 5 nm PNC film exciton transport behavior.
The advantage of the trap model compared to the subdiffusion model is not only the fact that the fit reproduces the data better. Importantly, since it is derived from a microscopic model, the fit parameter

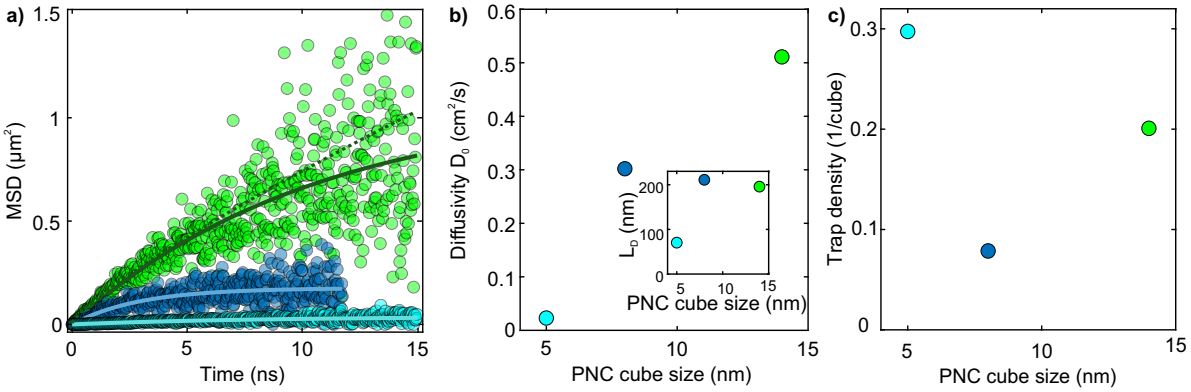

Figure 4.4: a) shows MSD curves for different-sized PNC cube films 14 nm (green), 8 nm (dark blue), and 5 nm (bright blue). The lines correspond to fit curves governed by the deep trap model discussed in the main text. The dashed dark green line is a subdiffusion fit to compare the deviation of both models for late times. Note that the time axis goes now to later times compared to the data shown in the previous section. b) depicts the extracted free diffusivity D_0 versus the PNC cube size. The inset shows the corresponding free diffusion length dependence on PNC cube size. c) shows the extracted trap density per cube for the three measured PNC cube sizes.

can be interpreted as a fundamental physical parameter revealing insight into the microscopic transport properties. In contrast, the subdiffusion model parameter can only describe the macroscopic exciton diffusion behavior which is based on diffusivity and diffusion length.
According to the microscopic model, one fit parameter can be interpreted as the free diffusivity D_0, which is shown for all PNC sizes in Fig. 4.4 b). The diffusivities for the three investigated PNC sizes are even more different from the trend predicted by the Monte Carlo simulations discussed previously. Clearly, the diffusivity does not follow the quadratic dependence on PNC cube size. Thus, the considered model for the Monte Carlo simulation does not reflect all features of exciton diffusion in PNC cube films and must be modified to match the experimentally determined MSD trends. The inset shows the calculated free diffusion lengths L_D according to Eqn. 2.27 for all three samples. The free diffusion lengths are the same for the two largest PNC cube systems, reflecting that the 14 nm PNC cubes' low exciton PL lifetime compensates for the system's larger free diffusivity. Unlike the subdiffusion prediction, the free diffusion length is even smaller for the larger PNC system. However, here only the free diffusivities and diffusion lengths are plotted, which are not the same quantities shown in the previous section in Fig. 4.3. The actual diffusivity, i.e., including the effect of traps, would be time-dependent and therefore has to be averaged temporally.
Besides the more complex explanation of the diffusivity, the deep trap model also allows calculation of the average trap density in the PNC cube film, i.e., $n_T = \frac{1}{\tau_d D_0}$. According to this model, the trap densities are between 10 and 15 traps per micrometer for the two larger PNC samples but approximately 60 per microns for the 5 nm PNCs, so approximately 6 times as large. This deviation mainly reflects that the absolute MSD values of the 5 nm PNC cube sample are so low compared to the other two film types. A large trap density shrinks the exciton diffusion performance within a film. However, the trapping time τ_d, which can be connected to the linearity of the curves, influences the trap density. This interplay of high D_0 and low τ_d for the 14 nm PNC film results in a similar trap density as the

8 nm PNC film, which has a lower initial diffusivity, however, also a larger trap time.
More important than the linear trap density is the density of traps per PNC, as depicted in Fig. 4.3 c). The trap density per cube for the 14 nm PNC cubes is only 1.5 times lower compared to the 5 nm PNC cube system. Thus, by considering the traps per cube the deviation is not as large as for the trap density per area. This reflects the fact that the coverage of the same area needs a different amount of cubes for different sized PNC cubes. The lowest trap density per cube appears for the 8 nm PNC cubes (see Fig. 4.4 c)), where only every 10th cube exhibits a trap. The smallest PNC cube film has the largest trap density per cube yielding a trap in every third PNC.
In this context, the traps are considered to be deep traps where no exciton detrapping is possible, which results in a constant MSD at later times and consequently in a diffusivity that approaches zero. The exciton traps can be of any nature, since we have not conducted measurements to evaluate the origin and location of those. Thus, the traps can be located within the PNC or at the surface. The exciton diffusion measurements cannot distinguish between them. Nonetheless, it allows the connection of the subdiffusive MSD trends to a quantitative deep trap density. Later on we will also consider shallow traps; however, these only decrease the absolute MSD values and do not disturb the linearity which would consequently decrease the exciton diffusivity. Shallow traps can be interpreted with the bright-dark MSD evolution results at low temperatures, which will be the main topic in Sec. 4.3.1.

4.1.2 Exciton Diffusion in PNPL Films

So far, exciton diffusion has been investigated in films of isotropically-shaped PNCs. The following section discusses the shape anisotropy of PNCs and its influence on the exciton diffusion process. PNPLs, as introduced in Sec. 3.1.4, possess one-dimension, which is far smaller than the other two, and the strong quantum confinement regime is present along the shortest dimension. As already seen for PNC cubes of different sizes (compare Sec. 4.1.1), the change of the PNC lateral size influences the PL emission spectra. This is visible in Fig. 4.5 a) where the room temperature PL spectra of three different PNC films are shown. The smaller the thickness of the sample, the more its PL spectrum is blue-shifted. Starting from a 14 nm PNC cube sample (green line) which can be considered as a PNPL with a large amount of MLs $\frac{14\ nm}{0.6\ nm} \approx 23$. The PL emission of the 5 ML PNPL sample (bright blue line) is shifted by 35 nm compared to the PNC cube PL spectrum, and for the 3 ML PNPLs film, the PL spectrum is further shifted by 22 nm to 458 nm (dark blue line).
The FWHMs are comparable, and all samples show an asymmetry on the low-energy side, i.e., to larger wavelengths. This asymmetry is mostly visible for the 3 ML PNPL film and can have different origins. It can reflect that the PNPL sample is not monodisperse, i.e., it has additional PNPL thicknesses deviating from its majority PNPL thickness within the film. For example, the presence of 5 ML PNPLs in 3 ML PNPLs sample would lead to an increase in the PL signal at 482 nm, while for 4 ML PNPLs would produce a PL signal between that of 3 and 5 ML PNPLs.
We recorded the PL spectrum of the 3 ML PNPL film at 4 K to ensure no PNPLs of other thicknesses are present within the ensemble (purple curve in Fig. 4.5 a)). At low temperatures, the PL spectrum temperature broadening is minimized, and the integer deviations in ML thickness would become visible as distinct peaks. Note, lateral deviations do not influence the PL spectrum crucially since along two axes the PNPLs are in the weak confinement regime, e.g., the expansion is about 20 nm, thus larger than the exciton Bohr radius. The broadening of the low temperature PL spectrum is mainly dictated by lateral deviations along the weakly confined axis.[90] This deviation between room

temperature and low temperature PL spectra suggests that the red PL sideband results from radiative trap states at room temperature. In contrast, those trap states are not emissive at low temperature or are not present at all, as traps become thermally activated only at higher temperatures. Interestingly, the PL maximum does not shift for the 3 ML PNPLs from room temperature to 4 K. This is a unique feature for this PNPL thickness type, i.e., not present for other thicknesses, e.g., 2 ML PNPLs have a blueshift and thicker PNPLs a redshift with decreasing temperature.[51] The 3 ML PNPL PL spectrum temperature dependence and the impact on exciton diffusion will be discussed in Sec. 4.3.
In Fig. 4.5 b) the TEM images for the PNC samples under consideration are depicted, the PNPLs stand on their smaller facets and stack together to form larger substructures. This sub-ordering will be

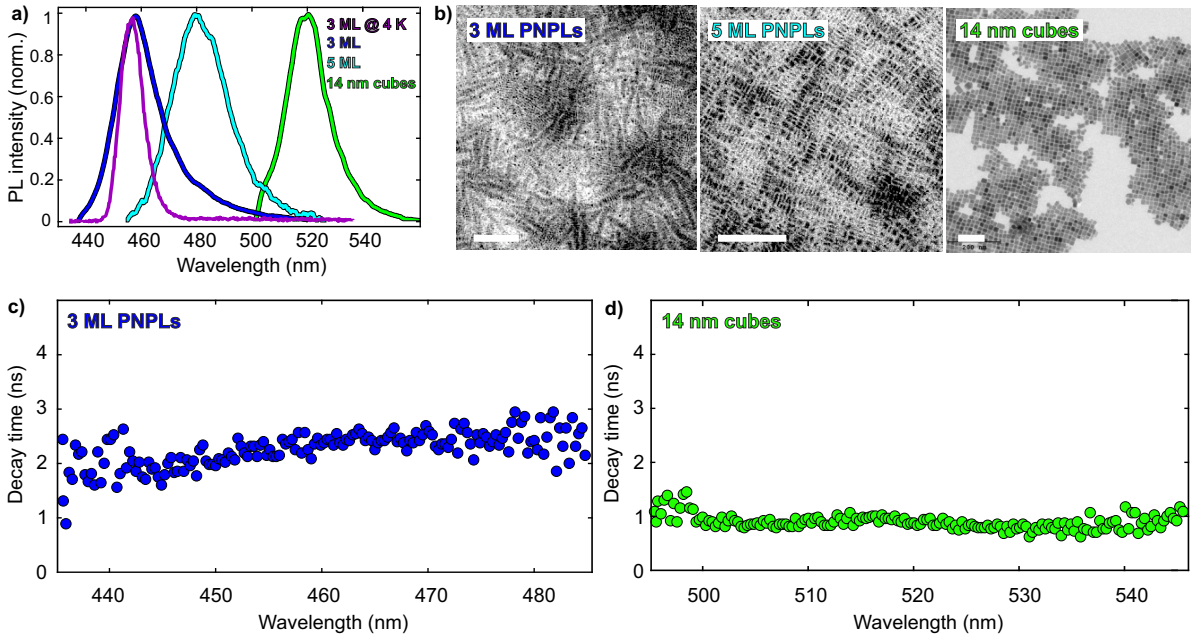

Figure 4.5: a) presents PL spectra for three different PNC films: 3 ML PNPLs (dark blue line), 5 ML PNPLs (bright blue line), and 14 nm PNC cubes (green line). For the 3 ML PNPL film, the PL spectrum at 4 K is also depicted (purple line). b) shows TEM images for the three PNC samples presented in a). The scale bars are 200 nm. c)+d) illustrate the PL decay time dependence on the PL emission wavelength for the c) 3 ML PNPLs film and d) 14 nm PNC cube film. The figure is adapted from[15].

discussed in the next section, where the PNC film order is investigated more closely. For the following discussion, most FRET transitions occur along PNPLs attached to each other on their larger facets. Thus, the PNPL center-to-enter distance can be assumed to be the PNPL thickness and ligand length, which is the most dominant FRET transfer distance in those systems.
In Fig. 4.5 c),d) the dependence of the PL decay time on the emission wavelengths are depicted for the 3 ML PNPL and the 14 nm PNC cube film at room temperature, respectively. For both PNC films, the exciton PL lifetime is not dependent on its emission wavelength. This suggests the underlying energy landscape is more homogeneous than in other NC types like CdSe, as energetic downhill migration would induce a strong dependence.[13] A flat energy landscape has previously been reported for PNC cubes.[14] Thus, individual size discrepancies do not greatly impact the radiative decay channel. The trap states mentioned earlier should be present, however, within the scope of the PL decay time analysis, those trap states do not impact the PL lifetime.[91]
In Fig. 4.6 a) the spatial PL profiles of a 5 ML PNPL film for increasing time mismatch between laser excitation pulse and probe is depicted, here every 25 ps up to a maximum time delay of 3 ns. Every PL profile is normalized to its maximum at each time step. Since the exciton number is not conserved

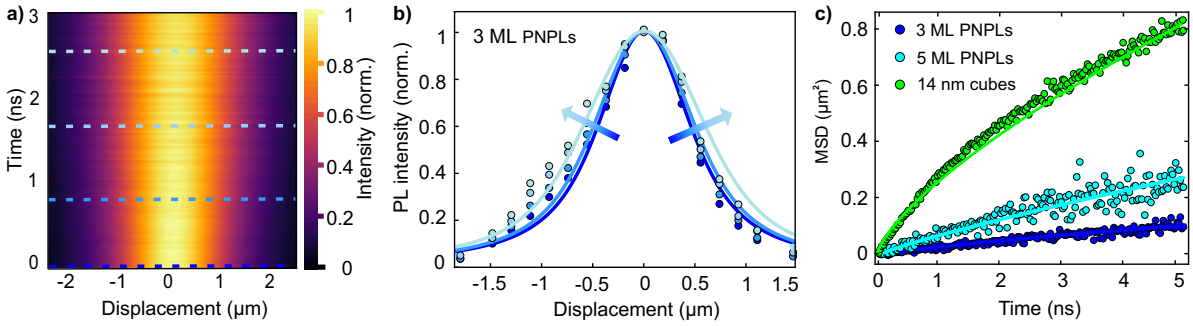

Figure 4.6: a) depicts the PL dynamics for the first 3 ns. Every time bin PL spectra are normalized to their maximum. b) shows only four PL profiles at different times (0 ns, 0.8 ns, 1.7 ns and 2.6 ns), and the corresponding Voigt profile fits (lines). The depicted time bins are highlighted in a) with the dashed lines. The actual profile broadening is more visible here. c) presents MSD temporal evolution for the measured samples: 14 nm PNC cubes (green), 5 ML PNPL (bright blue), and 3 ML PNPL (dark blue) films. The figure is adapted from[15].

due to the exponential decaying signal, the profiles would be hardly visible without normalization for the depicted linear intensity scale. The PL profiles broaden with increasing time since the laser excitation profile induces an inhomogeneous exciton distribution at $t = 0$ ns of a Gaussian shape. Those spatially inhomogeneously distributed excitons result in a density gradient that drives the exciton population to regions with lower exciton population following the macroscopic interpretation according to Sec. 2.4.1. The broadening is mainly visible within the first nanosecond, however, hardly detectable if one compares succeeding time steps. The temporal PL profile broadening can be seen more clearly in Fig. 4.6 b) where only four spatial PL profiles at different times are shown during the measurement. The four selected profiles are highlighted as dashed lines in Fig. 4.6 a). Those are all within the first 3 ns after laser pulse excitation and start from the PL trace detected right after the laser excitation, i.e., $t = 0$ ns (dark blue dashed line). The data points are measured PL intensities for the individual time step and PL lateral position. The lines correspond to Voigt profile fits. From those profile fits, the FWHM can be extracted, which is connected with the MSD as a quantity of profile broadening depicted in Fig. 4.6 c). At first glance, the broadening behavior is as expected from the previous sections. The film consisting of the largest PNC cubes, i.e., the 14 nm cubes (green points), exhibits the largest increase in MSD. In contrast, this temporal broadening decreases for decreasing PNC thickness and is lowest for the 3 ML PNPL sample (dark blue data points). Lines correspond to fits with the subdiffusive model, which nicely cover the MSD evolution within the first 5 ns after laser excitation.

sample	3 ML	5 ML	14 nm
β	0.77	0.85	0.72
D_a	0.09	0.28	0.68
scaling factor s	17/3.8	17/5	1
D_{th}	1.80	3.24	0.68

Table 4.2: Subdiffusion fit parameters of MSD curves for 3 ML, 5 ML PNPLs and 14 nm PNC cube film samples yielding the exponent β and the averaged diffusivity D_a. The theoretical scaling due to size differences is also presented, through the scaling factor s and the theoretical diffusivity D_{th}.

The subdiffusion model allows the extraction of macroscopic diffusion parameters, which are presented in Tab. 4.2. The exponents β of the sublinear law for the three PNC films, are comparable to each

other, thus the degree of subdiffusivity is similar. As stated above, deep traps can increase subdiffusion behavior and the PL red side fans of all three samples are comparable to each other, thus, one can trace back the same subdiffusion exciton transfer to those traps. Besides traps, we will see in Sec. 4.2.1 that also the PNC film structure can result in subdiffusion behavior due to voids.
The averaged diffusivities, calculated according to Eqn. 2.26, reflect the aforementioned absolute discrepancy of the MSD values, which results in the largest value for the 14 nm PNC cubes and the smallest diffusivity for the 3 ML PNPL sample. However, by reconsidering the simple scaling law (Eqn. 4.2) it appears that the actual diffusivities for the PNPL films are too high. This can be seen if the theoretical diffusivity D_{th} is calculated by applying the scaling law and regarding the PNPL thickness as the PNC size. This a reasonable approximation, as we consider all PNPLs to be standing on their sides aligned in stacks. Accordingly, the excitons will transfer along the highly confined axes which means the xy-plane. Transfer along the optical axis, namely the film thickness axis, can not be distinguished from in-plane diffusion. It is also suppressed since photons have to travel through the first PNC layers, and reversely after the diffusion process, the emitted photons have to find their way through the covering layers. By comparing the different diffusivities, the scaling factor can scale the 3 ML PNPLs diffusivity to a value the system theoretical will have if the 3 ML PNPLs have the size of the 14 nm PNC cubes, i.e., $D_{th} = s^2 D_a$. This scaling from the 3 ML PNPLs to the cubic system would result in a three times higher diffusivity (and for the 5 ML PNPL sample in a five times higher value) compared to the 14 nm PNC cube film. This astonishingly large diffusivity for the PNPL films after scaling can not be explained by only considering the PNPL thickness.
Therefore, other effects, like dipole alignment, should also be investigated. If the exciton dipoles of adjacent PNCs are aligned, the transition probability becomes maximized and, accordingly, the overall exciton diffusion. In PNPLs there are four first exciton states, one dark (dipole forbidden) and three bright (dipole allowed) states.[49] The bright-dark energy splitting is 18 meV for 3 ML PNPLs, thus, it is relatively low compared to the room temperature of 26 meV, and all exciton states can be regarded as degenerate. Thus, a change from dark to one of the bright states is easily possible and also intra bright state changes (bright exciton splitting of 10 meV for 3 ML PNPLs) are possible. The actual energetic ordering in PNPLs gets relevant for low temperature exciton diffusion measurements, which will be discussed in Sec. 4.3.1.2. If two PNPLs are now aligned with their large facets, the inplane exciton dipole moments of the adjacent PNPLs have maximum overlap. This also enhances exciton migration which was observed before in CdSe PNPL stacks.[92] There, CdSe PNPLs of 1.5 nm thickness and center to center distance of 5.7 nm yielding a FRET length of 500 nm and FRET rates of $1/1.5ps^{-1}$. For our system, the PNPL stacks also have micrometer size, therefore, the exciton transport behavior is best described by a one-dimensional exciton diffusion problem.[70]
Besides the favorable dipole alignment in PNPLs, one can also look at the present excited state, which can transfer its energy, namely, excitons. According to the Saha equation Eqn. 2.13 the number of excited states which are in the bound exciton phase rather than in a free charge carrier phase depends on the exciton binding energy, the system energy, i.e., its temperature, and its total number of excitations, i.e., absorption cross-section and pulse intensity. For the experimental conditions (room temperature, excitation power) the fraction of excited states which are in the excitonic phase are presented in Tab. 4.3. From the two extreme cases, namely the largest and thinnest PNCs, the difference for an excited state in the exciton phase is one-quarter lower in the 14 nm PNC cube than in the 3 ML PNPL sample. Of course, this damps the total transport performance since free charge carriers are not allowed to diffuse between PNCs, the transport can only happen if an exciton is present. If this is

included in the estimation mentioned in Tab. 4.2, one can scale the measured diffusivities again with the different excited state fractions of the samples. The reference is again the diffusivity for the 14 nm PNC cubes, and one ends up with $D_{th,Saha}$. This scaling considers the lower number of excitons in a weaker quantum confined system, i.e., it takes care of the overestimation of diffusion in the 3 ML PNPL sample. Thus, with this procedure both the weak and strong confinement systems exciton diffusivity are more comparable to each other, since only the actual formed excitons are considered. This results in a decreasing diffusivity for the 3 ML PNPL and 5 ML PNPL films compare to the 14 nm PNC films. However, by including the scaling law and the Saha equation $D_{th,Saha}$ is still larger for a 3 ML PNPL film up to twofold the unscaled exciton diffusivity measured in a 14 nm PNC film of 0.68 $\frac{cm^2}{s}$.

sample	3 ML	5 ML	14 nm
E_b in meV	180	120	30
$f = n_x/(n_x + n_{eh})$	0.99	0.96	0.72
$D_{th,Saha} = \frac{D_{th}}{f_i/f_{cubes}}$ in $\frac{cm^2}{s}$	1.31	2.43	0.68

Table 4.3: The table gives the exciton binding energies of the considered PNCs. f is the fraction of states in the exciton phase n_x compared to the total amount of excited states $n_x + n_{eh}$. The last row presents the theoretical diffusion parameter $D_{th,Saha}$ where the reduced excitons in a real system and the PNC size effects are considered.

For the two PNPL samples, the difference of the excited state fraction is smaller since those two systems have a large exciton binding energy, which mainly dictates the Saha equation (Eqn. 2.13). The influence of another tuning parameter, i.e., the temperature, will be considered in Sec. 4.3. Exciton coherence can also lead to enhanced exciton diffusion performance. However, exciton coherence gets only relevant at temperatures below 100 K.[93]

At room temperature, the exciton wavefunction can spread out to adjacent PNPLs since the center-to-center distance for the smallest PNPLs sample is smaller than the exciton Bohr radius for $CsPbBr_3$. This is termed exciton delocalization and was first observed in quantum dot solids at room temperature by Zhang et al..[16] For $CsPbBr_3$ the Bohr radius is 3.5 nm, thus, for the thinnest PNPLs, the fraction of exciton Bohr radius to PNPLs thickness yields $\frac{r_B}{r_{PNPL}} = 3.9$. Therefore, the exciton in the smallest PNPL system is spread over 4 PNPLs at most, enhancing exciton diffusion in those small PNC systems due to delocalization. However, this would not explain that for respecting the scaling law and the Saha equation, the 5 ML PNPLs are the best-performing shape concerning exciton diffusion. As announced above, the PNC film quality also influences the diffusion performance, as we will discuss in the next section.

4.2 Influence of PNC Assembly on Exciton Diffusion

The previous section's interest focus lay in the influence of exciton diffusion by single PNC characteristics, i.e., PNC cube size or PNPL thickness and energetic trap states. In this section, we will consider how exciton diffusion is affected by film properties, by investigating PNC assemblies. Imperfections like voids also influence exciton diffusion. To which extent is discussed in the following section. Since the film often consists of more layers along the optical axis, an additional question arises of whether the film thickness affects exciton diffusion.

4.2.1 Unordered PNC Cube Film and the Influence of Voids

When considering the impact of film properties on exciton diffusion behavior, discussing voids is unavoidable. If one or more PNCs are missing within the established film, it is not possible anymore for excitons to travel through such vacancies (or the FRET rate is strongly reduced if the transfer across the void is considered). Thus, applying the microscopic model mentioned above, the situation changes from a free random walk to a situation where those constraints, i.e., open boundary conditions, must be considered. That voids are present in general can be observed in the SEM images shown in Fig. 4.7 a)-c) upper panels. Here, dropcasts of dispersions with distinct dilution (1:19, 1:59 and 1:39) of 14 nm PNC cubes are used to create films and then imaged with an SEM. For the lowest dilution (see Fig. 4.7 a)), the film is densely packed with PNC cubes, only single PNC cubes are missing in the lattice. Below the SEM image, the MSD curves from the Monte Carlo simulated random walk are shown for such an undisturbed lattice. The black dots correspond to a linear exciton diffusion behavior for a void-free simulated lattice which is depicted as an inset in the upper left corner. Bright dots are the PNC cubes occupied with an exciton and dark spots are unoccupied PNC cubes. The image is a snapshot after some time. The other inset (lower right corner) shows the simulated lattice where separated voids are considered in the PNC cubic lattice. Voids can be deduced from the regular repeating black squares. One square consists of either 5 x 5 missing PNC cubes, resulting in an MSD trend depicted by the green data points, or 10 x 10 missing PNC cubes, yielding the blue MSD curve. The ratio of total void sites to actual present PNC cubes is held constant for both simulated void sizes and is set to 0.25, i.e., more PNC cubes are present than vacancies. Both simulated void sizes result in a similar MSD behavior, and the curves deviate from the void-free MSDs for elaborated time, i.e., the absolute MSD values are smaller, and the trend is not purely linear. In the early times, all three MSD curves are comparable. For the two films where different-sized voids are considered, the MSD curves are essentially the same. Thus, the actual MSD drop is mainly governed by the total void to PNC cube ratio and not by the individual void size (as long as the PNC cubes are connected on a macroscopic scale, as we will see below). The presence of voids that only intercept the perfect PNC lattice structure, i.e., all existing PNC sites are connected, seems to result in a decrease of the absolute MSD values compared to a free PNC cube film, however, the MSD temporal evolution still follows a linear trend. In Fig. 4.7 b) an opposite PNC cube structure to the lattice discussed in Fig. 4.7 a) is considered, i.e., only some PNC cube sites form connected patterns, whereas those patterns are separated from each other by voids. The upper panel presents the SEM image of a 14 nm PNC cube film where the stock solution was diluted the most, resulting in disconnected islands of 14 nm PNC cubes of different sizes. However, the voids are connected, i.e., this structure can be seen as an inverted lattice to the lattice presented in Fig. 4.7 a). The lower panel again shows the MSD curves for a regular lattice that mimics the features

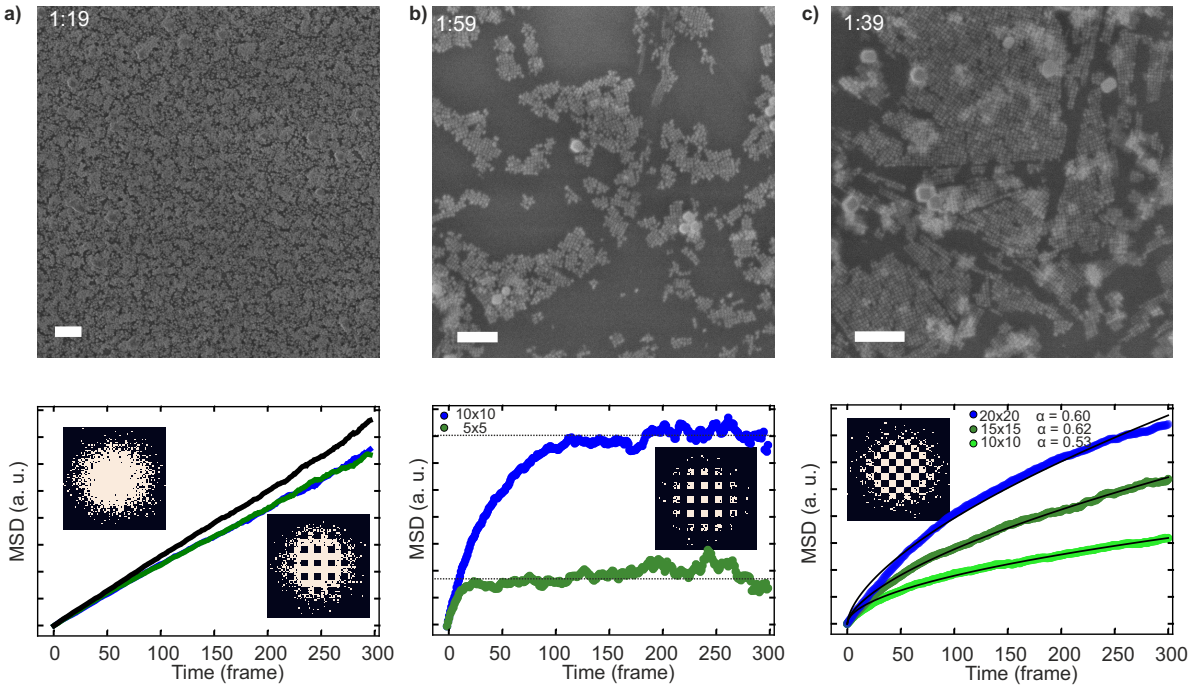

Figure 4.7: a) Upper panel: SEM image of 14 nm PNC cube film resulting from a 1:19 diluted stock solution dropcast with no voids. Lower panel: MSD temporal evolution for random walk Monte Carlo simulations performed on a lattice shown in the inset. The upper left inset is a void-free lattice, lower right inset depicts a regular void (5 x 5 PNC cubes, i.e., the dark squares) structure. Bright dots correspond to PNC cube sites occupied by an exciton. b) Upper panel: SEM image of a 1:59 diluted 14 nm PNC cube film where voids are in the majority. This means clusters of PNC cubes form isolated islands, illustrated in the lower panel inset. The lower panel shows two MSD temporal evolutions corresponding to PNC cube islands of 10 x 10 (blue data points) and 5 x 5 (green data points) PNC sites. c) The upper panel shows the SEM image of a 14 nm PNC cube dropcast of a 1:39 dilution. Voids are present, however, the PNC cube islands are connected as indicated in the inset in the lower panel. For the MSD simulation presented in the lower panel, three different PNC cube island sizes were simulated 20 x 20 (blue data points), 15 x 15 (dark green data points), and 10 x 10 (bright green data points) PNC cube sites. The MSD trends show subdiffusion behavior. The scale bars are 200 nm in all SEM images.

of the SEM image, i.e., disconnected PNC cube islands within a sub-lattice of connected voids. Two Monte Carlo simulations for different PNC island sizes were performed. The resulting MSD curves are shown for 5 x 5 large PNC islands (green data points) and 10 x 10 large PNC islands (blue data points). The PNC cube density is inverted to the lattice shown in Fig. 4.7 a) and yields a ratio of 0.75 for void to filled sites. Both MSD curves have a similar behavior again for early times, however, they deviate strongly at later times concerning their absolute MSD values. The smaller the PNC islands, the faster the MSD curve saturates and at a lower value. Thus, two different time regimes can be observed, one early time subdiffusive domain and a later one where no further diffusion occurs. The time which separates those regimes seems to depend on the PNC island size. This seems reasonable if the MSD behavior is interpreted utilizing the macroscopic diffusion description introduced in Sec. 2.4.1. Exciton diffusion happens as long as a density gradient exists. In early times, such a distorted exciton density profile exists since the excitation diameter (17 PNC cube sizes) covers some islands only partly. Even for PNC islands within the excitation diameter, the exciton density follows a Gaussian distribution in two dimensions. It thus has also a finite density gradient, i.e., a driving force to reach a homogeneously distributed exciton population. However, after some finite time, the exciton density gradient within the PNC cube island vanishes and the population is constant within the island (neglecting radiative and nonradiative recombinations, since these are spacial independent, therefore, decrease the exciton population with the same rate at all PNCs). This resolving exciton density gradient is not normal for

ordinary diffusion since there would be no possibility for an exciton density compression. However, for a system, where open boundary conditions are present, namely, existing void structures, excitons that reach voids can be backscattered to PNC cube sites where a higher exciton density is present. Between different islands, the exciton density also deviates according to the initial population and PL decay behavior, however, no inter-island transfer over the void structure is possible, i.e., the MSD is constant as far as the exciton density gradient is resolved in the individual PNC cube islands. Thus, it is clear that the two different time regimes depend on the PNC cube island size. The subdiffusion character for early times stems from different initial exciton populations of the individual islands resulting from different excitation laser spot coverage of the island. This means there are different exciton densities and, therefore, different exciton density gradients for individual PNC cube islands. Consequently, the time which is needed for resolving the exciton density gradient for separated islands differs. The time mentioned above, which separates the observed time domains, can be associated with the time at which all exciton density gradients in all PNC cube islands have vanished and no exciton transfers are possible. This implies that a constant MSD emerges at later times which is highlighted by the two dashed lines in the lower panel of Fig. 4.7 b).

The upper panel of Fig. 4.7 c) shows an SEM image of a PNC cube film which was produced with an intermediate 1:39 PNC cube dilution. The film contains some connected PNC islands and regions where voids are dominant, i.e., they separate PNC islands from others. To simulate such a structure, a combination of the previously discussed lattice types was established, namely, voids are present, and the PNC cube islands are connected. Such a system is shown in the lower panel inset and can be compared to a chess board. The void to PNC cube ratio is set to 0.5, and distinct void islands are connected as well as distinct PNC cube islands via a next nearest neighbor FRET transition. Thus, even when the exciton density gradient has essentially subsided within an individual island, inter-island density gradients exist further enabling exciton diffusion. The lower panel shows the MSD trends for three different simulated lattice types; however, all are chess board pattern-like. The MSD curve following the bright green data points results from a lattice structure where voids and PNC islands sizes are 10 x 10 lattice points large. The dark green data points represent MSD values for a 15 x 15, and the blue data points for 20 x 20 lattice point sizes of voids and PNC islands. The black lines are fits to the data with the subdiffusion model.

By comparing the three different simulated systems, it becomes evident that for larger individual PNC cube island sizes, the absolute MSD values are more extensive. In a larger PNC cube island, exciton diffusion can persist undisturbed for longer times. The free exciton diffusion process leads to the largest possible profile expansion (if the microscopic model parameters are the same, i.e., hopping rate, nonradiative trap density), thus, the absolute MSD values increase for larger PNC cube islands sizes. Not only the absolute MSD values are affected by the PNC cube island size, but the linearity of the MSD curve is also affected, which can be seen from the exponents of the subdiffusive fits. For the two largest PNC cube island systems, the exponent is closer to one ($\beta_{20x20} = 0.60$ and $\beta_{15x15} = 0.62$), i.e., the diffusion process is more linear compared to the smaller PNC cube island system which only consists of 10 x 10 PNC cube sites per island where the exponent of the subdiffusive model fit is $\beta_{10x10} = 0.53$. The different initial exciton density gradients of individual PNC cube islands result in a pronounced subdiffusive character of the MSD curves within the investigated systems. As before, the times at which the gradients resolve differ for the individual PNC cube islands, which results in the subdiffusion MSD behavior. Since the PNC cube islands are connected, there would, in principle, be no stop of the exciton profile broadening, i.e., the MSD would never converge to a constant like the

MSD curves presented in Fig. 4.7 b). However, the exciton populations tend to decrease to zero after some finite time since they all are recombined. Thus, no exciton density gradient exists, which drives the exciton diffusion.
Comparing the experimental results in Fig. 4.3 to the Monte Carlo simulations with a void sub-lattice, the closest simulated lattice structure to the experimental MSD curves would be the structure where PNC islands are connected to adjacent PNC islands. The simulation reflects the subdiffusion MSD character observed in PNC cube films found experimentally. Thus, the actual film coverage with sites where exciton diffusion can happen also plays a major role concerning subdiffusive behavior.
Of course, other void parameters will lead to distinct MSD behavior. The PNC cube islands can overlap, for instance, leading to a more linear diffusive behavior. This results in a subdiffusion model fit exponent closer to one, depending on the amount of PNC cube connections, i.e., allowed FRET transitions. The void to PNC cube site coverage as well as the PNC cube disorder results in different PNC cube distances, hence, a spreading of the FRET hopping rates can be, in principle, implemented and would also change the film performance in respect to exciton diffusion.

4.2.2 Semiordered PNPL Films

So far, only film types of cubic PNCs were considered, forming the lattice patterns mentioned above. If we turn our attention to PNPLs, we must likely consider a more complicated film formation structure. As announced in a previous section, PNPLs tend to stack together, leading to a semiordered network. From SEM images, it appears that PNPLs are partly ordered. This means PNPLs tend to stick together on their large facets and form stacks already mentioned in Sec. 4.1.2. These stacks are partly ordered, i.e., oriented in parallel or perpendicularly, however, the length and the stack orientation vary from stack to stack as seen in Fig. 4.8 a) left panel for a 3 ML PNPL film via SEM imaging. The stack length is several micrometers long and consists of several hundreds of PNPLs arranged in parallel. By evaluating those lateral expansions, it is clear that the individual stack length spreads from 100 nm up to some microns visible in the right panel, where the occurrence of different stack lengths is shown in a histogram. 200 individual stacks for the 3 ML PNPL film were evaluated. The average stack length is 649 nm, and the standard deviation is 308 nm supporting the qualitative observations from the left SEM image. In Fig. 4.8 b) a 5 ML PNPL film SEM image is presented, the stacks consisting of PNPLs form bundles of stacks, i.e., several PNPL stacks parallel to each other. However, the bundles are also oriented perpendicular to each other, like the 3 ML PNPL stacks in the film. The coverage of the SiO_2 substrate with PNPL stacks is not as high as for the 3 ML PNPL film. There are also void structures in the 5 ML PNPL film, which are visible as black rectangles. Nevertheless, for a PNPL film, those stacks or stack bundles are the favorable packing structure. The tendency of the PNC surrounding ligand shell to maximize its environment with ligands of adjacent PNPLs is favorable. The parallel or perpendicular PNPLs orientations are also beneficial for stabilizing the film by packing the space as dense as possible.
Since the FRET transition rate is crucially governed by the dipole alignment of the donor and acceptor exciton states, we take a closer look at the dipole orientation of the first excitonic levels. In Fig. 4.8 c) a single PNPL is depicted (bird's-eye view) with the dipole moments of the bright excitonic states (green), i.e., the out-of-plane p_z and the inplane p_x/p_y dipole moment orientations. The dark state (grey) is an isotropic singlet state, thus, the dark transfer rate should be independent of the directional PNPL orientation. Due to the PNPL stack formation, two fundamentally different PNPL orientation types

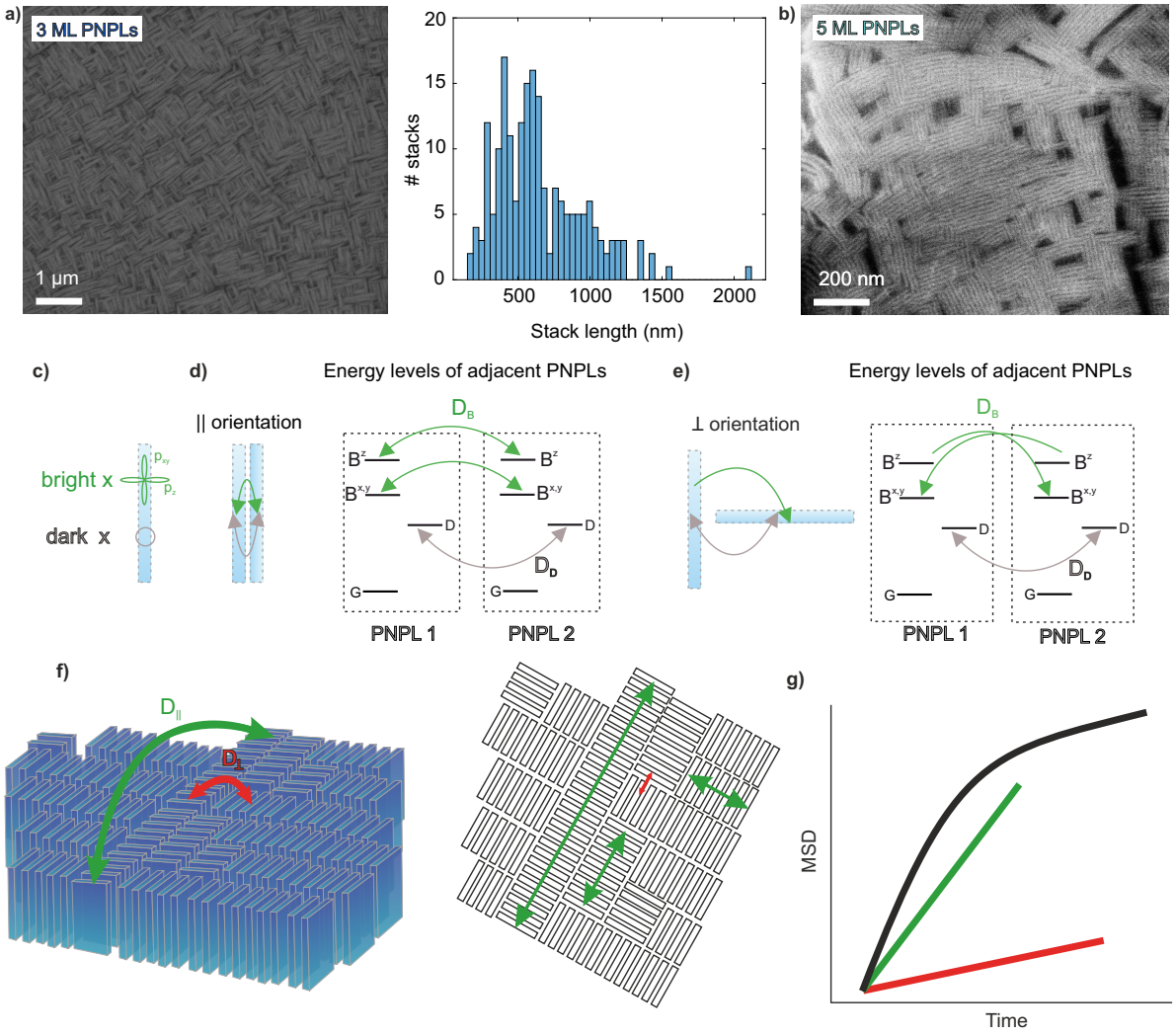

Figure 4.8: a) depicts SEM images of 3 ML (left panel) PNPL film and histogram of 200 stacks lengths (right panel). b) shows an SEM image of a 5 ML PNPL film where the stacks form bundles. c) show the lateral expansion of the four first exciton states in a PNPL. d)+e) illustrates two fundamental alignment types in a PNPL film: d) parallel and e) perpendicular alignment. The energy diagrams for both alignment types are also shown. f) presents schematics of PNPL film, PNPLs stand on their smaller facet and are attached to adjacent PNPLs along their large facet yielding PNPL stack formation of different lengths. Exciton diffusion is larger along a stack, denoted by the green arrow $D_{\parallel}$, and smaller, for inter-stack transfer, illustrated by the red arrow $D_{\perp}$. The right panel shows the schematics with a bird eye perspective. g) Schematic MSD evolution along one stack (green line) and diffusion between two differently oriented stacks (red line). The black curve is the interplay of both transfers and considers the variety of stack lengths.

must be considered. The parallel orientation, schematically depicted in the left panel of Fig. 4.8 d) with the corresponding energetic level ordering of the first excitonic levels and the orthogonal orientation depicted in Fig. 4.8 e). For the parallel orientation, there are four excitonic levels, three bright state and one dark state. The out-of-plane exciton (B_i^z) has higher energy compared to the degenerate inplane excitonic level ($B_i^{x,y}$).[49] In the left schematic, the $B_1^z B_2^z$ transition as well as the $B_1^{x,y} B_2^{x,y}$ FRET transitions, where the dipole moments are oriented in parallel are summarized by the green arrow which indicates the fast FRET process with a high FRET rate. The grey arrow in the schematics illustrates the dark-to-dark exciton level energy transition of adjacent PNPLs. This process was omitted for the previously discussed larger PNC samples, as the FRET distance between adjacent PNCs was too large. Here, we consider this process since, at least for the 3 ML PNPLs, the exciton Bohr radius for $CsPbBr_3$ is two times larger than the PNC thickness, and thus, the transition can,

in principle, happen. Note the dark transition rate is unimportant for the room temperature results since the dark state is rapidly depopulated via the bright state through thermal excitation followed by either a bright state FRET process or fast radiative recombination of the bright state. However, the dark-to-dark FRET transition rate becomes important if the dark states can not be depopulated via thermal excitation, i.e., at low temperatures, which will be discussed in Sec. 4.3.1.2. The FRET transitions in this section will happen in a homogeneous energy landscape if the PNCs are the same. The second fundamental PNPL orientation type is a perpendicular orientation of the PNPLs, depicted in Fig. 4.8 e), where the left panel shows schematically two PNPLs and the right panel shows the corresponding energy level ordering of the first excitonic states with corresponding FRET transitions of both adjacent PNPLs. Again, green arrows depict FRET transitions of bright states of adjacent PNPLs. However, the bright-to-bright exciton transition is either $B_1^z B_2^{x,y}$ or $B_1^{x,y} B_2^z$ due to the dipole orientation, whereas the transition from the energetic higher laying state B_i^z to the lower laying one $B_{i+1}^{x,y}$, is more likely than the energetically upwards processes, i.e., $B_1^{x,y} B_2^z$ and $B_2^{x,y} B_1^z$. The dark-to-dark FRET transition has the same rate as the parallel orientation, only considering the dipole alignment. In perpendicularly aligned PNPLs, the bright FRET transfer rates are both in an inhomogeneous energy landscape since both transitions have to be supported by a phonon emission or absorption. However, the dark-to-dark FRET transfer for this PNPL happens at the same energy.

Additionally to the dipole alignment considerations, the distance between the donator and acceptor has to be considered in PNPL systems. Suppose that the excited exciton is located in the PNPL center. In that case, the center-to-center distance is larger for PNPLs that are perpendicular to each other compared to parallelly-oriented PNPLs (compare Fig. 4.8 d),e)). For instance, for the 3 ML PNPLs, the center-to-center distance is 4.8 nm for parallelly aligned and 13.9 nm for perpendicularly oriented PNPLs (3 ML PNPL sizes (1.8 x 20 x 20) nm and ligand length 1.5 nm). This larger hopping distance tremendously reduces the microscopic FRET transfer probability due to the $1/r^6$ ($1/r^4$ in two dimensions) power law. This means the transfer rate is reduced by $1/(13.9/4.8)^4 = 0.0142$ and by $1/(13.9/4.8)^6 = 0.0017$ for the two-dimensional and three-dimensional case, respectively. Here, the inter PNPLs layer transfer can be neglected (the center-to-center distance between two PNPLs perpendicular to the layering axis is 23 nm which is even larger compared to the in-plane PNPLs perpendicular center-to-center distance. This reduces the problem to the two-dimensional plane and results in an estimated ratio of the transfer rates between perpendicularly oriented PNPLs to parallel PNPLs of $r_\perp / r_\parallel \approx 1.42$ %.

Of course, neglecting the exciton diffusion within the same PNPL is only a rough estimation. This intra-PNPLs exciton diffusion can result in th exciton being in a closer position to an adjacent PNPL, rendering FRET to this PNPL more likely. The inter-PNC diffusivity only increases the transfer rate for perpendicular PNPLs $r_\perp$ to some extent but not up to the parallel PNPLs rate $r_\parallel$, which is the extreme case. Thus, the crude estimation of $r_\perp / r_\parallel$ is only a lower bound for this fraction. However, it will never be equal to one or larger, implying a larger total diffusivity along PNPL stacks in comparison to perpendicular adjacent PNPLs. Note that the exciton diffusivity within a PNPL implies that the distance to other PNCs becomes larger or smaller depending on which direction the exciton probability moves. This yields a higher or lower transfer rate to those adjacent PNPLs. However, the distance-dependence of FRET rate is highly nonlinear, thus, this departure from the PNPL center position is beneficial for a perpendicular PNPL transfer.

The PNPL film structure is illustrated in Fig. 4.8 f) by a three-dimensional schematic (left panel) and from a bird's eye perspective in the right panel. The PNPLs stand on their smaller facets, and the

stacks have different lengths. For such a semi-ordered system, two macroscopic diffusion parameters can be assigned resulting from FRET transfers within a stack, depicted by the green arrow illustrating $D_{\parallel}$ which is the total sum of all FRET transition rates discussed for the parallel PNPL orientation. The inter-stack transfer process for vertical stacks, depicted by the red arrow $D_{\perp}$, is the sum of all FRET transfer rates discussed for the vertical PNPL orientation. $D_{\parallel}$ is generally larger than $D_{\perp}$. Firstly, due to the energetic homogeneity of adjacent PNPLs in the parallel alignment, and secondly, because of the appearing exciton delocalization in the parallel PNPL orientation, which was discussed above.
Thus, the assumption of two fundamentally different diffusivities is reasonable and results in a theoretical MSD trend shown by the schematics in Fig. 4.8 g) with two linear MSD curves. The green curve corresponds to exciton diffusion along stacks, and the red one results from exciton diffusion between adjacent stacks. The linear MSD curves correspond to exciton diffusion within those subsystems, where only one stack length is present, or a system where only perpendicular oriented PNPLs are present (impossible if the closed packed arrangement is a restriction). The actual MSD curves measured for PNPL films already shown in Fig. 4.6 c) deviate from those two linear MSD curves and are best represented by a subdiffusive MSD curve (black line in Fig. 4.8 g)).
The reason for the subdiffusive trend is the same as presented before for the PNC cube film with voids discussed in Sec. 4.2.1, where also two macroscopic diffusivities explained the subdiffusive MSD trends. In early times, exciton diffusion is fast and is mainly dictated by energy transfers along the stacks. Exciton density heterogeneities get resolved by the macroscopic exciton density gradient-driven force along those stacks. Since the stack lengths are broadly dispersed, there is no sharp time spot where all density gradients are resolved (analog to resolving the density gradients for the PNC cube islands shown in Fig. 4.7 c)).
The appearing stack ordering can falsely suggest that the macroscopic diffusion is not isotropic in those PNPL structures. This is not the case due to the random orientation of the PNPL stacks and their broad length distribution. The emission PL spot of the sample and the temporal PL evolution are isotropic in space.
After investigating the beneficial impact of semi-ordered PNPL structures on macroscopic exciton diffusion behavior, the question arises if increasing the order to a super-ordered PNC system, i.e., a SL, also drastically increases the exciton diffusion behavior. This will be discussed in the following section where we investigate the exciton diffusion performance in highly ordered structures.

4.2.3 Super Lattice

The order of PNCs can play a dominant role in exciton diffusion, as was already seen in the previous section, where stacks of PNPLs can be seen as a partly ordered superstructure. A similar structure can be established for PNC cubes as already introduced in Sec. 3.1.5. If the ordered system has a macroscopic size of several microns, those ensembles are called SLs. In Fig. 4.9 a) the PL image of SLs consisting of 8 nm large PNC cubes is shown (upper panel). These SLs are macroscopic, hence they can be resolved with an optical microscope. The middle panel in Fig. 4.9 a) depicts an SEM image of the SL surface. The highly ordered individual PNC cubes, forming the SL are visible. The lower panel illustrates the high quality of PNC order, i.e., absence of voids, as a schematic. This high quality becomes more obvious by comparing the SLs to ordinary PNC cube films produced via dropcasting (Fig. 4.2). Fig. 4.9 b) presents the same conceptional information as the panels shown in Fig. 4.9 a), however for SLs comprising 5 nm PNC cubes. The main difference to the 8 nm PNC cube SLs is that

there is a macroscopic rhombic shape of the SL. This results from slight size mismatches of the 5 nm cubes, which are not exactly cubic in shape.[37] We will discuss the exciton diffusion performance of

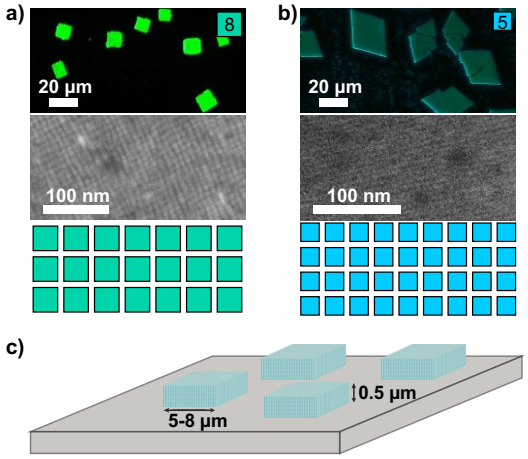

Figure 4.9: Thie figure shows PL images of several SLs consisting of 8 nm PNC cubes a) and 5 nm PNC cubes b), which have macroscopic size (upper panel), SEM image of a single SL (middle panel) and schematics of the perfect order of those PNC cubes forming the SL (lower panel). c) shows a schematic of a SiO_2 substrate with several super lattices present.

PNC SLs in Sec. 4.3 where the system temperature is also varied. To conclude the investigations, the following section discusses exciton diffusion within films which consist of more than one layer since those samples are the most realistic compared to our experiments.

4.2.4 Film Thickness

Until now, only the lateral exciton diffusion was considered, and the possible transfers along the optical axis, namely along the PNC film thickness, were omitted. Here, the influence of the PNC film thickness on the exciton diffusion is discussed. In Fig. 4.10 a) an SEM image of a 3 ML PNPL film cross-section is shown (highlighted in blue). Below this active layer, a layer of 300 nm SiO_2 is visible. Clear thickness deviations are observable, and the image suggests that the PNPL film consists of several layers of PNPLs. The same observation is detectable for a dropcasted 14 nm PNC cube film in Fig. 4.10 b). Both PNC films have similar thicknesses of around 100 nm, implying that the PNPLs film consists roughly of 5 PNPL layers and the PNC cube film out of seven PNC cube layers. Thus, it seems meaningful to discuss this deviation from a pure two-dimensional diffusion problem to a more elaborated description, where exciton transfer out of plane is possible.
The top PNC layer is impinged by the laser excitation beam, for this region the exciton diffusion is measured with the applied measurement method. The PL emission due to the radiative recombination of excitons from this layer is the most prominent part measured during TCSPC. Excited PNCs beneath

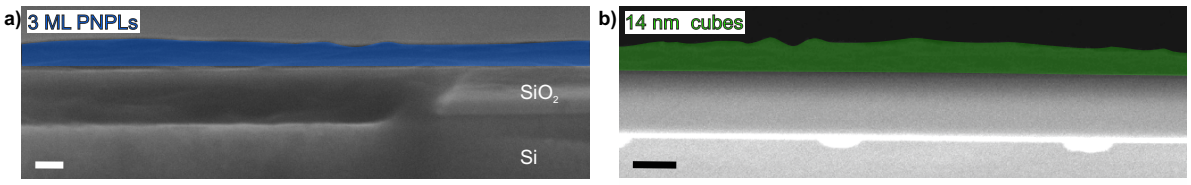

Figure 4.10: The figure shows the PNC film cross-section for an a) 3 ML PNPL film (blue) and a b) 14 nm PNC cube film (green). The PNC films cover a 300 nm thick SiO_2 layer. The scale bar is 100 nm.

the first layer can not couple out photons of the semiconductor film undisturbed. The lower-laying layers also receive less excitation power than the first layer due to absorption processes in the first layer. However, if excitons are excited within the film, they can transfer through FRET processes to adjacent PNC sites, at least for cubic systems. For diffusing excitons in PNPLs films, the inter-layer diffusion can be neglected due to the large center-to-center distance of PNPLs sitting in distinct layers, which was already mentioned in Sec. 4.2.2. Suppose isotropic transport expansion is assumed for PNC cubic systems. In that case, the distance dependence of the FRET transfer changes from a two-dimensional to a three-dimensional problem introduced above.[70] Thus, for a PNC film consisting of more than one layer, the exciton diffusion in theory should decrease. Unfortunately, we could not produce controlled film thicknesses to test this claim. Other techniques like PL tomography can be applied to distinguish between bulk and surface diffusion behavior by two- and one-photon excitation within a confocal microscope.[94,95]

The thickness of the active film also plays a major role if the system's temperature is varied since the thermal conductance of the active PNC film has to be considered. Until now, the initial PL broadening was always omitted for our exciton diffusion considerations. It was assumed that the exciton diffusion process starts at the initial excitation, i.e., within the first 100 ps after laser excitation. In contrast, no or only minor exciton transport happens within the small time range between excitation and the 100 ps. However, if one compares initial PL profiles, e.g., a 5 nm PNC cube film depicted in Fig. 4.11 a) (red data points and red Voigt profile line), with the setup IRF (green data points and green Voigt profile line) one has to explain the origin of the profile mismatch. By comparing those two, one can assume that exciton transport already happens from initial excitation until the first PL profile is recorded. Exciton delocalization has been claimed to explain the observed phenomena, however, it is

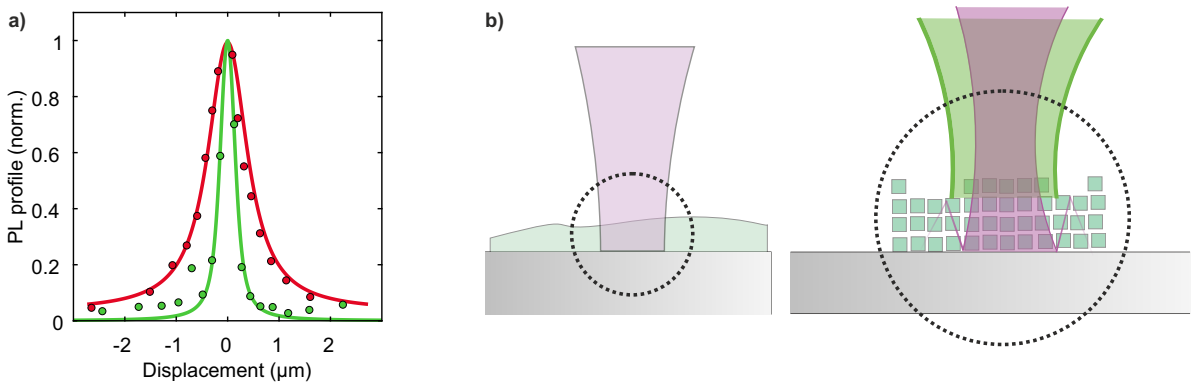

Figure 4.11: a) shows the setup PSF recorded from a single PNC cube PL emission (green) and the initial PL profile for a 5 nm PNC cube film. The left-hand side of b) depicts a laser exciting a PNC cube film on a SiO_2 substrate. The right-hand side shows a zoom of the region of interest where the excitation laser spot hits the PNC cube film. The film consists of several PNC cube layers. However, the excitation beam is only partly absorbed and reflected on the SiO_2 substrate. The laser gets broadened after reflection since the focus point is right at the film surface. Hence the laser impinging the substrate with an incident angle different from 90°. During the second path through the PNC cube film, the laser beam excites more excitons. The emission laser spot collected with the microscope is broader than expected, i.e., for a monolayer film.

only the dominant exciton transport mechanism in QDs where the exciton Bohr radius is far larger than the spatial extension of the QD. For example, in the work of Zhang et al., the exciton Bohr radius is 26 times larger than the NC radius. For $CsPbBr_3$ PNC cubes, the Bohr radius is 3.5 nm and is hence of comparable size to the examined PNC cube sizes. The Bohr radius is only larger than the PNC cube size for the 5 nm PNC cubes and results in a Bohr radius to NC radius ratio of $\frac{r_B}{r_{QD}} = 1.4$. Thus, the exciton in the smallest PNC cubic system is spread over 1.4 PNC cubes at maximum, which would

enhance exciton diffusion in those small PNC systems to some extent. However, the FWHM of the different sized PNC cubes' initial PL profiles are similar to each other. Thus, the possible delocalization of excitons in the smallest investigated PNC cubic system plays only a minor role in sub-picosecond fast diffusion processes.

The origin of the initial PL profile broadening discrepancy between excitation spot size and the profiles presented here can be explained by optical considerations as depicted in Fig. 4.11 b). The excitation laser beam is scattered at PNCs within the first layer of the investigated film in random directions. It thus excites adjacent PNCs, which are, in principle, out of reach of the excitation spot. Furthermore, the excitation beam is partly transmitted through the film of 100 nm thickness due to the finite absorption cross-section of the samples. The excitation laser beam gets reflected at the SiO_2 substrate. This reflection happens with an impinging angle, not 90°, since the focus point is set to the PNC film surface. After that, the beam diverges. Thus, the reflected beam is expanded and diverges, exciting PNCs again, however, also in regions that were not reachable for the laser beam in the first run. The PNC emission is not directed, i.e., it can be assumed to be isotropic. Thus, the optics can collect the PL, however, with a larger PL profile broadening than expected. The excitation beam is also partly reflected at the PNC film/air interface, which also broadens the PL profile.

4.3 Temperature Effect on Exciton Diffusion in PNC Ensemble

So far, only the intrinsic properties of PNCs have been discussed, e.g., single PNC characteristics or the quality of the films they form. Now, we want to focus on extrinsic properties like temperature and their effects on exciton diffusion in PNC films. Temperature is one form of energy and it is introduced in solid-state physics by describing it as phonons. Since the excitons are established in the PNCs, they can, in principle, interact with phonons. The previously introduced PNC types and films are reconsidered here, with a particular interest in exciton diffusion performance affected by temperature. Is there a fundamental difference between highly ordered SLs and unordered PNC cube systems? Do PNC shape or size affect diffusion performance differently if the temperature varies? Finally, a universal behavior can be observed in PNC systems, as discussed in this section's last part. The temperature variation was performed with a cryostat setup where heating to room temperature is possible. Thus, the film is not under ambient conditions and therefore protected from moisture and oxygen. The pressure in the cryostat chamber is around 10^{-6} mbar.

4.3.1 Low Temperature Performance

By conducting the exciton diffusion measurements, two temperature regimes are distinguishable and are fundamentally different concerning their exciton diffusivities. This section is devoted to the low-temperature regime which ranges from 9 - 100 K. However, the actual temperature separating these two regimes is PNC species- and size-dependent and is thus not always exactly at 100 K. Several important physical properties are temperature dependent, which can affect exciton diffusion, such as the decay channels to the ground state, radiative as well as non-radiative. For PNC cubes, a high radiative PL decay was observed by others.[42] Traps which are mainly responsible for the non-radiatve decay channel and often have a thermal activation energy, which means that the trap density is temperature dependent. However, detrapping can also be possible at elaborated temperatures by phonon assistance. The fine level splitting of the first excited excitonic states becomes relevant for low enough temperatures, i.e., when the thermal broadening is smaller than the splitting of the energetic fine level structure due to electron hole exchange interaction.[96] For the cubic PNCs in this work, the lateral size is too large for the bright exciton triplet fine level splitting to be relevant at the lowest possible temperature achievable with the setup. Energetically below the bright triplet states, lies a so-called dark state, whose transition to the ground state is dipole forbidden.[44–46]
Spectral overlap between absorption and emission of acceptor and donor PNC is crucial for a large exciton diffusivity. Here, homo-FRET is the dominant transfer mechanism, thus, a small Stokes shift of acceptor and donor is beneficial. The Stokes shift is temperature dependent in the material under consideration, i.e., the Stokes shift gets smaller for lower temperatures.[69] The Stokes shift is also size-dependent in PNC cubes, it increases for decreasing PNC edge length.[66]

4.3.1.1 Cubic PNC Ensembles

The low-temperature MSD curves for the PNC cubic systems are in strong contrast to the already shown MSD curves at room temperature. This is visible in Fig. 4.12 a) where the MSD curves for the 5 nm PNC SL are presented for 9 - 80 K (black to purple data points). The MSD curves for individual temperatures are offset for clarity. For the lowest temperature, the MSD value rises for early times

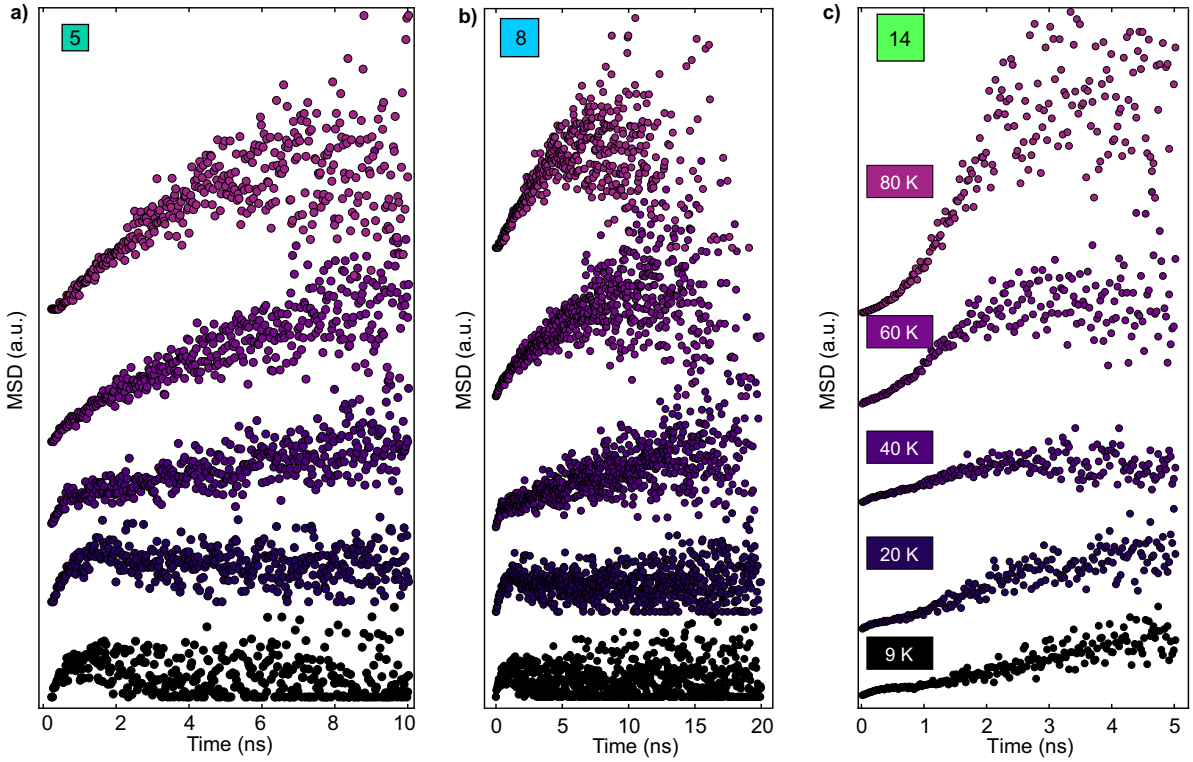

Figure 4.12: The figure presents temporal MSD evolution for temperatures starting from 9 K (black data points) up to 80 K (purple data points) for a) an SL out of 5 nm PNC cubes, b) 8 nm, and c) an unordered PNC 14 nm cube film. The curves are offset for clarity. Note the different time axis. The figure is adapted from[97].

(0 - 1 ns) like the MSD behavior observed at room temperature. However, this initial increase is followed by a plateau and a subsequent decrease in the MSD value after this maximum for the lowest temperatures, which was not observable until now. This downward trend starts at around one ns and ends when the MSD reaches its initial value, i.e., zero. This behavior is most apparent for the smallest applied temperature and can be naively interpreted macroscopically as negative diffusion. This implies that the diffusive particles move in the opposite density gradient direction, i.e., to regions with more particles. This counter intuitive behavior will be discussed later. Increasing the temperature leads to a shift of the MSD maximum position to shorter times and the temporal MSD downward trends vanish. Finally, this maximum disappears at a certain temperature, which for the 5 nm PNC SL system is 40 K. At this temperature, the MSD curve can be divided into two different linear diffusion regimes. An early one from 0 - 1 ns with a high diffusivity and a late one from one ns onward with low diffusivity. By increasing the temperature to 60 K or 80 K, the sharp separation of these linear diffusion regimes vanishes. The MSD curves follow a subdiffusive trend, i.e., a qualitatively similar trend to the room temperature curves discussed in Sec. 4.1.1.2.

The initial MSD evolution is similar for the presented temperature range, meaning comparable initial diffusivities irrespective of temperature. However, if MSD evolution at later times is investigated, the diffusivities, which are proportional to the derivative of the MSD curve, deviate strongly for different temperatures. Thus, we do not apply a single model which describes the MSD evolution over the whole temperature range. In Sec. 2.4.1.3 a novel method to estimate an averaged diffusivity is introduced to evaluate the different MSD curves over the entire temperature range.

Leaving the 5 nm PNC SL sample and turning our attention to the SL consisting of the 8 nm large PNC cubes, the MSD curves are quite the same as for the 5 nm PNC SL depicted in Fig. 4.12 b). The early

time evolution is similar for all temperatures with a maximum and negative diffusivity appearing for low temperatures and vanishing for higher temperatures. The similar behavior suggests a universal qualitative MSD behavior for low temperatures in PNC cube structures, irrespective of the actual PNC cube size. However, by investigating the exciton diffusion performance in a 14 nm PNC cube film not in a SL arrangement, the observed low-temperature characteristics for the SLs are missing, as clearly visible in Fig. 4.12 c). The MSD curves never decrease for low temperatures, even for the 9 K curve, where this feature is expected to be most visible.

Due to the fundamentally different MSD behavior at low temperatures, the question arises, whether the larger PNC cube size or the missing order for the larger PNC cube sample is responsible for these MSD trends. Unfortunately, we could not arrange the largest PNC cubes in SL configuration. Therefore, we will only consider the size hereafter. In principle, the PNC order can influence exciton diffusion behavior. But, we will see below that order only plays a minor role regarding macroscopic exciton transport in such ensembles, and PNC size outperforms order. The MSD values are obtained by scanning the spatial PL profile where, for every position, a PL decay is recorded and explained in more detail in Sec. 3.3. Therefore, the information about exciton diffusion is only indirectly accessible, i.e., if only on exciton species in the system is responsible for the PL broadening, the MSD curves will be directly connected to the exciton diffusion process. However, it is possible that more than one exciton population is present or that excitons can recombine non-radiatively after transporting its energy across the film. In that case, more work is needed to interpret the data. It is more precise to analyze the temporal change of the PL profiles by considering all possible transfer events, which results in a discrepancy of excited and emission spatial position. This would be, for instance, photo recycling[98] and waveguiding.[99] Waveguiding was observed in macroscopic single crystals like methylammonium lead iodide-based thin films where the material is monocrystalline over several microns, i.e., the refractive index is constant within a single crystal. This requirement of an unchanged refractive index over several hundreds of nanometers is not valid for PNC films due to imperfections like voids, strain as well as the surrounding ligand shell of the PNC, whose refractive index differs from the PNC.

A natural extension of the simple exciton diffusion model, i.e., one exciton species, is to consider two fundamentally different exciton species. The corresponding energetic level ordering is depicted in Fig. 4.13 a). The first excitonic levels of a PNC cube are depicted with respect to its ground state (G). A bright (dipole allowed) exciton level (B) has the highest energy. It corresponds to the degenerate triplet states (fine-level splitting is omitted here since the splitting energies are too low to be resolved at those temperatures). In contrast, the dark singlet state generally lies below the bright states.[100] The arrows in the schematic corresponds to possible transitions between the levels. The bright-to-ground state transition (BGT) and the dark-to-ground state transition (DGT), are radiative but have different radiative rates indicated by arrow thickness (thin means small, and thick means large radiative rate). The dipole-allowed transitions have a far higher rate (up to 100 times) than the dipole-forbidden DGT.[42] The transitions between the first excited excitonic levels, namely the temperature independent bright-to-dark transition (BDT) and the temperature-dependent dark-to-bright transitions (DBT), are also depicted by arrows. The transitions between the excited exciton states are non-radiative and mediated by phonons, which follow a Bose-Einstein distributed density $N_B = \frac{1}{exp(\Delta E_{BD}/k_B T)-1}$.[45,48,49] The DBT can only happen if the missing energy gap between B and D states is bridged, i.e., the splitting energy ΔE_{BD} is supplied by interacting phonons. The BDT is mainly temperature independent and is only affected by temperature indirectly due to the temperature dependence of the phonon density of states. Since phonons can not differentiate between the transitions, both the DBT and the BDT are

affected by the phonon density of states to the same extent. Thus one can understand the temperature dependence of the BDT by comparing both non-radiative transitions, i.e., $\frac{r_{DBT}}{r_{BDT}} \propto \exp(-\frac{\Delta E_{BD}}{k_B T})$.
As highlighted above, the activation rate is also dependent on the splitting energy between the bright-dark states ΔE_{BD}, which is PNC size dependent, as depicted in Fig. 4.13 b). The splitting energy

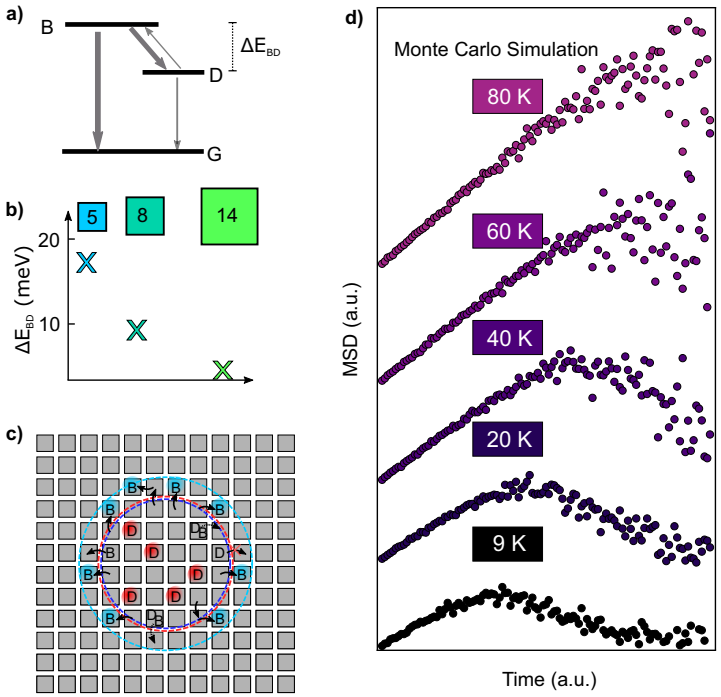

Figure 4.13: a) shows an energy diagram for a single PNC cube of the first four excited exciton levels. The dipole forbidden dark state (D), and the dipole allowed three-fold degenerate bright states (B), which are energetically separated by ΔE_{BD}. The arrows correspond to radiative transitions to the ground state (G) and the non-radiative conversion between B and D states. The arrow thickness represents the transition rate magnitude. b) depicts actual ΔE_{BD} values for the used PNC samples. c) presents the schematic of the inter-PNC cube hopping transitions (arrows). Dark states (red) cannot transfer, and bright states (blue) can occupy adjacent PNCs. Dashed circles correspond to excitation (dark blue), emission of dark excitons (red), and emission of bright excitons (bright blue). d) yields the temporal MSD trends for the bright-dark exciton model. The dark to bright phonon-supported transitions is varied from zero (black) to the temperature-independent bright-dark transition (purple). The MSD curves are offset for clarity, and the temperature correspondence was fitted to the experimental results from Fig. 4.12 a)-c). The figure is adapted from[97].

decreases for increasing PNC cube size, from 18 meV for the smallest PNC cube size to only 2 meV for the largest PNC cubes.[35–37] This small energy splitting inevitably affects the density of bright excitons for later times. The initial depopulation of the bright states via the BGT is slightly temperature dependent, however, in the low-temperature regime it can be assumed to be constant and large, due to the large oscillator strength of the bright excitons. For PNC cubes with small bright-dark splitting energies, the DBT can repopulate the bright state, and the exciton diffusion can be maintained. The exciton diffusion processes are depicted in the schematic Fig. 4.13 c). Excitons populating a dark state (PNCs denoted by a D) cannot hop to adjacent PNC cubes since their FRET rate is too low.[42] However, they can recombine radiatively with a long PL lifetime or be excited to the bright exciton state (blue PNCs denoted by a B).[44] The bright exciton states can transfer their energy to adjacent PNCs, similar to the model used in previous sections. As mentioned above, two fundamentally different exciton species are considered, not only by their differing PL lifetimes but also their different FRET rates. Here, the easiest possible FRET rate combination is implemented. The dark FRET rate is zero, and the bright

FRET rate is finite. Of course, this model can be changed to include two finite FRET rates where the dark one deviates from zero. If the FRET transfer rate of the dark states is not zero, an increasing MSD behavior should be observable for later times, with a less pronounced slope than the early time evolution. Additionally, the small but allowed dark-to-dark FRET lead to a MSD behavior that does not end up at the initial MSD value at longer times. A finite transfer between the dark excitonic states of adjacent PNC will be discussed for smaller PNC types like PNPLs.

The depicted model in Fig. 4.13 a),c) is tackled by a Monte Carlo simulation where the increasing temperature is taken into account by successively increasing the DBT rate whereas all other rates are kept constant (see Tab. 3.2). The resulting MSD curves are presented in Fig. 4.13 d) where the lowest MSD data curve (black dots) corresponds to zero DBT rate which is comparable to the behavior of the MSD curve at the lowest temperature. For this low-temperature simulation, the initial MSD time evolution is similar to the already obtained MSD curve behavior for a simpler simulated model, i.e., only one exciton species is present. However, there are two-time regimes, one where the MSD increases for evolving time and one where it decreases. Those time domains are separated by an intermediate time range, where the MSD reaches a maximum. If the DBT rate is successively increased, the MSD curve changes. The MSD maximum position shifts to later times for increasing DBT rate. This increase of the DBT rate results from increasing the system temperature. A direct consequence of this change is that the time domains with different diffusion behavior change. The initial time regime, where normal (sub) diffusion is present, gets longer, whereas the time domain where the MSD decrease is present shrinks. Besides the changing time domains, the clear visibility of the decreasing MSD values at later times (the compression) gets lost for increasing temperature, i.e., for large enough DBT rates, the final MSD value does not end up at zero like for the extreme case of $r_{DBT} = 0$ it seems to converge to a finite constant which also increases with increasing temperature.

By comparing the MSD curves resulting from the simulations Fig. 4.13 d) with the actual low-temperature MSD curves derived from the exciton diffusion measurements in the PNC SLs Fig. 4.12 a,b) the qualitative similarity is visible. Thus, the introduced bright-dark exciton model reflects the low-temperature MSD behavior for the smaller PNC cubes, i.e., 5 nm and 8 nm. However, it does not recover the trend of the 14 nm PNC cube system. The 14 nm PNC cube film shows a MSD behavior captured by taking only one exciton species into account like it was done for exciton diffusion measurements at room temperature discussed in Sec. 4.1.1.2. These MSD trends can be understood by the simpler normal or subdiffusion picture without visible negative diffusion.

It was already mentioned that the different PNC sizes lead to different bright-dark splitting energies (compare Fig. 4.13 b)). As the system temperature cannot be set to values below 9 K, one has to compare this value with the splitting energy. The splitting energy of the 14 nm PNC cubes (1.5 meV) is far closer to 9 K (0.78 meV) than for the other samples. Since the dark state hosts long living excitons compared to the bright states, the possibility for thermal activation of an exciton (Bose-Einstein distributed) from the dark to the bright state is high. The interaction time between the exciton density occupying the dark state with phonons is long. Thus, the possibility of bright exciton state repopulation via feeding by excitons that occupy a dark state is lifted.

Therefore, for such temperatures, the bright-dark splitting of 14 nm PNC cubes does not impact the exciton diffusion process like for systems with larger bright-dark splitting. Although the lifetime of excitons in the dark state is also quite high for PNC cubes with larger splitting energy, the phonon distribution at those larger splitting energies is exponentially suppressed and outperforms the larger lifetime. Therefore, the preferred depopulation channel for such systems is via the dipole-forbidden

radiative transition to the ground state. Note that for the 14 nm PNC cube film, the diffusion is hampered since the dark states can be seen as shallow traps, where excitons rest for a finite time until they get excited to the bright states and can transfer their energy to adjacent PNC cubes. This delay decreases the absolute MSD values, resulting in an overall lower diffusivity as discussed in Sec. 4.1.1.3. However, the detectable MSD curve is visible longer since the rapidly depopulated bright excitonic level is fed by the dark state excitons, which can than transfer to adjacent PNCs leading to a longer visible MSD trend.

The PL decays of all PNC cube samples are under closer investigation for the low-temperature regime to support the above-stated bright-dark exciton model further. For instance, in Fig. 4.14 a) the PL decay curves at low temperatures are depicted on a log-log scale for all three samples. This unusual representation has a significant advantage over the usual semi-logarithmic presentation, as different time regimes, which differ by several orders of magnitude, become more pronounced. For example, the 14 nm PNC cube sample PL decay curve at 9 K shows two major characteristics: Within the first nanosecond, the PL decay is of (mono)exponential nature which strongly suggests an excitonic PL decay channel. The second time domain, from 2 - 100 ns, deviates from an exponential PL decay. According to the fit (dark green straight line), the functionality is captured by a power law $I = t^{-\beta}$. A PL decay following a power law is not excitonic, it can result from delayed fluorescence, as it was previously discovered for $CsPbBr_3$ nanocrystals.[101] They explained the delayed fluorescence with an extended trapping model, containing single and double trap states and biexciton states, which can also be trapped. Note that the exponent resulting from the fits (≈ 1.5) is two times higher than measured by Becker et al. (≈ 0.7) although they measured PNC cubes of comparable size (6 nm) to the smallest PNC cubes discussed here.

By turning our attention to the smaller PNC samples, i.e., the 5 nm and 8 nm, at 30 K, one observes a similar PL decay behavior for the early time PL decay as for the 14 nm PNC cubes, however, for later times, the PL decay curves deviate from a power law, especially for the 5 nm PNC cube sample. For the smallest PNC cubes, the time range from 3 - 100 ns is also dominated by an exponential PL decay allowing the same interpretation as before, i.e., there exists a level where a monomolecular radiative recombination is possible. However, the second exponential PL decay rate is around two orders smaller than the fast PL decay rate. Radiative excitonic trap-assisted recombination can result in such PL decay behavior, which has longer PL decay times as the excitonic PL decays in such samples.[102,103] However, as will be explained below, some traps must be thermally activated, which seems to be the case in such structures and will result in a low trap density at low temperatures.[104] Besides the trap-assisted radiative recombination, the second exponential PL decay can also stem from an excitonic level which has a far lower radiative recombination rate than the recombination rate leading to the early time intensity behavior. This description fits quite well to the previously introduced dark states, whose radiative recombination to the ground state is dipole forbidden and so suppressed. However, if higher order interaction terms are considered, a radiative decay can still occur.

The fact that two excitonic levels, i.e., bright and dark states, are energetically separated gets even more concise by comparing the PL decay traces for different temperatures for the same PNC sample as presented in Fig. 4.14 b) for the 5 nm PNC SL. The two time regimes, where two mono-exponential PL decays are visible, are most apparent for 9 K. If the temperature is raised, the time domains change, as well as the qualitative PL decay for later times. Particular interest arises by following the temperature-dependent evolution of the PL decay tail. Departing from a mono-exponential PL decay behavior, it becomes more and more like a power law for higher temperatures. At elaborated temperatures, more

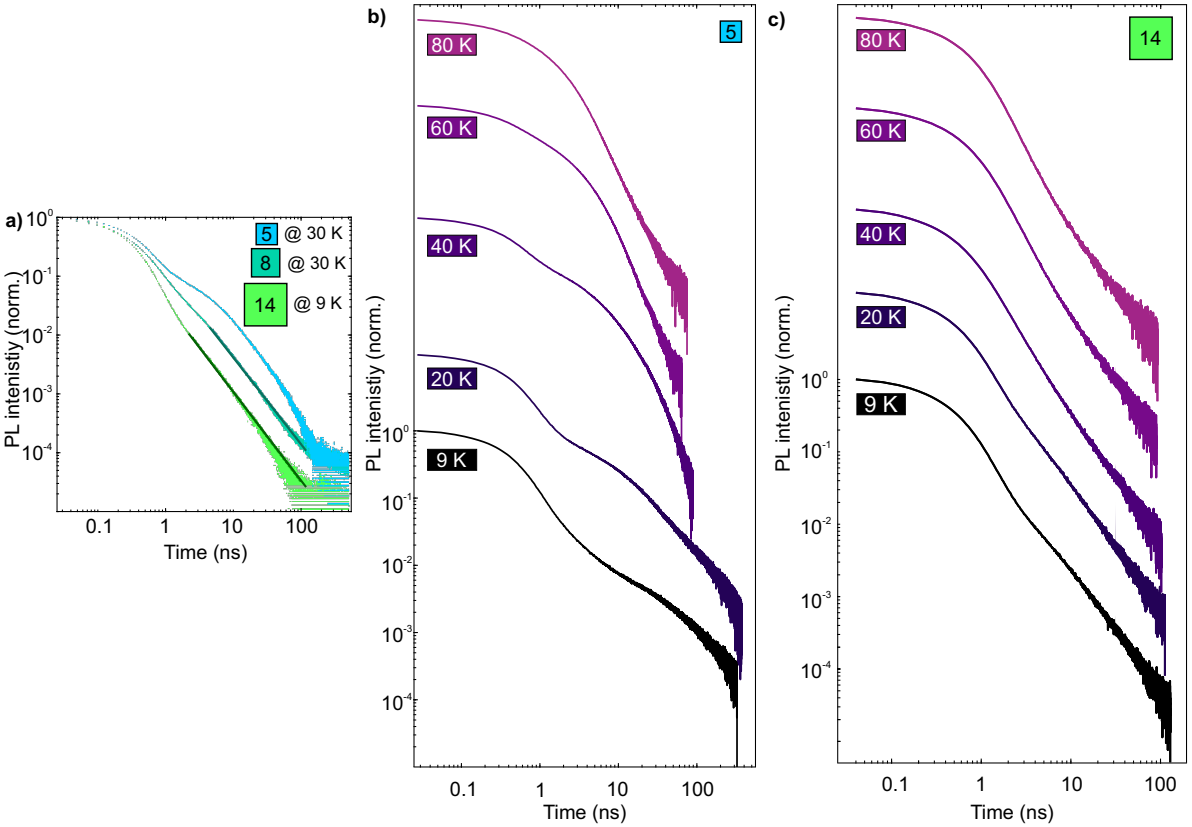

Figure 4.14: a) depicts the low-temperature PL decays for the 5 nm PNC SL (blue), 8 nm PNC SL (turquoise), and 14 nm (green) PNC cube samples displayed in a log-log scale. The lines correspond to power law fits of the PL decay signal for the 8 nm and 14 nm PNC cube samples. The other two panels show PL decay curves for the b) 5 nm PNC SL and c) 14 nm PNC cube film for different temperatures in the low-temperature regime, i.e., 9 - 80 K. The PL decay curves are offset for clarity. The figure is adapted from[97].

and more excitons that occupy the dark excitonic level can be transferred via phonon scattering to the bright level, where they can decay fast by a radiative PL decay to the ground state. Thus, this depopulation pathway is eventually faster than the direct (radiative) dipole-forbidden PL decay of the dark state to the ground state. Finally, the later time-domain PL decay is governed by a power law, for instance, due to delayed fluorescence, since the bright-dark splitting is not resolvable anymore at high temperatures.[44,45,49]

By turning our attention to the temperature-dependent, PL decay traces for the 14 nm PNC cubes presented in Fig. 4.14 c) it becomes clear, that even at the lowest measured temperature, no mono-exponential PL decay for later times is detectable. Only a power-law like shape of the PL decay curve is present for later times, and this behavior does not change if the sample temperature is increased. Thus, the later time domain does not result from a monomolecular recombination process like (dark state) exciton recombination. Note that for further decreasing temperature, below 9 K, the 14 nm disordered PNC cube film should show the same MSD trends as the smaller-sized PNC cube films at low temperatures. At a sufficiently low temperature, the bright-dark energy splitting of the 14 nm PNC cubes becomes far larger than the thermal energy. This will significantly reduce the DBT prohibiting, the bright states from being populated from the dark state level. The later time domain is again governed by the radiative PL decay channel of the dark exciton state.

Due to the close investigation of the PL decay traces within the low-temperature range, the model considering separated bright-dark exciton levels, which reproduce the negative MSD expansion, is justified. This, in return, allows a more comprehensive interpretation of the MSD evolution: There are

strongly diffusive and rapidly decaying bright excitons at early times (0 - 2 ns) for this low-temperature regime, explaining the steep initial increase of the MSD values. As the bright states are depopulated through radiative decay, the PL gradually contract. The dark states, which are the dominant exciton population at later times, are more localized in the center of the initial excitation because of dark level filling at earlier times from initial excitation (Gaussian distribution) as well as the early time filling from bright states. The dark excitons' slow radiative decay results in a PL profile which is narrower than the maximal expansion of the PL profile of the bright states. For temperatures where $k_BT \ll \Delta E_{BD}$, no dark exciton be thermally excited to the bright levels, and the dark excitons cannot diffuse via a two-step process of populating a bright exciton level followed by a FRET transition to an adjacent PNC cube consequently the MSD decreases to zero. Thus, at such low temperatures where the bright-dark splitting is much larger than the thermal energy, one has to consider two exciton species.

Since exciton diffusion is investigated at temperatures where effects like superflourescence, which can affect exciton transport, are possible,[36] we spend some time discussing those. Superfluorescence

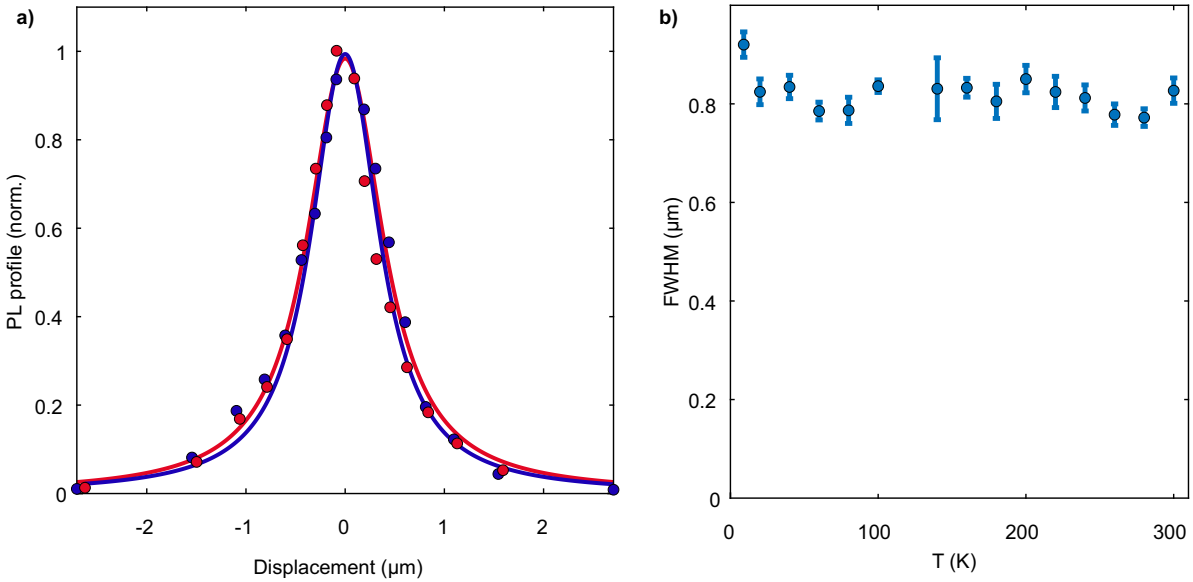

Figure 4.15: a) shows the initial PL profiles for 9 K (blue dots) and 290 K (red dots) right after excitation and corresponding Voigt fits for a 5 nm PNC SL (blue and red curve). b) presents the FWHMs for all measured temperatures of the 5 nm PNC SL. The figure is adapted from[97].

arises if several excitons couple together, decreasing the PL lifetime of this coupled state, which is energetically lower lying compared to the uncoupled system. Such a coupled state can also result in a rapidly broadened PL profile at very short times since superfluorescence appears only in the sub-nanosecond time regime. The coupled state is delocalized, i.e., more PNCs are hosts of this state. Thus, it is worthwhile to not only investigate the MSD values which were intensely studied to this point, but also the absolute broadening of the PL profile right after excitation. For this reason, two PL profiles are depicted in Fig. 4.15 a) where the dots correspond to the actual data and the lines are Voigt profile fits. The PL profiles result from 5 nm PNC SL at 9 K (blue curve and dots) and 290 K (red curve/dots). It can be seen that the profile widths immediately after excitation are identical and unaffected by the measurement temperature. The temporal resolution of the setup does not allow a temporal exciton transport interpretation for the initial sub-nanosecond regime, i.e., below 0.15 ns. However, the PL profiles depicted here can be understood as the early time steady state initial broadening, including all transport mechanisms that happen on a picosecond time scale. Since both

PL profiles have the same FWHM, those novel effects which appear only at low temperatures are not present within the investigated films and for the used measurement conditions. In addition to the two initial PL profiles at the two extreme temperatures, Fig. 4.15 b) shows the FWHM of exciton diffusion measurements for a 5 nm PNC SL over the whole investigated temperature range. The initial PL profile width is independent of temperature.

For additional insight into the exciton fine structure within the investigated samples, we investigated

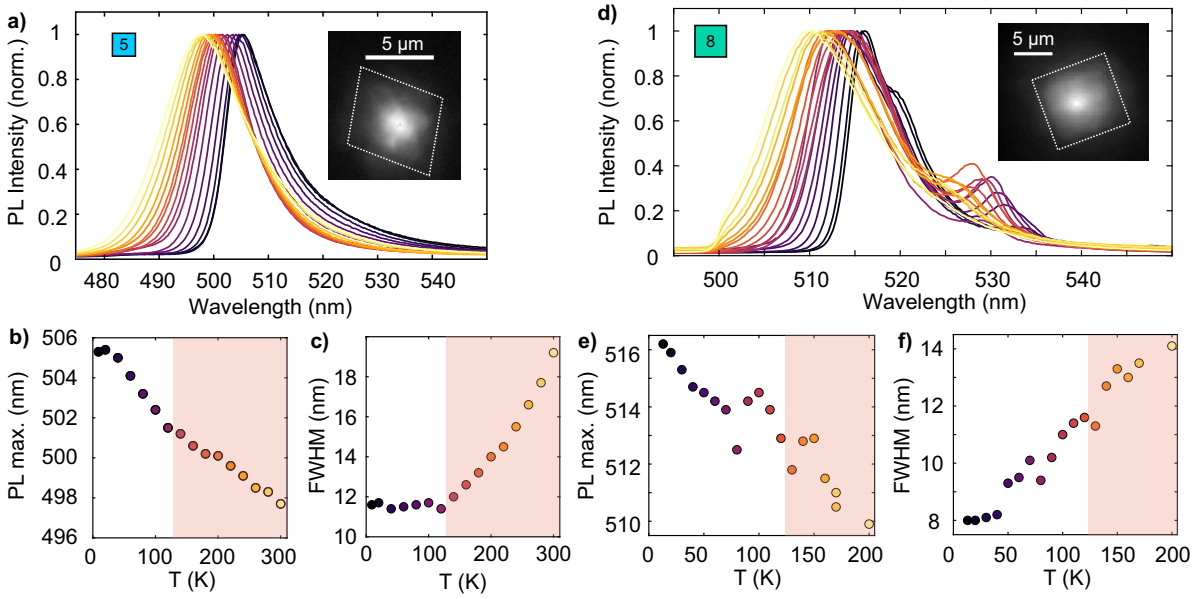

Figure 4.16: a) shows PL spectra from 9 K (black line) to 290 K (yellow line) for a 5 nm PNC SL sample. The inset depicts a steady-state PL image of the SL. b) depicts the PL maximum position and c) the FWHM of the PL spectra against temperature. d) illustrates PL spectra from 9 K (black line) to 200 K (yellow line) for an 8 nm PNC SL. The inset depicts a steady-state PL image of the SL. e) depicts the PL maximum position and f) the FWHM of the PL spectra against temperature.

the PL spectra particularly at low temperatures, as the reduced thermal broadening offers a better view of individual states. In Fig. 4.16 a) the steady state PL spectra for the 5 nm PNC SL are depicted from 9 K (black line) to 300 K (yellow line). For low temperatures, the PL spectra have an asymmetry to lower energies, which could be explained by shallow trap states or by the aforementioned bright-dark model. However, shallow traps can be out-ruled at such temperatures since they require thermal activation energy. Accordingly, we ascribe the asymmetry to the presence of the dark exciton, which cannot be resolved as a separate peak due to thermal broadening of the ensemble emission and the small bright-dark splitting energy. The PL spectra show a blue shift for increasing temperatures, which is more easily traced by following the PL peak positions as presented in Fig. 4.16 b). The red shaded area concerns the temperature range which will be discussed in the high-temperature section 4.3.2.1. The corresponding FWHMs of the PL spectra are plotted in Fig. 4.16 c) against temperature. Within the low-temperature range, i.e., between 9 K- 120 K, the FWHM seems to be constant. However, by taking a closer look at the PL spectra, one can see that the asymmetry present at low temperatures is lost for higher temperatures. This, in turn, results in a constant FWHM within this temperature range as the increasing symmetry compensates the larger thermal broadening of this PNC system.[68]

The 8 nm PNC SL PL temperature-dependent spectra, in contrast, exhibit two peaks visible in Fig. 4.16 d). There are almost always two peaks for all temperatures, i.e., 9 K (black line) to 200 K (yellow line), and for low temperatures, the high energy peak has a red shoulder. Raino et al. associates the appearing low energy peak with a coupled exciton state, i.e., coupled individual excitonic states where the

coupled state has lower energy. They investigated this appearing coupled state at 5 K. We can resolve this low laying state even at 200 K, which has 20 % PL intensity of the PL maximum intensity. However, the suggested coupled state exists only at low temperatures, thus, it cannot explain the peak observed here.[36] Additionally, we do not detect sub-picosecond fast exciton diffusion of the 8 nm PNC SL sample, which would be expected due to this exciton delocalization effect. The initial PL profile width of the 5 nm and 8 nm PNC SLs are the same. The low energy PL peak positions are comparable to the bulk $CsPbBr_3$ PL peak positions. Hence, we assume that the low energy PL peaks result from larger cubes at the SL surface, which are in the weak confinement regime. Those larger PNC cubes are only present at the surface since, due to the SL formation, only equally sized PNC cubes are incorporated into the system. Cubes that are too large diffuse to the periphery of the SL. The difference between 5 nm PNC SLs and 8 nm PNC SLs becomes more apparent by looking at SEM images. For the 5 nm PNC SL, the surface is very homogeneous, i.e., it consists only of the 5 nm PNC cubes. For the 8 nm PNC SL, larger structures assemble at the surface of the SL (Fig. 4.9 a),b)).

Since we expect those larger PNC cubes to be only at the SL surface, they do not influence the exciton diffusion within the PNC SL. They can serve as 'fast radiative trap' states since their PL emission and absorption is energetically lower than the 8 nm PNC SL PL emission. Fast means, in this context, a rather large radiative PL decay rate, thus, we can outrule those PNC cubes to be responsible for the novel MSD behavior we observe. The insets of Fig. 4.16 show the steady state PL images of the respective excited PNC SLs. The dashed white lines indicate the SL size and orientation. The pulsed laser excitation was managed to be right at the SL center, thus, SL boundary effects do not influence the exciton diffusion.

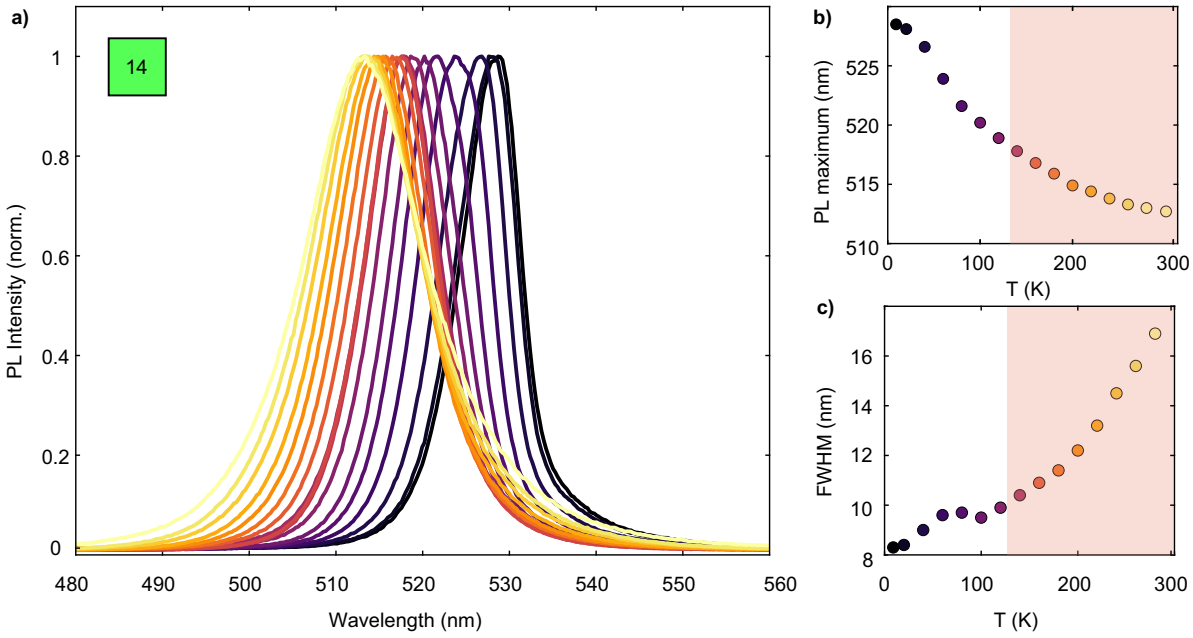

Figure 4.17: a) shows temperature-dependent PL spectra for an unordered 14 nm PNC cube film from 9 - 290 K (black to yellow). b) presents the PL maximum position temperature trend. c) represents the PL spectra FWHM behavior for the screened temperature range.

In Fig. 4.17 a) the PL spectra for the 14 nm PNC cube film in the temperature range from 9 K (black line) to 290 K (yellow line) are depicted. Interestingly, the symmetric nature of the PL spectra is nearly temperature independent, i.e., even at 9 K, the PL spectrum has a symmetric shape. For those large PNC cubes, a relatively small bright-dark splitting can be expected of around 2.5 meV. Thus, even

if the dark state is emissive and contributes to the total PL of the sample, the asymmetry should be smaller compared to the samples with larger bright-dark splitting. The larger degree of symmetry of the PL spectra for the 14 nm PNC cube film also strengthens the hypothesis that at low temperatures dark states are responsible for the asymmetry in the smaller PNC SL systems. Thus, the conclusion that the energetically low dark states are accountable for the negative MSD trends at low temperatures is justified. The maxima and FWHM of the PL spectra are shown in Fig. 4.17 b),c). We can see the common PL spectrum blue shift with increasing temperature. The FWHM of the PL spectra increases due to thermal broadening with temperature.
For a more comprehensive spectroscopic characterization, we measured ten different samples at 9 K, thus we can deduce whether SL heterogeneity plays a significant role within the samples. In Fig. 4.18

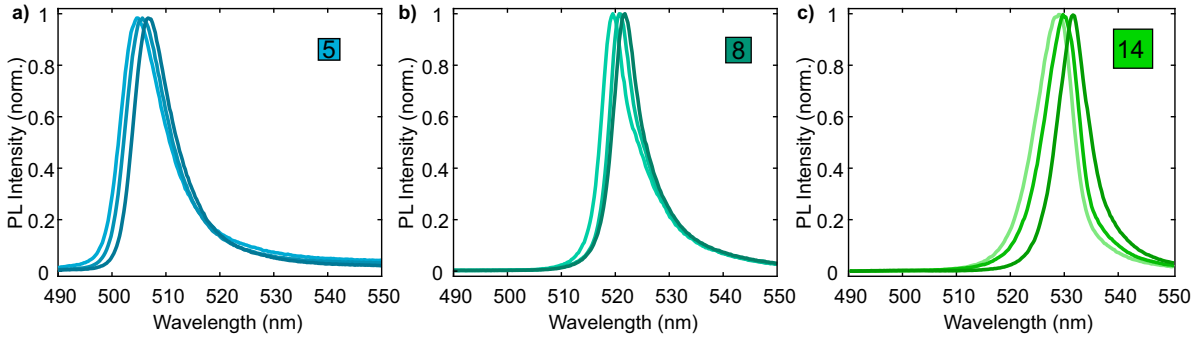

Figure 4.18: The figure presents PL spectra of three different a) 5 nm PNC cube SLs, b) 8 nm PNC cube SLs, and c) 14 nm PNC cube films at 9 K. The bright to dark color serves to distinguish the individual spectra. The figure is adapted from[97].

the PL spectra at 9 K for different SL or PNC film samples are depicted. Panel a) shows exemplary PL spectra for three different 5 nm PNC SLs, b) for the 8 nm PNC SLs, and c) for the 14 nm PNC cube film. Here we state the average peak position $\lambda_{max,5\ nm} = 505.9 \pm 1.4$ nm and the corresponding linewidth $FWHM_{5\ nm} = 10.7 \pm 1.1$ nm. For the 8 nm PNC SLs, the peak position is shifted to lower energies $\lambda_{max,8\ nm} = 522.1 \pm 2.3$ nm with a linewidth of $FWHM_{8\ nm} = 8.5 \pm 1.5$ nm. The 14 nm PNC cube film low-temperature spectrum position is even more red-shifted to $\lambda_{max,14\ nm} = 530.9 \pm 1.4$ nm and narrower than the other two spectra $FWHM_{14\ nm} = 7.1 \pm 0.9$ nm.
The PL peak position heterogeneity seems to be larger in PNC SLs than in the 14 nm PNC cube film. The individual PNC SLs consist of PNCs of the same size, however, the small PNC size deviations within the PNC dispersion prior the PNC SL formation shows PNC size deviations. The individual PNC SL may consist of very similar PNC sizes, however their can be a discrepancy between the individual PNC SLs. The film consisting of the 14 nm PNC cube film, however, is not as size selective as the PNC SL formation process. Thus, different PL spectra of distinct spots within the same film can have indeed a smaller PL peak position variance. The PL spectrum width is also more prominent in smaller PNCs which was discussed within the room temperature section (Sec. 4.1.1.2).
The natural question arises if the MSD compression is only present in cubic systems where the bright-dark energy splitting is high enough. Does this trend also occur in samples that deviate from the cubic PNC structure, i.e., PNPLs, where the bright-dark energy splitting is even higher? This will be discussed in the next section.

4.3.1.2 PNPLs

The previous section investigated the low-temperature MSD behavior of exciton diffusion in PNC cube assemblies. Here, we want to improve our understanding about low-temperature exciton diffusion performance in PNPL systems. These PNCs are more complicated compared to the PNC cubes concerning their excitonic energetic level ordering since anisotropy splits the bright excitonic triplet level into two sub-levels, one out-of-plane exciton (B^z) and two in-plane excitons (B^x and B^y) which was already introduced in Sec. 4.3.1.2. This splitting of the bright triplet states can become relevant for low temperatures in addition to the already introduced bright-dark splitting, which was the main topic of the previous section.

In Fig. 4.19 a) MSD curves of a 3 ML PNPL film for low temperatures (10 - 60 K) are shown. The data

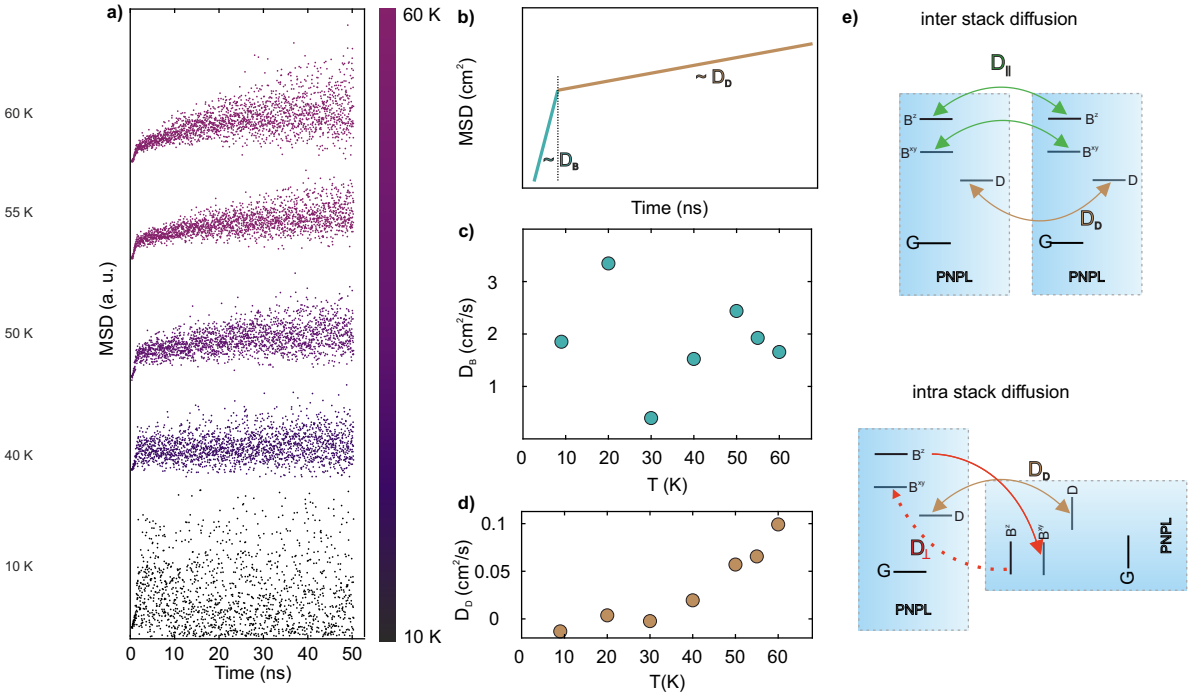

Figure 4.19: a) shows low temperature (10 - 60 K) MSD curves for a 3 ML PNPL film. b) illustrates schematic of two separated time domains where linear MSD behavior is detectable. The MSD behavior for initial times is governed by a fast diffusion of the bright excitons D_B followed by the dark state exciton transport D_D. c) presents the bright exciton diffusivities extracted from the initial MSD slopes against temperature. d) shows the dark exciton diffusivities originate from the later MSD slopes for the covered low-temperature range. e) depicts transfer schematics of excitons to adjacent PNPLs. Two structures arise: inter-stack diffusion across parallel aligned PNPLs (upper panel) and intra-stack exciton transfer across perpendicular oriented PNPLs (lower panel).

points at the bottom represent the MSD values for the lowest applied temperature 10 K (black data points). The other MSD values for the temperatures up to 60 K are offset for clarity (dark purple to purple). For the lowest temperature, there is an initial rise of the MSD value, as already seen before for the PNC cube assembly at low temperatures, which was assigned to fast bright exciton transfer. However, in contrast to the cubic systems, there is no downward trend of the MSD signal detectable. For instance, the MSD values for a system at 10 K at later times have such a large spread that a subsequent MSD decrease is barely visible. For temperatures higher than 10 K, e.g., 20 K, the negative MSD evolution after reaching a maximum is missing. Furthermore, the MSD trend seems to be separated into two time domains (as for the PNC cube systems), one initial fast MSD evolution (a large increase of the MSD values) followed by a second linear MSD increase, however, with a slope

which is smaller than the initial fast increase. The linearity of the long term MSD evolution smears out at elaborated temperatures visible for the 60 K MSD curve in comparison to the 20 K MSD long term trend. This will be discussed in the section where PNPLs exciton diffusion at higher temperatures is investigated. Note that the slow MSD expansions hold on up to 50 ns, whereas the bright exciton PL lifetime is around one ns. Thus, the slow-expanding MSD values have to originate from either excitons, stored in the dark state and which are indirectly transferred to an adjacent PNC via a bright state hop, or the dark exciton undergoes a dark-to-dark state energy transfer. The indirect transfer via the bright state should be very unlikely since the bright-dark exciton splitting in 3 ML PNPL is 20 meV, thus, hardly reachable for low temperatures. Note that until now, it was always assumed that dark exciton states are not allowed to diffuse. This perspective is changed here since the missing apparent negative diffusion at low temperatures suggest a finite transfer rate between dark excitonic states. The small center-to-center distance of PNPLs might cause the dark exciton FRET to become relevant (see discussion in Sec. 4.1.2).

The two distinct time domains are depicted in Fig. 4.19 b), where the slope of the initial time is connected to the bright exciton diffusion (green D_B) and the second time domain (with a smaller slope) to the dark exciton diffusivity (brown D_D). In Fig. 4.19 c),d) the actual bright and dark diffusivities extracted from linear fits of the MSD curves of Fig. 4.19 a) are shown. The bright exciton diffusivity exhibits large variations and there is no obvious temperature-dependence. The deviations could be a result of the short fitting range. As the bright exciton diffusion is visible only in the first two ns at low temperatures, thus, there are only a few data points available for the fit. The temperature independence of the bright exciton diffusivity is in sharp contrast to the evolution of the dark exciton diffusivity. This later value increases from nearly zero to 0.1 cm^2/s from 10 K to 60 K, showing a clear temperature dependence. This may be the first hint that the dark-to-dark FRET transitions are phonon-assisted.

In Fig. 4.19 e) the transfer channels of adjacent PNPLs are depicted which were already shown in Sec. 4.3.1.2, however, at low temperatures the splitting between the bright states also has to be considered. Two main PNPL arrangements are possible: the PNPLs stack together on their large facets, which is depicted in the upper panel. The bright exciton triplet states can represent two inplane excitons $B^{x,y}$ and one out-of-plane exciton B^z. If the platelets stack on their larger facet, there is no FRET transition possible between the $B^{x,y}$ to B^z since those states are perpendicular to each other. However, $B^{x,y}$ and the $B^{x,y}$ and B^z to B^z are allowed, and those transitions are depicted with green arrows. The dark-to-dark exciton transition is depicted via a brown arrow, and this transition has been neglected so far for other systems. In principle all those transitions happen at the same energy level if the dispersity of the PNPLs sample is not considered. For FRET transitions between parallel PNPLs, no energetic downhill migration happens. However, by considering that the dipole allowed FRET transitions are energetically downhill, as depicted in Fig. 4.19 e) the inter-stack transition between vertical PNPLs is more likely to occur once the initial exciton density gradient has been resolved. Hence, the exciton density gradient across different stacks is not resolved as fast as along stacks or may not resolve at all.

After discussing exciton transport in films and SLs consisting of PNC cubes and PNPLs at low temperatures, we will progress by investigating diffusion at higher temperatures, i.e., temperatures where the bright-dark splitting of the excitonic levels becomes irrelevant.

4.3.2 High Temperature Performance

In the previous section, exciton diffusion in the low temperature regime (10 - 100 K) was investigated. Some attempts were made to explain the MSD trends. This section is devoted to a paradigm change in temperatures within the hereafter called high-temperature regime. Namely, it deals with the downward trend of the MSD curves for increasing temperature, which has not been discovered in NC systems until now. The PNC sizes and shapes are as previously separately discussed, i.e., different-sized PNC cubes in SLs or disordered films and PNPL ensembles.

4.3.2.1 PNC Cube Ensembles

Here we will discuss the exciton diffusion behavior for PNC cube SLs comprising 5 nm and 8 nm cubes, and 14 nm PNC cube films at temperatures between 120 - 280 K. Fig. 4.20 a) depicts the MSD temporal

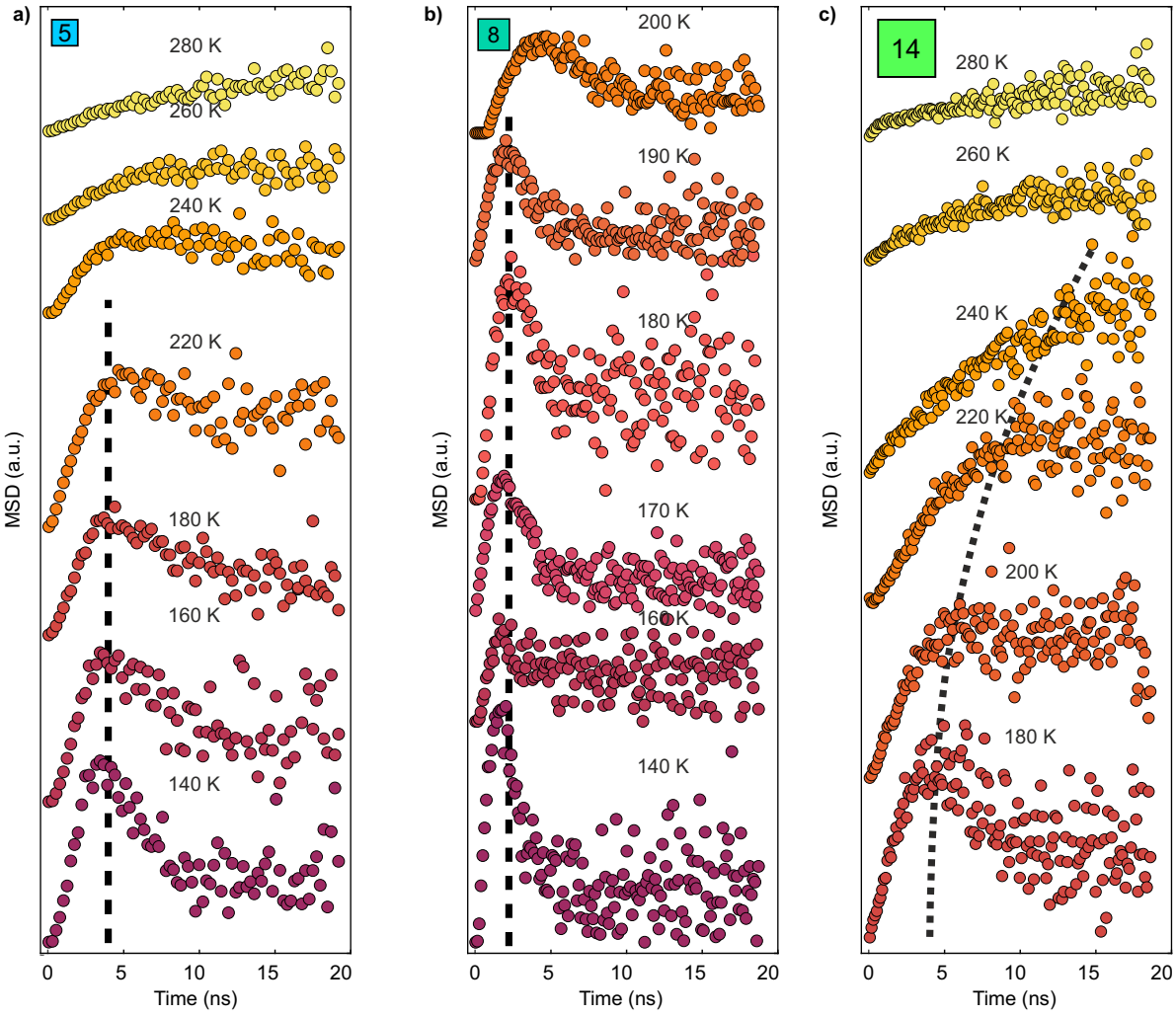

Figure 4.20: The figure presents MSD temporal evolution for all investigated PNC cube systems within the high-temperature regime. a) shows the MSD trends measured in a 5 nm PNC SL from 140 - 280 K. b) depicts the MSD behavior of a 8 nm PNC SL from 140 - 200 K. c) represents the MSD curves for a 14 nm PNC cube unordered film from 140 - 280 K. The three dashed lines are guides to the eye, highlighting the time the MSD maxima appears.

trends for the 5 nm PNC SL sample for various temperatures. The applied temperature range starts from 140 K (bottom panel, purple dots) to 280 K (top panel, yellow dots). For the lowest temperature

(140 K), the MSD initially rises to a maximum at four ns, decreasing subsequently. This MSD behavior is qualitatively the same as for the 5 nm PNC SLs at 10 K. However, the maximum, indicated by the dashed vertical line (appears later), has a fundamentally different origin for low temperatures, which will be discussed below. At higher temperatures 160 - 220 K, the MSD curves show the same behavior as for 140 K, i.e., a maximum appears, and the MSD decreases for later times. The maximum position and the absolute MSD values are temperature independent for those temperatures. However, the MSD decreases at a lower rate for higher temperatures after four ns. Furthermore, the PL profile compression ends before the MSD becomes zero. The MSD reaches a constant, e.g., at 140 K after ten ns. This constant MSD value increases for increasing temperature. By increasing the temperature even further, up to 240 K and above, the constant MSD value is the same as the MSD maximum value. Therefore, there is no clear distinction possible anymore. At 280 K, the MSD trend recovers the room temperature behavior which was already discussed above. Note that the depicted period is 20 ns, suggesting that only very few excitons are left at later times due to the fast radiative recombination of the bright excitons and the temperature-enhanced depopulation of the dark exciton states.
The MSD trends for the 8 nm PNC SLs look quite similar to the 5 nm PNC SLs (Fig. 4.20 b)). The maximum appears even earlier than for the smaller system, i.e., at 2.5 ns at 140 K. The maximum position is constant with temperature until 190 K. For higher temperatures, the MSD compression gets weaker, as for the smaller PNC SL system. The MSD trend for 200 K shows a shifted maximum which appears at later times. Unfortunately, we can present only MSD curves for 8 nm PNC SL systems up to 200 K. Therefore, we are not able to observe MSD trends where the MSD compression is absent eventually. The MSD trends for the largest (14 nm) PNC cube system (Fig. 4.20 c)) show similar behavior as the smaller systems. However, the maximum appears at higher temperature, and the maximum position exhibits a much more prominent shift to later times for higher temperatures. The MSD maximum positions are detectable up to 220 K and the shift is indicated by the dashed line.
Fig. 4.21 a) shows seven normalized PL profiles (green data points) with their corresponding Voigt profiles (green lines) from 0 - 20 ns (solid to transparent) for the 14 nm PNC cube sample measured at 140 K. The PL profiles fit exceptionally well to the actual normalized PL data points, which can be seen for the lowest depicted PL Voigt profile fit (solid green), corresponding to the initial PL profile. For $t > 0$ the system's total amount of excited states decreases due to the exponential PL decay with a PL lifetime of around one ns or below. However, at those late times, the PL profile data points also fit pretty well to a Voigt profile. Even at the latest time presented here, i.e., 20 ns, there are still radiative states left, which emit photons summing up in the PL data points at the upper position in the panel. The difference in FWHM of the PL profiles at zero ns and 20 ns is visible in Fig. 4.21 b). The two PL profiles are offset along the y-axis for clarity and have similar FWHM, i.e., reflecting that the MSD becomes nearly zero at later times. Even more impressive is the normalized Voigt profile PL evolution over all time steps from 0 - 20 ns presented in Fig. 4.21 c). The broadest PL profile is visible at 3 - 4 ns followed by profiles with decreasing width back down to the initial value. The early time evolution has a normal trend, i.e., increasing FWHM with time.
A direct comparison of the MSD trends for different-sized PNC cubes, i.e., 5 nm PNC SL (turquoise data points), 8 nm PNC SL (blue data points), and 14 nm PNC cubes (green data points), is depicted in Fig. 4.22 a) for 140 K. The absolute MSD values are size dependent, i.e., larger absolute MSD values for larger PNC cube sizes, which will be discussed in more detail by considering the averaged diffusivities in Sec. 4.3.3. The MSD trends have increasing and decreasing characteristics, as already seen for low temperatures in Sec. 4.3.1.1. The time where the maximum appears is comparable. This changes if

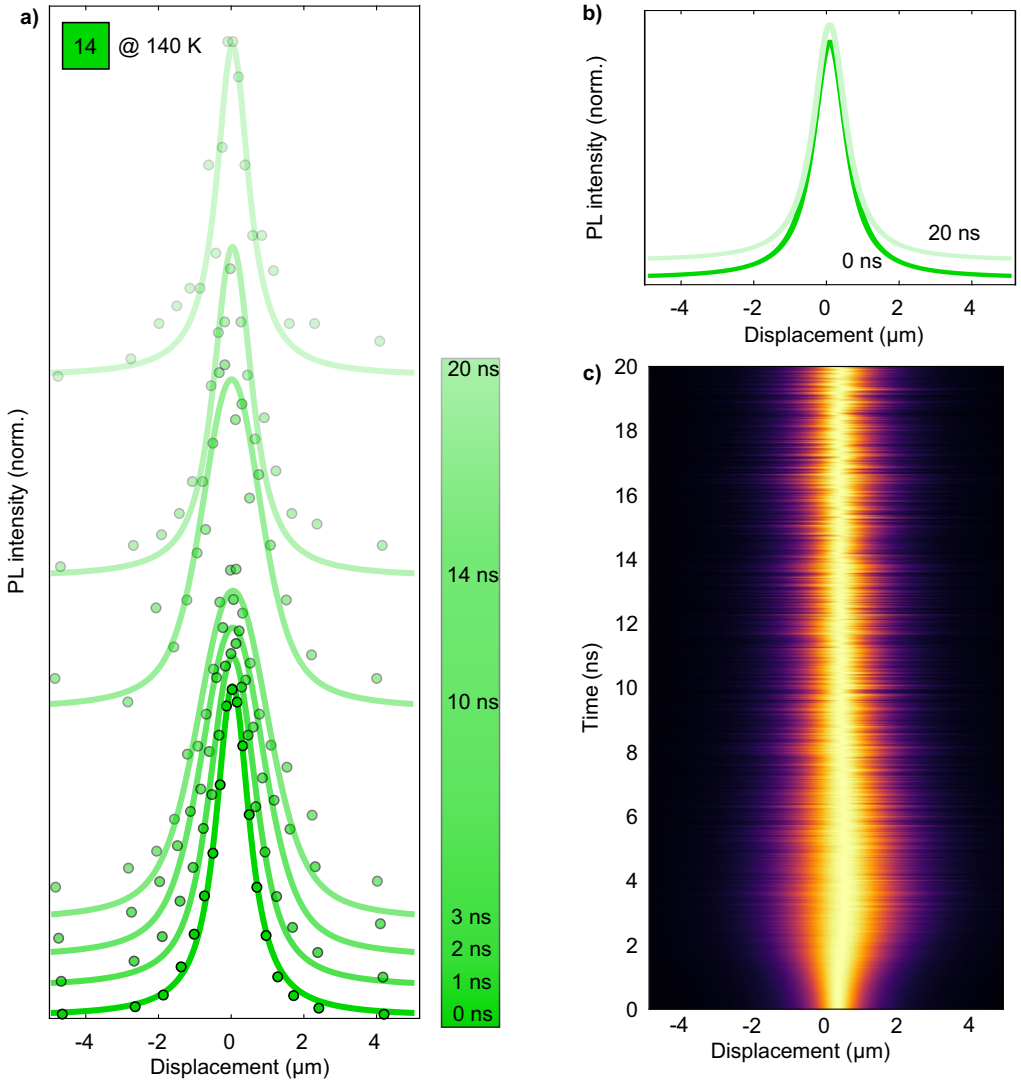

Figure 4.21: a) shows normalized PL profile data (green dots) and corresponding Voigt profiles (green lines) for 0 - 20 ns measured in a film of 14 nm PNC cubes at 140 K. The profiles are offset along the y-axis according to the time when they were recorded. b) The initial (bold green) and latest (transparent green) PL Voigt profiles are depicted, offset for clarity. c) PL Voigt fit profile dynamics for all time steps. The figure is adapted from[97].

the temperature is raised to 220 K. There, the MSD peaks at different times for different-sized PNC cube systems, which is depicted in Fig. 4.22 b). The maximum for the 14 nm PNC cube film is hardly visible and appears at times later than ten ns, whereas the maximum for the smaller PNC cubes appears earlier. The MSD maximum is better visible compared to the larger PNC system. The actual maximum position for the high-temperature regime, i.e., 100 - 220 K, for all PNC cube sizes is depicted in Fig. 4.22 c). There are two separate regions visible: 1) The temperature range (100 to 180 K) where the MSD maximum position is nearly constant for all PNC cubic systems. 2) The temperature range, where the MSD peak positions shift to later times for higher temperatures for the 14 nm PNC cube ensemble. This shift is most visible for the largest PNC cube systems (4 - 18 ns), whereas it is not present for the 5 nm PNC SL. For the 8 nm PNC SL there is only a slightly increase in t_{max} visible at 190 K from two ns to 5.5 ns at 210 K.

As noted before, the MSD decrease, accompanied by an appearing MSD maximum for all PNC systems investigated for temperatures from 140 - 240 K, has a fundamentally different origin than the already discussed MSD compression trend at low temperatures. There, the bright-dark exciton splitting

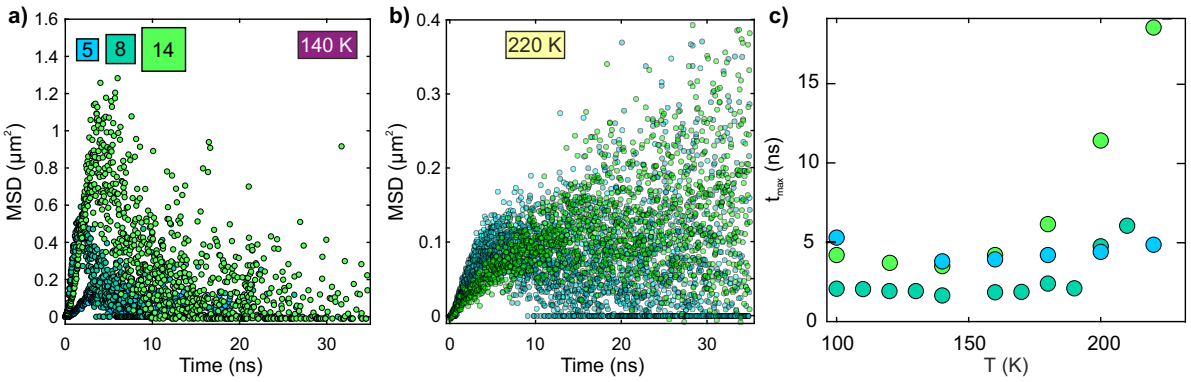

Figure 4.22: a) shows the MSD temporal evolution (0 - 35 ns) of all PNC cube systems 5 nm and 8 nm SL (blue and turquoise data points), and 14 nm unordered film (green data points) at 140 K. b) presents the MSD temporal evolution for all PNC cubic systems at 220 K (color scheme is the same as in a)). c) depicts the MSD maximum position against temperature for all investigated PNC cube samples, i.e., 5 nm SL (blue data points), 8 nm SL (turquoise data points), and 14 nm (green data points) unordered film (green data points). The figure is adapted from[97].

with the lower laying dark states is responsible for the MSD decrease at later times. However, the temperatures discussed in this section are so high that the bright-dark splitting energy cannot induce the MSD compression. Since, the bright state can be quickly populated via thermal activation of the dark state, the total exciton diffusion is still reduced.

We assume that the MSD compression results from deep radiative traps, residing several hundreds of meVs below the dark states. The corresponding energetic level of a single PNC cube is depicted in Fig. 4.23 a). The bright-dark exciton degeneracy can be neglected since the splitting energy is too low, yielding a four-fold degenerate excitonic level denoted by B/D in the schematics. The energetically lower lying state is a trap state (T), which can be populated from the excitonic level. However, a thermal activation back to the excitonic level is highly unlikely since the thermal energy is too low compared to the splitting between the deep trap state and the excitonic levels. Both states, the excitonic state and the trap state, can be depopulated via radiative or nonradiative recombination to the ground state. The recombination rate from the trap state to the ground state is far lower than the exciton radiative recombination rate (illustrated with the arrow thickness). The lower panel shows the interaction between PNC cubes, i.e., FRET transitions of excitons (red/blue colored circles) to adjacent PNC cubes depicted by yellow arrows. The excitation laser area is illustrated by the purple dashed circle (FWHM of the excitation source), whereas the green dashed circle depicts the steady-state PL emitted from the sample. The steady-state PL emission FWHM is generally larger than the excitation spot size since exciton diffusion does broaden the exciton distribution.

Fig. 4.23 b) depicts MSD temporal trends resulting from Monte Carlo simulations of the model presented in Fig. 4.23 a) where the trapping rate, i.e., the rate from the B/D level to the T level is varied. The MSD curves are offset for clarity. The largest trap rate results in an MSD behavior depicted by the dark purple data points. For decreasing trap rate, the MSD maximum shifts to later times, as visible from the other MSD trends in the panel. The horizontal black arrow denotes this shift. The evaluation of the maximum positions according to the simulated trap rate is presented in Fig. 4.23 c). There, starting from the highest applied trap rate of 2.5 %, t_{max} has the smallest value of around 35-time steps, and t_{max} shifts to later times as the trapping rate is reduced. This behavior sounds reasonable since, for a lower trap rate, more excitons survive in the B/D level where they can transfer to other PNC cubes. Once they get trapped, they can not diffuse anymore, and they can only recombine radiatively

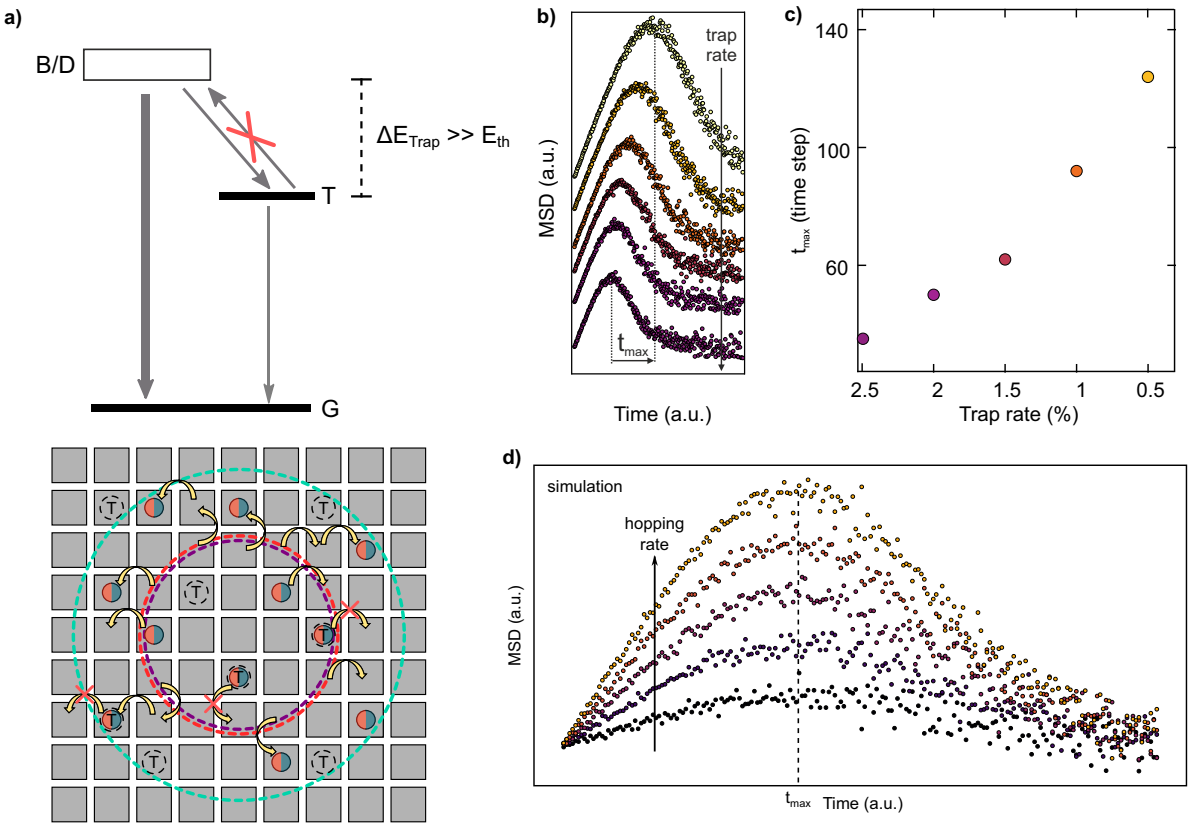

Figure 4.23: a) shows the energy level diagram of a single PNC cube at high temperatures. The bright-dark exciton level is degenerate, and a deep radiative trap state lies below them. All states have radiative recombination rates to the ground state. A transition from the trap to the exciton level is forbidden. However, states occupying the excitonic level can be trapped. The lower panel depicts interactions of excitons in a PNC ensemble. FRET transitions are allowed for excitons that are not trapped. b) presents the MSD behavior for simulated systems according to the model presented in a) with varying trap rates, i.e., large to low trap rates (purple to yellow data points). The two dashed lines show the MSD maximum for the largest and smallest trap rates and illustrate the temporal change of the MSD maximum. c) yields the occurring MSD maximum position in b) versus the trap rate. d) depicts the MSD trends for systems where the hopping rate varies from small to large values (black to yellow dots). The dashed line corresponds to the time when the MSD maximum appears. The figure is adapted from[97].

to reach the ground state. So normal diffusion occurs longer in a simulated system where the trap rate is low. By changing the PNC exciton trap rate one sees that the shifting to later times also happen for systems where the temperature is increased. Therefore, the increasing temperature can result in a decreasing trap rate, i.e., decreasing trap density of the investigated system. The MSD maximum position change is the largest in the largest PNC cubes. Thus, the changing temperature only affects the 14 nm PNC cube systems through a decreasing trap rate. For the smaller PNC cubes, the trap rate appears constant within the temperature region discussed here. The changing total trap rate can result from detrapping effects, which inevitably happen at high enough temperatures (note that detrapping events will happen even though they are not considered in the above-described model). Of course, this detrapping can also occur for the smaller PNC cubes. A trap depth size dependence in PNC cubes would explain the described phenomena. Suppose that for smaller PNC cubes the traps are deeper than for larger PNC cubes. This size dependent trap depth would explain the transient trend observed for the PNC cube sizes, i.e., the maximum shift is the largest for the largest PNC system. In contrast, no maximum changing position is detectable for the 5 nm PNC SL sample, whereas, for the 8 nm PNC SL sample, a small increasing MSD maximum position with increasing temperature is noticeable.
To exclude that other parameters are responsible for the shifting MSD maximum time, Fig. 4.23 d)

shows the MSD trends if the FRET hopping rate is changed. The absolute MSD values increase for increasing hopping rate since the excitons can diffuse further in a system with higher FRET rate. The larger hopping rate also manifests in a sharper increase of the MSD for early times. The slope of the temporal MSD evolution is directly connected to the diffusivity, which should be larger in a system with a higher FRET probability. However, the time when the MSD maximum appears is independent of the hopping rate. Even though the increase and decrease of the MSD values depend on the hopping rate, the point where the exciton distribution reaches its largest expansion is constant. The MSD behavior should also be independent of the radiative PL decay rates of the excitonic and trap states. The radiative rates only influence the signal-to-noise ratio of the MSD curves. The ratio of both radiative rates dictates the decreasing MSD behavior for later times, i.e., the steepness. The initial occupation of the states is assumed to be temperature independent, for early times, mainly the B/D state would be occupied over the whole screened temperature regime. Only after some finite time a significant amount of excitons are trapped where their PL contribution to the MSD outperform the part originating from the B/D excitonic level due to the fast depopulation of the B/D level (via trapping or recombination).

4.3.2.2 PNPLs

As we have seen for PNC cube systems, the exciton diffusion behavior at higher temperatures deviates from the low-temperature behavior, where the bright-dark exciton level splitting dictates exciton diffusion. Similar observations of the MSD trends can be made by turning our attention to 3 ML PNPL films visible in Fig. 4.24. The MSD curves are recorded from 40 - 180 K (dark purple to yellow data points) over a time-span of 100 ns. The fits correspond to a phenomenological model which combines subdiffusion and the trap model for two different time regimes. The low-temperature MSD curve, i.e., 40 K, was already shown when discussing the low-temperature MSD behavior for PNPLs. No MSD contraction happens up to 100 ns, and one sees two distinct time regimes with two separated diffusivities. Increasing the temperature further above 60 K, an MSD maximum appears, and MSD contraction begins. For a stepwise increase of the temperature, the MSD maximum appears at earlier times. The contraction reduces the MSD to its initial value. At 80 K this occurs after 50 ns. Surprisingly, this shifting of the MSD maximum position to earlier times for increasing temperature follows an opposite trend compared to the PNC cube systems where the appearing MSD maximum shifts to later times and disappears finally.
To explain the MSD behavior for increasing temperature within 3 ML PNPL films, one can consequently adapt the conclusions made for the PNC cube systems, i.e., deep radiative traps are responsible for the MSD contraction. Those deep radiative traps are thermally induced, thus, the trap density increases with increasing temperature. This explains why the MSD expansion terminates at early times. For an increasing amount of exciton trap states, the ratio between free and trapped excitons decreases and therefore the MSD contraction starts at earlier times.
The absolute MSD values also decrease for increasing temperatures above 80 K, visible in the left panel of Fig. 4.24. As the trap state density increases, excitons not only reach their maximum expansion at earlier times, they also do not reach MSD expansions like in undisturbed systems, i.e., where only a few or no traps are present.

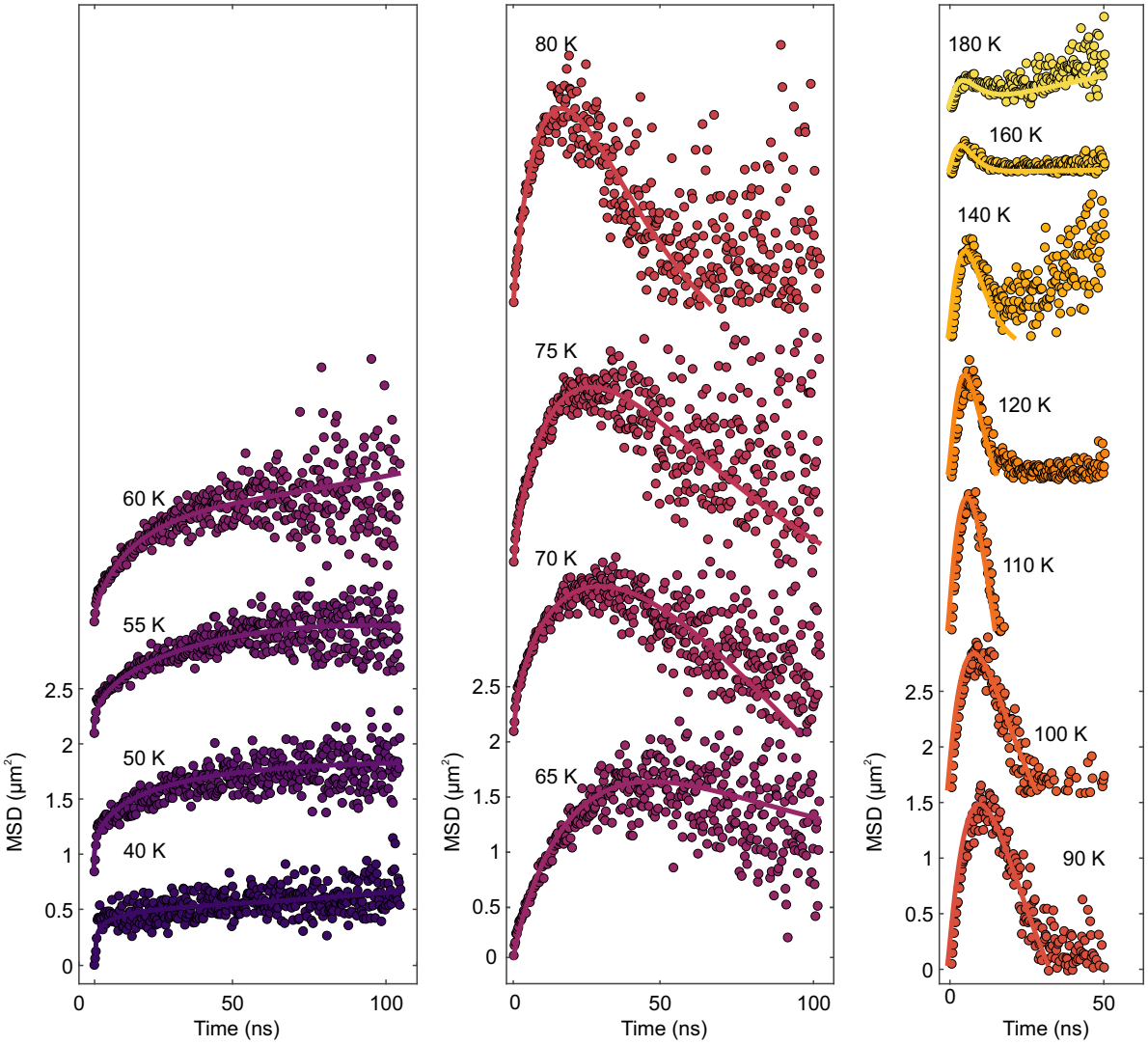

Figure 4.24: The figure shows the temporal MSD trends measured for exciton diffusion in a 3 ML PNPL film for temperatures from 40 - 180 K (dark purple to yellow data points). The lines correspond to phenomenological fits covering the subdiffusive and trap state limited model.

4.3.3 Universal Exciton Diffusion Behavior

As investigated so far, there are two fundamentally different temperature regimes where the MSD values, i.e., the diffusivities, show different responses to an increasing temperature. Here we will pay more attention to the actual MSD values since, as stated above, the total MSD value initially rises with increasing temperature in the low-temperature regime. In contrast, this trend changes in the high-temperature range. The total MSD values are tightly connected to the exciton diffusivity. Above, some methods were discussed to calculate the diffusivity by applying macroscopic or microscopic models which forecast different MSD behavior like subdiffusion, which generally results in a time-dependent or normal diffusion, i.e., time-independent diffusivity. For a nontrivial functional MSD dependence on time, we can apply the weighted average diffusivity calculation introduced in Sec. 2.4.1.3 which can be used for all MSD curves for all temperatures. Nontrivial means that a direct connection of the diffusivity to the MSD behavior according to a microscopic model can not be established in this context.

The resulting diffusivities for the whole investigated temperature range, i.e., 9 - 300 K, are shown

for the two SL PNC systems, i.e., 5 nm (blue data points) and 8 nm (turquoise data points), and the unordered 14 nm PNC cube film (green data points) in Fig. 4.25 a). The temperature which separates

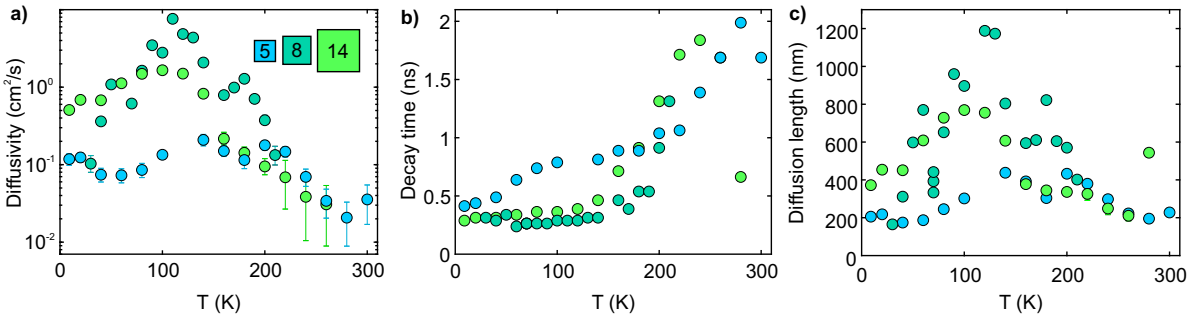

Figure 4.25: a) shows the averaged diffusivity b) PL decay time and c) diffusion length for temperatures 10 - 30 K. The averaged diffusivity is calculated with the weighted numerical model introduced in the main text. The diffusivity error originates from the Voigt profile fit error, estimated by calculating the MSD. The investigated samples are 5 and 8 nm PNC SL (blue and turquoise data points) and 14 nm PNC cube film. The figure is adapted from[97].

the two temperature regimes is slightly dependent on the PNC cube size, e.g., for the 5 nm PNC SL, the diffusivity stops to increase at 140 K. The diffusivity maximum for the 8 nm PNC SL is reached at 110 K, and for the largest cubic PNC system investigated here, the maximum appears at the smallest temperature, i.e., at 100 K. The absolute diffusivity at a constant temperature also has a PNC size dependency. The smallest PNC cubes have a diffusivity that is one order of magnitude smaller at 10 K than the largest tested PNC system (0.12 cm^2/s and 0.5 cm^2/s, respectively). Unfortunately, we could not measure exciton diffusion in the 8 nm PNC SL at these lowest temperatures. However, at 30 K, the average diffusivity of the 8 nm PNC SL is in between the 5 nm PNC SL and 14 nm PNC cube film diffusivity values for the whole low temperature regime. Therefore, it is plausible to assume that the diffusivities for the 8 nm PNC SL also have intermediate values for temperatures from 10 to 30 K. The temperature-dependent diffusivities for the different PNC systems are present in Fig. 4.25 a) as a semi-logarithmic plot. Therefore, a straight line corresponds to an exponential increase or decrease. The steepness of the diffusivity, i.e., the exponential rate, has no size-dependent trend. The 14 nm and 5 nm PNC systems show a similar increase, i.e., an exponentially growing trend for increasing temperature with the same exponent up to 120 K. In contrast, the 8 nm PNC SL has a far more prominent exponent. This faster-increasing rate for the 8 nm PNC SL leads to the highest diffusivities for the here measured samples in the temperature range 90 - 150 K. The maximal diffusivity for the 8 nm PNC SL is 9 cm^2/s, the highest diffusion parameter for a NC system up to date. The maximum diffusivity of the 14 nm PNC cube film and 5 nm PNC SL are 1 cm^2/s and 0.2 cm^2/s, respectively substantially smaller than the maximal diffusivity in the 8 nm PNC SL.

For the high-temperature regime, i.e., 120 - 300 K, the diffusivities generally decrease with increasing temperature for all PNC cube systems. The diffusivity decrease follows a linear trend in the semi-logarithmic plot. Therefore, it corresponds to an exponential decline. The exponential decreasing rate differs for different PNC sizes. It is largest for the 8 nm PNC SL and smallest for the 5 nm PNC SL. For instance, the exciton diffusion performance is better in a 5 nm PNC SL than in a 8 nm PNC SL at 200 K. In Fig. 4.25 b) the PL decay times for the total radiative PL decay channel is shown for the whole investigated temperature range. The PL decay time is the time at which the PL intensity has decreased to 1/e of its initial volume. The PL decay time is relatively fast for PNC systems compared to other NCs like CdSe where the PL decay is two orders of magnitude slower.[42,105] Especially for low temperatures, the PL lifetime often drops significantly to sub-nanosecond values as for the PNC systems investigated

here.[106] The PL decay times are below one ns for all three PNC systems up to 200 K. The PL decay times are shorter for larger PNC systems in the low-temperature regime. There is only a slight PL decay time increase for the 8 nm and 14 nm PNC systems, whereas the PL decay measured in the 5 nm PNC SL sample increase rapidly from 0.4 ns to 0.8 ns as the temperature is increased from 10 K to 100 K. After a threshold temperature of 140 K, the PL decay times for the larger PNC system rise with comparable steepness up to two ns. For temperatures between 200 - 300 K, the PL decay times of all PNC systems are close to each other, and the PL decay time increases with increasing temperature, which is typical for PNCs.[42] Note that this is not a general observation for NCs, e.g., for CdSe, the PL decay time increases for low temperatures due to the energy level ordering within those NCs where the PL decay is mainly dictated by a dipole forbidden recombination with a low radiative recombination rate.[43]

The corresponding diffusion lengths of all exciton diffusion measurements in PNC cube systems are depicted in Fig. 4.25 c). The trends mimic the temperature behavior of the diffusivities, i.e., initial rise of the diffusion length followed by a decrease with increasing temperature. The maximal diffusion length for different PNC cube systems seems to be size dependent. The maximal diffusion length appear to increase with PNC size at lower temperatures like the behavior already discovered for the diffusivities. The largest diffusion length for the 14 nm PNC cube sample of 800 nm and 1000 nm for the 8 nm PNC SLs are astonishingly large for a PNC system. In contrast, the maximal diffusion length for the 5 nm PNC SL is only 400 nm. The difference between the diffusion length in the low-temperature regime between the largest and smallest measured PNC system is not as high as their corresponding diffusivity difference. This reflects that the smaller PNC cubes have a longer PL lifetime in this temperature range and the square root dependency of the diffusion length to the diffusivity. The observed size dependence of the exciton diffusivity and diffusion length, especially in the low-temperature regime, hints strongly that PNC size outperforms PNC order concerning excitation transport for temperatures below 60 K. However, at higher temperatures, i.e., above 80 K, the diffusivities measured in the 8 nm PNC SL are higher than that of the 14 nm PNC cube film. After reaching the maximum, the diffusivity measured in an SL out of 8 nm PNC cubes decreases faster than for the other systems. Consequently, at temperatures above 220 K, the diffusivities measured in the 5 nm PNC SL even become slightly larger than in the other larger PNC systems.

To explain the complex exciton diffusion behavior for the two temperature regimes, several mechanisms have to be considered. Some of those mechanisms are phonon-assisted hopping, enhanced exciton transport and decreased exciton diffusivity, like a thermal-induced breakup of excitons. The contribution of the different effects to exciton diffusion performance is also temperature dependent, as we will see below. Here, we will investigate the diffusivity increase with increasing temperature, which is observable for the low-temperature regime. As discussed in Sec. 4.3.1.1, in the low-temperature regime, the bright-dark splitting of the exciton level becomes relevant. Excitons can only transfer to adjacent PNCs if they occupy a bright state. Thus, the averaged diffusivity is crucially dependent on the amount of bright excitonic states in the PNC system. Since fast exciton recombination from the bright exciton level happens within the first nanoseconds, the average amount of excitons occupying the dark level will sometimes be dominant. For successively increasing temperature, the bright exciton states can be repopulated with excitons occupying the dark level, and the exciton diffusion persists for longer times. This Boltzmann activation from a dark excitonic state to one of the three bright states is shown in Fig. 4.26 a) for the three different sized PNC cubes. The Boltzmann term is crucially dependent on the bright-dark exciton energy splitting depicted in the inset and already discussed

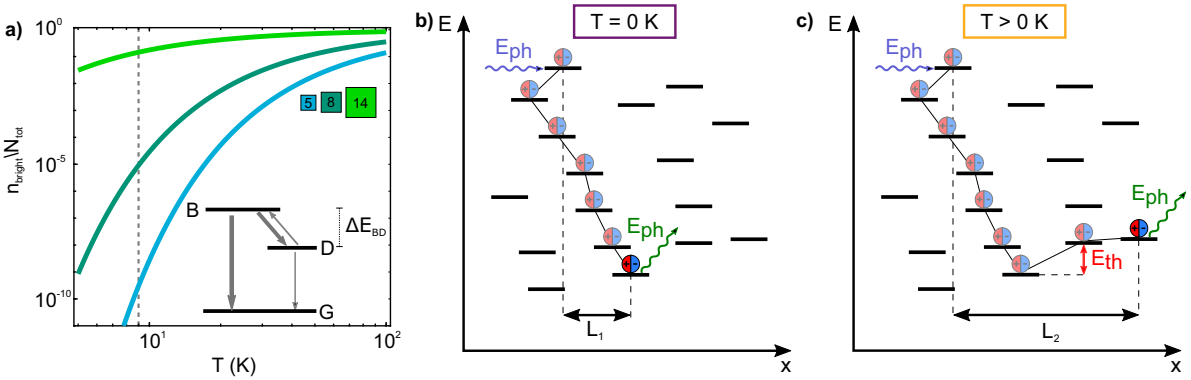

Figure 4.26: a) shows the probability of exciting an exciton occupying a dark state to a bright state for the three different PNC cube sizes. The inset shows the underlying energy level ordering of bright and dark states, separated by the size-dependent splitting energy ΔE_{BD}. b) shows a heterogeneous energy level landscape of different PNC cubes and an exemplary exciton transfer for some finite time at zero K. The exciton transfers stop at the lowest reached energy level. The exciton finally recombines radiatively since no system temperature is present to support a population of a higher laying adjacent PNC energy level. c) depicts the same schematics as b), whereas the system temperature is zero K. Hence, thermally induced FRET transfer between a lower laying energetic level of adjacent PNC cubes is, in principle, possible. The figure is adapted from[97].

above. The splitting energy is PNC size dependent, i.e., smaller-sized PNC cubes possess the larger bright-dark energy splitting, which in reverse makes it more unlikely to thermally excite an excitation in a dark state to a bright state. The possibility of exciting an exciton from the dark to the bright level is shown for the three different-sized PNC cubes, i.e., 5 nm, 8 nm, and 14 nm PNC cubes (blue, turquoise, and green, respectively), against the system temperature. Due to the larger splitting energy of the 5 nm PNC cubes (18.5 meV) the probability of exciting an exciton from the dark to the bright state is very small at 9 K (depicted by the dashed gray line), i.e., only 10^{-10}. The situation drastically changes for larger PNC cubes, with a thermal activation probability of 10^{-5} and 10^{-1} for the same temperature for 8 nm and 14 nm PNC cubes, respectively. Thus, the pure amount of bright states is higher for larger PNCs, especially for later times when the initially excited bright states have recombined radiatively or populate a dark state.

The exciton diffusivity is mainly dictated for early times, since the averaged diffusivities shown in Fig. 4.25 a) are calculated via Eqn. 2.32 which weights the MSD slope with the exciton PL decay. After some finite time, excitons can relax to the dark state from the bright excitonic levels. The total number of excitons in the system becomes exponentially lower with time due to nonradiative and radiative recombination. Therefore, the amount of dark excitonic states contributing to exciton diffusion via thermal activation to the bright state increases with time and progressively increase the exciton diffusivity. At earlier times, the initially bright excitons dominate the diffusivity. Nevertheless, for later times, the increase of the MSD is visible for the low-temperature regime for all PNC cubic systems (compare Fig. 4.20). The MSD behavior and values for earlier times stay qualitatively the same over a large temperature range; however, the MSD values increase slightly. This reflects that the initial transport due to the bright state level seems to be only quantitatively enhanced by the temperature increase. In contrast, the MSD values for later times increase and change qualitatively and quantitatively for higher temperatures. Therefore, this feeding process from the dark to the bright exciton level benefits exciton transport in PNC cube systems. Thus, it leads to an increasing exciton diffusivity with temperature.

Fig. 4.26 b) shows the schematics of a PNC cube system with a heterogeneous energy landscape of

different PNCs. For example, such an energy landscape can result from dispersed PNC sizes within a sample.[13] If such an energy landscape is present, thermal activation is needed to transfer the excitonic state from one PNC cube to an adjacent one with an energetically higher (bright) excitonic level. The figure depicts the active downhill transport over several PNC cubes. The reverse, i.e., thermal-induced exciton transfer to an adjacent PNC with a higher energy level, is prohibited due to the low system temperature. Therefore, the exciton transport stops at a host PNC where no PNC energy level is reachable which has at least the same (or a lower) energy as the host one. The exciton diffusion maintains even for the situation described above if the system temperature is comparable to the broadness of the energetic heterogeneity, as depicted in Fig. 4.26 c). For such conditions the systems' thermal energy can supply the missing energy to excite an exciton to an adjacent energetically higher state.[107]

A higher system temperature can also bridge the Stokes shift, which is always present in PNC systems and consequently enhances exciton diffusion for increasing temperature.[68] Since the FRET transfer rate depends on the overlap of the absorption and emission spectra of the acceptor and donor emitter, maximizing this overlap supports exciton transport. The donors and acceptors in the investigated samples are of the same kind, i.e., PNCs of roughly the same size. Therefore, the overlap is strongly affected by the Stokes shift in those PNCs. Thus, increasing the system temperature benefits exciton transport in PNC systems when considering only the above-mentioned effects. However, as we observe for the high-temperature regime, the exciton diffusivities experience an overall decreasing trend for increasing temperature, which the above-mentioned effects can not explain. Other mechanisms have to be considered which affect exciton diffusion negatively and outperform the exciton diffusion enhancing effects.

Fig. 4.27 a) depicts the energy diagram of the already introduced trap model explicitly for the high-temperature regime. Traps generally hamper exciton transport. The above-made conclusions of a decreasing trapping density for increasing temperatures in PNC systems were only valid for the deep trap model. Additionally, shallow traps are present, which delay the exciton transport via a normal FRET between two adjacent PNCs and consequently decrease diffusion. Some of the deep traps considered by the deep trap model can be transformed into shallow traps once the temperature becomes high enough. This leads to an absolute decrease in the deep trap density. However, the shallow trap density becomes larger. Additional pathways for producing shallow traps may also be open for larger temperatures as introduced in Sec. 2.1.3. Fig. 4.27 b) depicts schematically the exciton diffusion in a system where deep traps are present. However, shallow traps can also be present at any PNC site which will result in a diminished diffusion.

The above-mentioned Stokes shift is also temperature dependent in NCs. Especially in PNCs, it increases for rising temperatures as it is shown in Fig. 4.27 c). Note, this trend is reversed in other NCs like CdSe. Since the Stokes shift increases with increasing temperature, the overlap between donor emission and acceptor absorption spectra gets smaller. This larger Stokes shift at higher temperatures consequently leads to a reduced FRET rate, and thus the diffusivity decreases for increasing temperature. The temperature-dependent Stokes shift is also PNC size dependent, which can also be used to explain why the diffusivities decline of different rates in the high temperature regime.[69]

The excitons can also be ionized, i.e., break up into an unbound electron-hole pair. The Saha equation describes this ionization qualitatively and is mainly dictated by the exciton binding energy of the PNCs and the system temperature. The ratio of free charge carriers to bound electron-hole pairs is crucially dependent on the PNC size and the exciton binding energy. Fig. 4.27 d) depicts the ratio

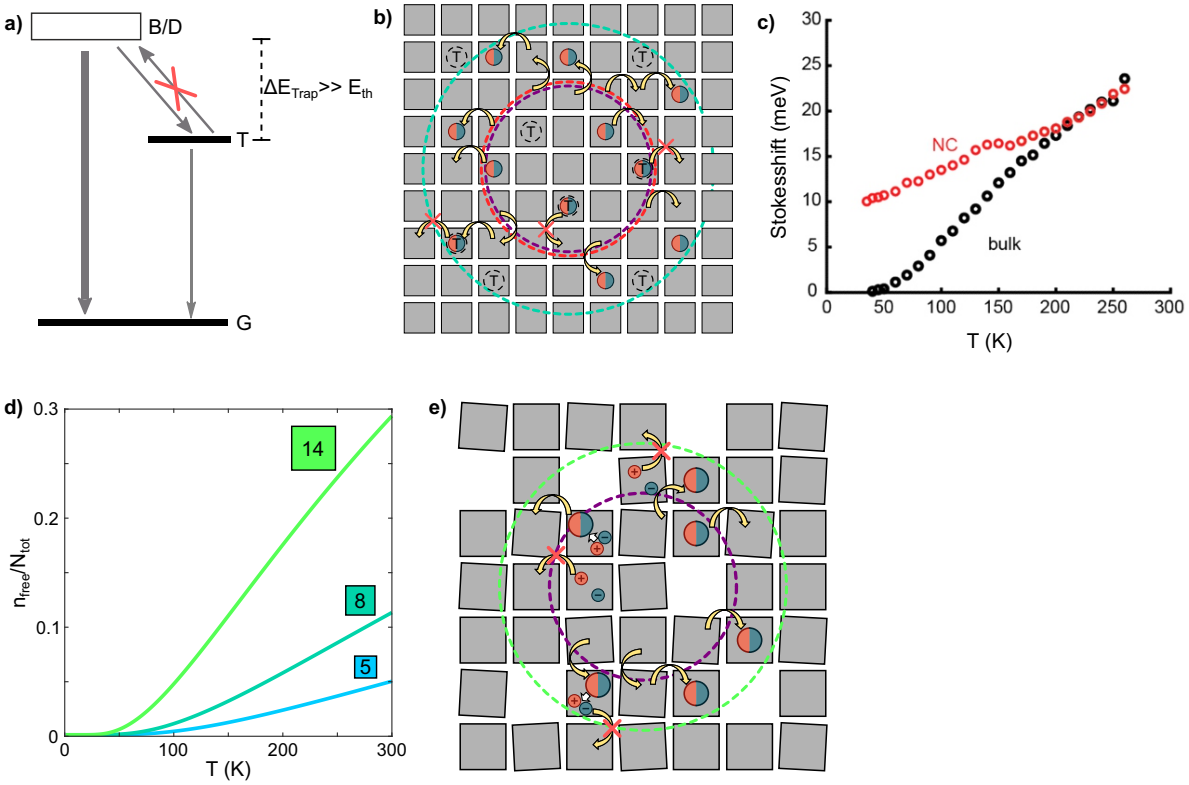

Figure 4.27: a) shows the energy diagram of a PNC cube where bright and dark states are degenerate and an energetic lower-laying radiative trap state. Detrapping is not possible since the thermal energy of the system is supposed to be smaller than the energetic exciton trap state distance, i.e., $\Delta E_{Trap} >> E_{th}$. b) depicts the schematics of many PNC cubes interacting with each other, i.e., excitons can transfer to neighboring PNC sites if they are in the B/D state located, whereas transfer is prohibited for trapped excitons. Dashed circles correspond to the excitation source (purple), trap state emission (red), and free exciton state emission (turquoise). c) depicts the Stokes shift in 7.2 nm large $CsPbBr_3$ cubes and $CsPbBr_3$ bulk material for temperatures of 50 - 250 K adapted from[69]. d) shows the fraction of free charge carriers to the entire excited states for the three different-sized PNC cubes. e) Scheme of exciton transfer in a disordered film. Free charge carriers can not transfer, as indicated by the crossed arrows. The dashed circles represent the laser excitation (purple) and PL emission (green).

of the number of free electron holes to the entire excited states, which is always larger the larger the PNC size, as shown for the sizes of the PNCs used in this thesis. Moreover, the temperature at which the amount of free charge carriers rises significantly is PNC size-dependent and coincides with the temperature which separates the low and high exciton diffusion regimes. This follows since only excitons can transfer to adjacent PNCs; therefore, a larger amount of excited states in the free charge carrier phase reduces the macroscopic diffusivity. Fig. 4.27 e) shows the schematic of such a system, where excitons can be formed from free charge carriers or vice versa. Transfer between adjacent PNCs is only allowed for excitons. The dashed circles illustrate the excitation laser (purple) and emission spot (green) FWHM.

From here on, the question arises if the temperature-dependent diffusivity evolution also expands to temperatures above room temperature which will be discussed in the following section.

4.3.4 Above Room Temperature Diffusion in PNPL and 14 nm Cube Films

So far, the influence of different shapes and thicknesses of all inorganic PNCs on exciton diffusion has been discussed for temperatures below room temperature, with all samples being mounted in a cryostat. What happens if the PNC film is installed in ambient conditions, i.e., temperatures around

room temperature (without protection layer against moisture or oxygen)? As already stated above, the temperature is a crucial parameter of exciton transport since it can not only supply the necessary missing energy for a non-radiative inter NC transfer, it also governs the ratio of bound to unbound electron-hole pairs in the system. According to Saha, there should be an equilibrium of the number of bound to free electron-hole pairs in individual NCs. This fraction depends on the exciton binding energy E_B and the system temperature T. These two effects are competing: The beneficial effect of additional energy to enable upwards FRET against the lower amount of excitons at higher energies. In Fig. 4.28 a) the MSD temporal evolution for four temperatures from 15 - 40 ℃ (blue to black data

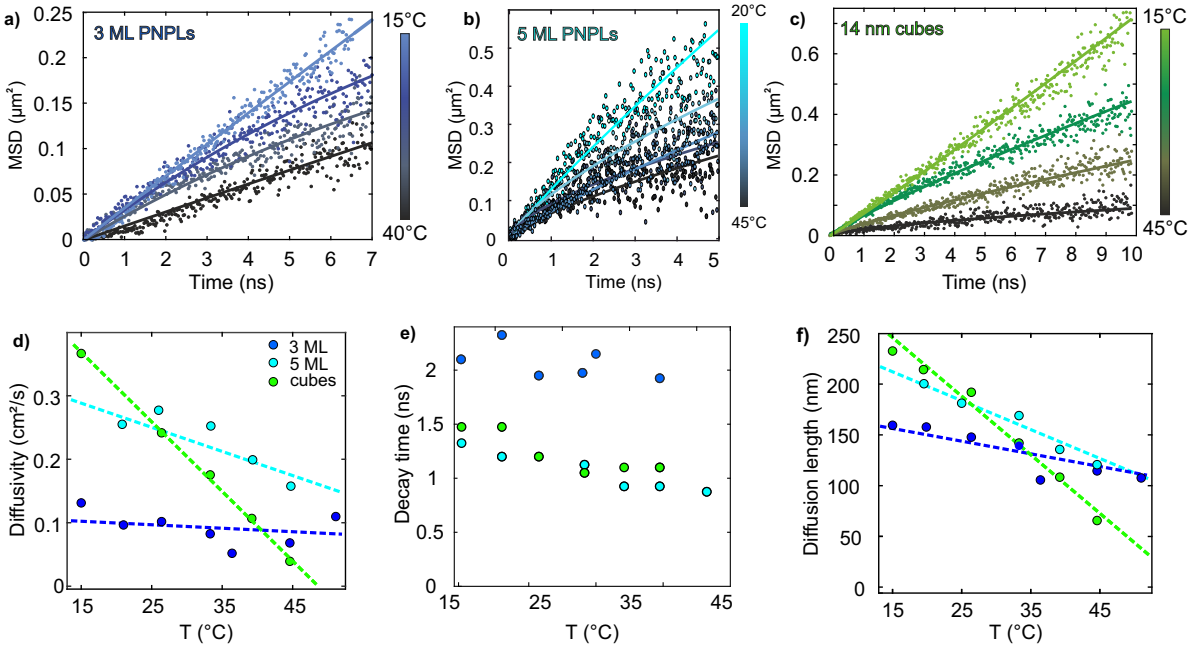

Figure 4.28: The figure presents the MSD curves for exciton diffusion measurements conducted around room temperature (15 - 45 ℃, bright to dark data points) in a a) 3 ML PNPL film, b) 5 ML PNPL film and c) a 14 nm PNC cube film. The lines correspond to subdiffusive fits to the recorded temperature MSD curves and have the same color code as the data points. d) yields the exciton diffusivities which result from fits to the subdiffusive model for the 3 ML (dark blue data points) and 5 ML (bright blue data points) PNPL films and for the 14 nm PNC cube (green data points) film. e) depicts the corresponding PL decay times and f) diffusion lengths for the same films (same color code). The dashed lines in d9+f) are guides to the eye with the same color code as the data points. The figure is adapted from[15].

points, respectively) are depicted for exciton diffusion measurements in a film consisting of 3 ML PNPLs. The lines correspond to subdiffusion fits of the corresponding temperature. The overall MSD behavior is as expected for exciton diffusion in the high temperature regime discussed for PNC cube structures in Sec. 4.3.2.1, i.e., decreasing MSD values for increasing temperature. The subdiffusive nature also becomes more pronounced for higher temperatures. Fig. 4.28 b) depicts the MSD values measured in a 5 ML PNPLs film for three different temperatures starting from light blue to black, 20 - 45 ℃ respectively. The MSD trends are the same as for the thinner PNPLs, i.e., decreasing MSD values and increasing subdiffusive behavior for increasing temperature. However, the pure MSD values are larger compared to the other PNPL film for all temperatures. The decrease in the MSD values versus temperature becomes even more pronounced by measuring the exciton diffusion behavior in a film consisting of PNC cubes with lateral expansion of 14 nm with corresponding MSD trends depicted in Fig. 4.28 c) for temperatures around room temperature (green data points). However, the absolute MSD values become smaller for increasing temperature for all measured PNC films. The temperature-induced decrease of the absolute MSD values is PNC size or thickness dependent. The

decrease rate is most prominent for the 14 nm PNC film and the smallest for the 3 ML PNPL film. To capture these exciton diffusion trends quantitatively, Fig. 4.28 d) presents the diffusivities according to subdiffusion fits for the 3 ML (blue data points), 5 ML (light blue data points) PNPL films, and the 14 nm PNC cube film (green data points) for temperatures from 15 to 50 ℃. Since the diffusivity is time-dependent for subdiffusive MSD behavior, the diffusivities here are averaged over time. The dashed lines are guides to the eye with the same color code as the presented data points. These trend lines show that the already observed overall decreasing diffusivity behavior for increasing temperature happens with rates which are PNC size dependent. This is accompanied by the fact that the absolute diffusivities are also size dependent, i.e., for temperatures slightly lower than room temperature (19 ℃) the exciton diffusion performance is better in a film consisting of larger PNCs (or cubes). At room temperature, the size dependency of the diffusivity is as expected, i.e., for smaller (thinner) PNCs the diffusivity is lower. However, at larger temperatures, the diffusivity size dependence vanishes. Accordingly, there are turning temperatures where the diffusivity for films consisting of larger individual PNCs becomes lower than for films comprising smaller PNCs. This appears for example at 26 ℃, where the diffusivity of a 5 ML PNPL film becomes larger than the diffusivity of a 14 nm PNC cube film. At 45 ℃, the 3 ML PNPL film outperforms the 14 nm PNC cube film with respect to their diffusivities.

Fig. 4.28 e) shows the PL decay times for 3 ML (blue data points) and 5 ML (bright blue data points) PNPLs, and 14 nm PNC cubes (green data points) for all considered temperatures. At room temperature, the 5 ML PNPLs and the 14 nm PNC cubes exhibit PL decay times of around one ns, while the thinner PNPLs have a PL decay time of approximately twice that. The PL decay times for all PNCs follow the same trend of a slightly decreasing PL decay time for increasing temperature. This general trend may be caused by a larger nonradiative PL decay channel due to an increasing trap state density. Fig. 4.28 f) presents the diffusion lengths for the investigated PNC films and all investigated temperatures. The temperature dependence of the diffusion length mimics the diffusivity temperature dependence qualitatively, since the PL decay time for the 3 ML PNPLs within the investigated temperature range is generally larger than for the other PNCs, the diffusion length in 3 ML PNPL films is larger than would be expected if only considering the diffusivity. Additionally, the turning temperature, at which the 3 ML PNPLs film outperforms the 14 nm PNC film with respect to diffusion length, is slightly lower (33 ℃) than for the corresponding diffusivity in the PNC systems.

To explain the MSD behavior observed at temperatures above room temperature, we considered that the ratio of the two different phases of the excited state in a PNC, i.e., bound electron-hole pairs to free charge carriers, is mainly responsible for the different decreasing rates of the diffusivity in different PNC systems. These phases are schematically shown in Fig. 4.29 a) where the X represents the bound electron-hole pair, i.e., the exciton, whose state is energetically below that of the free charge carriers, i.e., holes and electrons. Both levels are separated by the exciton binding energy E_B, which is highly size dependent, as shown in the right panel. Due to the large differences in the size of the exciton binding energy in 14 nm PNC cubes (30 meV), 5 ML (80 meV), and 3 ML (200 meV) PNPLs, the ratio of excitons to the total amount of excited states in systems with temperatures above zero K is crucially PNC species dependent, as depicted in Fig. 4.29 b). The gray marked area is the temperature region of interest. The 14 nm PNC cubes have the lowest fraction of excitons (green line), whereas the 5 ML (light blue) and 3 ML (blue) PNPLs have higher fraction. The different diffusivity downward rate for the PNC systems originates from the lower amount of excitons in larger PNCs for increasing temperature. For the 14 nm PNC cubes, the decreasing rate with increasing temperature is

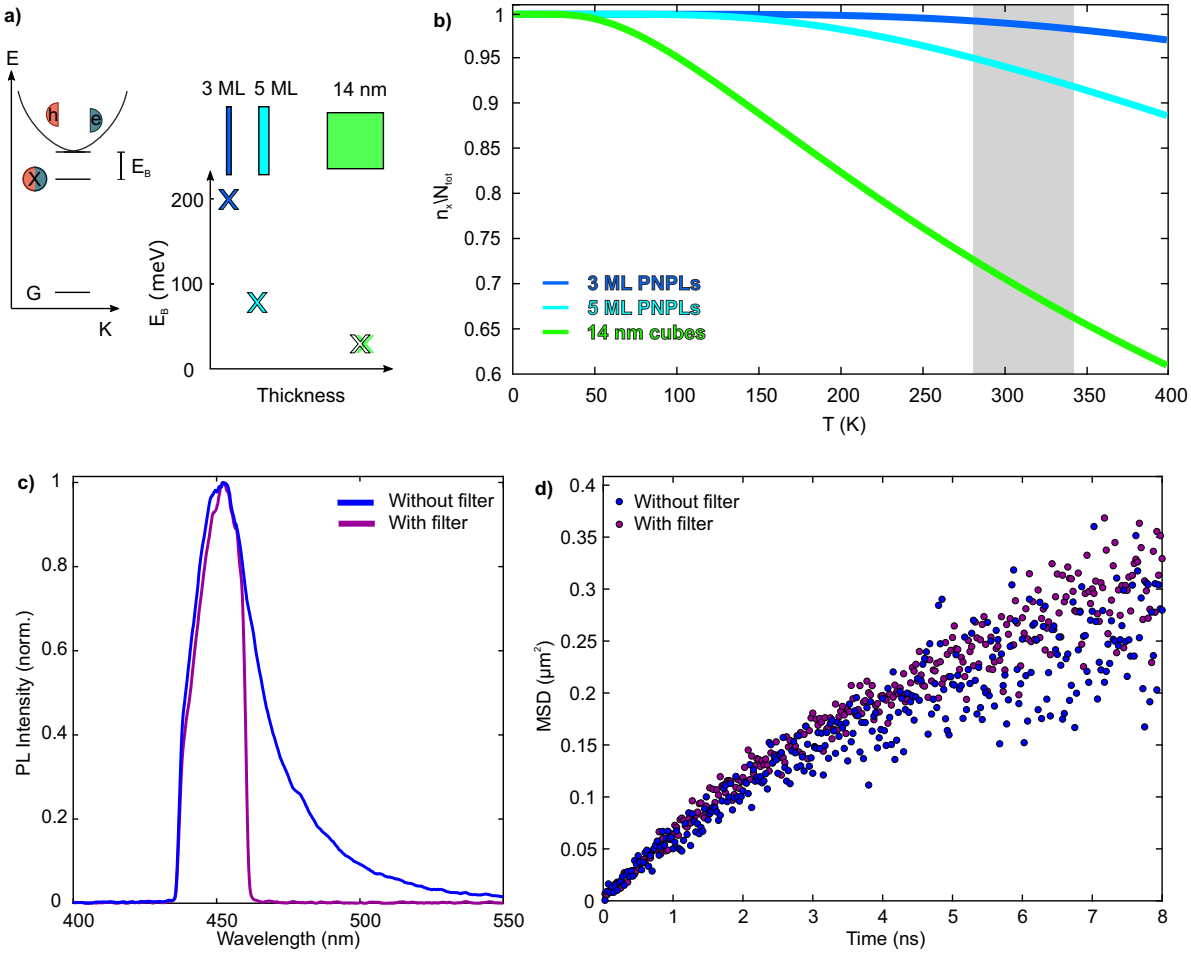

Figure 4.29: a) depicts the energy diagram of a single PNC with two excited phases, i.e., free charge carriers presented by the separated electron and hole in the upper parabola, and bound states, i.e., excitons, sitting in the lower parabola. b) illustrates the fraction of excitons to the total amount of excited states in the PNC system for a 3 ML (dark blue), 5 ML (light blue) PNPL film, and a 14 nm PNC cube film. The curves follow the Saha equation, and the gray area indicates the temperature region of interest. c) shows the PL spectra of the same 3 ML PNPL film with a tunable bandpass filter (purple) and without such a filter. d) yields the MSD values form exciton diffusion measurements in the same 3 ML PNPL film with a tunable bandpass filter (purple) and without such a filter.

highest, whereas the curve flattens for the PNPLs, i.e., for thinner PNCs. Only excitons can transfer between PNCs. For the cubes, the ratio of free charge carriers is larger, thus, not all excited states contribute to the macroscopic exciton diffusion process. However, for temperatures around room temperature, the amount of excitons in 14 nm PNC cubes seems to be sufficient to result in an overall larger diffusivity than for the PNPL films, since, excitons in a PNC film with larger individual sized PNCs are able to diffuse farther (see in Sec. 4.1.1). For increasing temperature, the amount of excitons in the PNC cube systems goes down faster compared to the amount of excitons in PNPLs. Thus, at some temperature (the above termed turning temperature), the average amount of excitons in a cube film is so low that the individual larger PNC size cannot compensate this lack of transferable excited states. Consequently, the exciton diffusivity for PNC cubes drops below the diffusivities of the PNPL films. The same would happen for the two PNPL films, however, we where not able to explicitly measure the turning temperature, since PNC degradation starts at high temperatures and we can only estimate the turning temperature (approximately 55 ℃) by following the dashed guides to the eye of the PNPL exciton diffusivity trends presented in Fig. 4.28 d).

The FWHM of the PNPLs' PL spectra are generally larger than of the 14 nm PNC cubes, as discussed

in Sec. 4.1.2 and shown in Fig. 4.5 a). Additionally, the PNPLs' PL spectrum also has a red tail which is absent in the 14 nm PNC cubes. To exclude trap states from being responsible for the lower exciton diffusion performance in PNPLs, we perform measurements at room temperature for the 3 ML PNPL film with and without an optical filter to remove the low energy PL shoulder. These two resulting spectra are depicted in Fig. 4.29 c), where the blue curve is the full PL spectrum of a 3 ML PNPL film without any optical filter in the emission beam path and the purple curve represents the PL spectrum when a tunable bandpass filter was inserted into the emission beam path. Exciton diffusion measurements were conducted for both setups. The MSD trend for the configuration without an optical filter in the emission path, is depicted in Fig. 4.29 d) represented by the blue data points. The trend is as previously observed: subdiffusive at room temperature. The recorded temporal PL profiles can only result from recombining states which are located at energies within the optical band pass window. Therefore, the red tail of the 3 ML PNPL film's PL spectra does not contribute to the recorded PL profiles and thus also not to the MSD trend which is shown by the purple data points. However, both MSD trends, with and without optical bandpass filter, are essentially identical. Therefore, we can exclude that trap states are responsible for the non-linear exciton diffusion performance at room temperature for 3 ML PNPL films.

4.4 Exciton Diffusion Affected by Excitation Laser Power

The excitation power affects the number of excited states in a semiconductor. Therefore, the amount of excitons in a PNC film depends on the laser power. The number of excitons should be small to conduct exciton diffusion measurements. This way, exciton-exciton annihilation can be neglected, and the free diffusion process of the majority carrier, i.e., electrons, holes, or excitons, happens undisturbed. To exclude power-dependent non-radiative PL decay channels like Auger recombinations, we recorded the total PL against the applied fluence over four orders of magnitude for a 14 nm PNC cube film (Fig. 4.30 a)). The green data points follow a linear trend (green line) over the investigated fluence range up to 60 $\mu J/cm^2$. Thus, the PL output linearly depends on the excitation power/fluence input. According to Eqn. 2.17, the PL output does not follow a linear law if power-dependent non-radiative recombination processes get relevant, like Auger recombinations, trion, or bi-exciton recombination. These non-linear processes also alter the exciton PL decay behavior: a deviation from a mono-exponential decaying intensity. Therefore, the simple derivation of the MSD resulting from a temporal Gaussian profile broadening (introduced in Sec. 2.4.1) is not applicable if these higher processes are present. Since the whole spatial PL profile deviates from the simple Voigt/Gaussian form, which was investigated by Kulig et al. in WSe_2 and described as the halo effect. The one-dimensional PL distribution can be characterized by two separate Gaussian profiles, which are not in the laser excitation center where the PL is suppressed.[81]

However, the above-mentioned non-linear decay channels can be neglected due to the linearity of PL output to excitation fluence in an extensive power range (0.05 - 100 $\frac{\mu J}{cm^2}$). Therefore, the MSD evolution has to be independent of the excitation power according to Sec. 2.4.1. Surprisingly, the MSD trends depicted in Fig. 4.30 b) for the 14 nm PNC cube film show a clear positive correlation to the power dependency over four orders of fluence, i.e., from 0.1 - 100 $\mu J/cm^2$ (light green to dark green data points, respectively). The lines correspond to subdiffusion model fits to the corresponding data. Since we excluded power-dependent non-radiative decay channels being present at such fluences,

another physical reason has to be responsible for the power-dependent exciton diffusion performance. Since the exciton diffusion is positively correlated with excitation power, we investigate the influence of traps. Due to the linear PL intensity dependence presented in Fig. 4.30 a) the trap density is generally

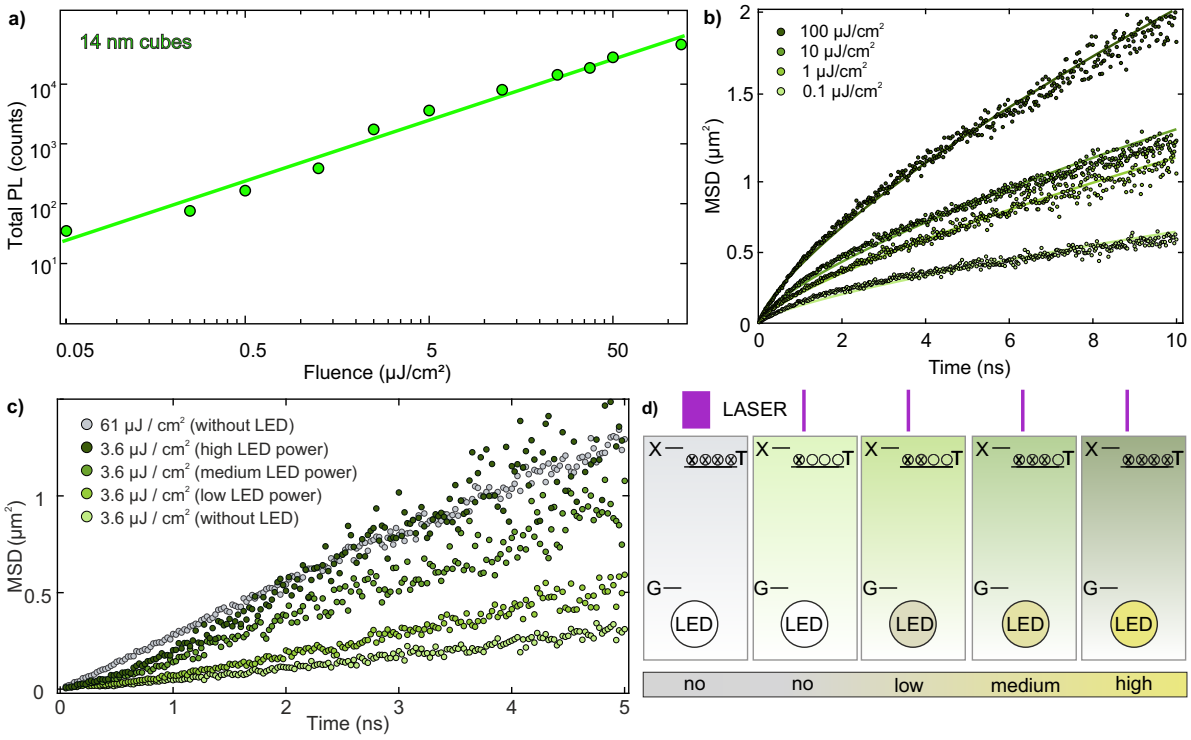

Figure 4.30: a) shows the total PL dependence on excitation power in a 14 nm PNC cube film, the green data points correspond to the actual measurements, and the green line represents the linear trend. b) presents the temporal MSD evolution in a 14 nm PNC cube film for different applied fluences, given in the inset, at the same film position. The dots represent the measured data, whereas the lines are subdiffusion model fits for each MSD curve. c) depicts the MSD temporal evolution for a 14 nm PNC cube film for a low (3.6 $\frac{\mu J}{cm^2}$, light green data points) and high (61 $\frac{\mu J}{cm^2}$, gray data points) laser fluence, where no additional continuous white light LED is coupled into the excitation path. The other three MSD trends correspond to exciton diffusion measurements conducted with the low laser fluence, whereas an additional white light LED is coupled into the excitation path. d) illustrates the schematic, which explains the increasing absolute MSD values for an increasing additional excitation source with trap state filling. The left panel corresponds to the high laser power (purple) with no LED light. All traps are filled (energy diagram of shallow traps (T), which lay below the first excited exciton level depicted by the X level). The other panels correspond to exciton diffusion measurements where the laser excitation fluence is kept low, and the LED power gradually increases from left to right.

low or the traps are mainly radiative or shallow traps. Radiative traps do not influence the excitation power dependency of the PL output intensity and shallow traps can be easily excited to radiative states at room temperature. However, the exciton diffusion is diminished by shallow traps as we have seen in previous sections.

To test the trap state hypotheses, we modify the setup, i.e., in addition to the pulsed excitation laser, a continuous white light LED is coupled into the excitation beam path to ensure exciton trap filling. The LED has to be a continuous light source since it should not affect the PL decay within the PNC film. Therefore, the LED constantly excites excitons in the PNC cube film, and the PL decay of those excitons can be seen as a continuous background. The resulting MSD measurements are presented in Fig. 4.30 c). Here, two different laser fluences are used, i.e., 3.6 and 61 $\frac{\mu J}{cm^2}$. For the low laser excitation power, the LED is also coupled into the excitation path and its power varied. The MSD is lowest for the low laser intensity and without the LED. As the LED power is raised, the MSD increases, and consequently, the macroscopic exciton diffusivity. For the highest LED power, the MSD curve approaches that of

the curve at the high laser power. All MSD curves show a similar linear diffusion behavior. As we have seen in Sec. 4.2.1, the qualitative deviations from sub to linear diffusion can be the result of voids. This explains the qualitative difference of the MSD evolutions presented in Fig. 4.30 b) and Fig. 4.30 c), since for both measurement series two different spots within a 14 nm PNC cube film were investigated. To explain the power dependence of the MSD curves, we apply a trap state model, which is schematically depicted in Fig. 4.30 d). The left panel shows the measurement setting where a high laser fluence is used and no additional excitation light (LED) is applied. Due to the high laser fluence, all shallow trap states of the PNC cubes within the film are filled, i.e., the untrapped excitons sitting in the X level can undergo FRET transitions to their neighboring PNC cubes without the possibility of getting trapped. Thus, the excitons can transfer unimpeded in this case. The trapped excitons can either become detrapped and contribute to the overall exciton diffusion process, or they survive and recombine radiatively after hundreds of nanoseconds. The situation changes if the laser power is reduced, as illustrated in the second panel from the left, where no additional LED excitation source is applied. Only some trap states are filled by excitons excited by the laser. Consequently, a portion of the initial free excitons can be trapped, i.e., cannot contribute to the exciton diffusion process, reducing the resulting MSD values. Turning the LED on and conducting the exciton diffusion measurement (middle panel in Fig. 4.30 d)), the excitons excited by the laser see a reduced trap density compared to the LED off configuration. Thus, more free excitons stay untrapped than for the same laser power without the LED. Therefore, the absolute MSD values increase with increasing LED power.

5
Conclusion

We have investigated $CsPbBr_3$ PNC systems with a particular focus on exciton diffusion. In particular, the first part of this thesis is devoted to intrinsic PNC properties affecting exciton transport. Traps within the PNCs diminish exciton diffusion performance, whereas increasing the PNC size has a beneficial influence on exciton transport. The film structure affects the exciton diffusion, voids within the ensemble decrease the diffusivity as well as exciton traps and are responsible for a subdiffusive MSD trend. The larger the voids, the higher the degree of subdiffusivity, as observed experimentally and confirmed by Monte Carlo simulations.
The second part of this thesis is devoted to unraveling how extrinsic factors affect exciton transport. The system temperature changes the diffusivity over more than one order of magnitude as the temperature is varied from 10 K to 280 K. The exciton diffusion process can be described in two different temperature regimes, a low temperature regime ranging from 10 - 100 K and a high temperature regime ranging from 100 - 280 K. Within the low-temperature regime, exciton diffusion increases with increasing temperature. This can be explained by thermally-induced hopping and a feeding effect of repopulating the bright exciton level with dark excitons in the smallest PNCs. For larger PNCs, the size-dependent bright-dark exciton splitting is too small to be resolved at cryogenic temperatures for ensembles. Exciton diffusivity stagnates and finally decreases with increasing temperature which characterizes the high temperature regime (100 - 280 K). For those temperatures, the bright-dark exciton splitting becomes irrelevant, like for the larger PNCs at low temperatures, and the negative effect of thermally activated traps on exciton diffusion outcompetes the diffusion enhancing bright-dark exciton splitting effect. Furthermore, as described by the Saha equation, more excited states exists as free charge carriers at higher temperatures, contributing to a decreasing diffusivity for increasing temperature since free charge carriers can not transfer in PNC ensembles. The temperature separating both regimes is dependent on the size and shape of the PNCs and lies in the range of 100 - 140 K.
The trap state dominance at room temperature is further validated by investigating trap state filling with the help of a secondary excitation source. This results in a power-independent exciton diffusion behavior if the secondary continuous light source saturates all trap states. Exciton traps also

become filled for high enough power of the probe pulse excitation source resulting in a trap saturation. However, this pulsed excitation power is more intense than normal sunlight sources and may cause damage within the PNC ensemble. Consequently, the power has to be kept low enough to ensure PNC film stability. Thus, there are indeed free exciton trap sites within the PNC ensembles which diminish exciton diffusion unless they are saturated at high enough excitation densities. This can be accomplished by the probe pulsed laser or a continuous light source.

This work includes a fundamental examination of PNC properties, particularly exciton transport performance in films or SLs. Surprisingly, the exciton transport performance obeys a complex temperature dependence, the diffusivity initially improves with increasing temperatures before reaching a maximum and then decreasing again. Thus, the best exciton diffusion performance will be reached at different temperatures depending on PNC size and shape. Concerning applications, one has to plan the device architecture, i.e., the active semiconductor layer, with respect to the operating temperature. However, this temperature is not of a universal nature, i.e., different PNC shapes, thicknesses, or ensemble structures have different temperatures where the diffusion maximum is reached. Therefore, one can tailor the active layer by considering the temperature that best fits the device, e.g., if the device will work in space at 4 K or in a desert on earth at 330 K.

Also, it would be insufficient to merely consider exciton diffusivity as the sole parameter for device engineering. Exciton diffusivity only governs the speed of exciton transport and, as was shown in this thesis, it is a time-averaged quantity which has to be treated carefully when comparing absolute values with literature results. Instead, the exciton diffusion length is more appropriate to describe exciton transport as it denotes the average distance excitons travel in a given material. The temperature-dependent trend of the exciton diffusion length is qualitatively the same as for the exciton diffusivity since the exciton lifetime does not vary as strongly over the investigated temperature range as the diffusivity, which changes by over two orders of magnitude.

Finally, the absolute values of the parameters characterizing exciton diffusion, namely exciton diffusion length and diffusivity are astonishingly high for the investigated NC types. They easily outcompete any other NC material investigated to date. PNC ensembles therefore represent excellent candidates for future applications.

References

[1] Maksym V. Kovalenko, Loredana Protesescu, et al. "Properties and Potential Optoelectronic Applications of Lead Halide Perovskite Nanocrystals." In: *Science* 358.6364 (2017), pp. 745–750. DOI: 10.1126/science.aam7093 (cited on pages 1, 28).

[2] Xiaoyu Zhang, Chun Sun, et al. "Bright perovskite nanocrystal films for efficient light-emitting devices." In: *The journal of physical chemistry letters* 7.22 (2016), pp. 4602–4610. DOI: 10.1021/acs.jpclett.6b02073 (cited on page 1).

[3] He Huang, Maryna I. Bodnarchuk, et al. "Lead Halide Perovskite Nanocrystals in the Research Spotlight: Stability and Defect Tolerance." In: *ACS energy letters* 2.9 (2017), pp. 2071–2083. DOI: 10.1021/acsenergylett.7b00547 (cited on pages 1, 20).

[4] Young-Hoon Kim, Sungjin Kim, et al. "Comprehensive defect suppression in perovskite nanocrystals for high-efficiency light-emitting diodes." In: *Nature Photonics* 15.2 (2021), pp. 148–155. DOI: 10.1038/s41566-020-00732-4 (cited on page 1).

[5] Mingming Liu, Qun Wan, et al. "Suppression of temperature quenching in perovskite nanocrystals for efficient and thermally stable light-emitting diodes." In: *Nature Photonics* 15.5 (2021), pp. 379–385. DOI: 10.1038/s41566-021-00766-2 (cited on page 1).

[6] Quinten A. Akkerman, Marina Gandini, et al. "Strongly emissive perovskite nanocrystal inks for high-voltage solar cells." In: *Nature Energy* 2.2 (2016), pp. 1–7. DOI: 10.1038/nenergy.2016.194 (cited on page 1).

[7] Feng Liu, Chao Ding, et al. "Colloidal Synthesis of Air-Stable Alloyed $CsSn_{1-x}Pb_xI_3$ Perovskite Nanocrystals For Use in Solar Cells." In: *Journal of the American Chemical Society* 139.46 (2017), pp. 16708–16719. DOI: 10.1021/jacs.7b08628 (cited on page 1).

[8] Donglin Jia, Jingxuan Chen, et al. "Dual Passivation of $CsPbI_3$ Perovskite Nanocrystals with Amino Acid Ligands for Efficient Quantum Dot Solar Cells." In: *Small* 16.24 (2020), p. 2001772. DOI: 10.1002/smll.202001772 (cited on page 1).

[9] Junzhi Ye, Mahdi Malekshahi Byranvand, et al. "Defect Passivation in Lead-Halide Perovskite Nanocrystals and Thin Films: Toward Efficient LEDs and Solar Cells." In: *Angewandte Chemie* 133.40 (2021), pp. 21804–21828. DOI: 10.1002/ange.202102360 (cited on page 1).

[10] Michaela Meyns, Mariano Perálvarez, et al. "Polymer-Enhanced Stability of Inorganic Perovskite Nanocrystals and Their Application in Color Conversion LEDs." In: *ACS applied materials & interfaces* 8.30 (2016), pp. 19579–19586. DOI: 10.1021/acsami.6b02529 (cited on page 1).

[11] Andreas Singldinger, Moritz Gramlich, et al. "Nonradiative Energy Transfer Between Thickness-Controlled Halide Perovskite Nanoplatelets." In: *ACS Energy Letters* 5.5 (2020), pp. 1380–1385. DOI: 10.1021/acsenergylett.0c00471 (cited on page 1).

[12] Robert M. Clegg. "Förster resonance energy transfer—FRET what is it, why do it, and how it's done." In: *Laboratory techniques in biochemistry and molecular biology* 33 (2009), pp. 1–57. DOI: 10.1016/S0075-7535(08)00001-6 (cited on page 1).

[13] Gleb M. Akselrod, Ferry Prins, et al. "Subdiffusive Exciton Transport in Quantum Dot Solids." In: *Nano letters* 14.6 (2014), pp. 3556–3562. DOI: 10.1021/nl501190s (cited on pages 1, 2, 27, 29, 31, 32, 49, 53, 54, 57, 94).

[14] Erika Penzo, Anna Loiudice, et al. "Long-Range Exciton Diffusion in Two-Dimensional Assemblies of Cesium Lead Bromide Perovskite Nanocrystals." In: *ACS nano* 14.6 (2020), pp. 6999–7007. DOI: 10.1021/acsnano.0c01536 (cited on pages 1, 28, 29, 31, 32, 53, 57).

[15] Michael F. Lichtenegger, Jan Drewniok, et al. "Electron–Hole Binding Governs Carrier Transport in Halide Perovskite Nanocrystal Thin Films." In: *ACS nano* 16.4 (2022), pp. 6317–6324. DOI: 10.1021/acsnano.2c00369 (cited on pages 1, 21, 48, 57, 58, 96).

[16] Zhilong Zhang, Jooyoung Sung, et al. "Ultrafast exciton transport at early times in quantum dot solids." In: *Nature Materials* 21.5 (2022), pp. 533–539. DOI: 10.17863/CAM.80070 (cited on pages 1, 2, 49, 60).

[17] Bernhard J. Bohn, Yu Tong, et al. "Boosting Tunable Blue Luminescence of Halide Perovskite Nanoplatelets Through Postsynthetic Surface Trap Repair." In: *Nano Letters* 18.8 (2018), pp. 5231–5238. DOI: 10.1021/acs.nanolett.8b02190 (cited on pages 2, 13, 14, 20, 39).

[18] Charles Kittel. *Introduction to Solid State Physics*. Vol. 8. Wiley New York, 2004. DOI: 10.1119/1.1974177 (cited on page 5).

[19] Gary Hodes. "Perovskite-Based Solar Cells." In: *Science* 342.6156 (2013), pp. 317–318. DOI: 10.1126/science.1245473 (cited on page 6).

[20] Xiaoli Zhang, Bing Xu, et al. "All-inorganic perovskite nanocrystals for high-efficiency light emitting diodes: dual-phase $CsPbBr_3$-$CsPb_2Br_5$ composites." In: *Advanced Functional Materials* 26.25 (2016), pp. 4595–4600. DOI: 10.1002/adfm.201600958 (cited on page 6).

[21] Jia Liang, Caixing Wang, et al. "All-Inorganic Perovskite Solar Cells." In: *Journal of the American Chemical Society* 138.49 (2016), pp. 15829–15832. DOI: 10.1021/jacs.6b10227 (cited on page 6).

[22] Feliciano Giustino and Henry J. Snaith. "Toward Lead-Free Perovskite Solar Cells." In: *ACS Energy Letters* 1.6 (2016), pp. 1233–1240. DOI: 10.1021/acsenergylett.6b00499 (cited on page 6).

[23] Nozomi Ito, Muhammad Akmal Kamarudin, et al. "Mixed Sn–Ge Perovskite for Enhanced Perovskite Solar Cell Performance in Air." In: *The journal of physical chemistry letters* 9.7 (2018), pp. 1682–1688. DOI: 10.1021/acs.jpclett.8b00275 (cited on page 6).

[24] Ievgen Levchuk, Andres Osvet, et al. "Brightly Luminescent and Color-Tunable Formamidinium Lead Halide Perovskite $FAPbX_3$ (X= Cl, Br, I) Colloidal Nanocrystals." In: *Nano letters* 17.5 (2017), pp. 2765–2770. DOI: 10.1021/acs.nanolett.6b04781 (cited on page 6).

[25] Shunsuke Hirotsu, Jimpei Harada, et al. "Structural Phase Transitions in $CsPbBr_3$." In: *Journal of the Physical Society of Japan* 37.5 (1974), pp. 1393–1398. DOI: 10.1143/JPSJ.37.1393 (cited on page 6).

[26] Constantinos C. Stoumpos, Christos D. Malliakas, et al. "Crystal Growth of the Perovskite Semiconductor $CsPbBr_3$: a New Material for High-Energy Radiation Detection." In: *Crystal growth & design* 13.7 (2013), pp. 2722–2727. DOI: 10.1021/cg400645t (cited on page 6).

[27] Mujtaba Hussain, Muhammad Rashid, et al. "Spin–orbit coupling effect on energy level splitting and band structure inversion in $CsPbBr_3$." In: *Journal of Materials Science* 56.1 (2021), pp. 528–542. DOI: 10.1007/s10853-020-05298-8 (cited on page 7).

[28] Jacky Even, Laurent Pedesseau, et al. "Importance of Spin–Orbit Coupling in Hybrid Organic/Inorganic Perovskites for Photovoltaic Applications." In: *The Journal of Physical Chemistry Letters* 4.17 (2013), pp. 2999–3005. DOI: 10.1021/jz401532q (cited on pages 6, 8, 16).

[29] Jun Kang and Lin-Wang Wang. "High Defect Tolerance in Lead Halide Perovskite $CsPbBr_3$." In: *The journal of physical chemistry letters* 8.2 (2017), pp. 489–493. DOI: 10.1021/acs.jpclett.6b02800 (cited on pages 8, 9, 11).

[30] Peter Y. Yu and Manuel Cardona. *Fundamentals of Semiconductors: Physics and Materials Properties*. Springer, 2010. DOI: 10.1007/978-3-642-00710-1 (cited on pages 10, 12, 22).

[31] Jacov Frenkel. "On the Transformation of light into Heat in Solids. I." In: *Physical Review* 37.1 (1931), p. 17. DOI: 10.1103/PhysRev.37.17 (cited on page 12).

[32] Gregory H: Wannier. "The Structure of Electronic Excitation Levels in Insulating Crystals." In: *Physical Review* 52.3 (1937), p. 191. DOI: 10.1103/PhysRev.52.191 (cited on page 12).

[33] Loredana Protesescu, Sergii Yakunin, et al. "Nanocrystals of Cesium Lead Halide Perovskites ($CsPbX_3$, X= Cl, Br, and I): Novel Optoelectronic Materials Showing Bright Emission with Wide Color Gamut." In: *Nano letters* 15.6 (2015), pp. 3692–3696. DOI: 10.1021/nl5048779 (cited on page 13).

[34] Dengbao Han, Muhammad Imran, et al. "Efficient Light-Emitting Diodes Based on in Situ Fabricated $FAPbBr_3$ Nanocrystals: the Enhancing Role of the Ligand-Assisted Reprecipitation Process." In: *ACS nano* 12.8 (2018), pp. 8808–8816. DOI: 10.1021/acsnano.8b05172 (cited on page 13).

[35] Yu Tong, Eva Bladt, et al. "Highly luminescent cesium lead halide perovskite nanocrystals with tunable composition and thickness by ultrasonication." In: *Angewandte Chemie* 55.44 (2016), pp. 13887–13892. DOI: 10.1002/anie.201605909 (cited on pages 14, 37, 74).

[36] Gabriele Rainò, Michael A Becker, et al. "Superfluorescence from lead halide perovskite quantum dot superlattices." In: *Nature* 563.7733 (2018), pp. 671–675. DOI: 10.1038/s41586-018-0683-0 (cited on pages 14, 38, 40, 74, 78, 80).

[37] Simon C. Boehme, Maryna I. Bodnarchuk, et al. "Strongly Confined $CsPbBr_3$ Quantum Dots as Quantum Emitters and Building Blocks for Rhombic Superlattices." In: *ACS nano* 17.3 (2023), pp. 2089–2100. DOI: 10.1021/acsnano.2c07677 (cited on pages 14, 40, 68, 74).

[38] Leonid V. Keldysh. "Excitons in Semiconductor–Dielectric Nanostructures." In: *physica status solidi (a)* 164.1 (1997), pp. 3–12. DOI: 10.1002/1521-396X(199711)164:1<3::AID-PSSA3>3.0.CO;2-S (cited on page 15).

[39] Ana V. Rodina and Alexander L. Efros. "Effect of Dielectric Confinement on Optical Properties of Colloidal Nanostructures." In: *Journal of Experimental and Theoretical Physics* 122.3 (2016), pp. 554–566. DOI: 10.1134/S1063776116030183 (cited on page 15).

[40] David J. Griffiths and Darrell F. Schroeter. *Introduction to Quantum Mechanics*. Cambridge University Press, 2018. DOI: 10.1017/9781316995433 (cited on page 16).

[41] Mark Fox. *Optical Properties of Solids*. Oxford University Press, 2002. DOI: 10.1119/1.1691372 (cited on pages 16, 23).

[42] Michael A. Becker, Roman Vaxenburg, et al. "Bright triplet excitons in caesium lead halide perovskites." In: *Nature* 553.7687 (2018), pp. 189–193. DOI: 10.1038/nature25147 (cited on pages 16–18, 45, 71, 73, 74, 91, 92).

[43] Andrey L. Rogach. "Semiconductor Nanocrystal Quantum Dots." In: *Verlag: Wien* (2008). DOI: 10.1007/978-3-211-75237-1 (cited on pages 17, 92).

[44] Daniel Rossi, Xiaohan Liu, et al. "Intense Dark Exciton Emission from Strongly Quantum-Confined $CsPbBr_3$ Nanocrystals." In: *Nano Letters* 20.10 (2020), pp. 7321–7326. DOI: 10.1021/acs.nanolett.0c02714 (cited on pages 18, 48, 49, 71, 74, 77).

[45] Daniel Rossi, Tian Qiao, et al. "Size-dependent dark exciton properties in cesium lead halide perovskite quantum dots." In: *The Journal of Chemical Physics* 153.18 (2020), p. 184703. DOI: 10.1063/5.0027972 (cited on pages 18, 48, 71, 73, 77).

[46] Philippe Tamarat, Maryna I Bodnarchuk, et al. "The ground exciton state of formamidinium lead bromide perovskite nanocrystals is a singlet dark state." In: *Nature Materials* 18.7 (2019), pp. 717–724. DOI: 10.1038/s41563-019-0364-x (cited on pages 18, 48, 71).

[47] Shuli Wang, Mateusz Dyksik, et al. "Thickness-Dependent Dark-Bright Exciton Splitting and Phonon Bottleneck in $CsPbBr_3$-Based Nanoplatelets Revealed via Magneto-Optical Spectroscopy." In: *Nano Letters* 22.17 (2022), pp. 7011–7019. DOI: 10.1021/acs.nanolett.2c01826 (cited on page 18).

[48] Elena V. Shornikova, Louis Biadala, et al. "Addressing the exciton fine structure in colloidal nanocrystals: the case of CdSe nanoplatelets." In: *Nanoscale* 10.2 (2018), pp. 646–656. DOI: 10.1039/C7NR07206F (cited on pages 18, 73).

[49] Moritz Gramlich, Michael W. Swift, et al. "Dark and Bright Excitons in Halide Perovskite Nanoplatelets." In: *Advanced Science* (2021), p. 2103013. DOI: 10.1002/advs.202103013 (cited on pages 18, 19, 45, 59, 65, 73, 77).

[50] Claudiu M. Iaru, Annalisa Brodu, et al. "Fröhlich Interaction Dominated by a Single Phonon Mode in $CsPbBr_3$." In: *Nature communications* 12.1 (2021), p. 5844. DOI: 10.1038/s41467-021-26192-0 (cited on page 20).

[51] Moritz Gramlich, Carola Lampe, et al. "How Exciton–Phonon Coupling Impacts Photoluminescence in Halide Perovskite Nanoplatelets." In: *The Journal of Physical Chemistry Letters* 12.46 (2021), pp. 11371–11377. DOI: 10.1021/acs.jpclett.1c03437 (cited on pages 20, 25, 26, 57).

[52] Andrei Buin, Patrick Pietsch, et al. "Materials Processing Routes to Trap-Free Halide Perovskites." In: *Nano letters* 14.11 (2014), pp. 6281–6286. DOI: 10.1021/nl502612m (cited on page 21).

[53] Quinten A: Akkerman, Silvia Genaro Motti, et al. "Solution Dynthesis Approach to Colloidal Cesium Lead Halide Perovskite Nanoplatelets with Monolayer-Level Thickness Control." In: *Journal of the American Chemical Society* 138.3 (2016), pp. 1010–1016. DOI: 10.1021/jacs.5b12124 (cited on page 21).

[54] Alexander Biewald, Nadja Giesbrecht, et al. "Local Disorder at the Phase Transition Interrupts Ambipolar Charge Carrier Transport in Large Crystal Methylammonium Lead Iodide Thin Films." In: *The Journal of Physical Chemistry C* 124.38 (2020), pp. 20757–20764. DOI: 10.1021/acs.jpcc.0c06240 (cited on page 21).

[55] J. Szczytko, L. Kappei, et al. "Determination of the Exciton Formation in Quantum Wells from Time-Resolved Interband Luminescence." In: *Phys. Rev. Lett.* 93 (13 Sept. 2004), p. 137401. DOI: 10.1103/PhysRevLett.93.137401 (cited on page 21).

[56] Valerio D'innocenzo, Giulia Grancini, et al. "Excitons versus free charges in organo-lead tri-halide perovskites." In: *Nature communications* 5.1 (2014), pp. 1–6. DOI: 10.1038/ncomms4586 (cited on pages 21, 22).

[57] Meghnad N. Saha. "On a physical theory of stellar spectra." In: *Proceedings of the Royal Society of London. Series A, Containing Papers of a Mathematical and Physical Character* 99.697 (1921), pp. 135–153. DOI: 10.1098/rspa.1921.0029 (cited on page 21).

[58] R. Cingolani, L. Calcagnile, et al. "Radiative recombination processes in wide-band-gap II–VI quantum wells: the interplay between excitons and free carriers." In: *JOSA B* 13.6 (1996), pp. 1268–1277. DOI: 10.1364/JOSAB.13.001268 (cited on page 21).

[59] Aurora Manzi, Yu Tong, et al. "Resonantly enhanced multiple exciton generation through below-band-gap multi-photon absorption in perovskite nanocrystals." In: *Nature communications* 9.1 (2018), p. 1518. DOI: 10.1038/s41467-018-03965-8 (cited on page 22).

[60] Michael A. Becker, Lorenzo Scarpelli, et al. "Long Exciton Dephasing Time and Coherent Phonon Coupling in $CsPbBr_2Cl$ Perovskite Nanocrystals." In: *Nano letters* 18.12 (2018), pp. 7546–7551. DOI: 10.1021/acs.nanolett.8b03027 (cited on page 23).

[61] Jiaming Li, Xi Yuan, et al. "Temperature-dependent photoluminescence of inorganic perovskite nanocrystal films." In: *RSC advances* 6.82 (2016), pp. 78311–78316. DOI: 10.1039/C6RA17008K (cited on page 23).

[62] See Mak Lee, Cheol Joo Moon, et al. "Temperature-Dependent Photoluminescence of Cesium Lead Halide Perovskite Quantum Dots: Splitting of the Photoluminescence Peaks of $CsPbBr_3$ and $CsPb(Br/I)_3$ Quantum Dots at low Temperature." In: *The Journal of Physical Chemistry C* 121.46 (2017), pp. 26054–26062. DOI: 10.1021/acs.jpcc.7b06301 (cited on page 23).

[63] Jagdeep Shah. *Ultrafast spectroscopy of semiconductors and semiconductor nanostructures*. Vol. 115. Springer Science & Business Media, 2013. DOI: 10.1007978-3-662-03770-6 (cited on page 24).

[64] Christian Wehrenfennig, Mingzhen Liu, et al. "Homogeneous Emission Line Broadening in the Organo Lead Halide Perovskite $Ch_3NH_3PBi_{3-x}Cl_x$." In: *The journal of physical chemistry letters* 5.8 (2014), pp. 1300–1306. DOI: 10.1021/jz500434p (cited on page 25).

[65] Hamid Pashaei Adl, Setatira Gorji, et al. "Homogeneous and inhomogeneous broadening in single perovskite nanocrystals investigated by micro-photoluminescence." In: *Journal of Luminescence* 240 (2021), p. 118453. DOI: 10.1016/j.jlumin.2021.118453 (cited on page 25).

[66] Michael C. Brennan, Jessica Zinna, et al. "Existence of a Size-Dependent Stokes Shift in $CsPbBr_3$ Perovskite Nanocrystals." In: *ACS Energy Letters* 2.7 (2017), pp. 1487–1488. DOI: 10.1021/acsenergylett.7b00383 (cited on pages 26, 71).

[67] Michael C. Brennan, John E. Herr, et al. "Origin of the Size-Dependent Stokes Shift in $CsPbBr_3$ Perovskite Nanocrystals." In: *Journal of the American Chemical Society* 139.35 (2017), pp. 12201–12208. DOI: 10.1021/jacs.7b05683 (cited on page 26).

[68] Michael C. Brennan, Aaron Forde, et al. "Universal Size-Dependent Stokes Shifts in Lead Halide Perovskite Nanocrystals." In: *The Journal of Physical Chemistry Letters* 11.13 (2020), pp. 4937–4944. DOI: 10.1021/acs.jpclett.0c01407 (cited on pages 26, 79, 94).

[69] Wenbi Shcherbakov-Wu, Peter C. Sercel, et al. "Temperature-Independent Dielectric Constant in $CsPbBr_3$ Nanocrystals Revealed by Linear Absorption Spectroscopy." In: *The Journal of Physical Chemistry Letters* 12.33 (2021), pp. 8088–8095. DOI: 10.1021/acs.jpclett.1c01822 (cited on pages 26, 71, 94, 95).

[70] Andrey L. Rogach, Thomas A. Klar, et al. "Energy transfer with semiconductor nanocrystals." In: *Journal of Materials Chemistry* 19.9 (2009), pp. 1208–1221. DOI: 10.1039/B812884G (cited on pages 27, 48, 59, 69).

[71] Andrey L. Rogach. "Fluorescence energy transfer in hybrid structures of semiconductor nanocrystals." In: *Nano Today* 6.4 (2011), pp. 355–365. DOI: 10.1016/j.nantod.2011.06.001 (cited on pages 27, 28).

[72] Th Förster. "Zwischenmolekulare Energiewanderung und Fluoreszenz." In: *Annalen der physik* 437.1-2 (1948), pp. 55–75. DOI: 10.1002/andp.19484370105 (cited on page 27).

[73] Theodor Förster. "Experimentelle und theoretische Untersuchung des zwischenmolekularen Übergangs von Elektronenanregungsenergie." In: *Zeitschrift für naturforschung A* 4.5 (1949), pp. 321–327. DOI: 0.1515/zna-1949-0501 (cited on page 27).

[74] David L. Andrews and David S. Bradshaw. "Virtual Photons, dipole fields and energy transfer: a quantum electrodynamical approach." In: *European journal of physics* 25.6 (2004), p. 845. DOI: 10.1088/0143-0807/25/6/017 (cited on page 27).

[75] Garth A. Jones and David S. Bradshaw. "Resonance Energy Transfer: From Fundamental theory to recent applications." In: *Frontiers in Physics* 7 (2019), p. 100. DOI: 10.3389/fphy.2019.00100 (cited on page 27).

[76] Michael Seitz, Alvaro J. Magdaleno, et al. "Exciton diffusion in two-dimensional metal-halide perovskites." In: *Nature communications* 11.1 (2020), pp. 1–8. DOI: 10.1038/s41467-020-15882-w (cited on pages 29, 32, 48).

[77] Gleb M. Akselrod, Parag B. Deotare, et al. "Visualization of exciton transport in ordered and disordered molecular solids." In: *Nature communications* 5.1 (2014), pp. 1–8. DOI: 10.1038/ncomms4646 (cited on page 31).

[78] Jean-Philippe Bouchaud and Antoine Georges. "Anomalous Diffusion in Disordered Media: Statistical Mechanisms, Models and Physical Applications." In: *Physics reports* 195.4-5 (1990), pp. 127–293. DOI: 10.1016/0370-1573(90)90099-N (cited on page 31).

[79] Brendan D. Folie, Jenna A. Tan, et al. "Effect of Anisotropic Confinement on Electronic Structure and Dynamics of Band Edge Excitons in Inorganic Perovskite Nanowires." In: *The Journal of Physical Chemistry A* 124.9 (2020), pp. 1867–1876. DOI: 10.1021/acs.jpca.9b11981 (cited on page 32).

[80] Michael Seitz, Marc Meléndez, et al. "Mapping the Trap-State Landscape in 2D Metal-Halide Perovskites Using Transient Photoluminescence Microscopy." In: *Advanced Optical Materials* 9.18 (2021), p. 2001875. DOI: 10.1002/adom.202001875 (cited on pages 33, 34, 48).

[81] Marvin Kulig, Jonas Zipfel, et al. "Exciton Diffusion and Halo Effects in Monolayer Semiconductors." In: *Phys. Rev. Lett.* 120 (20 May 2018), p. 207401. DOI: 10.1103/PhysRevLett.120.207401 (cited on pages 35, 48, 99).

[82] Albert Einstein. *Investigations on the Theory of the Brownian Movement*. Courier Corporation, 1956 (cited on page 35).

[83] Yitong Dong, Tian Qiao, et al. "Precise Control of Quantum Confinement in Cesium Lead Halide Perovskite Quantum Dots via Thermodynamic Equilibrium." In: *Nano letters* 18.6 (2018), pp. 3716–3722. DOI: 10.1021/acs.nanolett.8b00861 (cited on pages 38, 39).

[84] Mahmut Ruzi. *voigt line shape fit*. MahmutRuzi(2023).voigtlineshapefit(https://www.mathworks.com/matlabcentral/fileexchange/57603-voigt-line-shape-fit),MATLABCentralFileExchange.RetrievedJuly4,2023.. "[Online; accessed October 31, 2021]". 2023 (cited on page 43).

[85] Raul Perea-Causin, Samuel Brem, et al. "Exciton Propagation and Halo Formation in Two-Dimensional Materials." In: *Nano letters* 19.10 (2019), pp. 7317–7323. DOI: 10.1021/acs.nanolett.9b02948 (cited on page 48).

[86] Shiekh Zia Uddin, Hyungjin Kim, et al. "Neutral Exciton Diffusion in Monolayer MoS_2." In: *ACS nano* 14.10 (2020), pp. 13433–13440. DOI: 10.1021/acsnano.0c05305 (cited on page 48).

[87] Jonas Zipfel, Marvin Kulig, et al. "Exciton diffusion in monolayer semiconductors with suppressed disorder." In: *Physical Review B* 101.11 (2020), p. 115430. DOI: 10.1103/PhysRevB.101.115430 (cited on page 48).

[88] Samuel D. Stranks, Giles E. Eperon, et al. "Electron-hole diffusion lengths exceeding 1 micrometer in an organometal trihalide perovskite absorber." In: *Science* 342.6156 (2013), pp. 341–344. DOI: 10.1126/science.1243982 (cited on page 48).

[89] Silvia G. Motti, Franziska Krieg, et al. "$CsPbBr_3$ Nanocrystal Films: Deviations from Bulk Vibrational and Optoelectronic Properties." In: *Advanced Functional Materials* 30.19 (2020), p. 1909904. DOI: 10.1002/adfm.201909904 (cited on page 48).

[90] Alexander W. Achtstein, Sabrine Ayari, et al. "Tuning exciton diffusion, mobility and emission line width in CdSe nanoplatelets via lateral size." In: *Nanoscale* 12.46 (2020), pp. 23521–23531. DOI: 10.1039/D0NR04745G (cited on page 56).

[91] Mingrui Yang, Pavel Moroz, et al. "Energy Transport in $CsPbBr_3$ Perovskite Nanocrystal Solids." In: *ACS Photonics* 7.1 (2019), pp. 154–164. DOI: 10.1021/acsphotonics.9b01316 (cited on page 57).

[92] Jiawen Liu, Lilian Guillemeney, et al. "Long Range Energy Transfer in Self-Assembled Stacks of Semiconducting Nanoplatelets." In: *Nano Letters* 20.5 (2020), pp. 3465–3470. DOI: 10.1021/acs.nanolett.0c00376 (cited on page 59).

[93] Daria D. Blach, Victoria A. Lumsargis, et al. "Superradiance and Exciton Delocalization in Perovskite Quantum Dot Superlattices." In: *Nano letters* 22.19 (2022), pp. 7811–7818. DOI: 10.1021/acs.nanolett.2c02427 (cited on page 60).

[94] Camille Stavrakas, Géraud Delport, et al. "Visualizing Buried Local Carrier Diffusion in Halide Perovskite Crystals via Two-Photon Microscopy." In: *ACS energy letters* 5.1 (2019), pp. 117–123. DOI: 10.1021/acsenergylett.9b02244 (cited on page 69).

[95] Changsoon Cho, Sascha Feldmann, et al. "Efficient vertical charge transport in polycrystalline halide perovskites revealed by four-dimensional tracking of charge carriers." In: *Nature Materials* (2022), pp. 1–8. DOI: 10.1038/s41563-022-01395-y (cited on page 69).

[96] Julien Ramade, Léon Marcel Andriambariarijaona, et al. "Fine structure of excitons and electron–hole exchange energy in polymorphic $CsPbBr_3$ single nanocrystals." In: *Nanoscale* 10.14 (2018), pp. 6393–6401. DOI: 10.1039/C7NR09334A (cited on page 71).

[97] Andreas Bornschlegl, F. Michael Lichtenegger, et al. "Dark-Bright Exciton Splitting Dominates Low-Temperature Diffusion in Halide Perovskite Nanocrystal Assemblies." In: *researchsquare* (2023). DOI: 10.21203/rs.3.rs-2450378/v1 (cited on pages 72, 74, 77, 78, 81, 86–88, 91, 93).

[98] David Giovanni, Marcello Righetto, et al. "Origins of the long-range exciton diffusion in perovskite nanocrystal films: photon recycling vs exciton hopping." In: *Light: Science & Applications* 10.1 (2021), p. 2. DOI: 10.1038/s41377-020-00443-z (cited on page 73).

[99] Richard Ciesielski, Frank Schäfer, et al. "Grain Boundaries Act as Solid Walls for Charge Carrier Diffusion in Large Crystal MAPI Thin Films." In: *ACS applied materials & interfaces* 10.9 (2018), pp. 7974–7981. DOI: 10.1021/acsami.7b17938 (cited on page 73).

[100] R Ben Aich, I Saïdi, et al. "Bright-Exciton Splittings in Inorganic Cesium Lead Halide Perovskite Nanocrystals." In: *Physical Review Applied* 11.3 (2019), p. 034042. DOI: 10.1103/PhysRevApplied.11.034042 (cited on page 73).

[101] Michael A. Becker, Caterina Bernasconi, et al. "Unraveling the Origin of the Long Fluorescence Decay Component of Cesium Lead Halide Perovskite Nanocrystals." In: *ACS nano* 14.11 (2020), pp. 14939–14946. DOI: 10.1021/acsnano.0c04401 (cited on page 76).

[102] Freddy T. Rabouw, Johanna C. van der Bok, et al. "Temporary Charge Carrier Separation Dominates the Photoluminescence Decay Dynamics of Colloidal CdSe Nanoplatelets." In: *Nano letters* 16.3 (2016), pp. 2047–2053. DOI: 10.1021/acs.nanolett.6b00053 (cited on page 76).

[103] A. A. Kurilovich, V. N. Mantsevich, et al. "Trapping-influenced photoluminescence intensity decay in semiconductor nanoplatelets." In: *Journal of Physics: Conference Series*. Vol. 2015. 1. IOP Publishing. 2021, p. 012103. DOI: 10.1088/1742-6596/2015/1/012103 (cited on page 76).

[104] Michael J. Trimpl, Adam D. Wright, et al. "Charge-carrier Trapping and Radiative Recombination in Metal Halide Perovskite Semiconductors." In: *Advanced Functional Materials* 30.42 (2020), p. 2004312. DOI: 10.1002/adfm.202004312 (cited on page 76).

[105] Yuan Gao and Xiaogang Peng. "Photogenerated Excitons in Plain Dore CdSe Nanocrystals with Unity Radiative Decay in Single Channel: the Effects of Surface and Ligands." In: *Journal of the American Chemical Society* 137.12 (2015), pp. 4230–4235. DOI: 10.1021/jacs.5b01314 (cited on page 91).

[106] Gabriele Rainò, Georgian Nedelcu, et al. "Single Cesium Lead Halide Perovskite Nanocrystals at Low Temperature: Fast Single-Photon Emission, Reduced Blinking, and Exciton Fine Structure." In: *ACS nano* 10.2 (2016), pp. 2485–2490. DOI: 10.1021/acsnano.5b07328 (cited on page 92).

[107] Alan Baldwin, Géraud Delport, et al. “Local Energy Landscape Drives Long-Range Exciton Diffusion in Two-Dimensional Halide Perovskite Semiconductors.” In: *The Journal of Physical Chemistry Letters* 12.16 (2021), pp. 4003–4011. DOI: 10.1021/acs.jpclett.1c00823 (cited on page 94).

List of Figures

List of Tables

List of Abbreviations

ABS	Absorption spectrum
B	Bright exciton state
BDT	Bright-to-dark transition
BGT	Bright-to-ground state transition
CBM	Conduction band minimum
Cs-DOPA	Cesium diisooctylphosphinate
D	Dark exciton state
DBT	Dark-to-bright transitions
DC	Dichroic
DDAB	Didodecyldimethylamonium bromide
DGT	Dark-to-ground state transition
DLS	Defect localized state
EM	Emission spectrum
FRET	Förster resonant energy transfer
FWHM	Full width of half maximum
G	Ground exciton state
HAADF-STEM	High-angle annular dark-field scanning transmission electron microscopy
ML	Monolayer
MSD	Mean squared displacement
NC	Nanocrystal
PL	Photoluminescence
PLQY	Photoluminescence quantum yield
PNC	Perovskite nanocrystal
PNPL	Perovskite nanoplatelet
PSF	Point spread function
QD	Quantum dot
SEM	Scanning electron microscope
SL	Superlattice
TCSPC	Time correlated single photon counting
TOPO	Trioctylphosphine oxide
VBM	Valence band maximum

Acknowledgements

Within these final pages, I want to thank everyone that was with and around me during the past four years of doing my Ph.D. project. First, I want to thank **Alex** from the bottom of my heart. He was/is my professional supervisor, but he is quite more than that. What I have learned from him, whether in science or in the interaction between him and his students I have never seen before. His excellent mood every day and the sessions with him after work turned the daily work routine into time that I enjoyed a lot. But soft skills is not the only thing I learned from him. His fascination for physics and real-world applications as well as his problem-solving enthusiasm spread over me during the past years. I hope I can maintain those throughout my entire life. I wish him all the best in his professional and personal life, you deserve it, and I hope I can call you a friend.
I also want to mention the people around me at the Nano Institute. When I started as a newbie, I got a warm welcome from **Caro** and **Moritz**, my predecessors. My gained lab skills, which I mainly learned from them, accelerated the fastest during my Ph.D. I also enjoyed the friendly atmosphere in our office where the job was not always the only or most important subject.
Andi started in the Nanospectroscopy group before me as a master's student and started after me with his Ph.D. project. I was impressed by his skills as the "alignment-Papst" and his sense for perfection. Also his cooking skills in managing "warme Seelen," which always costs 1 €, will be a constant in my life. Our computer expert **Ulrich**, who helped me with my computer problems during the Ph.D. phase and by setting up my private PC, was my chosen expert. I also want to mention my other Ph.D. colleagues from the former chemistry department, **Nina** and **Patrick**, who eventually decided to be on the good side of history. As I didn't know Patrick's surname until now, I had to ask him "wer er überhaupt sei" quite often; I hope I got it now. I appreciated the time being in the same office as Nina since she had a close connection to plants which I definitively miss. Due to her presence, not all of the plants in the office died. Both of you, I wish you all the best.
The crucial people for this written version of my work are the internal reviewers **Andi**, **Nina**, **Borni**, **Patrick**, and **Ulrich**. I am very grateful for all of your critical discussions and suggestions that helped to improve the final written work a lot.
Furthermore, I want to thank all my former students with whom I worked closely and fruitfully over the past four years. Starting with the exciton diffusion team consisting of **Jan**, **Borni**, **Leo**, and **Ole**, with whom I collaborated and published. I had great benefits from you guys, and I hope you can say this also vice versa. There are also my PNC printing students **Marc**, **Johannes**, **Levin** and **Tena** who struggled with the tedious project and setup I supervised on the behalf of **Randy**, the previous master student on the project (who is a cool dude). All of you managed the lab work excellently, and I hope I collaborate with people like you in my future life. Thanks also to the lonely wolf on the BIC project at the end of my Ph.D., **Matthias**, who originally built up the first exciton diffusion setup supervised by Andi.
Special thanks I want to say to **Stefan** and **Juri**. Them being master students within our group, we started out as working colleagues. Over the years, we became friends. I hope you feel the same way. I enjoyed the after-work beer with both of you and the "Raucherpausen" with Juri. They were perfect opportunities to sneak out of the office for a little break and chat.
Alex's group expanded, and there were also many other master students whose presence and expertise I appreciated: **Markus**, **Michelle**, **Fiona**, **Schubi** and **Xenia**. I wish you all the best in your personal and professional life.
I also want to mention the challenging competition from other Nano institute chairs **Matthias** Kestler and **Phillip** Bootz, who often came by for an after-work beer or a chat (or destroy our office basketball hoop). I hope I will always take Matthias philosophy of work seriously: "Wer früh kommt darf auch früh gehen". Besides that, I also enjoyed our scientific exchange. I am sure both of you will be successful during your academic life.

Was wäre das Leben ohne Freunde - möglicherweise erfolgreich, aber wahrscheinlich langweilig. Ich möchte hier allen danken, die mich während meiner Schulzeit und Ausbildungszeit unterstützt haben. Auch meinen längsten Freunden aus Alteglofsheim, wo meine Wurzeln lagen und immer liegen werden. Auch allen Freunde, die ich während meiner Studiumszeit kennen lernen durfte, sei es im Studium selbst, im Wohnheim (Barteam) oder durch andere Zufälle des Lebens. Durch euch war mir meine Zeit in München ein wunderbares Erlebnis, das ich niemals missen wollen würde.
Und natürlich euch, **Mama** und **Papa**. Nur durch euch hatte ich die volle Unterstüzung, die es mir während des Studiums, aber auch davor, erheblich leichter gemacht hat. Eure Art und Zuversicht und auch das Verständnis von Scheitern oder Misserfolg lässt mich verstehen, was Familie bedeutet. Es ist ein Band das ein Leben lang hält und auch allen Widrigkeiten trotzen kann. Für das alles danke ich euch von Herzen und hoffe, dass ich euch nur einen Bruchteil davon zurückgeben kann. **Stefanie**, als ältere Schwester bist du auch mit dem Studium früher fertig geworden als ich. Auf dich konnte ich stets bauen und deine kleine neu gegründete Familie gibt mir auch zusätzlich Rückhalt und Stabilität, die ich nicht missen wollen würde. Ich freue mich, das ich darin auch einen kleinen Teil ausfüllen darf.